Deformation properties of sand with initial static shear in undrained cyclic torsional shear tests and their modeling

（初期せん断を受けた砂の非排水繰返しねじりせん断試験時の変形挙動とそのモデル化）

by

Chiaro Gabriele

(キアロ　ガブリエル)

A thesis submitted in partial fulfillment
of the requirements for the degree of

Doctor of Philosophy

Department of Civil Engineering
University of Tokyo
Tokyo, Japan
September, 2010

Abstract

Slope failure has been one of the most serious geotechnical disasters caused by earthquakes that produced substantial economic loss and killed a great number of people. Yet, its mechanism is not well understood; in particular the catastrophic liquefaction-induced failure behavior of natural and artificial slopes of sandy deposits and the consequent development of extremely large ground deformation is only poorly understood.

Soil elements within the sloped ground are subjected to an initial static shear stress on the horizontal plane or an assumed failure plane. During earthquake shaking, these elements are subjected to additional cyclic shear stress due to shear waves propagating vertically upward from the bedrock. The superimposition of static and cyclic shear stresses can have major effects on the response of soil, leading to liquefaction-induced failure of natural and artificial slopes of sandy deposits and the consequent development of extremely large ground deformation.

As far as the authors have investigated in the literature, there exists no previous study on the role of initial static shear stress on the undrained cyclic behavior of saturated sand in which the strain level could exceed more than 20 %. In previous studies, in the case of simple shear tests or torsional shear tests, the shear strain level was limited to 10 % due mainly to mechanical limitation of the employed apparatus; as well, in the case of triaxial tests, due to larger extents of non-uniform deformation of the specimen at higher strain levels, the axial strain level could not exceed 20 %.

With the intention of investigating the effects of initial shear stress on the large deformation properties of loose sand with initial static shear, a series of undrained cyclic torsional shear tests were performed on saturated loose Toyoura sand specimens up to single amplitude of shear strain of about 50 % under various combinations of static and subsequent cyclic shear stresses.

From the study of failure mechanisms, based on the difference in the effective stress path and the modes of development of shear strain during both monotonic and cyclic undrained torsional shear loading, the observed types of failure could be distinguished into three types: cyclic liquefaction (LQ), rapid flow liquefaction (RF) and residual

deformation (RD) failures.

It was found that the failure behavior is a consequence of the degree of reversal loading. In fact, in case of stress reversal and intermediate loadings, failure could be associated with full liquefaction, followed by extremely large deformation in the post-liquefaction process (i.e., LQ and RF failure behaviors). On the other hand, in the case of non-reversal loading, the residual deformation brought the specimen to failure (i.e., formation of spiral shear band) although liquefaction did not occur.

The test results showed that the presence of initial static shear does not always lead to an increase in the resistance to liquefaction and strain accumulation; in fact, both can either increase or decrease by increasing the static shear depending on the extent of stress reversal and the failure behavior. However, in this study it was found that the two-phase change in liquefaction resistance (i.e., strictly speaking resistance against strain accumulation) can be associated with a two-phase change in the failure behavior from LQ to RF and from RF to RD.

The mode of development of residual deformation exceeding 50% was also investigated. It was found that large deformation could be developed in different ways according with the type of failure that sand experienced.

To simulate the behavior of saturated sand under undrained cyclic loading which leads to liquefaction and large cyclic shear strain development, an elasto-plastic constitutive model which can describe both monotonic and cyclic torsional shear behaviors of saturated sand under drained or undrained condition was developed at IIS (Institute of Industrial Science), University of Tokyo.

It is noteworthy that the motivation of the current study comes from the successful attempts as above described in simulating the liquefaction behavior of sand as well the cyclic large deformation behavior. However, no attempt has been made so far to model the undrained behavior of sand by considering the effect of static shear.

With the aim of simulating the behavior of saturated sand with initial static shear undergoing undrained cyclic loading which leads to liquefaction and large cyclic shear strain development, an elasto-plastic constitutive model which can describe both monotonic and cyclic torsional shear behaviors of saturated sand with initial static shear under drained or undrained condition was presented in this study.

The proposed model could simulate the behavior of loose saturated sand subjected to

undrained torsional shear loading, under general conditions of stress reversal, intermediate and non-reversal loadings by varying the initial static shear and the amplitude of the subsequent cyclic shear stresses (i.e., varying the degree of reversal stress).

The liquefaction behavior of sand, described in terms of effective stress path, could be qualitatively modeled until the specimen enters into a full liquefaction state ($p' \cong 0$), as well as during the cyclic mobility process. The stress-strain relationship could be qualitatively simulated up to a strain level of 8% until the specimens enter into a steady state.

The simulation results of both monotonic and cyclic undrained behavior could be employed to evaluate the failure behavior of sand. Therefore, cyclic liquefaction (LQ), rapid flow liquefaction (RF) and residual deformation (RD) failures were simulated. As well, by conducting additional numerical simulations, the behavior called as no-liquefaction and no-failure (NN), in which either liquefaction or failure did not take place even after applying several tens of cycles, could be defined.

Simulation results confirmed that the resistance against strain accumulation can either increase or decrease depending on the extent of reversal stress and the type of failure; in addition, it was confirmed by numerical simulations that the mode of development of residual deformation depends on the type of failure of sand.

Soils that are susceptible to liquefaction consist substantially of saturated uniform grain size distributions deposited in loose states. However, the fact that a soil is susceptible to liquefaction does not guarantee that liquefaction will be actually initiated during an earthquake event. It is also recognized that the stress conditions (confining pressure, cyclic shear and initial static shear stresses) play an important role in the liquefaction behavior of soil, the type of failure mechanism and the mode of development of soil deformation, especially in the case of slopes of sandy deposits. Many studies on the liquefaction of sand, including the current one, show that under non-reversal stress conditions saturated loose sand most likely will not experience liquefaction. However, this does not mean that sand is very resistant against seismic loading; in fact, a significant magnitude of combined static and cyclic shear stresses may cause failure of soil even though liquefaction does not take place. For these reasons, it is definitely important not only to have a clear understanding of the liquefaction mechanisms, but also to carry out in

depth investigation on the effects of static shear on the failure modes of saturated sandy soil during undrained shearing.

With the scope of gaining a better understanding of the failure mechanisms of saturated sand, a method used to assess the failure behavior of sand specimens with initial static shear under undrained cyclic torsional shear loading was presented.

The proposed method is defined by means of three parameters namely: (i) static stress ratio $SSR = \tau_{static} / p_0'$, (ii) cyclic stress ratio $CSR = \tau_{cyclic} / p_0'$, and (iii) undrained monotonic peak stress ratio $MPSR = \tau_{peak} / p_0'$; where: τ_{static} = the initial static shear stress; τ_{cyclic} = the single amplitude cyclic shear stress; τ_{peak} = the shear stress at peak state during the undrained monotonic loading ; and p_0' = the initial effective confining pressure. The *SSR* corresponds to the driving shear force induced by the inclination of slopes; the *CSR* represents the inertial force exerted by earthquakes; while the *MPSR* takes into account the strength of soil which depends on the soil properties (e.g., relative density, etc) and the stress conditions.

By this method, called the "*Four-zone CSR/MPSR vs. SSR/MPSR method*", the initial static shear stress and the cyclic shear stress, measured in terms of SSR/MPSR and CSR/MPSR, respectively, were compared with the stress reversal line (i.e., SSR/MPSR = CSR/MPSR) and the undrained peak strength line (i.e., SSR/MPSR + CSR/MPSR =1). In accordance with the failure zone that these stress conditions correspond, the type of failure behavior of sand (i.e., LQ, RF, RD or NN) could be established.

Its applicability was investigated on a wide range of combinations of static and cyclic shear stresses on very loose, loose and dense sand by referring to: (i) the results of undrained cyclic torsional shear tests; and (ii) a number of single-element numerical simulations by employing the elasto-plastic constitutive model presented in this study.

On the basis of field data investigations from case histories of liquefaction-induced failure of sandy slopes during past earthquakes, the proposed method was used to compare the sand failure characteristics observed in the laboratory with the failure of slopes on site.

Acknowledgement

First and foremost I would like to express my deepest and sincerest gratitude to my supervisor, Professor Junichi Koseki, Institute of Industrial Science, The University of Tokyo, for his valuable suggestions, constructive criticisms and amazing patience, in making this research a reality. His wide knowledge and his logical way of thinking have been of great value for me. His understanding, encouraging and personal guidance have provided a great basis for the present thesis. His warmhearted care and attention grew on me an ever lasting love to laboratory soil testing.

Besides, I am deeply grateful to the Ph.D. thesis committee members, Professor Kazuo Konagai and Associate Professor Reiko Kuwano (Institute of Industrial Science), Professor Ikuo Towhata and Associate Professor Taro Uchimura (Geotechnical Engineering Laboratory), all from The University of Tokyo, for their valuable comments, criticisms, suggestions and important support for my research.

I wish to express my warm and sincere thanks to Associate Professor Giuseppe Modoni, Universita' degli Studi di Cassino, Italy, who introduced to me The University of Tokyo. His consistent support and encouragement all though the period of Ph.D. enrollment are greatly appreciated.

I am deeply indebted to Associate Professor Takashi Kiyota for sharing its experiences about the problem issues involved as well as discussing on many aspects regarding the large deformation behavior of sand in undrained cyclic torsional shear tests.

My special appreciation goes to Mr. Takeshi Sato, Koseki Laboratory, for his highly cooperative supports in assembling both the mechanical and electronic components of the employed testing apparatus, teaching me the basic procedures of laboratory soil testing, and advising on trouble shooting. Thanks also for being smiling and offering a fun in every occasion.

I am grateful to Miss Michie Torimitsu, the secretary of Koseki Laboratory, for her kind support in handling the administrative aspects during the course of my study.

My special appreciation goes to Miss Yukika Tsutsumi, the technician of Koseki Laboratory, for all the supports she gave me.

Thanks are due to Mrs. Chieko Nohara, the secretary of Kuwano Laboratory, for her

help in some administrative concerns.

My sincere appreciation is also forwarded to both the Koseki Laboratory and the Kuwano Laboratory members. Especially thanks due to my tutor Mr. Hiroyuki Watanabe for helping me in numerous ways during my first step of life in Japan. Thanks to Dr. Susumu Nakajima and Dr. Nalin De Silva for teaching me how to perform torsional shear tests. Dr. Ruta Wicaksono, Dr. Ko Dong Hee, Dr. Tomonori Mikami, Mr. Sarju Mulmi, Miss Jina Lee, Miss Adriana Beltran, Mr. Cokorda Bagus, Mr. Laxmi Suwal, Mr. Javad Jalili (visiting researcher from Iran), Miss Jeanelle Fevrier and Mr. Seto Wahyudi, their kind and cooperative supports during my stay is highly appreciated. I fell to be very fortunate to meet Mr. Tadao Enomoto, a former student in Koseki Laboratory, who is a true warm and kind hearted friend. I also express my sincere gratitude to all fellow members not listed above. I wish them all the best in their own study and future life.

Thanks to Mr. Carlos Bacca for being my partner as striker in our international soccer team. If I scored several goals, it was due meanly to his great assistance.

I would like to thank all my friends in Italy, in Japan and all around the world for keeping our friendships alive by sending mails and letters, giving calls, etc.

I sincerely acknowledge the Ministry of Education, Science and Culture, Japan for providing the financial assistance for my graduate studies in Japan.

Last but not least, I would like to express my deepest gratitude to my family members, especially to my parents, for their never-ending support and encouragement during my whole course of study. My special gratitude is due to my brother Luca and his wife Monica, and my sister Candida for their loving support. I owe my loving thanks to Sangyoon, without her encouragement and understanding it would have been impossible for me to finish this work. This thesis and my future achievements are all dedicated to them with genuine appreciation and respect.

Tokyo in August 2010

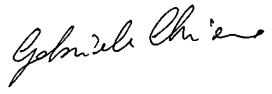

Contents

Chapter 3 : *Test conditions: material, apparatus and procedure*

3.1 Introduction……. 3-2
3.2 Test material……..... 3-3
3.3 Hollow cylinder torsional shear tests apparatus.…… 3-5
3.3.1 Medium-size hollow cylindrical specimen……..... 3-5
3.3.2 Vertical and torsional loading systems.……..…….…….....…….....…….....

Chapter 5 : ***Modeling the effects of initial static shear on the undrained cyclic behavior of sand***

Chapter 6 : *A method for assessing the failure behavior of sand with initial static shear*

Chapter 7 : *Conclusions and recommendations for future study*

Appendix A: *Sensitivity of the correction factors $\Delta\tau$ and $\Delta p'$*

Appendix B: *Sensitivity of the correction factors $\Delta\tau$ and $\Delta p'$*

LIST OF TABLES

LIST OF FIGURES

Chapter 1

Chapter 2

Chapter 3

Chapter 4

Chapter 5

Chapter 6

Appendix A

Appendix B

CHAPTER 1

Introduction

1.1 Landslides during earthquakes due to liquefaction

Slope failure has been one of the most serious geotechnical disasters caused by earthquakes that produced substantial economic loss and killed a great number of people. Yet, its mechanism is not well understood; in particular the catastrophic liquefaction-induced failure behavior of natural and artificial slopes of sandy deposits and the consequent development of extremely large ground deformation is only poorly understood.

Following large-magnitude earthquake events, such as 1964 Niigata and 1983 Nihonkai-Chubu earthquakes, extremely large lateral ground deformation has been observed in liquefied gentle slopes of sandy deposits. Although the gradient of the ground surface was merely of a small percent, lateral spreading reached several meters inducing serious damage to buildings, infrastructures and lifeline facilities (Hamada et al., 1986, 1988 and 1994).

With respect to the mechanism of the occurrence of large ground displacement, it is recognized that, due to liquefaction, flow failure of a slope, known as lateral spread, tends to occur when the mobilized shear stress of soil in its liquefied state exceeds the shear stress required for the static equilibrium of soil mass. Once liquefaction-induced deformations are triggered, they may become extremely large depending on the acting static shear stress.

To study the mechanism of permanent ground displacement due to liquefaction, Yasuda et al. (1992) conducted shaking table model tests. In these models the gradient of the slope surface, the thickness of liquefied layer, the density of liquefiable layer and other factors were changed. The main conclusion of this series of model tests was that permanent ground displacements did not occur on the boundary between the liquefied layer and the lower non-liquefied layer, but occurred within the liquefied layer with a constant shear strain.

However, although shaking model tests can provide important information about mechanism of liquefaction, it can not assess the liquefaction potential of specified sites. This assessment can be done by running undrained cyclic triaxial or torsional shear tests on undisturbed soil samples collected at the sites.

Many laboratory element tests under different conditions (in terms of density, confining pressure, stress ratio, over consolidation ratio, severity of liquefaction, etc…) have shown that large ground deformation always occurs after liquefaction of sand, and it can be developed when the effective mean principal stress in sand momentarily achieves zero state during undrained loading (Ishihara and Yasuda, 1975; Ishihara et al., 1975; Tatsuoka et al., 1986a and 1986b; Yasuda et al., 1995; Koseki and Ohta, 2001; Koseki et al., 2005 and 2007; among others). The test results obtained by Kiyota et al. (2008), who were the first to reach double amplitude shear strain exceeding 100% by using an innovative hollow cylinder torsional device, were remarkable.

However, it should be noted that, all these undrained cyclic torsional or triaxial tests are designed to simulate the stress condition in soil elements beneath the level ground; therefore they are carried out on isotropically consolidated specimens. Consequently, on these soil elements there is no initial static shear stress acting on the horizontal planes before undrained shearing.

It is a known fact that there are many cases of practical interest in which soil elements are subjected to initial static shear stress on the horizontal plane (e.g., natural slopes, slopes of dams and embankments, and level ground underneath structures). During a seismic event, the behavior of saturated sands in such stress conditions is not clear because it varies in a complicated manner depending on the magnitude of initial static shear and the subsequent cyclic stresses.

Yet, a limited number of studies have been conducted on the effects of static shear stress on the undrained behavior of sandy soils undergoing large deformation, due mainly to mechanical limitation of the employed apparatus and/or large extents of non-uniform deformation of the specimen at higher strain levels in triaxial compression tests.

In the last two decades, the records of major landslides, lateral movements of bridge supports and failures of waterfront structures reported as results of soil liquefaction have led to increasing efforts in the development of procedures for evaluating the liquefaction-induced large ground displacement of sandy deposits (e.g., Yasuda et al., 1992 and 1995; Hamada et al, 1994; Ishihara et al., 1996; Shamoto et al., 1997; among others), but until now, complete information regarding earthquake-induced displacements in the case of liquefaction domain for a given sand structure has not been available.

To understand the stress-strain response of sand in its pre- and post-liquefied state becomes essential for developing more cost-effective mitigative measures to minimize the effects of the natural disaster caused by slope failure triggered by earthquakes, and take the effect of liquefied ground displacement into the consideration in the seismic resistance design of structures.

In this regard, various approaches have been used by researchers to establish valid constitutive models useful for guiding engineers in their designs. As usual in the field of geotechnical engineering however, it is very difficult to propose practical tools; in fact, liquefaction represents a complicated problem and its solution requires the use of realistic constitutive equations and failure criteria.

Since it is almost impossible to describe the full soil behavior by existing constitutive model in many cases, laboratory investigations represent an essential tool in improving such models by simulating experimental observations.

1.1.1 Soil liquefaction

Under high frequency cyclic loading (i.e., earthquake shaking), cohesionless soils such as sands and in limited cases gravels, may completely lose their strength becoming more similar to a liquid than to a solid. This phenomenon, well known as “soil liquefaction”, may cause dramatic consequences to buildings, infrastructures (bridges, dams, embankments) and natural slopes, as often observed following severe earthquake events (Anchorage, Alaska, 1964; Niigata, Japan, 1964; San Fernando, California, 1971; Emperial Valley, California, 1979; Nihonkai-Chubu, Japan, 1983; Superstition Hills, California, 1987; Loma Pietra, California, 1989; Kobe, Japan, 1995; Kokaeli, Turkey, 1999; Niigata, Japan, 2004; etc…).

As it is well known that, coarse grained soils are made of individual grains, and that each grain is in contact with its neighboring particles. Due to the weight of the overlying soil strata, contact forces arise between the contiguous soil grains, with a normal and a shear component. Since the behavior of soil is mainly dictated by friction, its strength depends on the extent of the normal forces. According to the well known principle of effective stresses, the strength of a cohesionless saturated soil depends on the normal effective stress components, which are equal to the difference between the total normal stress components and the pore water pressure. If the total stress components remain

unchanged, an increase in pore water pressure has the effect of reducing the normal effective stresses and may thus lead to the collapse of soil.

Liquefaction may occur on saturated loose sands under the effect of quick cyclic loading like those excited by earthquakes. In fact, under such loading conditions the soil structure is deeply modified with the particles tending to move in a denser configuration. In case of fine sands there is not enough time for the water to be expelled out from the soil pores and thus a build up of water pressure occurs. When this pressure becomes equal to the total stress acting on the soil, the normal effective stresses are totally erased and thus the soil particles become free to move independently from the neighboring ones; in other words, the soil behaves like a liquid. The occurrence of this phenomenon is regulated by the extent of the seismic event (magnitude, peak ground acceleration) and by the density and the mechanical characteristics of the soil.

Practical methods for evaluating the liquefaction potential on site are traditionally based on the results of field investigations (Seed and Idriss, 1971; Seed, 1979; Seed et al., 1983 and 1985; among others) such as SPT and CPT tests, which summarize the mechanical properties of soil based on formulas defining the seismic events and on considerations based on past experiences.

1.1.2 Large displacement of gentle slopes due to liquefaction

During past earthquakes, large areas of ground were observed to shift laterally due to soil liquefaction. These liquefaction-induced lateral ground deformations have amplitudes ranging from small (1 cm) to very large (> 10 m) in the case of flow slides. They can take place for gently sloping ground conditions (0.1% to 6%). These deformations are usually driven by a combination of transient and static shear stresses and attributed to the loss of shear strength of underlying saturated soils.

In Japan, liquefaction-induced extremely large ground deformations could be observed on gentle slopes of sand, following the 1964 Niigata and 1983 Nihonkai-Chubu earthquakes (Hamada et al., 1994).

Hamada et al. (1986 and 1988) measured the permanent ground displacements caused by both of the above-mentioned earthquakes, by pre- and post-event aerial surveys. It was made clear that extremely large ground displacements, up to several meters,

occurred in the ground liquefied during the two earthquakes, although the ground surface was almost flat.

1.1.2.1 Ebigase area during the 1964 Niigata earthquake (Hamada et al., 1994)

On 16 June 1964, a magnitude 7.5 earthquake hit Niigata City and its neighboring area. The peak acceleration at ground surface in those areas was on the order of 0.16 g (Hamada et al., 1994). Due to the severity of the seismic shaking and particular soil conditions, a large area suffered liquefaction which caused breakage of foundation piles, settlement and tilting of buildings and tanks, failure of embankments, and serious damage to bridges and buried lifeline facilities.

Large permanent horizontal displacements, subsidence and rising zones, a number of ground fissures and various sand boils observed at Ebigase area in Niigata City, were the evidence that the gentle slope of a natural sandy levee was extensively damaged due to liquefaction (Fig. 1.1).

According to the arrows depicted in Fig. 1.1, the natural levee moved toward the old river bed. The ground surrounding the Ohgata Primary School, which was located on the top of the sandy deposit, moved in the north-west, north and north-east directions. The ground displacements in the north-west direction were predominant and continuous through 400 meters. Even though the gradient of the ground surface in that area was generally below 2%, the maximum horizontal displacement was over 8 meters. According to measurements of vertical displacement, extensively topographical changes took place. In fact, a wide subsided area was noted close to the top of the levee where the horizontal displacement began, and in the neighborhood area of Ohgata School a large number of ground fissures originated by tensile strain were observed. On the contrary, the ground rose at many points in the vicinity of the Tsusen River where the ground displacement ended and various sand and water boils were evident.

Field surveys revealed that the soil consists mostly of sand from sand dune, alluvial sandy soil and alluvial clayey soil. The alluvial sandy layer was very loose to loose since its SPT N values were below 10. The estimated liquefied soil had a thickness of 4 to 7 meters and extended from Ohgata School to Tsusen River.

1.1.2.2 Noshiro City during the 1983 Nihonkai-Chubu earthquake (Hamada et al., 1994)

On 26 May 1973, a magnitude 7.7 earthquake struck an ample area along Japan Sea coast in between Akita and Aomori prefectures. In Noshiro City, located about 100 km from the epicenter, liquefaction caused large ground displacement on the slopes of the Maeyama sand dune, which resulted in extensive damages to houses, quay walls, buried pipes and lifeline systems. The peak acceleration at the ground surface was on the order of 0.25 g (Hamada et al., 1994)..

Fig. 1.2 shows displacements on the gentle slopes of Maeyama sandy hill. On the northern slope of the hill, horizontal displacements were predominant; they began near the top and extended for more then 300 meters in a northerly direction. The maximum horizontal displacement achieved more than 5 meters. Ground failures consisting of sand boils, fissures and vertical gaps of the ground surface were observed on the slopes surrounding the top of the hill. A considerable number of fissures were found on the top part of the northern slope of the hill, where large tensile strains occurred due to the horizontal ground displacements that took place in the downward direction; in that area the ground surface subsided by 50 to 100 cm. On the other hand, the ground level rose at some locations near the toe of the slope, and a number of sand and water boils were observed. This phenomenon is very similar to the one at Ebigase area in Niigata City during the 1964 Niigata Earthquake, as described above.

Field surveys revealed that the soil consists mostly in sand, alluvial sand and alluvial clayey soil. The alluvial sandy layer was loose since its SPT N values are on the order of 10. The estimated liquefied soil, underlying the gentle sloped ground surface, ranged between 1 to 5 meters of thickness.

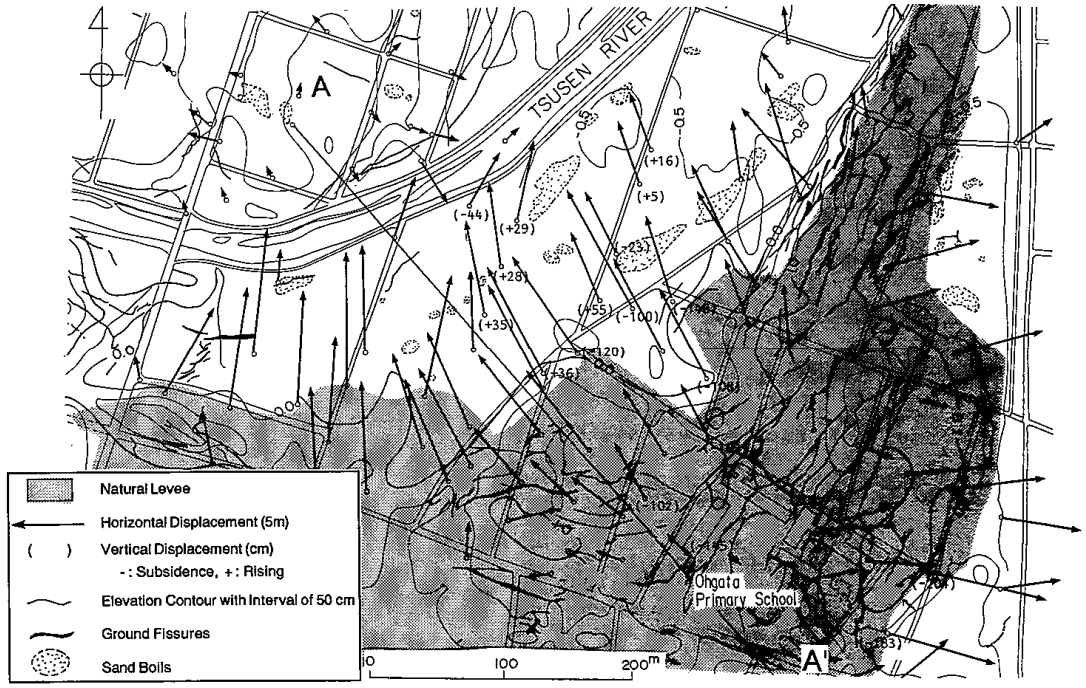

(a)

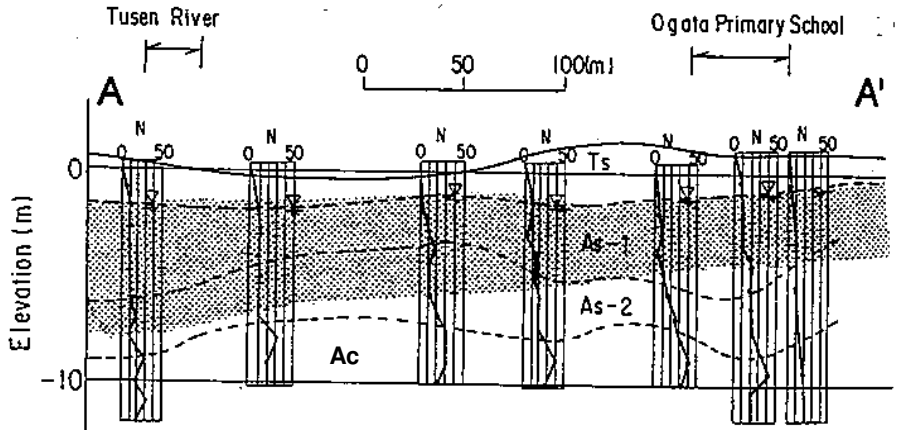

(Ts) surface dune sand; (As) alluvial sandy soil; (Ac) alluvial clayey soil

(b)

Fig. 1.1: Effects of the 1964 Niigata earthquake at Ebigase area in Niigata City (Hamada et al., 1994): (a) Liquefaction-induced ground displacement; (b) Soil conditions and estimated liquefied layer along section A-A'.

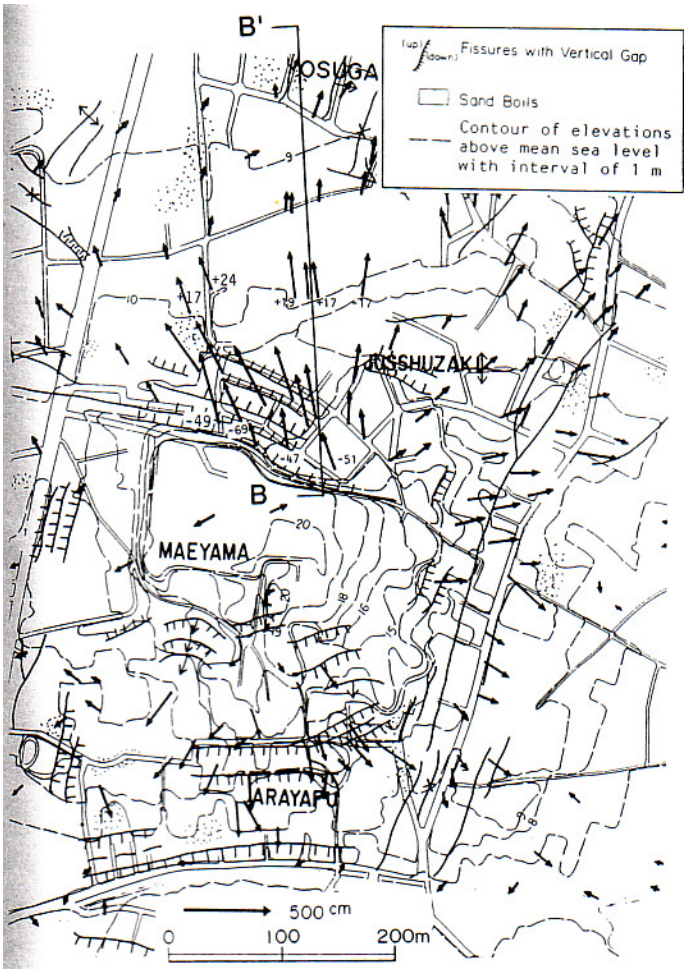

(a)

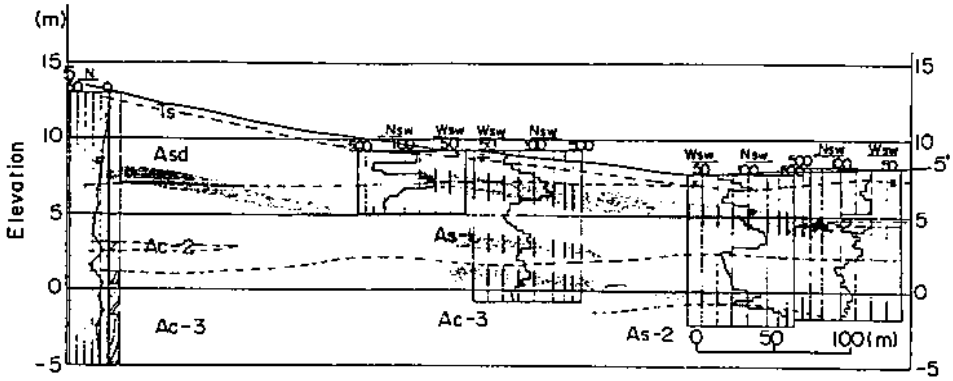

(Ts) surface soil; (Asd) dune sand; (As) alluvial sandy soil; (Ac) alluvial clayey soil

(b)

Fig. 1.2: Effects of the 1983 Nihonkai-Chubu earthquake in Noshiro City (Hamada et al., 1994): (a) Liquefaction-induced ground displacement; (b) Soil conditions and estimated liquefied layer along section B-B'

1.1.3 Previous studies on the effect of initial static shear stress

It is recognized from previous studies and some case histories of past earthquakes that the behavior of slopes or ground underneath structures (Fig. 1.3 and Fig. 1.4) composed by saturated sands is different from that of level ground during cyclic loading because the soil elements are subjected to an initial static shear stress on the horizontal plane or assumed failure surface. During earthquake shaking, these elements are subjected to additional cyclic shear stress due to shear waves propagating vertically upward from the bedrock. The superimposition of static and cyclic shear stresses can have major effects on the response of soil, leading to liquefaction and development of extremely large ground deformation.

Even though the behavior of saturated sand is known to be affected by the influence of initial static shear stress, a limited number of studies have been conducted on the effects of static shear stress on the undrained behavior of sandy soils undergoing large deformation, due mainly to mechanical limitation of the employed apparatus (e.g., simple shear tests) or large extents of non-uniform deformation of the specimen at higher strain levels (e.g., triaxial or torsional tests).

The results of pioneering studies on anisotropically consolidated sand sheared under undrained cyclic triaxial conditions (Lee and Seed, 1967; Seed, 1968) showed that the larger the ratio of initial static shear stress to initial confining pressure acting on a horizontal plane, the greater the horizontal cyclic shear stress required to induce liquefaction in a given number of stress cycles. In other words, the resistance to liquefaction increases with an increase in the static shear stress level.

On the other hand, the opposite tendency was observed by Yoshimi and Oh-oka (1975) as a result of ring torsional shear tests. In addition, they pointed out that to induce liquefaction and the development of large cyclic shear strain, the reversal of shear stress is necessary.

Castro (1975) and Castro and Poulus (1977) by considering the initial static shear level and the undrained residual shear strength (i.e., steady state) distinguished between sand failure by liquefaction and cyclic mobility. They concluded that the resistance to liquefaction decreases but the strain accumulation resistance increases with an increase in

initial static shear stress. As well, they discussed on the effect of axial extension during cyclic triaxial tests; they complained that the larger deformations observed in extension with respect to compression for a given deviator stress do not correspond to the field conditions, therefore generally cyclic triaxial tests overestimate the cyclic deformations that may be developed in the field due to liquefaction.

Vaid and Finn (1979) evaluated cyclic loading behavior of Ottawa sand under plane strain condition using a simple shear device. They clarified that in general the resistance to liquefaction can either increase or decrease due to the presence of static shear depending on the relative density of the sample.

Since it is considered that simple shear tests simulated field stress condition more closely, Tatsuoka et al. (1982) investigated the stress-strain behavior of sand under torsional simple shear conditions including the case with static shear. The results show that the strength defined at sufficiently large strain values was not reduced by the presence of initial shear stress but increased in some cases especially for dense sand. These results were well in accordance with those reported by Vaid and Finn (1979), confirming that a torsional simple shear apparatus could be used as a very useful tool for evaluating cyclic undrained stress-strain behavior of sands.

Further, Vaid and Chern (1983) showed that the contradictory conclusion in past studies were due to the difference in density of the sample, magnitude of static shear and the definition of liquefaction resistance. In addition, it was found that the cyclic strength can either increase or decrease due to the presence of static shear stress; in particular it was also observed that, during cyclic loading on loose sand with higher initial static shear, the cyclic strength was reduced due to flow deformation.

Mohamad and Dobry (1986) found that the initial static shear stress is also an important parameter to identify the behavior of sands between contractive and dilative.

Hyodo et al. (1991 and 1994) classified the behavior of anisotropically consolidated sample, sheared under undrained cyclic triaxial conditions, into three types: stress reversal, non-reversal and intermediate. Based on the difference in the effective stress paths and the stress-strain relationships, they observed that in the cases of stress reversal and intermediate on loose samples, failure could be associated with liquefaction, while in the other case residual deformation brought the sample to failure even though no liquefaction occurred; failure was not observed in the case of non-reversal on dense sample.

However, it should be noted that in all of the above studies, due to mechanical limitation of the employed apparatus and/or due to large extents of non-uniform deformation of the specimen at higher strain levels, as well technical difficulties in correcting for the effects of membrane force during the tests, the shear strain levels employed were limited to the range of 10% to 20%.

Therefore, they are not able to fully describe the occurrence of the liquefaction-induced ground deformations of several meters, which means that ground strain reaches over 100% on the slightly sloped ground.

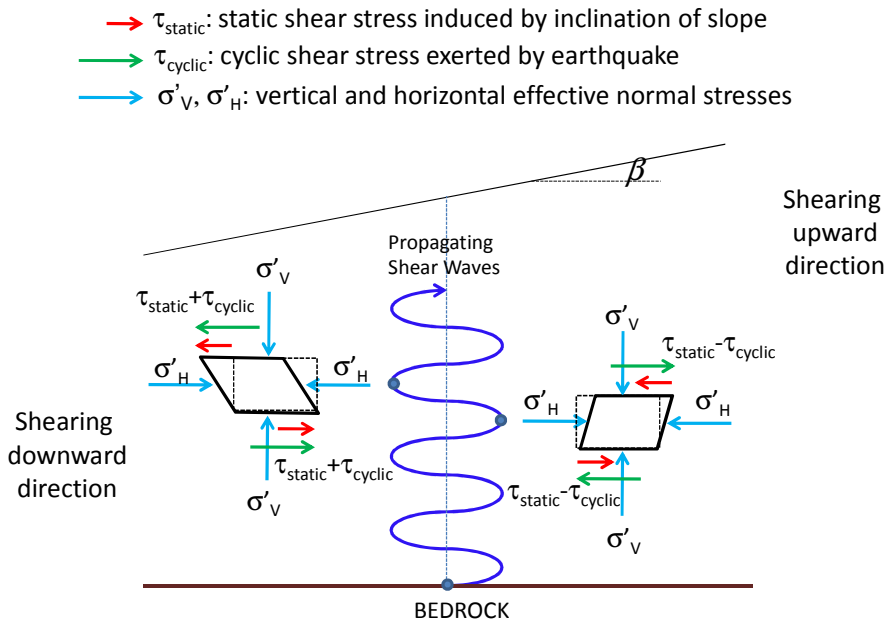

Fig. 1.3: Schematic stress conditions in a sloped ground.

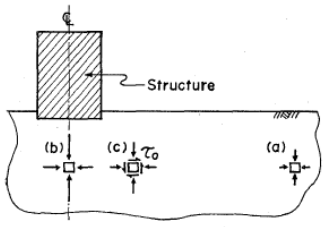

Fig. 1. Stress conditions before earthquake

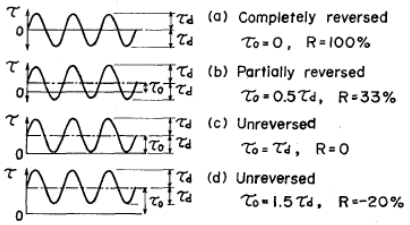

Fig. 2. Degree of stress reversal

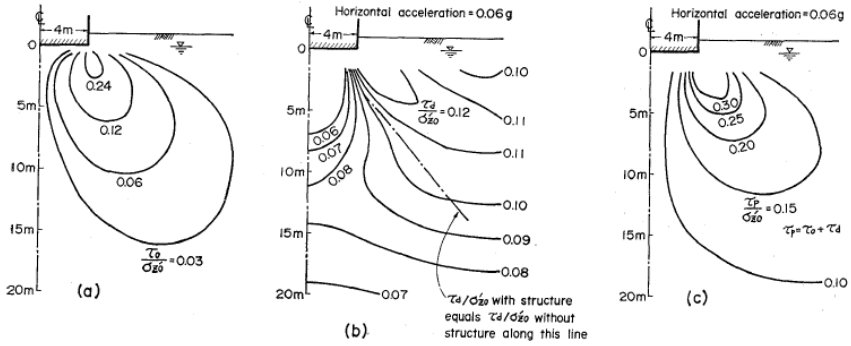

Fig. 3. Stress conditions below a structure : (a) Contours of initial shear stress ratios, (b) Contours of dynamic shear stress ratios, (c) Contours of peak shear stress ratios

Fig. 1.4: Stress conditions below a structure (Yoshimi and Oh-oka, 1975).

1.2 Modeling of drained and undrained soil behaviors

1.2.1 Modeling of quasi-elastic deformation characteristics

It is well known that the deformations of ground under general daily perturbations are usually less then 0.1 % of strain (Burland, 1989; Tatsuoka and Kohata, 1995). Therefore, it is recognized that elastic components are playing an important role in deformation characteristics of geomaterials.

A pure elastic behavior region of soil is not easy to identify since soil is a natural material with a lot of inhomogeneity. However, it can be reasonably assumed that at strain levels less than 0.001% the behavior of soil is quasi–elastic (Jardine, 1992; Tatsuoka et al., 1997; Clayton and Heymann, 2001). Although the behavior of soil looks reversible, due to the granular nature of sand, some energy loss may occur even at strain levels less than 0.001%, therefore the term quasi is suffixed to elastic.

Techniques used in the laboratory for evaluating the quasi-elastic deformations of geomaterials (i.e., Young's modulus E, shear modulus G and Poisson's ratio ν) consist essentially of two types, namely dynamic and static measurements.

The dynamic methods can be distinguished in resonant column (Hardin and Richard, 1963; Hardin and Black, 1968), wave propagation method using bender elements (Schulhessis, 1981; Dyvik and Madshus, 1985; Viggiani and Atkinson, 1995; Chaudhary et al., 2004, Wicacsono et al., 2007, Mulmi et al., 2008), wave propagation method using triggers and accelometers (AnhDan et al., 2002; Maqbool, 2005; Wicacsono et al., 2007; Kiyota et al., 2008), and wave propagation method using plate transducers (Laxmi et al., 2009; Laxmi and Kuwano, 2009). Since the waves tend to propagate along the stiffest part of the specimen, quasi-elastic deformation properties evaluated by employing wave propagation methods represent the properties of stiffest part of the specimen. In addition, the corresponding strain for dynamically evaluated quasi-elastic properties is less than 0.0001%.

Evaluation of quasi-elastic deformation characteristics by employing several small unload-reload cycles to the specimen within the quasi-elastic strain range is called static method. Under the category of static measurement techniques, two types namely external and local measurement methods can be found. The measurement based on measuring the

movement of the top cap and/or the pedestal is known as external measurement, while measuring directly the deformation of the specimen is referred to local measurement. It is evident that the local measurements can detect more closely the true deformations of soil.

Presently, due to the development in local strain measurement techniques such as inclinometer (Burland, 1989), LTD (Goto et al., 1991), LVDT (Cuccovillo and Coop, 1997), non proximity transducer, i.e. gap sensors, (Hird and Yung 1987 and 1989), and Pin-typed LDT for hollow cylindrical specimens (Hong Nam, 2004; De Silva et al., 2005), small strain deformation properties of the order 0.001% can be measured.

By using the Pin-typed LDT system (De Silva et al., 2005) it was observed that the externally evaluated quasi-elastic shear stiffness of Toyoura sand was about 20% larger than that evaluated by PLDT system, while the Young's modulus was unchanged.

Quasi-elastic bulk modulus, K, is another important parameter which is usually indirectly evaluated by using E and ν with the main assumption that soil is isotropic, which may not be true. However, direct evaluation of K is not an easy task due to many technical difficulties such as accurate evaluation of volume change of the sample at quasi-elastic strain range and effects of end restraint and membrane penetration on volume change measurement.

De Silva et al. (2008) attempted to directly evaluate K by using volume change detected by an electronic balance. It was found that locally evaluated K during isotropic consolidation, by assuming the isotropy of horizontal bedding plane, was very similar to the one evaluated by using high-sensitive electronic balance data without any correction for membrane penetration.

To date, there have been various attempts to model the quasi-elastic deformation properties of geomaterials based on experimental approach and void ratio (Hardin and Richard, 1963), stress state (Hardin, 1978), inherent and stress induced anisotropies (Hoque and Tatsuoka, 1998), rotation of principal stress direction and stress history (Hong Nam, 2004) have been taken into consideration.

Tatsuoka et al. (1999) proposed a hypo-elastic model to describe the inherent and stress induced anisotropies of sand without considering the rotation of principal stress direction. Whereas, Hardin and Blandford (1989) proposed a generalized model in which the inherent and stress induced anisotropies of sand were not fully taken into account.

On the contrary, to simulate the inherent and stress induced anisotropies while considering the rotation of principal stress direction, Hicher and Chang (2006) proposed a model based micromechanics consideration, i.e. considering the soil as an assembly of particles.

Hong Nam (2004) proposed a new hypo-elastic model called IIS model which can successfully simulate the inherent and stress-induced anisotropies of sand with the rotation of principal stress direction. This model is based on a few empirical rules on quasi-elastic deformation properties and coordinates transformation; it is also capable of taking into account the damage to quasi-elastic deformation properties at higher stress ratio as well.

1.2.2 Elasto-plastic models for soil

Soils are frequently subjected to large deformation due mainly to cyclic loading such as traffic load, sea waves, earthquake, excavation and filling, and subsequent construction of civil engineering structures. Therefore, in order to design economical structures with adequate safety and to analyze the performance of existing earth structures, it is required to qualitatively predict the behavior of soils under large strain conditions.

Application of plastic theory to model the soil behavior under large strain goes back many decades. So far, many elasto-plastic models have been proposed by researchers, while essentially they have been developed by following the framework of the elasto-plastic theory. The main components for an elasto-plasic model are:

- *Elastic regions*. The soil is assumed to undergo a recoverable deformation inside the yield surface;
- *Yield surface (f)*. A yield surface is usually defined as stress space. Deformations within the yield surface are assumed to be purely elastic, while both elastic and plastic deformations can be developed when the current stress moves outward from the yield surface. Yield surface expands in such a way that the stress state never exceeds it;
- *Plastic potential (g)*. The direction of plastic strain increment is governed by plastic potential, which is always normal to the plastic potential boundary surface regardless of the stress increment. Some models employ the simplifying assumption that $f = g$, therefore they are called associated flow rule models; on the contrary, other models

employ two different functions to describe f and g, therefore they are called non-associated flow rule models. In general, soil behavior follows the non-associated flow rule;

- *Hardening rule*. The expansion of yield surface (i.e. hardening of the soil) follows basically two types of hardening rules, namely isotropic hardening and kinematic hardening.

Cam clay model developed by Roscoe et al. (1963) at Cambridge University is recognized to be the first model in which the idea of elasto-plasticity was employed. This model assumes associated flow rule and isotropic hardening rule; in addition, the yield surface can be described by two parameters namely critical state parameter M and stress ratio η. However, the original cam-clay model has a limitation in its applicability such that plastic shear strain should be mobilized when following the isotropic stress path (i.e., p'=0). Thus its modification has been proposed by using an ellipsoidal yield locus (Roscoe and Burland, 1968).

Even though the original and modified Cam clays models can describe the behavior of clay in triaxial testing, they are insufficient to model soil behavior under more general stress paths. In order to address the above issue, a modified stress ratio parameter of the Cam clay model was proposed by Sekiguchi and Ohta (1977).

More recently with the development of more advanced laboratory testing apparatus such as true triaxial apparatus and torsional shear device, the importance of the effects of intermediate principal stress and rotation of principal stress directions on the behavior of soil was introduced, leading to the development of more sophisticated elasto-plastic models with more general flow rules and hardening mechanisms. Nakai and Mihara (1984) proposed a model which can describe the effects of the intermediate principal stress on the elasto-plastic soil behavior. On the other hand, Gutierrez et al. (1991) attempted to model the combined effects of both intermediate principal stress and rotation of principal stress directions.

Since it is recognized that soil experiences large deformation more easily under cyclic shear loading conditions, many cyclic elasto-plastic models have been proposed by a number of researchers (Ghaboussi and Momen, 1979; Pastor and Zienkiewicz, 1986;

Nishi and Kanatani, 1990, Ishihara and Kabilamany, 1990; Prevost and Keane, 1990; Oka, 1992; among other). Oka et al. (1992) simulated the liquefaction of a sandy sea bed due to ocean waves; Oka et al. (1994) attempted to model seepage failure of loose sand layers.

In general, even though this model can qualitatively predict the excess pore water pressure generation and development of deformation during undrained loading conditions, they are not able to simulate the full liquefaction since simulation often ends up giving a closed loop with an effective stress much larger than the zero stress state even for very loose soil. In order to address the above, Oka et al. (1999) modified their original model by introducing the improved stress-dilatancy relationships and damage of plastic properties at higher stress levels.

However, with the rapid development of laboratory test apparatus and measurement devices more accurate and/or additional characteristics of soil can be identified and described, therefore more additional concepts such as hardening mechanisms and virtual loading surface can be defined to model the real behavior of soil, at the expense of the intrinsic simplicity and robustness of elasto-plastic theory.

1.2.3 Constitutive model based on multiple shear mechanism

A different approach to model the general behavior of soil including the rotation of principal stress directions was proposed by Towhata and Ishihara (1985a). In this model called “multi spring concept”, based on the assumption of multi shear mechanisms in a soil element, inelastic springs connected to a rigid wall are employed to describe the stress-strain behavior of soil. Deformation of springs is taken as equivalent to shear strain in the corresponding shear mechanism and the overall shear deformation is modeled as the sum of contributions from multi shear mechanisms. External force on the soil element is assumed to be counter-balanced by the forces in springs.

A constitutive model to describe the cyclic undrained behavior of sand based on multi spring concept was developed by Iai et al. (1992). In this model, known as “Towhata-Iai model”, shear deformation was modeled by employing the multi spring concept and the generation of excess pore water pressure was modeled by using a correlation between excess pore water pressure increment and shear work as proposed by Towhata and Ishihara (1995b). Despite its excellent performance in simulating undrained

behavior of sand, Towhata-Iai model has some limitations such as that, it can be applied only for two-dimensional problems under undrained conditions.

In order to address the above issue, Nishimura (2002) proposed a constitutive model based on the multi spring concept in which generation of excess pore water pressure was modeled by correlating consolidation with an empirical stress-dilatancy relationship. In addition, the modified model can simulate the behavior of sand under more general drainage conditions with three dimensional loading. However, there still are several limitations such as that inherent anisotropy of the material (Arthur and Menzies, 1972) is not considerate and the steady state and continuous increase of shear deformation during liquefaction can not be modeled.

1.2.4 Experimental approach to model soil behavior

The use of hyperbolic type equation is another widely used approach to model non-linear stress-strain behavior of soil under drained condition. Hyperbolic equation has only two parameters with clear physical meanings namely, initial stiffness and peak strength, which can be determined by laboratory tests. In addition, its extended version (Tatsuoka and Shibuya, 1991a and 1991b) can model most given stress-strain relations satisfactorily by selecting appropriate parameters.

Kondner (1963) is widely regarded as the pioneer in using the hyperbolic equation to model stress-strain behavior of soil. However, it was later found that the simulation from the original hyperbolic equation as proposed by Kondner (1963) is not in total agreement with actual test data particularly at small strain levels.

On the other hand, Hardin and Drnevich (1972a and 1972b) proposed that the equivalent peak to peak shear modulus G_{eq} can be correlated to single amplitude shear strain $d(\gamma)_{SA}$ by a form of hyperbolic relation. Although this relation can simulate stress strain relations under cyclic loading conditions reasonably, it does not fit the corresponding monotonic stress strain relations well (Teachavorasinskun et al., 1991).

Therefore, in order to obtain a better degree of fitting with experiment data, models have been proposed with coefficients of correlation to modify the parameters of original hyperbolic model. Some models assume constant coefficients of correlation, while some assume that the coefficients of correlation are functions of strain.

Tatsuoka and Shibuya (1991b) proposed a hyperbolic equation that has coefficients

of correlation, which are functions of strain to simulate stress-strain relations for a wide range of strain. This equation is well known as General Hyperbolic Equation (GHE). It has been verified that GHE can properly simulate the full stress-strain relationships of wide range of geomaterials under general loading conditions.

Tatsuoka et al. (2003) successfully attempted to simulate the behavior of Toyoura sand subjected to cyclic plane strain compression and extension under drained condition by combining GHE with the well known Masing's rule (1926) with modifications. GHE was employed to simulate the monotonic loading curves in compression and extension directions and the modified Masing's rules were used to simulate the subsequent unloading and reloading branches. They have shown that the original Masing's rule alone is not sufficient to simulate the cyclic behavior of sand as it reproduces the same curve (constant hysteresis damping ratio) for cyclic loading under the same stress amplitude while experimental evidences show that damping ratio decreases with the increase of number of cycles under the same stress amplitude due to rearrangement of particles. In order to take this into account, in the simulation they proposed to shift the monotonic loading curve in the corresponding loading direction to the opposite direction. This phenomenon is known as "drag" (Masuda, 1998; Tatsuoka et al., 2003).

Balakrishnaiyer (2000) employed the same approach as Tatsuoka et al. (1999) to simulate the drained behavior of Chiba gravel subjected to cyclic triaxial loading. In addition, he attempted to propose some general rules that can be applied to any geomaterial in selecting the appropriate parameters for GHE.

The applicability of GHE and modified Masing's rules in simulating the behavior of Toyoura sand subjected to drained cyclic torsional shear was investigated by Hong Nam (2004). In addition, to better simulate the cyclic torsional behavior of sand, a modification to the original drag concept proposed by Tatsuoka et al. (2003) which consists of employing a hyperbolic drag function was introduced.

However, it should be noted that all of the above attempts were applied to simulating stress-strain behavior of soil under drained condition well before its peak state (or less than 1 % of strain).

In view of the shortcomings of the Masing's rules with drag, in order to simulate the stress-strain behavior of sand subjected to drained large cyclic torsional shear loading two conceptual modification factors, which take into account the hardening behavior during cyclic loading and the damage of plastic stiffness at large strain level, were introduced by

De Silva (2008).

1.2.5 Undrained behavior of soil: stress- dilatancy relationships

Modeling of stress-strain relationship as explained above is not sufficient to describe the volumetric behavior of soil. Therefore, a relationship that deals with the ratio of plastic strain increments to stress ratio is required to address this problem in addition to stress-strain relationship. This relationship is known as the stress-dilatancy relationship.

Various forms of stress-dilatancy relationships are proposed by various researchers for different loading conditions. Rowe (1962) derived stress-dilatancy relations for triaxial compression, triaxial extension and plane strain conditions by assuming that the ratio of energy increment input to the output is a constant (K).

Some other widely known stress-dilatancy relationships include sliding block theory (Tokue, 1978; Moroto, 1987, etc), Roscoe's energy dissipation equation (1963) and Taylor's energy dissipation equation (1948). It should be noted that all the above stated stress-dilatancy relations are originally developed for monotonic loading conditions.

Pradhan and Tatsuoka (1989a) modified these stress-dilatancy relations to apply to cyclic loading conditions and concluded that they are in reasonable agreement with the corresponding experimental evidences.

Although there are various theoretical proposals for stress-dilatancy relationships, limited experimental investigations can be found in literature. It can be partly due to the technical difficulties involved in getting reliable and high resolution volume change measurements. Pradhan and Tatsuoka (1989b) were able to obtain stress-dilatancy relationships of Toyoura sand subjected to cyclic triaxial and simple shear loadings by employing a high-sensitive electronic balance to measure the volume change of specimen. Shahnazari (2001) also experimentally investigated stress-dilatancy relationships of Toyoura sand under different loading conditions. Balakrishnaiyer (2000) obtained stress-dilatancy relationship of Chiba gravel subjected to cyclic triaxial loading.

However, it should be noted that the theoretical stress-dilatancy relations were derived only for either triaxial ($d\varepsilon_2 = d\varepsilon_3$, axial symmetric conditions) or plane strain (or simple shear) ($d\varepsilon_2 = 0$) conditions. Therefore, in order to deal with more general deformation modes such as torsional shear or true triaxial, empirical stress-dilatancy

relationships have been employed.

A promising framework for modeling undrained behavior of soil is to relate the elastic volume change increment due to consolidation to plastic volume change increment due to dilatancy.

Consolidation of soil alone is a widely investigated and well known phenomenon, while combination of consolidation and dilatancy as occurs during undrained cyclic loading is only poorly understood.

It has been experimentally observed that over-consolidation significantly alters the stress-dilatancy relationships (Pradhan and Tatsuoka, 1989). On the other hand, effects of over-consolidation seem to vanish with the cyclic loading as well. Oka et al. (1999) proposed an elasto-plastic model to simulate undrained behavior of sand, which employs a stress-dilatancy relation that considers the effects of over-consolidation.

1.2.6 An elasto-plastic model developed at IIS, University of Tokyo

With the aim of simulating the behavior of saturated sand undergoing undrained cyclic loading which leads to liquefaction and large cyclic shear strain development, an elasto-plastic constitutive model which can describe both monotonic and cyclic torsional shear behaviors of saturated sand under drained or undrained condition was developed at IIS (Institute of Industrial Science), University of Tokyo.

To simulate drained and undrained large cyclic behavior of sand, the proposed model requires accurate evaluation of irreversible strain component. Therefore, the quasi-elastic constitutive model, named IIS model (Hong Nam, 2004), is used as an additional tool to evaluate the elastic shear strain component. Hence, in analyzing hollow cylindrical torsional shear test data, the plastic shear strain component is obtained by subtracting from the measured total shear strain component the elastic one.

The drained monotonic loading behavior which is defined in terms of shear stress-plastic shear strain relationship (i.e., skeleton curve) is modeled by a GHE (Tatsuoka and Shibuya, 1991b).

Based on the experimentally obtained skeleton curves, behavior under cyclic shear loading is modeled by employing the extended Masing's rules considering: (a) rearrangement of particles during cyclic loading (drag effect), (Tatsuoka et al., 2003;

Hong Nam, 2004); (b) damage of plastic shear modulus at large level of shear stress (De Silva, 2008) and (c) hardening of the material during cyclic loading (De Silva, 2008).

In addition, in modeling undrained cyclic shear behavior it is assumed that the total volumetric strain increment during undrained loading, which consists of dilatancy and consolidation components, is equal to zero.

An empirical bi-linear stress-strain relationship which varies with the amount of damage to the plastic shear modulus of the material is introduced in order to model the accumulation of plastic strain due to the application of drained cyclic torsional shear loading (De Silva, 2008). This stress-dilatancy relationship considers the effects of over-consolidation into account, since it has been experimentally observed that over-consolidation significantly alters the stress-dilatancy behavior of sand.

Thus far, the elasto-plastic constitutive model developed at IIS, can simulate the liquefaction behavior of sand under undrained cyclic torsional shear loading until the specimen enters in a steady state. However, development of large deformation can not be simulated during the cyclic mobility.

It is noteworthy that the motivation of the current study comes from the successful attempts as above described in simulating the liquefaction behavior of sand as well the cyclic large deformation behavior. No attempt has been made so far to model the undrained behavior of sand by considering the effect of static shear. Therefore, the objectives of the present study were set by aiming at modeling the cyclic undrained torsional shear behavior of saturated sand with initial static shear ultimately.

1.3 Objectives of this study

In view of the above background, the following objectives of this study are set:

(a) Investigate the effects of initial static shear on the large deformation properties of saturated sand subjected to undrained cyclic torsional shear loading. This consists of following points:

a-i. Investigate the effect of static shear on the undrained cyclic torsional shear behavior of saturated Toyoura sand specimens up to single amplitude shear strain of about 50%.

It should be noted that, such extremely large deformations could not be achieved in past studies on the effects of static shear on the undrained cyclic shear behavior of sand, due mainly to mechanical limitation of the employed apparatus and/or larger extents of non-uniform deformation of specimens at higher strain levels. In this study, extremely large deformations will be achieved by employing a torsional shear device modified for enlarging the effective range of torsional displacement; on the other hand, with the aim of obtaining higher uniform deformation of specimens at higher strains levels, medium-size hollow cylindrical specimens (D_{out}=15cm; D_{in}=9cm: H=30cm) will be used.

a-ii. Examine the mechanism of extremely large liquefaction-induced deformation of sand under various combinations of static and cyclic stresses (i.e., reversal stress, intermediate and non-reversal conditions) while keeping simple shear deformation conditions ($\varepsilon_a=\varepsilon_r=\varepsilon_\theta=0$) during the undrained cyclic torsional shearing process, with the aim of simulating as much as possible the simple shear condition that the ground undergoes during horizontal excitation.

a-iii. Evaluate the effect of static shear on the failure behavior of saturated sand (i.e., failure due to liquefaction or residual deformation). To this scope, both monotonic and cyclic undrained behaviors of Toyoura sand specimens will be compared.

a-iv. Compare the behavior of sand observed in laboratory tests with the response of slopes of sandy deposits during past seismic events by using field investigation data reported in literature.

(b) Modeling the effects of initial static shear on the liquefaction resistance and the failure characteristics of saturated sand. This consists of following steps:

b-i. Simulate the stress-strain relationship of sand during the large undrained cyclic torsional shear loading by employing the GHE model and the extended Masing's rules considering the damage of plastic shear modulus at large shear stress level and the hardening of the material during cyclic loading. Above all, in this study the effects of initial static shear on the stress-strain behavior of sand will be investigated and simulated.

b-ii. Investigate the stress-dilatancy relationship of sand with considering the effects of initial static shear. The combined effects of over-consolidation and static shear on the stress-dilatancy will be examined and simulated as well.

b-iii. Final goal of the current study is to propose an elasto-plastic model which makes it possible to simulate the effects of initial static shear on the undrained cyclic torsional behavior of saturated sand under stress reversal, intermediate and non-reversal loading conditions. The simulation results will describe the behavior of sand specimen in terms of stress-strain relationship and effective stress path.

1.4 Organization of the thesis

In Chapter 1, the background of the proposed research plan and relevant previous studies are reviewed. The objectives of this study with regard to experimental observations and modeling are set on view of the background and previous studies.

Chapter 2 is dedicated to the formulation of stresses and strains using torsional shear apparatus on hollow cylindrical specimens. Advantages and limitations of cylinder torsional devices are also briefly reviewed.

In Chapter 3, first the testing material is identified by analyzing its index properties, particle shape and mineralogical components. Then the test apparatus which consists in a high-capacity torsional shear apparatus developed at the Institute of Industrial Science, University of Tokyo, is described in detail. Subsequently, the technique employed to prepare the specimens including the saturation methods are illustrated. Finally, the loading procedure is described.

In Chapter 4, the results from the investigations on the effects of initial shear stress on the undrained cyclic behavior of saturated Toyoura sand subjected to cyclic torsional shear loading up to single amplitude of shear strain of about 50 % under various combinations of static and subsequent cyclic shear stresses are presented. Effects of static shear on the types of loading, failure characteristics, resistance to liquefaction, modes of development of shear strain during cyclic shearing, specimen deformations and so on, are analyzed in order to have a comprehensive understanding of the role that the initial static shear plays on the undrained cyclic behavior of saturated Toyoura sand.

Chapter 5 entails the attempt to model the undrained cyclic behavior of loose Toyoura sand with initial static shear subjected to undrained cyclic torsional shear loading. An elasto-plastic constitutive model developed at IIS and the modifications made in the current study to take the effects of initial static shear into account are presented. The satisfactory simulation results, in terms of effective stress path and stress-strain relationship, are presented and compared with the experimental observations. Resistance against liquefaction and shear strain accumulation, failure behaviors and the mode of

development of residual shear strain during cyclic loading obtained by simulation are also shown.

In Chapter 6, a method to assess the failure behavior of sand specimens with initial static shear under undrained cyclic torsional shear loading is presented. Its applicability has been investigated on a wide range of combinations of static and cyclic shear stresses on very loose, loose and dense sand by referring to: (i) the results of undrained cyclic torsional shear tests; and (ii) a number of single-element numerical simulations by employing the elasto-plastic constitutive model developed in this study. In addition, the attempt made to directly compare tests results with the behavior of soil in site on the basis of filed data interpretation is presented.

Chapter 7 is dedicated to the conclusions of this study. Recommendations for future studies are also presented.

1.5 References

1. AhnDan, L. Koseki, J. and Sato, T. (2002): "Comparison of Young's moduli of dense sand and gravel measured by dynamic and static methods", Geotechnical Testing Journal, ASTM, 25 (4), 349-368
2. Arthur, J. R. F. and Menzies, B. K. (1972): "Inherent anisotropy in a sand", Geotechnique, 22 (1), 115-128
3. Balakrishnaiyer, K. (2000): "Modeling of deformation characteristics of gravel subjected to large cyclic loading", PhD thesis, Dep. of Civil Engineering, University of Tokyo, Japan
4. Burland, J. B. (1989): "Small is beautiful- the stiffness of soil at small strains", 9th Laurits Bjerrum memorial lecture, Canadian Geotechnical Journal, Vol. 26, 499-516
5. Castro, G. (1975): "Liquefaction and cyclic mobility of saturated sand", Journal of Geotechnical Engineering Division, ASCE, 101 (GT6), 551-569
6. Castro, G. and Poulus, S. J. (1977): "Factors affecting liquefaction and cyclic mobility", Journal of Geotechnical Engineering Division, ASCE, 103 (GT6), 501-516
7. Chaudhary, S. K., Kuwano, J. and Hayano, Y. (2004): "Measurement of quasi-elastic stiffness parameters of dense Toyoura sand in hollow cylinder torsional and triaxial apparatus with bender elements", Geotechnical Testing Journal, ASTM, 27 (1), 23-35
8. Clayton, C. R. I. and Heymann, G. (2001): "Stiffness of geomaterials at very small strains", Geotechnique, 51 (3), 245-256
9. Cuccovillo, T. and Coop, M. R. (1997): "The measurement of local axial strain in triaxial tests using LVDTs", Geotechnique, 47 (1), 167-171
10. De Silva, L.I.N. (2008): "Deformation characteristics of sand subjected to cyclic drained and undrained torsional loadings and their modeling", PhD thesis, Dep. of Civil Engineering, University of Tokyo, Japan
11. De Silva, L.I.N., Koseki, J., Sato, T. and Wang, L. (2005): "High capacity hollow cylinder apparatus with local strain measurement", Proc. 2nd Japan-U.S. Workshop on Testing, Modeling and Simulation, Geotechnical Special Publication, ASCE, Vol. 156, 16-28
12. De Silva, L.I.N., Koseki, J., Sato, T., Kiyota, T. and Honda, T. (2008): "Quasi-elastic bulk modulus of sand based on volume change and local deformation measurement of hollow cylindrical specimen", Proc. 4th International Symposium on Deformation Characteristics of Geomaterials, Atlanta

13. Dyvik, R. and Madshus, S. (1985): "Laboratory measurement of G_{max} using bender elements", Advances in the Art of Testing Soils under Cyclic Conditions, Proc. ASCE Convention, Detroit, 186-196

14. Ghaboussi, J. and Momen, H. (1979): "Plasticity model for cyclic behavior of sands", Proc. 3rd International Conference on Numerical Methods in Geomechanics, Aachen, 423-434

15. Goto, S., Tatsuoka, F., Shibuya, S., Kim, Y. S., and Sato, T. (1991): "A simple gauge for local small strain measurements in the laboratory", Soils and Foundations, 31(1), 169-180

16. Gutierrez, M., Ishihara, K. and Towhata, I. (1991): "Flow theory for sand during rotation of principal stress direction", Soils and Foundations, 31(4), 121-132

17. Hamada, M., O'Rourke, T. D. and Yoshida, N. (1994): "Liquefaction-induced large ground displacement", Performance of Ground Soil during Earthquake, 13th International Conference on Soil Mechanics and Foundation Engineering, 93-108

18. Hamada, M., Saito, K., Yasuda, S. and Isoyama, R. (1988): "Earthquake damage by liquefaction-induced ground displacement", Proc. 9th World Conference on Earthquake Engineering, Vol. 8, 213-218

19. Hamada, M., Yasuda, S., Isoyama, R. and Emoto, K. (1986): "Study on liquefaction induced permanent ground displacement", Association for the Development of Earthquake Prediction (ADEP), Tokyo, Japan

20. Hardin, B. O. and Drnevich, V. P. (1972a). "Shear modulus and damping in soils: Measurement and parameters effects", Journal of Soil Mechanics and Foundation Division, ASCE, 98 (SM6), 603-624

21. Hardin, B. O. and Drnevich, V. P. (1972b). "Shear modulus and damping in soils: Design equations and curves", Journal of Soil Mechanics and Foundation Division, ASCE, 98 (SM7), 667-692

22. Hardin, B. O. (1978): "The nature of stress-strain behavior of soils", State-of-the-Art Report, Proc. ASCE, Specialty Conference on Earthquake Engineering and soil Mechanics, Pasadena, CA, Vol. 1, 3-90

23. Hardin, B. O. and Black, W. L. (1968): "Vibration modulus of normally consolidated clay", Journal of Soil Mechanics and Foundation Division, ASCE, 94 (SM2), 353-369

24. Hardin, B. O. and Blandford, G. E. (1989): "Elasticity of particulate materials", Journal of Geotechnical Engineering Division, ASCE, 115(6), 788-805

25. Hardin, B. O. and Richard, F. E., Jr. (1963): "Elastic wave velocities in granular soil", Journal of Soil Mechanics and Foundation Division, ASCE, 89 (1), 33-65

26. Hicher, P. Y. and Chang, C. S. (2006): "Anisotropic nonlinear elastic model for particulate materials", Journal of Geotechnical and Geoenvironmental Engineering, ASCE, 132 (8), 1052-1061

27. Hird, C. C. and Yung, P. C. Y. (1987): "Discussion on a new device for measuring local axial strain on triaxial specimens", Geotechnique, 37 (3), 413-417

28. Hird, C. C. and Yung, P. C. Y. (1989): "The use of proximity transducers for local strain measurements in triaxial tests", Geotechnical Testing Journal, , ASTM, 12 (4), 292-296

29. Hong Nam, N. (2004): "Locally measured quasi-elastic properties of Toyoura sand in cyclic triaxial and torsional loadings", PhD thesis, Dep. of Civil Engineering, University of Tokyo, Japan

30. Hoque, E., and Tatsuoka, F. (1998): "Anisotropy in elastic deformation of granular material", Soils and Foundations, 38 (1), 163-179

31. Hyodo, M., Murata, H., Yasufuku, N. and Fujii, T. (1991): "Undrained cyclic shear strength and residual shear strain of saturated sand by cyclic triaxial tests", Soils and Foundations, 31 (3), 60-76

32. Hyodo, M., Tanimizu, H., Yasufuku, N. and Murata, H. (1994): "Undrained cyclic and monotonic triaxial behavior of saturated loose sand", Soils and Foundations, 34 (1), 19-32

33. Iai, S., Matsunaga, Y. and Kameoka, T. (1992): "Strain space plasticity model for cyclic mobility", Soils and Foundations, 32 (2), 1-15

34. Ishihara, K. and Kabilamany, K. (1990): "Stress dilatancy and hardening laws for rigid granular model of sand", Soil Dynamics Earthquake Engineering, 9 (2), 66-77

35. Ishihara, K. and Yasuda, S. (1975): "Sand liquefaction in hollow cylinder torsion under torsional irregular excitation", Soils and Foundations, 15 (1), 45-59

36. Ishihara, K., Tatsuoka, F. and Yasuda, S. (1975): "Undrained deformation and liquefaction of sand under cyclic stresses", Soils and Foundations, 15 (1), 29-44

37. Ishihara, K., Yasuda, S. and Nagase, H. (1996): "Soil characteristics and Ground damage", Special Issue of Soils and Foundations, 109-118

38. Jardine, R. J. (1992): "Some observations on the kinematic nature of soil stiffness", Soils and Foundations, 32 (2), 111-124

39. Kiyota, T., Sato, T., Koseki, J., and Mohammad, A.M. (2008): "Behavior of liquefied sands under extremely large strain levels in cyclic torsional shear tests", Soils and Foundations, 48 (5), 727-739

40. Koseki, J. and Ohta, A. (2001): "Effects of different consolidation conditions on liquefaction resistance and small strain quasi-elastic deformation properties of sands containing fines", Soils and Foundations, 41 (6), 53-62

41. Koseki, J., Kiyota, T., Sato, T. and Mohammad, A.M. (2007): "Undrained cyclic torsional shear tests on sand up to extremely large strain levels", International Workshop on Earthquake Hazard and Mitigation, Guwahati, India, 257-263

42. Kramer, S. L. (1996): "Geotechnical Earthquake Engineering", Prentice Hall, New Jersey

43. Konder, R. L. (1963): "Hyperbolic stress-strain response: cohesive soils", Journal of Soil Mechanics and Foundation Division, ASCE, 89 (SM1), 115-143

44. Laxmi, P. S. and Kuwano, R. (2009): "Development of disc shaped piezo-ceramic plate transducer for elastic measurements in laboratory soil specimens', Seisan-Kenkyu, Journal of Institute of Industrial Science, University of Tokyo, 61 (6), 123-128

45. Laxmi, P. S., Kuwano, R. Ebizuka, H. and Sato, T. (2009): "Performance of plate transducer fro dynamic measurement in laboratory specimens", Proc. 11th International Summer Symposium, JSCE, Tokyo, Japan, 113-116

46. Lee, K. D. and Seed, H. B. (1967a): "Cyclic stress conditions causing liquefaction of sand", Journal of Soil Mechanics and Foundation Division, ASCE, 93 (SM5), 47-70

47. Lee, K. D. and Seed, H. B. (1967b): "Dynamic strength of anysotropically consolidated sand", Journal of Soil Mechanics and Foundation Division, ASCE, 93 (SM5), 169-190

48. Maqbool, S. (2005): "Effects of compaction on strength and deformation properties of gravel in triaxial and plain strain compression tests", PhD thesis, Dep. of Civil Engineering, University of Tokyo, Japan

49. Masing, G. (1926): "Eiganspannungen und verfestigung beim messing" Proc. 2nd International Conference of Applied Mechanics, Zurich, 332-335

50. Masuda, T. (1998). "Study on the effect of pre-load on the deformation of excavated ground", *Doctor of engineering thesis*, Department of civil engineering, The University of Tokyo, Japan (in Japanese)

51. Mohamad, R. and Dobry, R. (1986): "Undrained monotonic and cyclic triaxial strength of sand", Journal of Geotechnical Engineering Division, ASCE, 112 (GT10), 941-958

52. Mulmi, S., Koseki, J. and Kuwano, R. (2008): "Simple size and shape effect in bender element tests", Proc. 10th International Summer Symposium, JSCE, Tokyo, 85-88

53. Moroto, N. (1987): "On deformation of granular material in simple shear", Soils and Foundations, 27 (1), 77-85

54. Nakai, T. and Mihara, Y. (1984): "A new mechanical quantity for soils and its application ton elastoplastic constitutive models", Soils and Foundations, 24 (2), 82-94

55. Nishi, K. and Kanatani, M. (1990): "Constitutive relations fro sand under cyclic loading based on elasto-plasticity theory", Soils and Foundations, 30 (2), 43-59

56. Nishimura, S. (2002). "Development of three dimensional stress-strain model of sand undergoing cyclic undrained loading and stress-axes rotation", M.Eng thesis, Dept. of Civil Engineering, University of Tokyo, Japan

57. Oka, F. (1992): "A cyclic elasto-viscoplastic constitutive model for clay based on the non-linear hardening rule", Proc. 4th International Symposium on Numerical Models in Geomechanics, 105-114

58. Oka, F., Yashima, A., Kato, M. and Nakajima, Y. (1994): "An analysis of seepage failure using an elasto-plastic constitutive equation and its application", A constitutive model for sand based on the non-linear kinematic hardening rule and its application", Journal of JSGE, III-27 (493), 127-135 (in Japanese)

59. Oka, F., Yashima, A., Kato, M. and Sekiguchi, K. (1992): "A constitutive model for sand based on the non-linear kinematic hardening rule and its application", Proc. 10th World Conference on Earthquake Engineering, 2529-2534

60. Oka, F., Yashima, A., Tateishi, Y., Taguchi, Y. and Yamashita, S. (1999): "A cyclic elasto-plastic constitutive model for sand considering a plastic-strain dependence of the shear modulus", Geotechnique, 49 (5), 661-680

61. Pastor, M. and Zienkiewicz, O.C. (1986): "A generalized plasticity, hierarchical model for sand under monotonic and cyclic loading" Proc. 2nd International Symposium on Numerical Models in Geomechanics, Jackson and Son (Eds.), London, 131-150

62. Pradhan, T. B. S. and Tatsuoka, F. (1989a): "On stress-dilatancy equations of sand subjected to cyclic loading", Soils and Foundations, 29 (1), 65-81

63. Pradhan, T. B. S., Tatsuoka, F. and Sato, Y. (1989b): "Experimental stress-dilatancy relations of sand subjected to cyclic loading", Soils and Foundations, 29 (1), 45-64

64. Prevost, J. H. and Keane, C. M. (1990): "Shear stress-strain curve generation for simple material parameters", Journal of Geotechnical Engineering Division, ASCE, 116 (9), 1924-1944

65. Roscoe, K. H. and Burland, J. B. (1968): "On the generalized stress-strain behavior of 'wet' clay", Engineering Plasticity, Heyman, J., Leckie, F. A. (Eds.), Cambridge, University Press, 535-609

66. Roscoe, K. H., Schofield, A. N. and Thurairajah, A. (1963): "Yielding of clays in states wetter then critical", Geotechnique, 13 (3), 211-240

67. Rowe, P.W. (1962). "The stress-dilatancy relation for static equilibrium of an assembly of particles in contact", Proc. of Royal Society of London, Series A, Vol. 269, 500-527

68. Schultheiss, P. J. (1981): "Simultaneous measurement of P and S wave velocities during conventional soil testing procedures", Marine Geotechnology, 4 (4), 343-367

69. Seed, H. B. (1968): "Landslides during earthquakes due to liquefaction", Journal of Soil Mechanics and Foundation Division, ASCE, 94 (SM5), 1055-1122

70. Seed, H. B. (1979): "Soil liquefaction and cyclic mobility evaluation for level ground during earthquakes", Journal of Geotechnical Engineering Division, ASCE, 105 (GT2), 201-255

71. Seed, H. B. and Idriss, I. M. (1971): "Simplified procedure for evaluating soil liquefaction potential", Journal of Soil Mechanics and Foundation Division, ASCE, 97 (SM9), 1249-1273

72. Seed, H. B., Idriss, I. M. and Arango, I. (1983): "Evaluation of liquefaction potential using field data", Journal of Geotechnical Engineering Division, ASCE, 109 (GT3), 458-482

73. Seed, H. B., Tokimatsu, K., Harder, L.F., Jr. and Chung, R. (1985): "Influence of SPT procedures in soil liquefaction resistance evaluations", Journal of Geotechnical Engineering Division, ASCE, 111 (12), 1425-1445

74. Sekiguchi, H. and Ohta, H. (1977): "Induced anisotropy and time dependency of clay", Proc. of Special Session 9th ICSMFE, 229-239

75. Shamoto, Y., Zhang, J. M. and Goto, S. (1997): "Mechanism of large post-liquefaction deformation in saturated sand", Soils and Foundations, 37 (2), 71-80

76. Shahnazari, H. (2001): "Experimental investigation on volume change and shear deformation characteristics of sand undergoing cyclic loading", PhD Thesis, Dep. of Civil Engineering, University of Tokyo, Japan

77. Tastuoaka, F. and Kohata, Y. (1995): "Stiffness of hard soils and soft rocks in engineering applications"' Keynote lecture, Proc. of International Symposium Pre-failure Deformation of Geomaterials, Shibuya (Eds.), Balkema, Vol. 2, 947-1063

78. Tatsuoka, F., Ishihara, K., Uchimura, T. and Gomes Correia, A. (1999): "Non-linear resilient behavior of unbound granular materials predicted by the cross-anisotropy hypo-quasi-elasticity model", Unbound Granular Materials, Gomes Correia (Eds.), Balkera, 197-204

79. Tatsuoka, F., Jardine, R. J., Lo Presti, D., Di Benedetto, H. and Kodaka, T. (1997): "Characterizing the pre-failure deformation properties of geomaterials, Theme lecture for the plenary session No.1", Proc. 14th International Conference on Soil Mechanics and Foundation Engineering, Hamburg, Vol. 4, 2129-2164

80. Tatsuoka, F., Muramatsu, M. and Sasaki, T. (1982): "Cyclic undrained stress-strain behavior of dense sand by torsional simple shear test", Soils and Foundations, 22 (2), 55-69

81. Tatsuoka, F., Ochi, K., Fujii, S. and Okamoto, M. (1986a): "Cyclic undrained triaxial and torsional shear strength of sands for different sample preparation methods", Soils and Foundations, 26 (3), 23-41

82. Tatsuoka, F., Toki, S., Miura, S., Kato, H., Okamoto, M., Yamada, S., Yasuda, S. and Tanizawa, F. (1986b): "Some factors affecting cyclic undrained triaxial strength of sand", Soils and Foundations, 26 (3), 99-116

83. Tatsuoka, F. and Shibuya, S. (1991a): "Modeling of non-linear stress-strain relations of soil and rocks- Part 1: Discussion of hyperbolic equation", Seisan-Kenkyu, Journal of Institute of Industrial Science, University of Tokyo, 43 (9), 409-412

84. Tatsuoka, F. and Shibuya, S. (1991b): "Modeling of non-linear stress-strain relations of soil and rocks- Part 1: New equation", Seisan-Kenkyu, Journal of Institute of Industrial Science, University of Tokyo, 43 (10), 435-437

85. Tatsuoka, F., Masuda, T., Siddiquee, M. S. A. and Koseki, J. (2003): "Modeling the stress-strain relations of sand on cyclic plane strain loading", Journal of Geotechnical and Geoenvironmental Engineering, ASCE, 129 (6), 450-467

86. Teachavorasinskun, S., Shibuya, S. and Tatsuoka, F. (1991): "Stiffness of sands in monotonic and cyclic loading in simple shear", Proc. of Geotechnical Engineering Congress, ASCE, Colorado, Vol. 2, 863-878

87. Tokue, T. (1978): "A consideration about Rowe's minimum energy ratio principal and a new concept of shear mechanism", Soils and Foundations, 18 (1), 1-10

88. Towhata, I. (2008): "Geotechnical Earthquake Engineering", Springer

89. Towhata, I. and Ishihara, K. (1985a): "Undrained strength of sand undergoing cyclic rotation of principal stress axes", Soils and Foundations, 25 (2), 135-147

90. Towhata, I. and Ishihara, K. (1985b): "Shear work and pore water pressure in undrained shear", Soils and Foundations, 25 (3), 73-84

91. Vaid, Y. P. and Chern, J.C. (1983): "Effects of static shear on resistance to liquefaction", Soils and Foundations, 23 (1), 47-60

92. Vaid, Y. P. and Finn, W.D.L. (1979): "Static shear and liquefaction potential", Journal of Geotechnical Engineering Division, ASCE, 105 (GT10), 1233-1246

93. Viggiani, G. and Atkinson, J. (1995): "Interpretation of bender element tests", Geotechnique, 45 (1), 149-154

94. Wicaksono, R. I., Tsustumi, Y., Sato, T. Koseki, J, and Kuwano, R. (2007): "Small strain stiffness of clean sand and gravel based on dynamic and static measurements", Proc. 9th International Summer Symposium, JSCE, Yokohama, Japan

95. Wood, D. M. (1990): "Soil behavior and critical state soil mechanics", Cambridge University Press, Cambridge, UK

96. Yasuda, S., Nagase, H., Kiru, H. and Uchida, Y. (1992): "The mechanism and a simplified procedure for the analysis of permanent ground displacement due to liquefaction", Soils and Foundations, 32 (1), 149-160

97. Yasuda, S., Yoshida, N., Masuda, T., Nagase, H., Mine, K. and Kiru, H. (1995): "Stress-strain relationship of liquefied soil", Earthquake Geotechnical Engineering, Ishihara (Eds.), Balkemena, Rotterdam, Vol. 2, 811-816

98. Yoshimi, Y. and Oh-oka, H. (1975): "Influence of degree of shear stress reversal on the liquefaction potential of saturated sand", Soils and Foundations, 15 (3), 27-40

CHAPTER 2

Formulation of stresses and strains using torsional shear apparatus

2.1 Introduction

In this study a torsional shear apparatus on hollow cylindrical specimen was employed to investigate the resistance to liquefaction and/or the development of extremely large deformation of saturated Toyoura sand specimens subjected to static shear.

In spite of the many advantages and the wide range of applications, torsional shear tests on hollow cylindrical specimens have several limitations (e.g., non-uniformity of stresses and strains along radial and vertical directions, end restraint effects, membrane force and membrane penetration effects, system compliance, etc…) that may cause some errors in the evaluation of the stresses and strains.

In addition, formulations of average stresses and strain on hollow cylindrical specimens are based on many assumptions on which there is no concrete agreement among researchers. Most researchers assume linear elasticity of the material when calculating the radial and circumferential stresses, and perfect plasticity when calculating the shear stresses.

Saturated sand when tested may behave almost elastically at the earliest stage of the cyclic loading process, but the behavior becomes more and more like a plastic material whilst proceeding in the loading stage. Therefore it may be reasonable to assume that the real behavior of the sand is somewhere in-between these two extreme cases for which the difference in the average shear stress is small.

In this chapter, first the main index properties of coarse granular soils are reviewed. Then, possible errors in the evaluation of stresses and strains are briefly illustrated; finally, a complete description of the stresses and strains formulation adopted in this study is given.

2.2 Soil index properties

Soils are made of solid particles with voids in-between. For most of the case the voids are filled with air and water. Therefore, soils are three-phase materials with solid, liquid and air constituents. Fig. 2.1 shows a soil sample of weight W and total volume V.

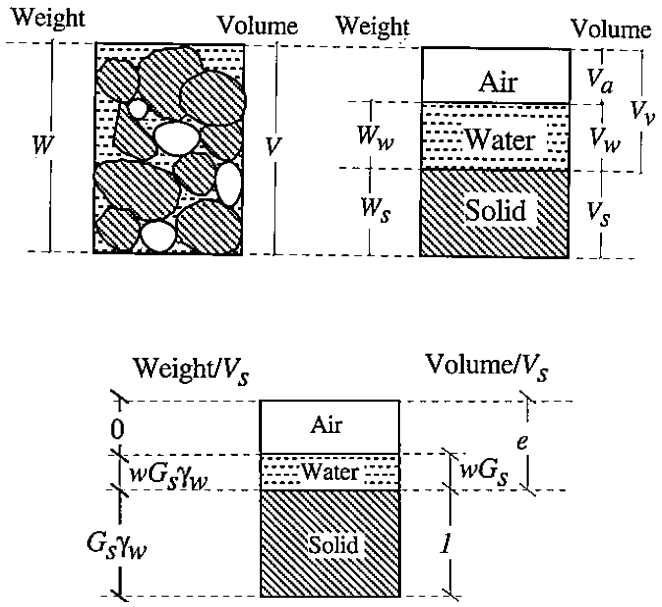

Fig. 2.1: Phase diagram of soils (Bardet, 1997).

In soil mechanics, the proportions of the solid, liquid and air constituents are characterized by five dimensionless quantities: e, n, w, S_r and D_r.

The void ratio (e) is the ratio of the volume of voids (V_V) to the solid volume (V_S):

$$e = \frac{V_V}{V_S} = \frac{V - V_S}{V_S} \tag{2.1}$$

The porosity (n) is the ratio of the volume of voids (V_V) to the total volume (V):

$$n = \frac{V_V}{V} \tag{2.2}$$

The water content (w) is the ratio of the weight of water (W_W) to the dry weight of the sample (W_S):

$$w = \frac{W_W}{W_S} \qquad (\%) \tag{2.3}$$

The degree of saturation (S_r) is the ratio of the volume of the water (V_W) to the volume of the void (V_V)

$$S_r = \frac{V_W}{V_V} \times 100 \qquad (\%) \tag{2.4}$$

S_r ranges from 100% when $V_W = V_V$ (i.e., fully saturated conditions) to 0 when $V_W = 0$ (i.e., perfectly dry conditions).

In case of coarse-grained soils, the relative density (D_r) is defined to characterize the degree of compaction:

where

e_{max} = maximum void ratio;

e_{min} = minimum void ratio;

e = current void ratio.

D_r varies from 0 when $e = e_{max}$ to 100 % when $e = e_{min}$. In reality, e_{max} and e_{min} are not the absolute maximum and minimum void ratios of a soil, respectively. They are just index void ratios obtained by standard procedures.

In laboratory tests, the current void ratio (e) is evaluated as

$$e = \frac{G_S \, \gamma_w}{\gamma_d} - 1 \tag{2.6}$$

where

G_s = specific gravity defined as the ratio of solid and water unit weight, γ_s / γ_w;

γ_d = dry unit weight of soil, W_S/V.

2.3 Errors in evaluating stresses and strains

Torsional shear devices are a natural extension of the standard triaxial apparatus and provide a much wider variety of stress paths to be investigated and/or simulate, including rotation of principal stress directions.

In particular, torsional shear tests on hollow cylindrical specimens are a good tool that can be used to investigate quasi-elastic properties of geomaterials (Di Benedetto et al., 1999; Connoly and Kuwano, 1999; Hong Nam and Koseki, 2005; De Silva et al., 2005) as well as liquefaction (Ishihara, 1975; Yoshimine et al., 1998; Koseki and Ohta, 2001; Oka et al., 1992 and 1999; Kiyota, 2007; Kiyota et al., 2008). Independent control of four stress components namely, axial stress, torque, inner and outer cell pressures makes it possible to reproduce actual stress conditions of the ground under earthquake loading and investigate the behavior of soil in a more realistic way.

In spite of the many advantages and a wider range of applications, torsional shear tests on hollow cylindrical specimens have several limitations that might cause some error in the evaluation of stresses and strains.

First of all, making a good quality reconstituted specimen is a challenge. The conventional procedure for preparing hollow cylindrical sand specimens using the air-pluviation technique employs an alternative change of pluviation direction from clockwise to anticlockwise. However, the reliability of the conventional procedure in minimizing the degree of anisotropy of specimens in the horizontal bedding plane is questionable (Hong Nam and Koseki, 2005; De Silva et al., 2006).

Secondly, boundary conditions in the horizontal direction of hollow cylindrical specimen are different form each other. The soil inside the hollow cylindrical specimen has rigid boundaries in the vertical plane, flexible boundaries in the radial plane and infinite boundaries in the circumferential plane. Therefore, even though the specimen is made with the utmost care to avoid possible anisotropy in the horizontal bedding plane, it is possible that the measured deformations in the radial and circumferential directions are significantly different from each other due to the different boundary conditions.

Furthermore, the presence of rigid boundaries at the top cap and the pedestal restrains the deformation in the horizontal direction near the top cap and pedestal. This is called the effects of end restraint. It is impossible to apply any form of lubrication as in the cases of triaxial or plane strain testing of soils, because the specimen needs sufficient frictional

resistance at the top cap and the pedestal to apply shear stress.

The membrane also contributes to error in the stresses and strains. There are two ways in which the membranes affect test results. The first one is related to the torsional resistance of the inner and outer membranes, while the second is related to membrane penetration. Generally, the membrane force is evaluated by employing the theory of elasticity which uses Young's modulus of the membrane (Eq. 2.40). However, Kiyota et al. (2008) and Chiaro et al. (2009) found that the deviation of the actual membrane deformation to the uniform one that is assumed in theory becomes larger with an increase in strain levels, therefore the membrane force should be addressed by performing specific calibration tests.

The membrane penetration is estimated with various equations and affects volume change measurements and pore water pressure in drained and undrained tests, respectively. This influence increases with the particle size for granular material; in addition, with the hollow cylinder specimens the area exposed to the membrane is larger than the one with solid cylinder specimens, therefore the membrane penetration more largely affects the measurement with the hollow cylinder specimens.

Another important consideration is the stress-strain non-uniformity along the radial and vertical directions of the specimen. Various proposals to quantify the non-uniformity of stresses in the hollow cylindrical specimen can be found in literature (Hight et al., 1983; Vaid et al., 1990; Yoshimine et al., 1998). This is unavoidable as the specimen has an inherent curvature and end restraint (Hight et al., 1983). Although it is preferable to reduce the wall thickness of the specimen to minimize such non-uniformity, effects of other factors as described above such as membrane effects, boundary conditions and anisotropy of the horizontal bedding plane can become significant in such cases. Therefore, selection of an appropriate specimen geometry and range of cell pressures is important to obtain reliable test data.

Finally, compliance errors in the apparatus, such as bedding error, alignment problems, possible rocking movement of the top cap during shear, and specimen disturbance are larger in torsional shear apparatus than those in triaxial or plane strain apparatuses.

Therefore, it necessary to have an understanding on the extent and nature of the above stated limitations and compliance problems in torsional shear testing of soils, and to take necessary precautions to minimize these effects as the torsional shear apparatus is

an all-in-one type soil testing device with a variety of loading possibilities.

2.4 Formulation of stresses

In the hollow cylinder torsional shear apparatus, four stress components on the specimen, namely radial stress (σ_r), circumferential stress (σ_θ), axial stress (σ_z) and shear stress ($\tau_{z\theta}$), can be defined by controlling the outer cell pressure (p_o), the inner cell pressure (p_i) the vertical axial load (F_z) and the torque (T), as shown in Fig. 2.2. For this reason, hollow cylindrical specimens have four degrees of freedom from the point of view of the loads.

In this study, the averaged stress components acting on hollow cylindrical components were calculated with reference to Ampadu (1991). Similar formulations were employed by Hight et al. (1983), Saada (1988), Pradhan et al. (1988), Pradel et al. (1990), among others.

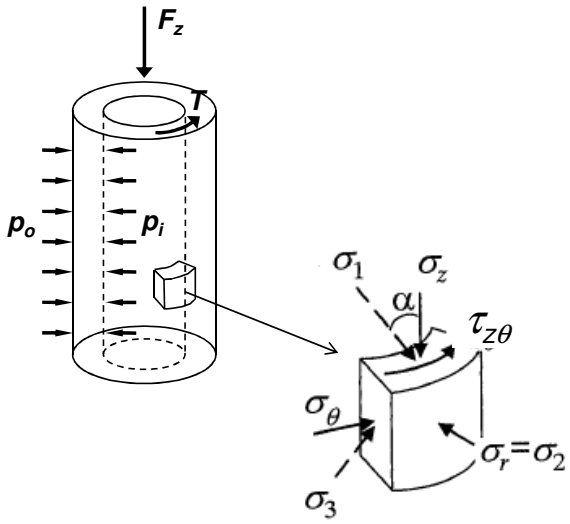

Fig. 2.2: External forces and stress components acting on hollow cylindrical specimen

2.4.1 Radial and circumferential stresses

It should be noted that the actual distribution of stresses in the specimen is very complicated due to the end restraint effect and bedding error. Timoshenko and Goodier (1970) gave a solution to the problem of a right hollow cylinder subjected to uniform inner pressure p_i and outer pressure p_o. Stress distribution is assumed to be symmetrical

with respect to the axis z of the hollow cylinder and the stress components do not depend on the radial angle θ and are a function of the radius r only. As a result, shear stress is equal to zero ($\tau_{r\theta} = 0$).

The equilibrium equation in the radial direction yields

$$\frac{\partial \sigma_r}{\partial r} + \frac{\sigma_r - \sigma_\theta}{r} + \omega = 0 \tag{2.9}$$

where ω is the body force. When $\omega = 0$, Eq. (2.9) is satisfied by

$$\sigma_r = \frac{A}{r^2} + 2C \tag{2.10}$$

$$\sigma_\theta = -\frac{A}{r^2} + 2C \tag{2.11}$$

where A and C are constants obtained by assuming the following boundary conditions:

$$\sigma_r \mid_{r=r_i} = p_i \tag{2.12}$$

$$\sigma_r \mid_{r=r_o} = p_o \tag{2.13}$$

in which r_o and r_i denote the current outer and inner radii of the specimen, respectively.

Due to conditions in Eq. (2.12) and Eq. (2.13), the Eq. (2.10) and Eq. (2.11) becomes

$$\sigma_r = \frac{p_o r_o^{\,2} - p_i r_i^{\,2}}{r_o^{\,2} - r_i^{\,2}} - \frac{r_i^{\,2} r_o^{\,2} (p_o - p_i)}{r_o^{\,2} - r_i^{\,2}} \frac{1}{r^2} \tag{2.14}$$

$$\sigma_\theta = \frac{p_o r_o^{\,2} - p_i r_i^{\,2}}{r_o^{\,2} - r_i^{\,2}} + \frac{r_i^{\,2} r_o^{\,2} (p_o - p_i)}{r_o^{\,2} - r_i^{\,2}} \frac{1}{r^2} \tag{2.15}$$

Finally, the average stress components are computed as follows:

$$\overline{\sigma}_r = \frac{\int_{r_i}^{r_o} \sigma_r dr}{\int_{r_i}^{r_o} dr} \tag{2.16}$$

$$\overline{\sigma}_\theta = \frac{\int_{r_i}^{r_o} \sigma_\theta dr}{\int_{r_i}^{r_o} dr} \tag{2.17}$$

and by substituting Eq. (2.14) into Eq. (2.16) and Eq. (2.15) into Eq. (2.17) the following equations are obtained:

$$\overline{\sigma}_r = \frac{p_o r_o + p_i r_i}{r_o + r_i} \tag{2.18}$$

$$\overline{\sigma}_\theta = \frac{p_o r_o - p_i r_i}{r_o - r_i} \tag{2.19}$$

In this study, the outer and inner cell pressures are kept equal to each other ($p_i = p_o$), therefore, Eq. (2.18) and Eq. (2.19) yield

$$\overline{\sigma}_r = \overline{\sigma}_\theta \tag{2.20}$$

2.4.2 Vertical stress

Average vertical stress at mid height of the specimen can be computed as follows:

$$\overline{\sigma}_z = \frac{L_C}{A_S} + \sigma_h + \sigma_g + \sigma_m \tag{2.21}$$

where

L_C = axial load detected by the inner load cell;

$A_S = \pi(r_o^2 - r_i^2)$, cross-sectional area of the specimen;

σ_h = horizontal stress (= σ_r = σ_θ);

$\sigma_g = \gamma' H/2$, overburden stress of the specimen due to its self-weight at its mid height;

$\gamma' = (G_S-1)/(1+e)\gamma_w$, unit weight of soil in water;

H = height of the specimen;

σ_m = correction for membrane stress (Tatsuoka et al., 1986).

In particular results

$$\sigma_m = 0 \qquad \text{(if} \quad \varepsilon_z > 0, \text{ compression)} \qquad (2.22)$$

$$\sigma_m = -\frac{3}{8}\varepsilon_z \frac{t_m E_m}{(r_o - r_i)} \qquad \text{(if} \quad \varepsilon_z < 0, \text{ extension)} \qquad (2.23)$$

where

ε_z = axial strain;

t_m = thickness of membrane;

E_m = Young's modulus of membrane.

2.4.3 Shear stress

Shear stress $\tau_{z\theta}$ acting on a soil element with area $dA = r\,d\theta\,dr$ can be linked with the torque T that is applied to the specimen as follows:

$$T = \int_{r_i}^{r_o}\int_{0}^{2\pi} \tau_{z\theta} r^2 d\theta dr = 2\pi \int_{r_i}^{r_o} \tau_{z\theta} r^2 dr \qquad (2.24)$$

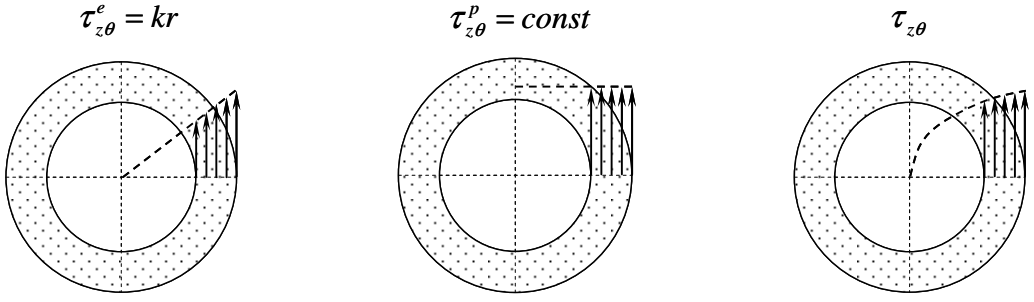

Fig. 2.3: Shear stress distributions in a hollow cylindrical specimen:
(a) linear elastic; (b) perfectly plastic; and (c) actual case

For a shear strain that is small enough for the specimen to be well within the elastic range, the shear stress increases in direct proportion with the distance to the center (Fig. 2.3a). In this case, the shear stress at any distance along the radial direction can be computed by the following equation:

$$\tau_{z\theta}^{e} = k\, r \tag{2.25}$$

Therefore Eq. (2.24) can be rewritten as

$$T = 2\pi \int_{r_i}^{r_o} k\, r^3 dr = \frac{\pi}{2}\left(r_o^4 - r_i^4\right)k \tag{2.26}$$

and the elastic component of shear stress can be evaluated as

$$\tau_{z\theta}^{e} = k\,\frac{r_o + r_i}{2} = \frac{T}{\pi\left(r_o^2 + r_i^2\right)\left(r_o - r_i\right)} \tag{2.27}$$

$$k = \frac{2T}{\pi\left(r_o^4 - r_i^4\right)} \tag{2.28}$$

On the contrary, when a large strain is imposed so that the stress reaches its ultimate value at all the points within the cross section, the shear stress is distributed uniformly (Fig. 2.3b); therefore, the shear stress at any distance along the radial direction can be computed by the following equations:

$$\tau_{z\theta} = \tau_{z\theta}^{p} = const \tag{2.29}$$

$$T = 2\pi\,\tau_{z\theta}^{p} \int_{r_i}^{r_o} r^2 dr = \frac{2}{3}\pi\,\tau_{z\theta}^{p}\left(r_o^{\,3} - r_i^{\,3}\right) \tag{2.30}$$

$$\tau_{z\theta}^{p} = \frac{3T}{2\pi\left(r_o^{\,3} - r_i^{\,3}\right)} \tag{2.31}$$

A specimen of saturated sand being tested may behave almost elastically at the early stage of cyclic loading, and it will become more and more like a plastic material as it proceeds in the loading stage. Eventually, when liquefaction sets in, the sand will exhibit the behavior as if it were a rigid-plastic material. Therefore it may be reasonable to assume that the real behavior of the sand (Fig. 2.3c) is somewhere in-between these two extreme cases for which the difference in the average shear stress is small. For this reason, in this study, the shear stress is averaged from Eq. (2.27) and Eq. (2.31) as shown below:

$$\bar{\tau}_{z\theta} = \frac{\tau_{z\theta}^{e} + \tau_{z\theta}^{p}}{2} = \frac{1}{2}\left[\frac{3T}{2\pi\left(r_o^{\,3} - r_i^{\,3}\right)} + \frac{T}{\pi\left(r_o^{\,2} + r_i^{\,2}\right)\left(r_o - r_i\right)}\right] \tag{2.32}$$

In Eq. (2.32), T is the torque acting on the soil which can be evaluated as

$$T = T_{CL} - T_m \tag{2.33}$$

where

T_{LC} = torque detected by the load cell;

T_m = membrane force (due to inner and outer membranes).

In a hollow cylindrical specimen the membrane force due to inner and outer membranes can be evaluated as

$$T_m = 2\pi\, t_m\left(r_o^2\ \tau_{z\theta,mo} + r_i^2\ \tau_{z\theta,mi}\right) \tag{2.34}$$

The rubber membrane is a linear elastic material with Poisson's ratio $\nu = 0.5$; its shear modulus G_m and shear stress τ_m can be calculated as

$$G_m = \frac{E_m}{2(1+\nu)} = \frac{E_m}{3} \tag{2.35}$$

$$\tau_{z\theta,m} = G_m\ \gamma_{z\theta,m} = \frac{E_m}{3}\gamma_{z\theta,m} \tag{2.36}$$

By using the definition in Eq.(2.36), Eq.(2.34) becomes

$$T_m = \frac{2}{3}\pi\, t_m E_m\left(r_o^2\ \gamma_{z\theta,mo} + r_i^2\ \gamma_{z\theta,mi}\right) \tag{2.37}$$

where

$\gamma_{z\theta,mo}$ = shear strain on the outer membrane;

$\gamma_{z\theta,mi}$ = shear strain on the inner membrane.

$$\gamma_{z\theta,mo} = \frac{r_o}{H}\theta \tag{2.38}$$

$$\gamma_{z\theta,mi} = \frac{r_i}{H}\theta \tag{2.39}$$

Therefore, the membrane force T_m in Eq. (2.33) can be evaluated as

$$T_m = \frac{2}{3}\pi\, t_m E_m\left(r_o^3 + r_i^3\right)\frac{\theta}{H} \tag{2.40}$$

where

r_o = outer radius of the specimen;

r_i = inner radius of the specimen;

t_m = thickness of membrane;

E_m = Young's modulus of membrane;

H = height of specimen;

θ = rotation angle at top cap detected by potentiometer.

2.4.4 Principal stresses

The principal stresses can be computed by the four stress components:

$$\begin{Bmatrix} \sigma_1 \\ \sigma_3 \end{Bmatrix} = \frac{\sigma_z + \sigma_\theta}{2} \pm \sqrt{\frac{(\sigma_z - \sigma_\theta)^2}{2} + \tau_{z\theta}^2} \tag{2.41}$$

$$\sigma_2 = \sigma_r \tag{2.42}$$

The angle between the directions of the major principal stress σ_1 with the vertical direction is

$$2\alpha = \arctan\left(\frac{2\tau_{z\theta}}{\sigma_z - \sigma_\theta} \right) \tag{2.43}$$

In addition the intermediate principal stress is defined as

$$b = \frac{\sigma_2 - \sigma_3}{\sigma_1 - \sigma_3} = \frac{1}{2}\left[\frac{\sigma_r - \frac{\sigma_z + \sigma_\theta}{2}}{\left(\frac{\sigma_z - \sigma_\theta}{2} \right)^2 + \tau_{z\theta}^2} + 1 \right] \tag{2.44}$$

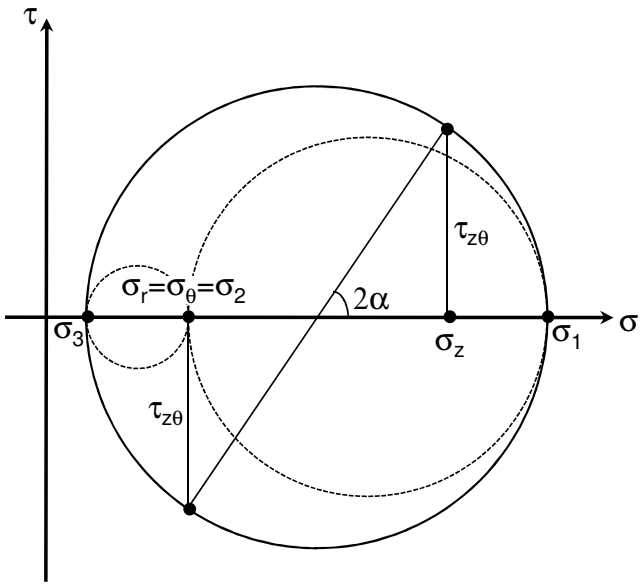

Fig. 2.4: Mohr's circles of stress

2.5 Formulation of strains

In this study, the averaged strains components acting on hollow cylindrical components were calculated with reference to Ampadu (1991).

Axial strain ε_z, radial strain ε_r, circumferential strain ε_θ, and shear strain $\gamma_{z\theta}$ are the four strain components of the soil element to be determined.

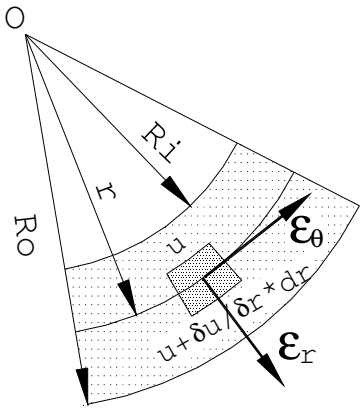

Fig. 2.5: Definition of radial and circumferential strains of a soil element

As shown in Fig. 2.5, ε_r and ε_θ of a soil element can be evaluated as

$$\varepsilon_r = -\frac{\left[u + \left(\frac{\delta u}{\delta r}\right)dr\right] - u}{dr} = -\frac{du}{dr} \tag{2.45}$$

$$\varepsilon_\theta = -\frac{(u+r)d\theta - rd\theta}{rd\theta} = -\frac{u}{r} \tag{2.46}$$

where

u = deformation of a soil element in radial direction;

r = distance to the centre of the soil element from the centre of the specimen.

Combining Eq. (2.45) and Eq. (2.46) yields

$$\frac{d\varepsilon_\theta}{dr} + \frac{1}{r}\left(\varepsilon_\theta - \varepsilon_r\right) = 0 \tag{2.47}$$

If it is assumed that distribution of u is linear in the radial direction

$$u = \frac{u_o - u_i}{r_o - r_i}\, r + \frac{u_i r_o - u_o r_i}{r_o - r_i} \tag{2.48}$$

then the average radial strain $\bar{\varepsilon}_r$ results

$$\bar{\varepsilon}_r = \frac{\int_{r_i}^{r_o} \varepsilon_r\, r\, dr}{\int_{r_i}^{r_o} r\, dr} = -\frac{u_o - u_i}{r_o - r_i} \tag{2.49}$$

whereas, the average circumferential strain $\bar{\varepsilon}_\theta$ can be calculated as

$$\bar{\varepsilon}_\theta = \frac{\int_{r_i}^{r_o} \varepsilon_\theta\, r\, dr}{\int_{r_i}^{r_o} r\, dr} = -\frac{u_o + u_i}{r_o - r_i} \tag{2.50}$$

where

u_o = displacement in the radial direction at the distance of the outer radius;

u_i = displacement in the radial direction at the distance of the inner radius;

r_o = outer radius of the specimen;

r_i = inner radius of the specimen.

On the other hand, the average axial strain $\bar{\varepsilon}_z$ and the average shear strain $\bar{\gamma}_{z\theta}$ can be calculated by

$$\bar{\varepsilon}_z = -\frac{dw}{dz} = -\frac{\Delta H}{H} \qquad \text{(positive in compression)} \tag{2.51}$$

$$\bar{\gamma}_{z\theta} = \frac{\int_{r_i}^{r_o} \gamma_{z\theta}\, r dr}{\int_{r_i}^{r_o} r dr} = \frac{2\theta\left(r_o^3 - r_i^3\right)}{3H\left(r_o^2 - r_i^2\right)} \tag{2.52}$$

where

H = height of the specimen;

θ = rotation angle at top cap detected by potentiometer.

Evaluation of volumetric strain in a hollow cylindrical specimen is generally not easy, due to technical difficulties on the measurement of the change of the inner and outer diameters.

To overcome these troubles, it is possible to employ a method to evaluate the change of both inner and outer diameters during the consolidation process, which is made based on the assumption of same ratio of change in the inner and outer radius of the specimen by using the following formulae (JGS, 1998):

$$d_i = d_{i0}\sqrt{\frac{1-\varepsilon_{vol}}{1-\varepsilon_z}} \tag{2.53}$$

$$d_o = d_{o0}\sqrt{\frac{1-\varepsilon_{vol}}{1-\varepsilon_z}} \tag{2.54}$$

where,

ε_{vol} = volumetric strain of the specimen;

ε_z = axial strain of the specimen;

d_{i0} = initial inner diameter of the specimen;

d_{o0} = initial outer diameter of the specimen.

2.6 Membrane penetration effects

Whenever the effective confining stress increases, the membrane penetrates into the voids of the granular material creating an error in the measured volume change as schematically illustrated in Fig. 2.6. The occurrence of volume change in undrained tests due to membrane penetration was first recognized by Newland and Alley (1959). Vaid and Negussey (1984) critically assessed the membrane penetration in triaxial tests and proposed two methods to assess the membrane penetration (MP).

Multiple specimen method

Three or more triaxial specimens of the same density and different diameters are subjected to the same type of isotropic compression or swelling or both. Then the measured volume change per unit surface area of the membrane covered by soil is plotted against the diameter of the specimen. The amount of membrane penetration per unit surface area of membrane can be obtained by the intercept of the plot. It is assumed in this method that the true volumetric strains occurred are the same in all the specimens with different diameters.

Single specimen method

One triaxial specimen is subjected to isotropic compression and swelling. It is assumed that the behavior of sand is truly isotropic during isotropic unloading ($\varepsilon_z = \varepsilon_r = \varepsilon_\theta$). Hence the difference between the measured volumetric strain and the calculated volumetric strain by assuming truly isotropic behavior ($\varepsilon_{vol} - 3\varepsilon_z$) during isotropic unloading is the amount of volumetric strain due to membrane penetration.

Vaid and Negussey (1984) and Tanimoto and Tanaka (1986) compared the assessed membrane penetration by the above two methods and found no significant difference.

Goto (1987) evaluated membrane penetration per unit surface area (ΔMP) of latex membrane of 0.3 mm thickness for a cylindrical Toyoura sand specimen as follows:

$$\Delta MP = 1.7\times10^{-3}\times\log_{10}\left(\sigma_r^{'}/\sigma_{r0}^{'}\right) \qquad (\mathrm{cm}^3/\mathrm{cm}^2) \qquad (2.55)$$

where $\sigma_r^{'}$ and $\sigma_{r0}^{'}$ are current and initial effective confining pressures, respectively.

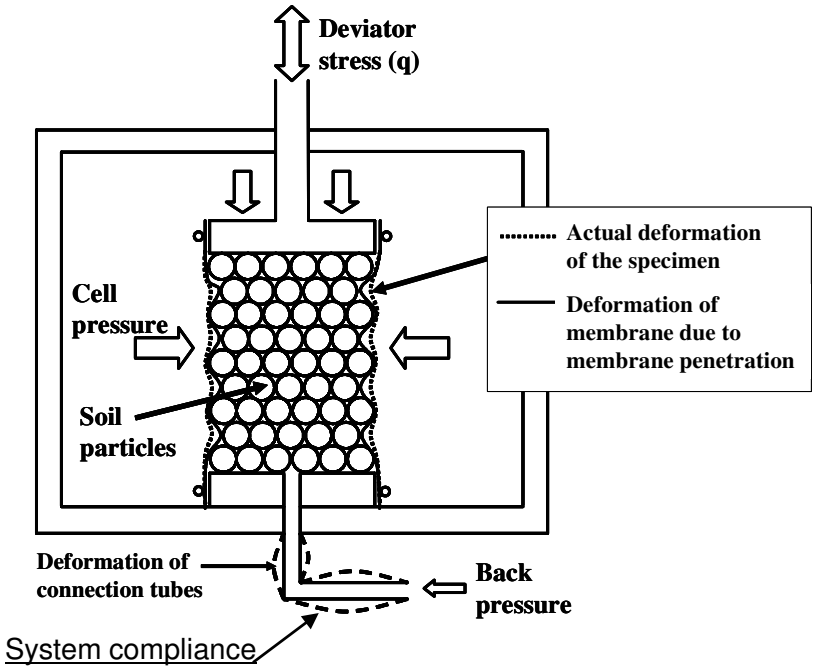

Fig. 2.6: Schematic illustration of membrane penetration and system compliance (after De Silva, 2008)

2.7 References

1. Ampadu, S. I. K. (1991): "Undrained behavior of kaolin in torsional simple shear", PhD thesis, Dep. of Civil Engineering, University of Tokyo, Japan
2. Bardet, J. P. (1997): "Experimental soil mechanism", Prentice Hall, Los Angeles
3. Chiaro, G., Kiyota, T., De Silva, L.I.N., Sato, T., and Koseki, J. (2009): "Extremely large post-liquefaction deformations of saturated sand under cyclic torsional shear loading", Proc. of Earthquake Geotechnical Engineering Satellite Conference, 17th International Conference on Soil Mechanics and Geotechnical Engineering, Alexandria, Egypt
4. Connolly, T. M. and Kuwano, R. (1999): "The measurement of G_{max} in a resonant column, bender element, torsional shear apparatus", Pre-failure Deformation Characteristics of Geomaterials, Jamiolkowski, Lancellotta and Lo Presti (Eds.), Balkema, Rotterdam, Vol. 1, 73-80
5. De Silva, L.I.N. (2008): "Deformation characteristics of sand subjected to cyclic drained and undrained torsional loadings and their modeling", PhD thesis, Dep. of Civil Engineering, University of Tokyo, Japan
6. De Silva, L.I.N., Koseki, J., and Sato, T. (2006): "Effect of different pluviation techniques on deformation property of hollow cylinder sand specimens", Proc. of International Symposium on Geomechanics and Geotechnics of Particle Media, Ube, Yamaguchi, Japan, 29-33
7. De Silva, L.I.N., Koseki, J., Sato, T. and Wang, L. (2005): "High capacity hollow cylinder apparatus with local strain measurement", Proc. 2nd Japan-U.S. Workshop on Testing, Modeling and Simulation, Geotechnical Special Publication, ASCE, Vol. 156, 16-28
8. Di Benedetto, H., Geoffroy, H., Suzeat, C. and Cazacliu, B. (1999): "Sand behavior in very small to medium strain domains", Pre-failure Deformation Characteristics of Geomaterials, Jamiolkowski, Lancellotta and Lo Presti (Eds.), Balkema, Rotterdam, Vol. 1, 89-96
9. Goto, S. (1987): "Strength and deformation characteristics of granular materials in triaxial tests", PhD thesis, Dep. of Civil Engineering, University of Tokyo, Japan
10. Hight, D. W., Gens, A. and Symes, M. J. (1983): "The development of a new hollow cylinder apparatus for investigating the effects of principal stress rotation in soils", Geotechnique, 33 (4), 355-383

11. Hong Nam, N. and Koseki, J. (2005): "Quasi-elastic deformation properties of Toyoura sand in cyclic triaxial and torsional loadings and their modeling", Soils and Foundations, 45 (5), 19-38

12. JGS (1998); "Standards of Japanese geotechnical society for laboratory shear tests", Japanese Geotechnical Society, 5550-1998 (English version)

13. Kiyota, T. (2007); "Liquefaction strength and small strain properties of in-situ frozen and reconstituted sandy soils, PhD thesis, Dep. of Civil Engineering, University of Tokyo, Japan

14. Kiyota, T., Sato, T., Koseki, J., and Mohammad, A.M. (2008): "Behavior of liquefied sands under extremely large strain levels in cyclic torsional shear tests", Soils and Foundations, 48 (5), 727-739

15. Koseki, J. and Ohta, A. (2001): "Effects of different consolidation conditions on liquefaction resistance and small strain quasi-elastic deformation properties of sands containing fines", Soils and Foundations, 41 (6), 53-62

16. Newland, P. and Alley, B. H. (1959): "Volume changes during undrained triaxial tests on saturated dilatants granular material", Geotechnique, 9 (4), 174-182

17. Oka, F., Yashima, A., Tateishi, Y., Taguchi, Y. and Yamashita, S. (1999): "A cyclic elasto-plastic constitutive model for sand considering a plastic-strain dependence of the shear modulus", Geotechnique, 49 (5), 661-680

18. Pradel, D., Ishihara, K. and Gutierrez, M. (1990): "Yielding and flow of sand under principal stress axes rotation", Soils and Foundations, 30 (1), 87-99

19. Pradhan, T. B. S. (1990): "The behavior of sand subjected to monotonic and cyclic loadings", PhD thesis, Dep. of Civil Engineering, University of Tokyo, Japan

20. Pradhan, T. B. S., Tatsuoka, F. and Horii, N. (1988): "Simple shear testing on sand in a torsional shear apparatus", Soils and Foundations, 28 (2), 95-112

21. Saada, A. S. (1988): "Hollow cylindrical torsional devices: their advantages and limitations", Advanced Triaxial Testing of Soil and Rock, ASTM STP 977, Donaghe R. T., Chaney, R. C. and Silver, M. L. (Eds.), Philadelphia, 766-795

22. Tanimoto, K. and Tanaka, Y. (1986): "Yielding of soil as determined by acoustic emission", Soils and Foundations, 26 (3), 69-80

23. Tatsuoka, F., Sonoda, S., Hara, K., Fukushima, S. and Pradhan, T. B. S. (1986). "Failure and deformation of sand in torsional shear", Soils and Foundations, Vol. 26, No. 4, pp. 79-97.

24. Timoshenko, S. P. and Goodier, J. N. (1970): "Theory of Elasticity", 3rd Edition, McGraw-Hill Book company, Inc., N.Y., 65-71

25. Vaid, Y. P. and Negussey, D. (1984): "A critical assessment of membrane penetration in the triaxial tests", Geotechnical Testing Journal, ASTM, 7 (2), 70-76

26. Vaid, Y. P., Sayao, A., Hou, E., and Negussey, D. (1990): "Generalized stress-path-dependent soil behavior with a new hollow cylinder torsional apparatus", Canadian Geotechnical Journal, 27 (5), 601-616

27. Yoshimine, M., Ishihara, K. and Vargas, W. (1998): "Effects of principal stress direction and intermediate principal stress on undrained shear behavior of sand", Soils and Foundations, 38 (3), 179-188

CHAPTER 3

Test conditions: material, apparatus and procedure

3.1 Introduction

Toyoura sand (Toyoura silica sand or Toyoura standard sand) is the most employed sand for laboratory tests in Japan, due to its uniformity and its negligible percentage of fines content, as well as its wide availability. The shape of its particles is mostly sub-angular. From a mineralogical point of view Toyoura sand consists mainly of quartz.

It is considered that simple shear tests simulate field stress conditions more closely than triaxial tests. However, due to mechanical limitations in performing simple shear tests the shear strain levels employed are limited to less than 10%. On the contrary, the torsional shear apparatus can aid in the investigation of the stress-strain behavior of sand under simple shear conditions up to larger deformation.

In this study, in order to observe the effect of initial static shear on the undrained cyclic behavior of sand, a series of torsional shear tests on saturated Toyoura sand specimens were performed. During the process of the undrained cyclic torsional loading the vertical displacement of the top cap was prevented with the aim to simulate as much as possible the simple shear condition that the ground undergoes during horizontal excitation.

In this chapter, first the testing material is identified by analyzing its index properties, particle shape and mineralogical components. Then the test apparatus which consists in a high-capacity torsional shear apparatus developed at the Institute of Industrial Science, University of Tokyo, is described in detail. Subsequently, the technique employed to prepare the specimens including the saturation methods are illustrated. Finally, the loading procedure is described.

3.2 Test material

In this study, all the tests were performed on Toyoura sand (known also as Toyoura silica sand as well as Toyoura standard sand), which is uniform sand with negligible fines content under 75μm. The properties of this material are listed in Table 3.1, while the grain size distribution curve is shown in Fig. 3.1.

Table 3.1 Material properties

Material	*Gs*	e_{max}	e_{min}	D_{50} *(mm)*	F_C *(%)*	C_U	C_C
Toyoura sand	2.656	0.992	0.632	0.18	0.1	1.65	1.20

G_S: specific gravity; e_{max}: maximum void ratio; e_{min}: maximum void ratio; D_{50}: mean diameter; F_C: fines content; C_U: coefficient of uniformity; C_C: coefficient of curvature.

An important physical parameter to identify coarse soils is the shape of soil particles. In this regard, the standards for testing materials suggest that a visual observation on the grain of coarse soil be performed in order to define the shape of the particles. The particle shape of silts, sands and gravels ranges between very angular to well rounded (Fig. 3.3). Very angular particles can be found usually on the vicinity of rock slopes as product of rock weathering; on the other hand, well rounded particles can be found far from the original deposits and usually they have suffered the process of erosion due to wind and/or water action.

By analyzing the picture in Fig 3.2 in which the single particles can be easily distinguished and compared with respect to their shape in Fig. 3.3, it is possible to say that the shape of Toyoura sand particles is mostly sub-angular.

Another parameter useful to classify soils is the mineralogical composition. In this study, a mineralogical analysis revealed that the employed Toyoura sand consists mainly of quartz and limestone, with residual amounts of mica (i.e., biotite) and other iron-magnesium minerals (Fig. 3.2). A similar classification of sand was presented by Chiaro (2007) to describe the mineralogical composition of Fossanova sand (Italy).

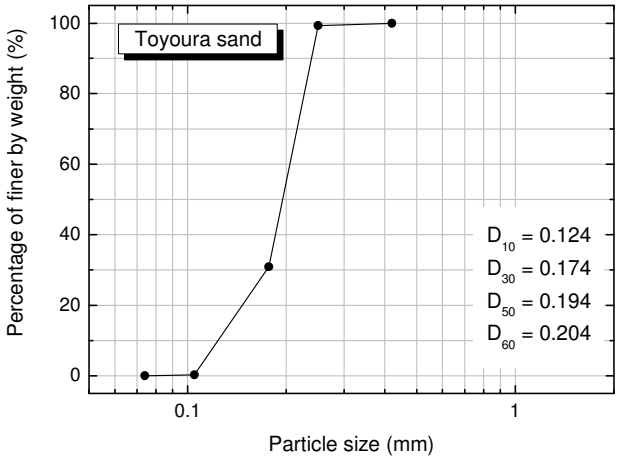

Fig. 3.1: Grain distribution curve obtained for Toyoura sand.

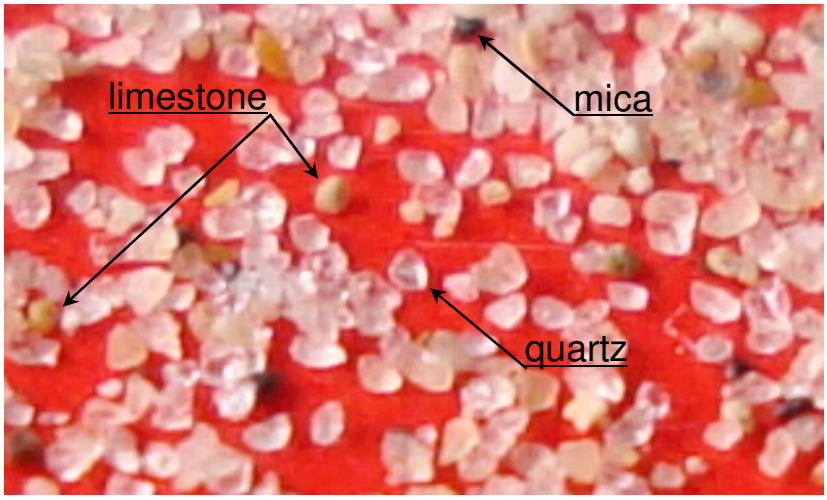

Toyoura sand consists mainly of sub-angular quartz particles over 85-90%. Prevalent is the presence of limestone with sub- rounded particle shape. Residual amount of mica and iron-magnesium minerals can also be found.

Fig. 3.2: Toyoura sand grain characteristics and mineralogical composition.

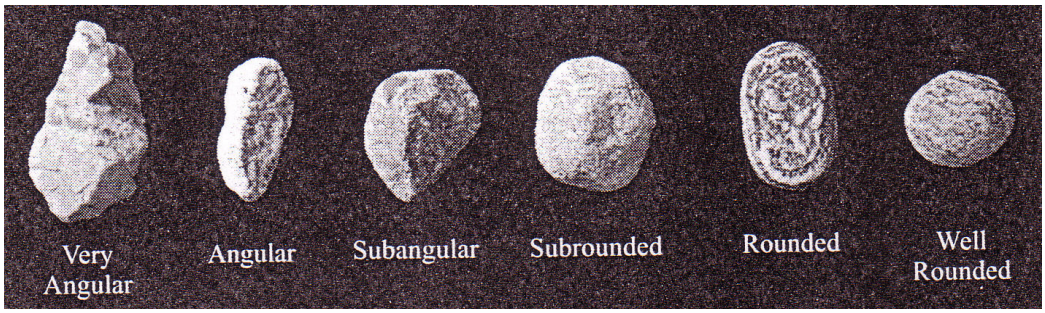

Fig. 3.3: Classification of particle shapes of silts, sands and gravels (Coduto,1999)

3.3 Hollow cylinder torsional shear test apparatus

In this study, a high-capacity torsional shear test apparatus developed at the Institute of Industrial Science, University of Tokyo was employed (Fig. 3.4a).

After being modified in order to enlarge the range of torsional shear displacement level, it was made possible to achieve double amplitude shear strain levels exceeding 100% by employing a belt-driven torsional shear system which is connected to an AC servo motor through electro-magnetic clutches and a series of reduction gears. The details of the torque-transmission parts after the modification are shown in Fig. 3.4b and Fig. 3.4c.

This apparatus mainly consists of a cell, loading devices, and measurement devices. The loading system of this apparatus consists of servo-controlled axial and torque loading devices. The axial load and torque are simultaneously and independently applied on the hollow cylindrical specimen via two servo-motors at constant strain rates, in principle. Each loading device has an electro-magnetic clutch which can reverse the loading direction instantly. The axial and torque loading and cell pressure are automatically controlled by a computer during the test including the consolidation stage before the shear loading. By using a lucid acrylic cell and drawing a grid on the external face of the outer membrane, specimen deformation behavior can be observed from the outside of the cell and its visual analysis can be performed by taking a series of pictures.

3.3.1 Medium-size hollow cylindrical specimen

This apparatus is capable of testing specimens with various dimensions ranging from 200 mm in outer diameter, 120 mm in inner diameter and 300 mm in height to 90 mm in outer diameter, 60 mm in inner diameter and 200 mm in height.

Larger specimen sizes make it possible to investigate the properties of soils with larger particles such as gravel; on the contrary, medium-size specimens with an outer diameter of 150 mm make it possible to perform tests on in-situ frozen specimens (Kiyota, 2007; and Kiyota et al., 2008) as they are usually available in the form of cylinders of 150 mm in diameter.

In this study, a hollow cylindrical specimen with outer diameter of 150 mm, inner diameter of 90 mm and height of 300 mm was employed.

3.3.2 Vertical and torsional loading systems

The vertical and torsional loading systems are schematically shown in Fig. 3.4b. Vertical and torsional loading capacities of the system are 8 kN and 0.15 kNm, respectively.

The axial loading system consists of an AC servo-motor, a reduction gear system with two gears, electro magnetic clutches and brakes, and a ball screw with a pre-pressured nut. The motor always drives in one direction. Simultaneously, the upper gear is rotating in one direction and the lower gear is rotating in the opposite direction. The movement of the loading shaft is switched from downwards to upwards without any backlash by using the electric clutch.

The torsional loading system also consists of similar devices. Torque is transmitted to the loading shaft by means of a metal band. Both vertical and torsional loading systems are designed to have nearly zero backlashes.

3.3.3 Cell pressure

Cell pressure is applied through an electro-pneumatic transducer (E/P) with a capacity of 1000 kPa. Inner and outer cell pressures were kept equal to each other throughout the tests in the present study. Control of cell pressure and loading system was fully computerized.

3.3.4 Measurement devices

The employed system has 24 channels to measure stresses, strains and volume changes. Seven channels were used in this study: two channels for the two-component load cell (axial and torque loads), one channel for the External Displacement Transducer (ETD), two channels for inner and external potentiometers, and one channel each for High Capacity Differential Pressure Transducer (HCDPT) and Low Capacity Differential Pressure Transducer (LCDPT). The remaining channels were used in previous studies for proximity transducers (Gap Sensors) as well as Local Deformation Transducers (LDTs).

The function of each employed devices is described below:

Two-component load cell

A two-component load cell (Fig. 3.4a and Fig. 3.5) with a negligible coupling effect (i.e., no effect of axial load on torque measurement and vice versa) located inside the cell is employed in this apparatus. The capacities of vertical load and torque are of 8 kN and 0.15 kNm, respectively.

Inner potentiometer

An inner potentiometer with a pulley having a diameter of 50 mm (Fig. 3.6) is attached to the top cap for measuring its rotational angle. It can detect shear strain levels up to 6%.

External potentiometer

An external potentiometer, as illustrated in Fig. 3.4c and Fig. 3.7, is employed to measure extremely large shear strain levels exceeding 100% in terms of double amplitude.

High Capacity Differential Pressure Transducer (HCDPT)

The HCDPT measures the confining stress by the difference in pressures between the cell pressure and the pore water pressure. The positive terminal of the HCDPT is connected with the cell chamber to measure the cell pressure, while the negative one is connected to both the top and bottom drainage tubes of the specimen in order to measure the pore water pressure. The employed HCDPT (Fig. 3.8) has a maximum capacity over 600kPa.

Low Capacity Differential Pressure Transducer (LCDPT)

The LCDPT (Fig. 3.9) measures the volume change by the difference in water heads between two burettes, one that collects drained water from the specimen and the other used as a reference.

External Displacement Transducer

Axial deformations outside the cell are measured by an EDT with a maximum range of 30 mm (Fig. 3.10) located along the loading shaft.

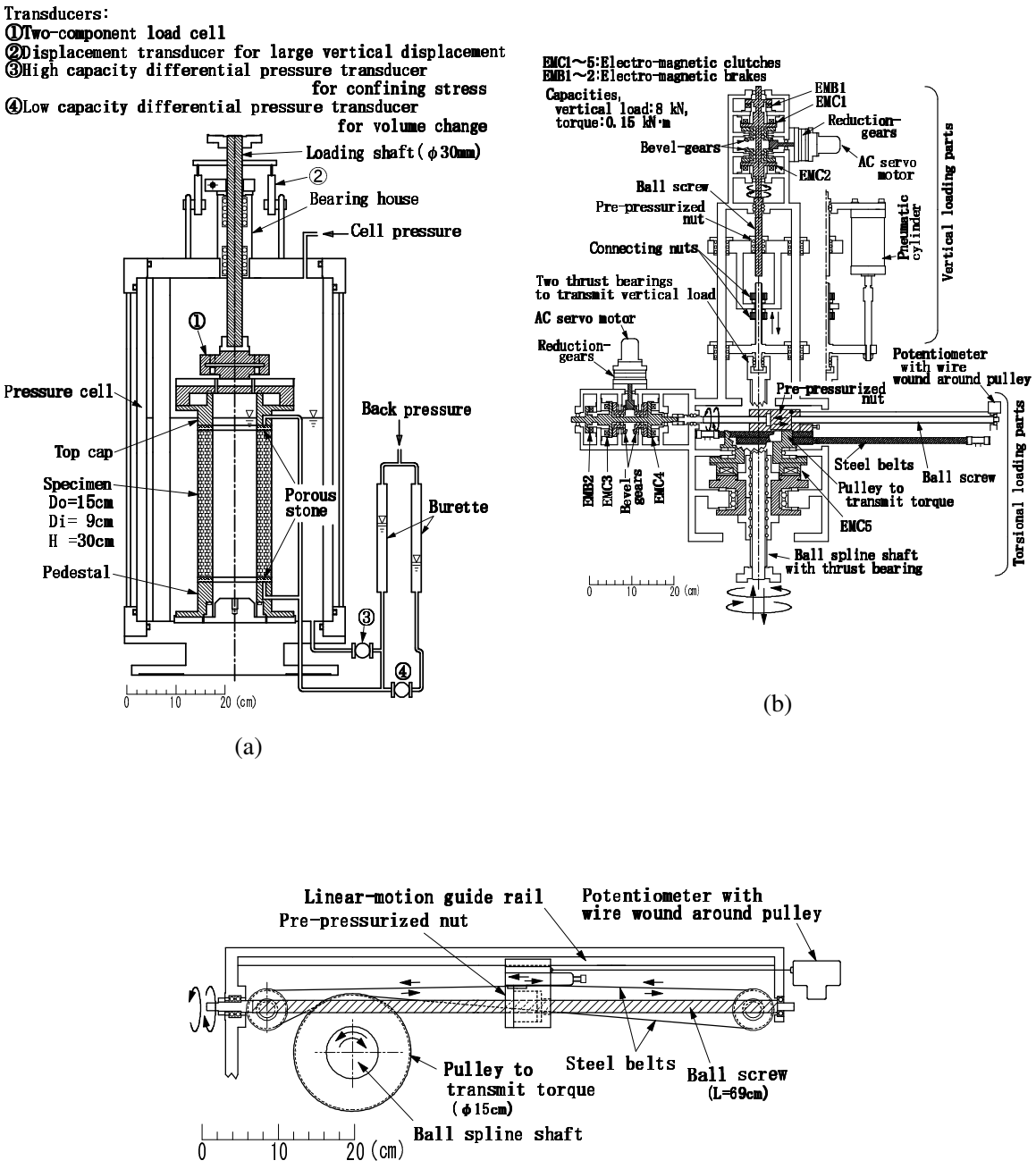

Fig. 3.4: (a) Torsional shear test apparatus on hollow cylindrical specimen; (b) loading device; and (c) plan view of torque-transmission part

3.3.5 Calibration of transducers

Fig. 3.5 through Fig. 3.10 show the calibration test results obtained for the transducer devices employed in this study.

(a)

(b)

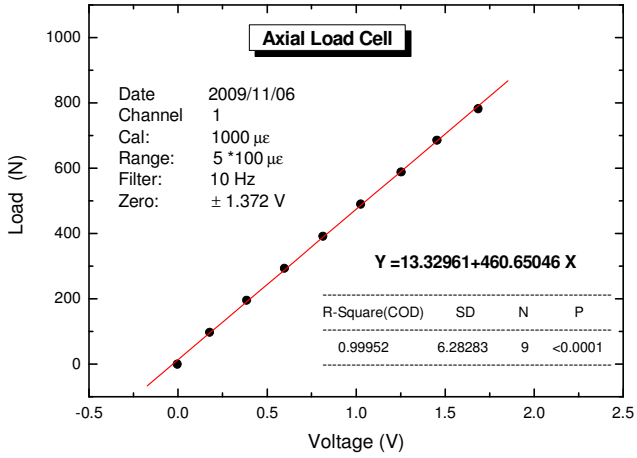

(c)

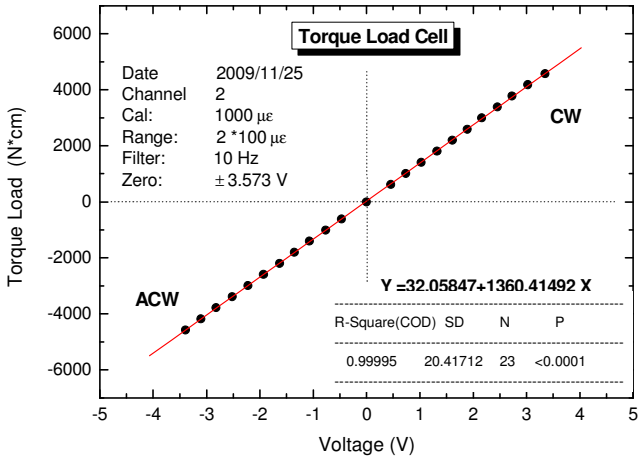

Fig. 3.5: (a) Two-component load cell (axial and torque loads); (b) axial load calibration; and (c) Torque calibration

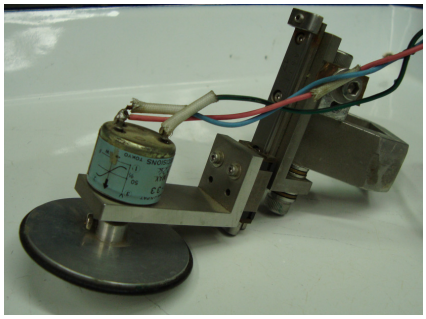

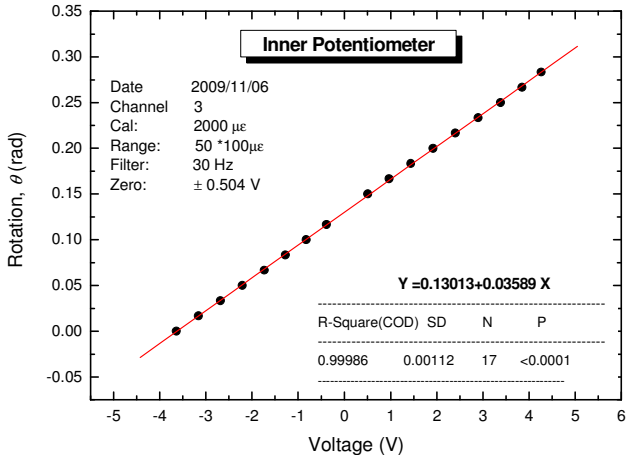

Fig. 3.6: Inner potentiometer and its calibration

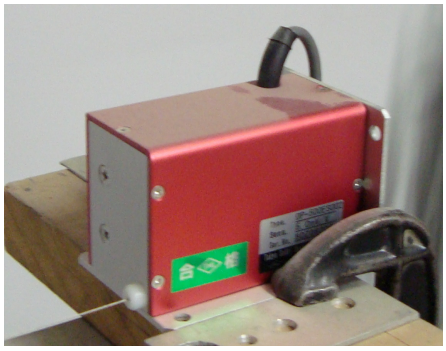

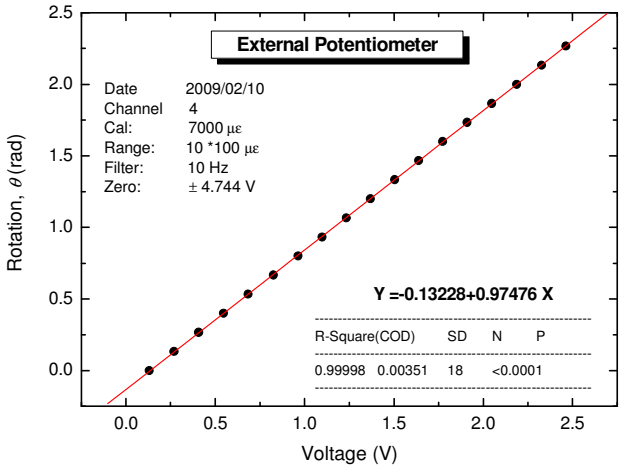

Fig. 3.7: External potentiometer and its calibration

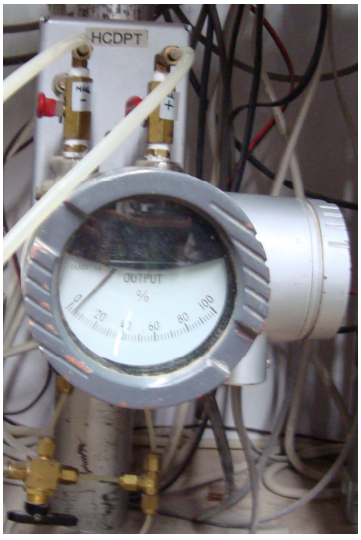

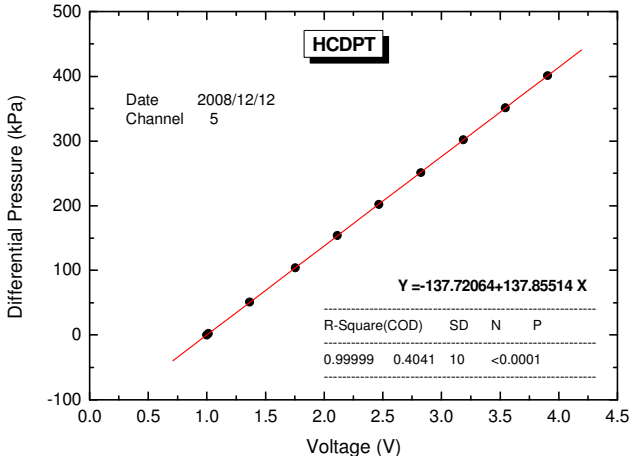

Fig. 3.8: HCDPT and its calibration

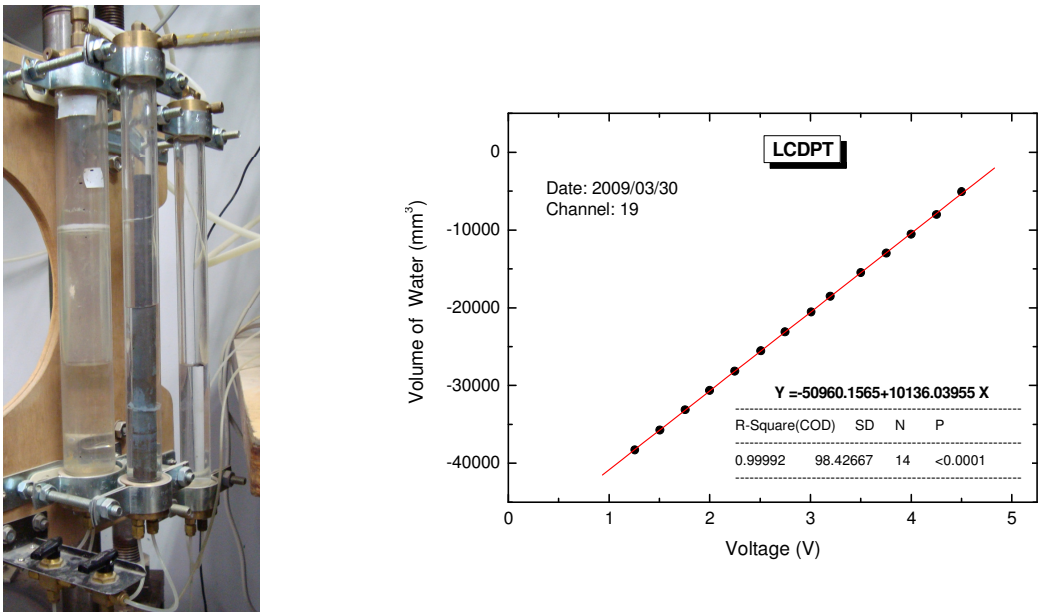

Fig. 3.9: LCDPT and its calibration

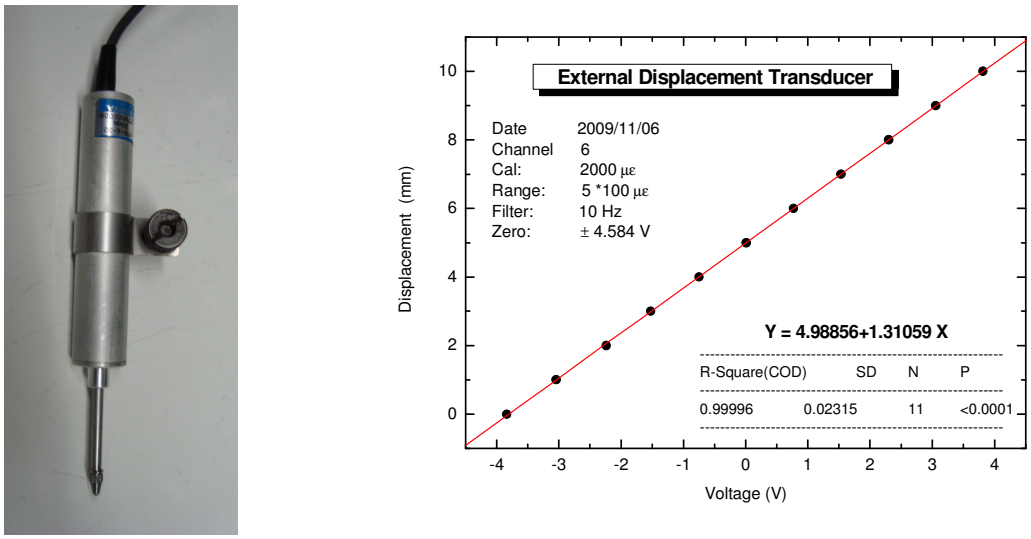

Fig. 3.10: External Displacement Transducer (EDT) and its calibration

3.4 Specimen preparation

First the outer latex membrane of 0.3 mm thick was placed over the pedestal which contains a porous stone with blades in order to apply the necessary friction during the torsional shear loading. Then the gap between the outer membrane and the pedestal was sealed by using a rubber band and a rubber O-ring.

The inner latex membrane of 0.3 mm thickness was placed over a metal ring, which has a rubber O-ring at the top. Following this the metal ring together with the membrane was placed into the pedestal hole while taking the inner membrane out from the hole of the pedestal. Extreme care was taken not to damage the membranes at all times. The pedestal was then screwed into the apparatus base firmly.

The inner mould was then set. The inner mould consists of four metal parts, which makes a perfect cylinder, a steel ring that is used to keep the four parts together and a steel rod screwed at the end to keep the inner mould fixed in a vertical position. All four parts of the inner mould were placed inside the inner membrane, which comes out from the pedestal, and the mould was firmly fixed using the ring and rod.

Subsequently, the outer mould was then fixed. This outer mould consists of two symmetrical metal parts with two clamps to tighten them together. A small amount of lubricant (grease) was applied along the edges of the outer mould before fixing it. After fixing the outer mould, the extra part of the outer membrane was put over the outer mould, and it was ensured that the gap between outer membrane and the outer mould was perfectly sealed. A partial vacuum of 30 kPa was then applied to the space between outer membrane and outer mould.

The specimens were prepared by employing the air pluviation method proposed by Hong Nam (2004), which is a slight modification of the one described in the relevant standard procedure (JGS, 1998). This method was introduced in order to reduce the degree of inherent anisotropy in radial direction of the hollow cylindrical sand specimens (Hong Nam, 2004; and De Silva et al., 2006). Following this method, the specimens were prepared by pouring the sand into a mold while moving radially (R) the nozzle of the pluviator and at the same time circumferentially in alternative directions, i.e. first in clockwise (CW) and then anti-clockwise (ACW) directions, as shown in Fig. 3.11. To obtain specimens with initial relative density (D_r) (i.e., measured after achieving isotropic consolidation of 100 kPa) of about 45%, the falling height was selected to be 25.5 cm.

The falling height was kept constant during the pluviation process to get a specimen with highly uniform density.

After pluviating the material to the full height of the specimen, the top surface of the specimen was leveled horizontally by using a metal strip, and the waste material was collected and weighed.

The next step was to place the top cap over the specimen. First the top cap guider was fixed to one of the four steel poles that come from the base of the apparatus. Then a steel cable with three bolts connected to one end and with dead weight attached to the other end was attached to the top cap using the three bolts. After that the cable attached to the top cap was put over the pulleys of the guider and balanced using counter balances. The horizontality of the top cap surface was maintained by adjusting the three bolts before it was placed on the top of the specimen. Finally the top cap was placed very carefully over the specimen until it touched the top surface. Two clamps were then fixed symmetrically to two steel poles and the top cap was held in position by attaching it to the clamps using the bolts. After clamping, the extra part of the inner membrane was pulled gently over the top cap inner ring, and the extra part of the outer membrane was placed over the top cap outer ring. The specimen was perfectly sealed by using rubber bands, covering the inner and outer rings of the top cap.

The counter balance was then applied again, and the clamps were removed. After a partial vacuum of 30 kPa was applied to the specimen, the outer mould was removed. The top cap was clamped again, and the inner mould was removed.

The top cap was connected firmly to the load cell which was previously set on zero voltage reading. The other transducers such as inner and external potentiometers, HCDPT and LCDPT were set after, before the specimen was covered with the cell.

The cell was filled with water and finally, the cell pressure was increased gradually up to 30 kPa, while reducing the partial vacuum applied to the specimen down to the atmospheric pressure, in order to maintain the same effective stress state acting on the specimen. When changing the vacuum into cell pressure, the dead weight above the specimen was counter-balanced every step of the way.

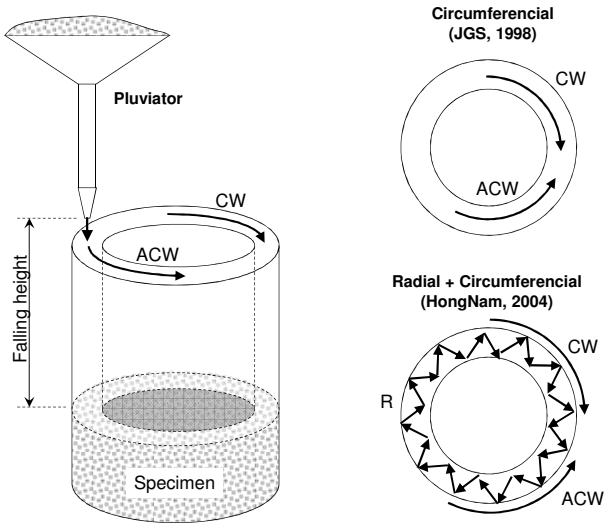

Fig. 3.11: Schematic illustration of air-pluviation technique employed in this study

3.5 Saturation of specimen

The saturation of the specimen was achieved by using either CO_2 method (Fig. 3.12) or double vacuum method (Fig. 3.13). To saturate using the CO_2 method, the specimen was kept under cell pressure without any back pressure. Then the voids inside the specimen were filled with CO_2. It took at least 3 hours to complete this process for the specimen sizes used in the current study. CO_2 was used because it dissolves in water allowing water to easily replace the air voids. Then the de-aired distilled water prepared in advance was allowed slowly to enter from the bottom of the specimen replacing the air in voids. Expelled air was taken out from the top of the specimen into a drainage tank. The specimen was assumed to be fully saturated when no air bubbles could be seen in the drainage tank. Usually it took about 6 hours to achieve this state for the specimen sizes used.

The CO_2 method was employed to saturate the first few tests of the current study. However, it was observed that the *B* value (Skempton, 1954) was less than 0.95 in some tests. Some uncertainty could be observed in saturating the specimen using CO_2 method due possibly to the large size of the specimen.

Therefore, in the following series, the double vacuum method (Ampadu, 1991) was employed to saturate the specimens. In the double vacuum method, a complete vacuum (-98 kPa) was applied to the specimen as a back pressure, while keeping the effective stress constant at 38 kPa by applying a partial vacuum of 60 kPa to the cell. The specimen was kept for about 3 hours under this state before allowing the water to enter. Then the de-aired distilled water was allowed to enter the specimen similar to that in the case of the CO_2 method. A complete vacuum was applied to both the distilled water tank and the drainage water tank (Fig. 3.13).

After the saturation process was completed, a back pressure of 200 kPa was applied, while keeping the effective stress constant, to further increase the degree of saturation of the specimen by compressing any remaining air.

In general, laboratory tests are performed on water-saturated samples because unsaturated sand is significantly less liquefiable than saturated sand (Fig. 3.14).

The extent of water saturation of tested specimens can be evaluated by using Skempton's *B* value, because B value is a more sensitive index than the degree of saturation when a specimen is near complete saturation.

Skempton (1954) described the increment of pore water pressure in soil undergoing undrained stress increments by

$$\Delta u = B\{\Delta\sigma_3 + A(\Delta\sigma_1 - \Delta\sigma_3)\} \qquad (3.1)$$

where:

Δu = increment of pore water pressure;

$\Delta\sigma_1$ = increment of major total principal stress;

$\Delta\sigma_3$ = increment of minor total principal stress.

In particular, in Eq. (3.1), the first term ($\Delta\sigma_3$) stands for the contribution as result of the isotropic stress increment, while the latter ($\Delta\sigma_1$- $\Delta\sigma_3$) corresponds to the component produced by shear-induced dilatancy.

Under the undrained isotropic loading, equal stress increments ($\Delta\sigma_1$= $\Delta\sigma_3$) are applied to

the specimen, therefore Skempton's A value becomes zero ($A=0$). Hence, the extent of saturation can be evaluated by comparing the measured pore water pressure increment with the theoretical value of fully saturated sand (i.e., for ideally and fully saturated specimen $B=1.0$ and $\Delta u = \Delta\sigma_3$)

$$B = \frac{\Delta u}{\Delta \sigma_3} \tag{3.2}$$

The correlation between B value and the degree of saturation S_r is expressed by Eq. (3.3).

$$B = \frac{\Delta u}{\Delta \sigma_3} = \frac{1}{1 + \frac{e}{1+e}\left(\frac{S_r}{K_W} + \frac{1-S_r}{P_{BP}}\right)\frac{1}{m_V}} \tag{3.3}$$

As shown in Fig. 3.15, saturation can be considered to be satisfactory for a B value greater than 0.96. When saturation is not satisfactory, the back pressure (P_{BP}) is raised to higher values so that the pore air solves into the water and the remaining size of the babbles is compressed and decreases further.

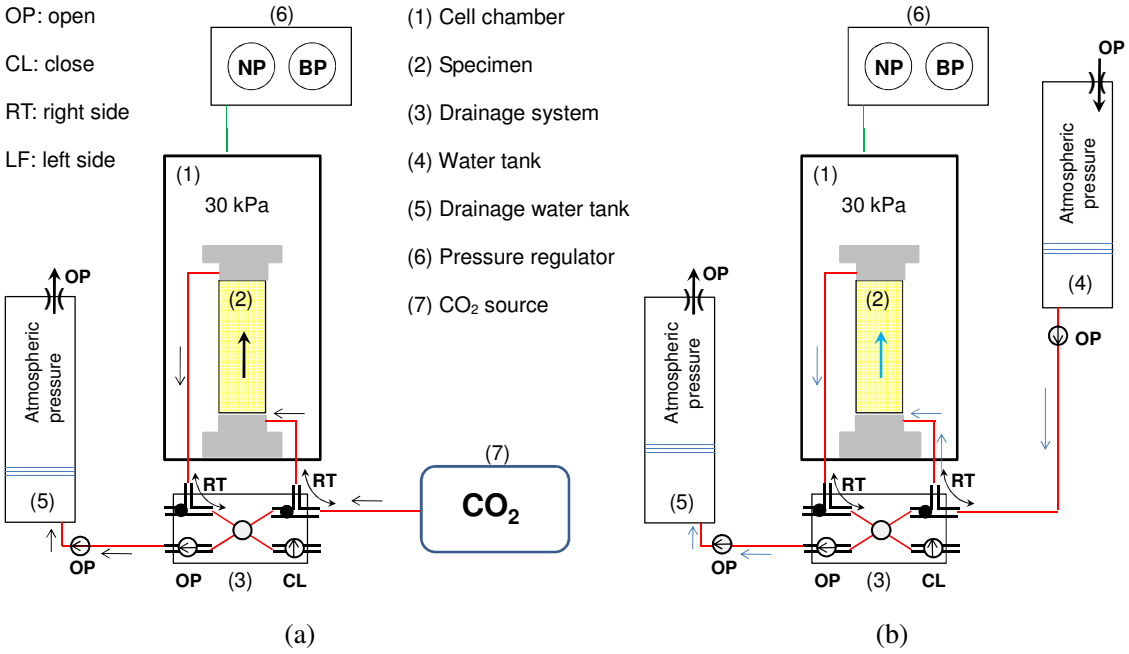

Fig. 3.12: CO_2 method as used in this study: (a) before saturation to remove air into the specimen; and (b) while saturating the specimen by using de-aired distilled water

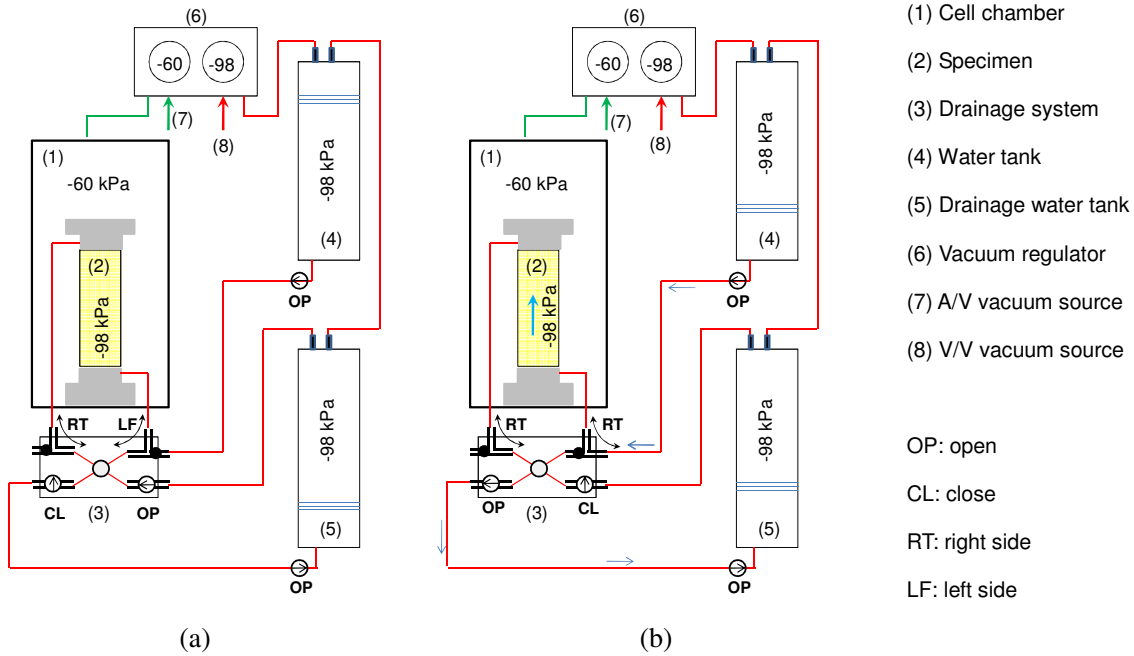

Fig. 3.13: Double vacuum method as used in this study: (a) before saturation to remove air into the specimen; and (b) while saturating the specimen by using de-aired distilled water

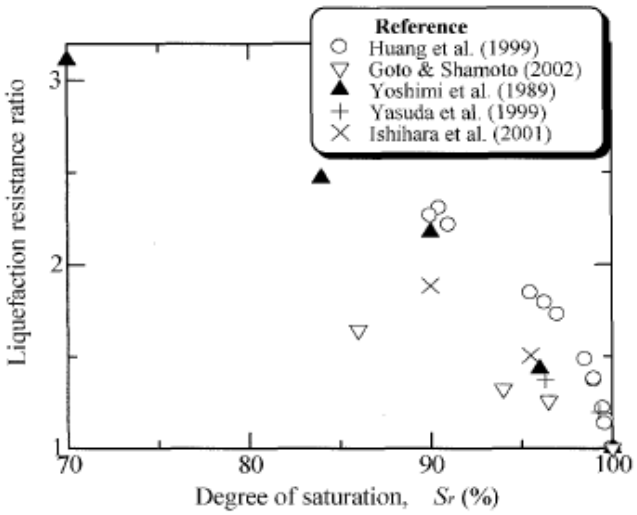

Fig. 3.14: Results of tests showing the effects of the degree of saturation on liquefaction resistance (Okamura and Soga, 2006)

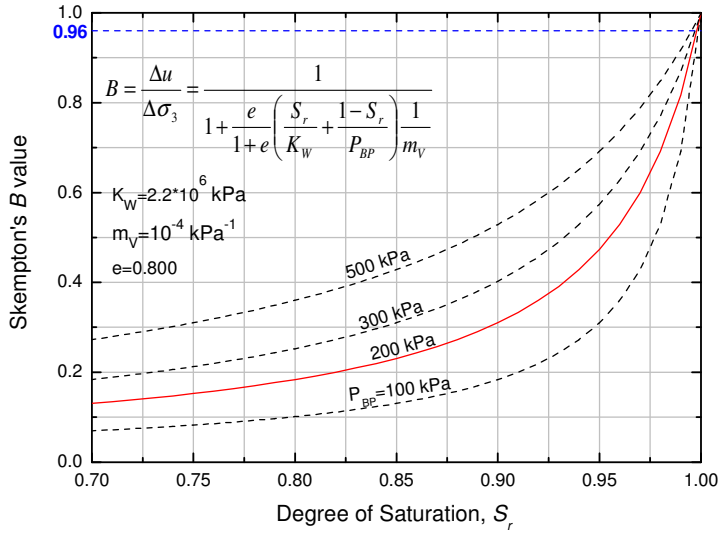

Fig. 3.15: Example of correlations between Skempton's *B* value and the degree of saturation by varying the back pressure (after Towhata, 2008)

3.5 Tests procedure

All the tests were performed on Toyoura sand specimens with relative density (*Dr*) of about 44-48 %, as defined at an isotropic effective stress state of 100 kPa. After completing the saturation process by employing the CO_2 method or the double vacuum method, a back pressure of 200 kPa was applied in order to achieve higher degree of saturation ($B > 0.96$). The specimens were subjected to three steps of loading as follows:

i) *Isotropic consolidation*

All the specimens were isotropically consolidated by increasing the effective stress state up to 100 kPa, with a back pressure of 200 kPa;

ii) *Drained monotonic torsional shear loading*

The isotropically consolidated specimens were monotonically sheared at strain rate of 0.5 %/min under drained conditions, in order to apply a specified value of initial static shear representative of sloping ground conditions, followed by a drained creep for about 5 min or even larger;

iii) *Undrained cyclic torsional shear loading*

Finally, in order to study the behavior of sandy specimens under seismic conditions (i.e., liquefaction resistance and/or development of large deformation), undrained cyclic torsional loading with constant amplitude of shear stress was applied at a constant shear strain rate of about 2.5 %/min.

As listed in Table 3.2, cyclic loading tests were performed over a wide range of initial static shear (τ_{static}) varying from 0 to 20 kPa. Two levels of cyclic shear stress (τ_{cyclic}), 16 kPa and 20 kPa in single amplitude, were employed in this study in order to consider various combinations of initial static and cyclic shear stresses.

The loading direction was reversed when the combined shear stress which was corrected for the effect of membrane force, reached the target value τ_{max} or τ_{min}. During the process of undrained cyclic torsional loading the vertical displacement of the top cap was prevented with the aim to simulate as much as possible the simple shear condition (Fig. 3.16) that the ground undergoes during horizontal excitation.

The membrane force was evaluated by conducting a special test which consists in filling water in between outer and inner membranes and shearing cyclically the water specimen under undrained condition up to a single amplitude shear strain of 50 %, as described in the details hereafter.

As listed in Table 3.3, in order to compare the monotonic and cyclic loading behaviors of saturated Toyoura sand specimens as well as to calibrate the GHE model parameters employed in the modeling, several drained and undrained monotonic torsional shear tests were performed, following similar procedures as above described.

Table 3.2 Undrained cyclic torsional shear tests with static shear performed in this study

Test	*e*	*Dr* (%)	p_0' (kPa)	τ_{cyclic} (kPa)	τ_{static} (kPa)	τ_{max} (kPa)	τ_{min} (kPa)
1 (16-00)	0.825	46.4	100	16	0	16	-16
2 (16-05)	0.828	45.5	100	16	5	21	-11
3 (16-10)	0.824	46.6	100	16	10	26	-6
4 (16-15)	0.833	44.2	100	16	15	31	-1
5 (16-16)	0.825	46.5	100	16	16	32	0
6 (16-17)	0.820	47.9	100	16	17	33	1
7 (16-20)	0.829	45.3	100	16	20	36	4
8 (20-00)	0.819	48.1	100	20	0	20	-20
9 (20-05)	0.819	48.0	100	20	5	25	-15
10 (20-10)	0.828	45.6	100	20	10	30	-10
11 (20-15)	0.832	44.4	100	20	15	35	-5
12 (20-20)	0.823	46.9	100	20	20	40	0

The shear stress τ is corrected for effect of membrane force. The cyclic shear stress is applied under undrained condition, while preventing any vertical displacement of top cap.

e = void ratio; *Dr* = relative density; p_0' = initial effective mean principal stress;

τ_{cyclic} = cyclic shear stress; τ_{static} = static shear stress;

$\tau_{max} = \tau_{static} + \tau_{cyclic}$, maximum reversal/combined shear stress;

$\tau_{min} = \tau_{static} - \tau_{cyclic}$, minimum reversal/combined shear stress

Table 3.3 Drained and Undrained monotonic torsional shear tests

Test	*e*	*Dr* (%)	p'_0 (kPa)	τ_{peak} (kPa)
14 (D1)	0.811	50.4	100	Not achieved
15 (D2)	0.810	50.6	100	77.5
16 (U1)	0.828	45.6	100	24.5
The shear stress τ is corrected for effect of membrane force. The shear stress is applied while preventing any vertical displacement of top cap.				
e = void ratio; *Dr* = relative density; p'_0 = initial effective mean principal stress; τ_{peak} = shear stress at peak state				

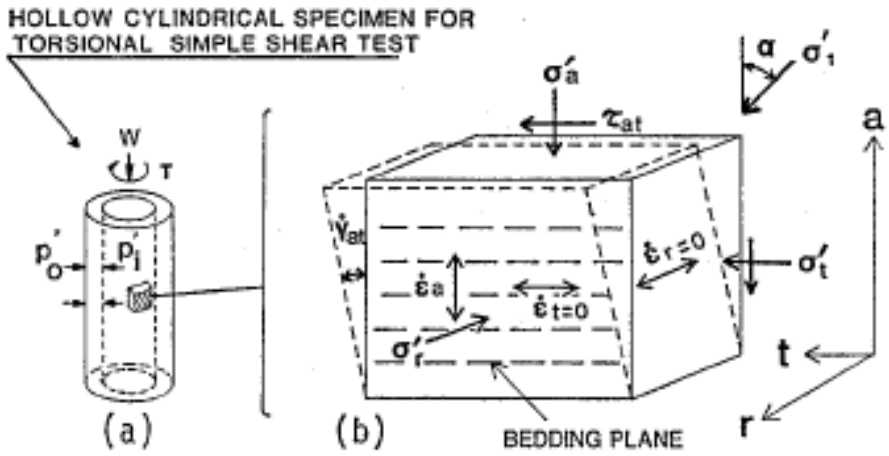

Fig. 3.16: Torsional simple shear deformation (Pradhan et al., 1988)

3.7 References

1. Ampadu, S. I. K. (1991): "Undrained behavior of kaolin in torsional simple shear", Ph.D. thesis, Dep. of Civil Engineering, University of Tokyo, Japan
2. Chiaro G. (2007): "Analisi sperimentale del compattamento dei mezzi granulari", Master thesis, University of Cassino, Italy (in Italian)
3. Coduto, D. P. (1999): "Geotechnical Engineering: Principles and Practices", Prentice Hall
4. De Silva, L.I.N., Koseki, J., and Sato, T. (2006): "Effect of different pluviation techniques on deformation property of hollow cylinder sand specimens", Proc. of International Symposium on Geomechanics and Geotechnics of Particle Media, Ube, Yamaguchi, Japan, 29-33
5. Hong Nam, N. (2004): "Locally measured quasi-elastic properties of Toyoura sand in cyclic triaxial and torsional loadings", Ph.D. thesis, Dep. of Civil Engineering, University of Tokyo, Japan
6. JGS (1998); "Standards of Japanese geotechnical society for laboratory shear tests", Japanese Geotechnical Society, 5550-1998 (English version)
7. Kiyota, T. (2007): "Liquefaction strength and small strain properties of in-situ frozen and reconstituted sandy soils", Ph.D. thesis, Dep. of Civil Engineering, University of Tokyo, Japan
8. Kiyota, T., Sato, T., Koseki, J., and Mohammad, A.M. (2008): "Behavior of liquefied sands under extremely large strain levels in cyclic torsional shear tests", Soils and Foundations, 48 (5), 727-739
9. Okamura, M. and Soga, Y. (2006): "Effects of pore fluid compressibility on liquefaction resistance of partially saturated sand", Soils and Foundations, 46 (5), 695-700
10. Pradhan, T. B. S., Tatsuoka, F. and Horii, N. (1988): "Simple shear testing on sand in a torsional shear apparatus", Soils and Foundations, 28 (2), 95-112
11. Skempton, A. W. (1954): " The pore pressure coefficients A and B ", Geotechnique, 4 (4), 143-147
12. Towhata, I. (2008): "Geotechnical Earthquake Engineering", Springer

CHAPTER 4

Effects of initial static shear on the undrained cyclic behavior of saturated loose Toyoura sand

4.1 Introduction

Soil elements within the sloped ground are subjected to an initial static shear stress on the horizontal plane or an assumed failure plane. During earthquake shaking, these elements are subjected to additional cyclic shear stress due to shear waves propagating vertically upward from the bedrock. The superimposition of static and cyclic shear stresses can have major effects on the response of soil, leading to liquefaction-induced failure of natural and artificial slopes of sandy deposits and the consequent development of extremely large ground deformation.

As far as the authors have investigated in the literature, there exists no previous study on the role of initial static shear stress on the undrained cyclic behavior of saturated sand in which the strain level could exceed more than 20 %. In previous studies, in the case of simple shear tests (Vaid and Finn, 1979) or torsional shear tests (Tatsuoka et al., 1982), the shear strain level was limited to 10 % due mainly to mechanical limitation of the employed apparatus; as well, in the case of triaxial tests, due to larger extents of non-uniform deformation of the specimen at higher strain levels, the axial strain level could not exceed 20 % (Vaid and Chern, 1983; Hyodo et al., 1991, among others).

In view of the above, the purpose of this study is set to better understand the effects of initial static shear on the liquefaction behavior and to investigate the large deformation properties of saturated sand subjected to undrained torsional shear loading.

In this chapter, the results from the investigations on the effects of initial shear stress on the undrained cyclic behavior of saturated Toyoura sand subjected to cyclic torsional shear loading up to single amplitude of shear strain of about 50 % under various combinations of static and subsequent cyclic shear stresses are presented.

Effects of static shear on the types of loading, failure characteristics, resistance to liquefaction, modes of development of shear strain during cyclic shearing, specimen deformations and so on, are analyzed in order to have a comprehensive understanding of the role that the initial static shear plays on the undrained cyclic behavior of saturated Toyoura sand.

4.2 Reversal, intermediate and non-reversal stress conditions

Most of the researches that have been conducted to study the liquefaction resistance of sands are concerned with the horizontal ground in which soil elements are assumed to be subjected to fully reversed cycles of shear stress during an earthquake.

However, soil elements within sloped ground are subjected to an initial static shear stress on the horizontal plane. During earthquake shaking, due to the superimposition of the static shear with the cyclic shear stress, these elements can experience partially reversed or non-reversed shear stress loading conditions.

It is widely recognized that the degree of reversal stress is an important parameter for evaluating the effects of initial static shear on the failure behavior of sand.

Among others, Hyodo et al. (1991) employed the ratio of cyclic deviator stress to the initial static shear stress (Eq. 4.1) to characterize the triaxial behavior of isotropically and anisotropically consolidated saturated sand specimens into stress reversal, intermediate and non-reversal:

$$R = \frac{q_{cyclic}}{q_{static}} \tag{4.1}$$

Therefore, the pattern of failure of sand specimen was distinguished into two kinds, liquefaction and residual deformation based on the degree of stress reversal, stress path and stress-strain relationship. In the cases of stress reversal and intermediate on loose sand specimen, failure was associated with liquefaction, while in the other cases it was found that residual deformation brought the specimen to failure even though no liquefaction occurred; also failure was not observed in the case of non-reversal on the dense sand specimens.

4.2.1 Types of loading in torsional shear tests

In this study, in order to evaluate the effects of initial static shear on the large deformation properties of saturated sand in undrained cyclic torsional shear tests, various combinations of initial static shear and subsequent cyclic shear stresses were considered. Depending on the relative magnitude of initial static shear and the cyclic shear stresses the degree of reversal loading was defined by Eq. (4.2).

Eq. (4.2) was proposed in this study, in order to define a degree of reversal within a range of finite value as listed in Table 4.1; in fact, the degree of reversal as defined by Hyodo et al. (1991) gives an infinite value ($R = \infty$) for a zero value of initial static shear.

Eq. (4.2) is the ratio between the double amplitude shear stress ($2\tau_{cyclic}$) and the maximum combined shear stress ($\tau_{max} = \tau_{static} + \tau_{cyclic}$) which is corrected by a convenient factor -1 in order to obtained $R^*=1$ in case of fully reversal loading and $R^*=0$ in case of intermediate loading conditions.

$$R^* = \frac{2\,\tau_{cyclic}}{\tau_{static} + \tau_{cyclic}} - 1 \begin{cases} 1 \geq R^* > 0 \;\; Reversal \begin{cases} R^* = 1 \;\; Fully\ Reversal \\ (i.e., \tau_{static} = 0) \\ 1 > R^* > 0 \;\; Partially\ Reversal \\ (i.e., \tau_{static} < \tau_{cyclic}) \end{cases} \\ R^* = 0 \;\; Intermediate \;\; (i.e., \tau_{static} = \tau_{cyclic}) \\ R^* < 0 \;\; Non-reversal \;\; (i.e., \tau_{static} > \tau_{cyclic}) \end{cases} \tag{4.2}$$

Eq. (4.2) can be rewritten in a simpler manner as follows:

$$R^* = \frac{-(\tau_{static} - \tau_{cyclic})}{\tau_{static} + \tau_{cyclic}} = -\frac{\tau_{\min}}{\tau_{\max}} \tag{4.3}$$

Later, it was found that the latter equation corresponds to the definition used by Yoshimi and Oh-oka (1975) for analyzing the behavior of sand with initial static shear in ring torsional shear tests.

Consequently, the cyclic loading paths could be classified into three groups: stress reversal, intermediate and non-reversal, as schematically shown in Fig. 4.1.

The definition of each type of loading as proposed in this study is given hereafter:

Reversal. In the tests in which $\tau_{static} < \tau_{cyclic}$, during each cycle of loading the combined static and cyclic shear stress value was reversed from positive ($\tau_{max} = \tau_{static} + \tau_{cyclic} > 0$) to negative ($\tau_{min} = \tau_{static} - \tau_{cyclic} < 0$), or vice versa (Fig. 4.1a); therefore, this type of loading path was called stress reversal.

Intermediate. In the case where $\tau_{static} = \tau_{cyclic,}$ the reversal of loading direction was made when the minimum combined shear stress (τ_{min}) achieved zero state during the torsional

undrained shear loading (Fig. 4.1b); this type of loading path was called stress reversal.

Non-reversal. On the other hand, when $\tau_{static} > \tau_{cyclic}$, the combined shear stress was kept always positive (Fig. 4.1c); this type of loading was called non-reversal.

Table 4.1 Definition of stress reversal, intermediate and non-reversal loading tests.

Test		τ_{cyclic} (kPa)	τ_{static} (kPa)	τ_{max} (kPa)	τ_{min} (kPa)	*R**	*Type of loading*
1	(16-00)	16	0	16	-16	1.00	Rev.
2	(16-05)	16	5	21	-11	0.52	Rev.
3	(16-10)	16	10	26	-6	0.23	Rev.
4	(16-15)	16	15	31	-1	0.03	Rev.
5	(16-16)	16	16	32	0	0.00	Int.
6	(16-17)	16	17	33	1	-0.03	N-Rev.
7	(16-20)	16	20	36	4	-0.11	N-Rev.
8	(20-00)	20	0	20	-20	1.00	Rev.
9	(20-05)	20	5	25	-15	0.60	Rev.
10	(20-10)	20	10	30	-10	0.33	Rev.
11	(20-15)	20	15	35	-5	0.14	Rev.
12	(20-20)	20	20	40	0	0.00	Int.

$\tau_{max} = \tau_{static} + \tau_{cyclic}$, maximum combined shear stress

$\tau_{min} = \tau_{static} - \tau_{cyclic}$, minimum combined shear stress

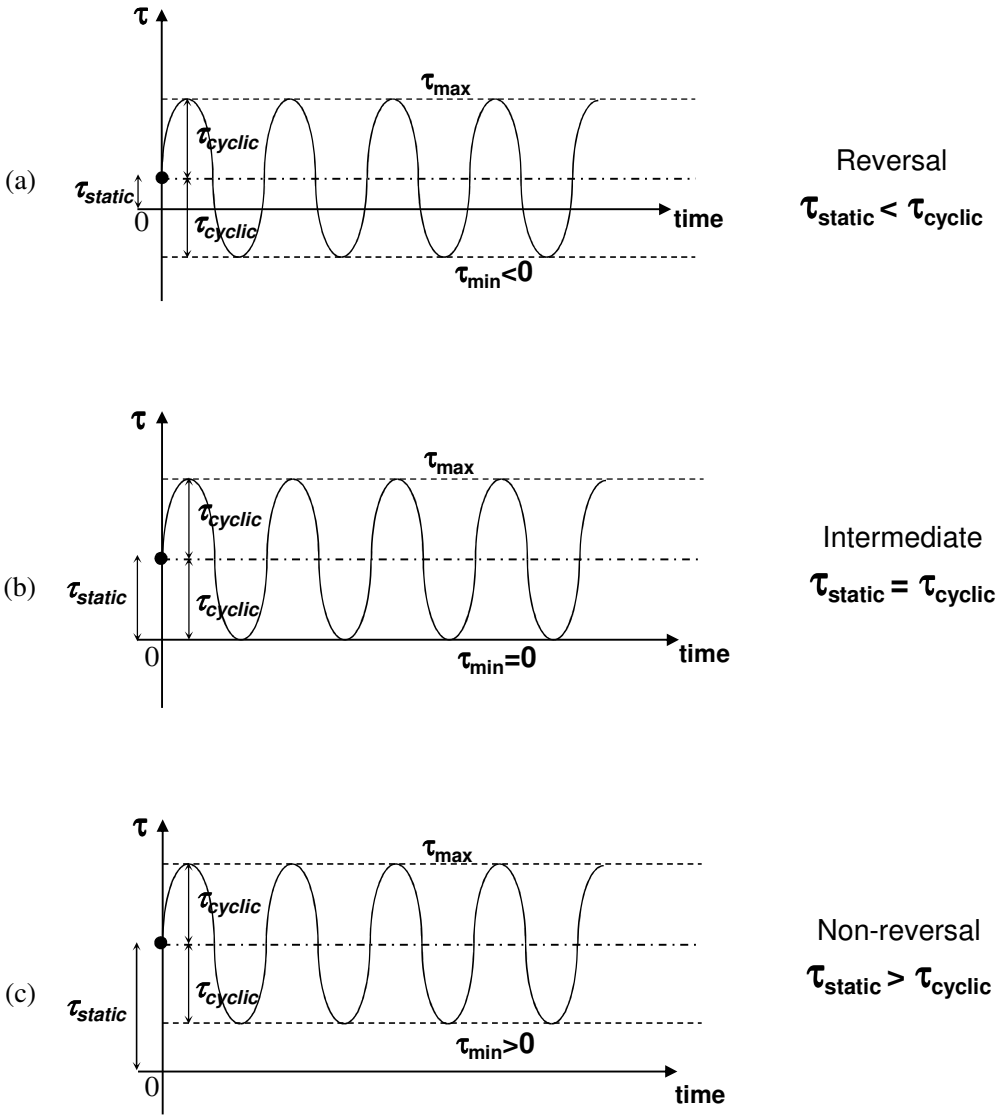

Fig. 4.1: Schematic loading types under torsional shear conditions while referring to Hyodo et al., (1991): (a) Reversal; (b) Intermediate; and (c) Non-reversal.

4.2.2 Reversal loading test results

Fig. 4.2 shows typical reversal loading test results (e.g., Test 2) in which cyclic mobility was observed in the effective stress path, where the effective stress recovered repeatedly after achieving the state of zero effective stress (i.e., full liquefaction). It was accompanied with a significant development of shear strain as evidenced by the stress-strain relationship.

4.2.3 Intermediate loading test results

Fig. 4.3 illustrates typical intermediate loading test results (e.g., Test 12). This type of tests shows similar behavior to that of the reversal cases, in the sense that after reaching a fully liquefied state ($p' = 0$), progressive large deformation are developed while showing cyclic mobility. However, it can be distinguished from the reversal case by looking at the failure characteristics, which will be explained later in section 4.3.

4.2.4 Non-reversal loading test results

Fig. 4.4 represents typical non-reversal loading test results (e.g., Test 7). In this case, the state of zero effective stress was not achieved even after applying 208 cycles of loading; however, even though liquefaction did not occur, a large shear strain level exceeding 50 % was reached, and formation of spiral shear band could be observed (see section 4.6 for the details of specimen deformation).

The results of the above non-reversal loading test indicate that, when the combined shear stress cannot achieve the zero state, full liquefaction (i.e., the zero effective stress state) does not occur. However, this does not mean that sand is very resistant against seismic loading; in fact, a significant magnitude of combined shear stress may cause failure as evidenced with the formation of shear band.

(a)

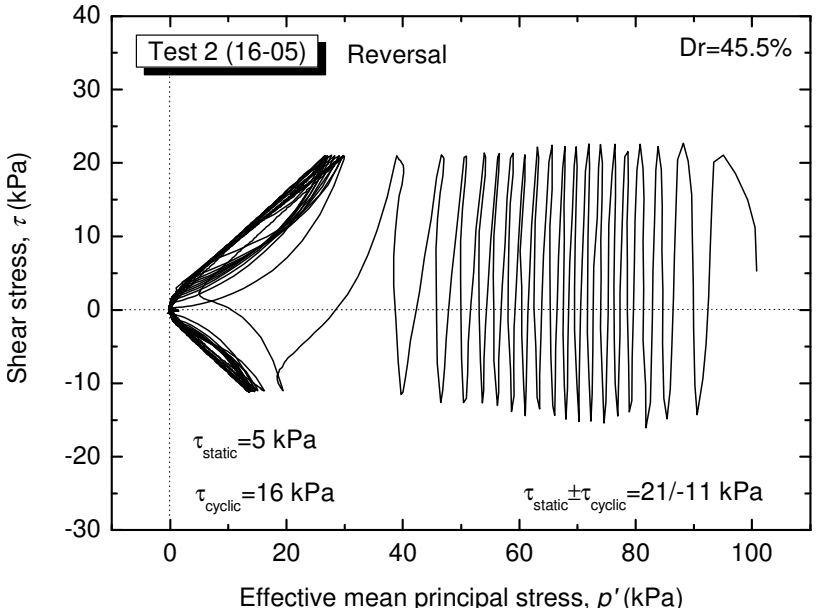

(b)

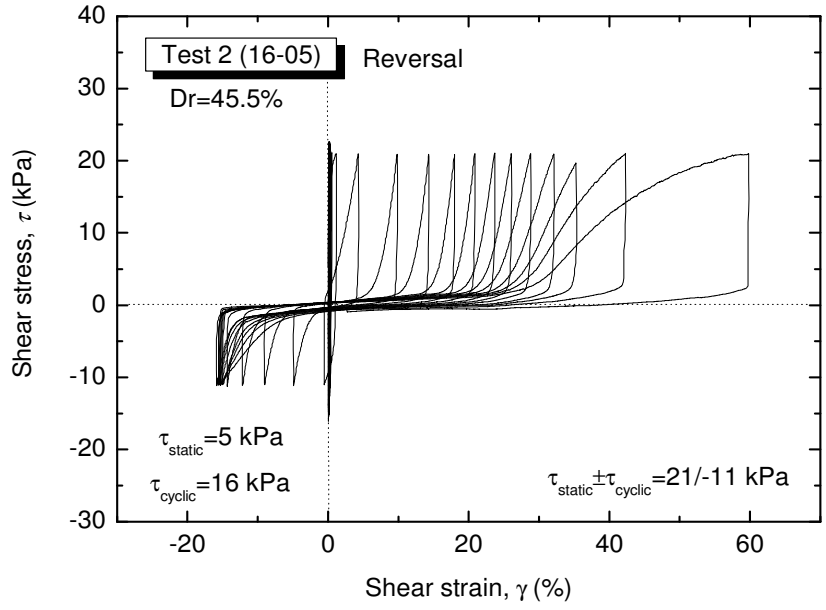

Fig. 4.2: Typical results of reversal loading tests:
(a) Effective stress path; and (b) Stress-strain relationship.

(a)

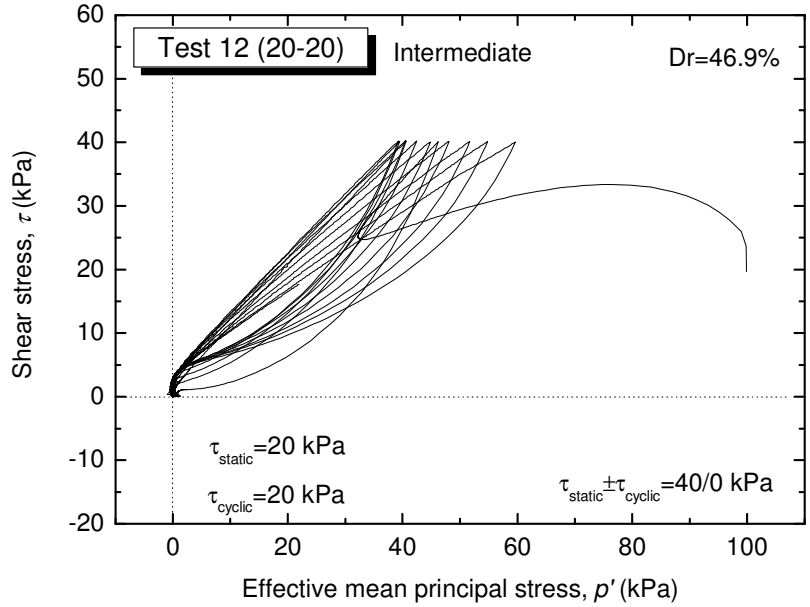

(b)

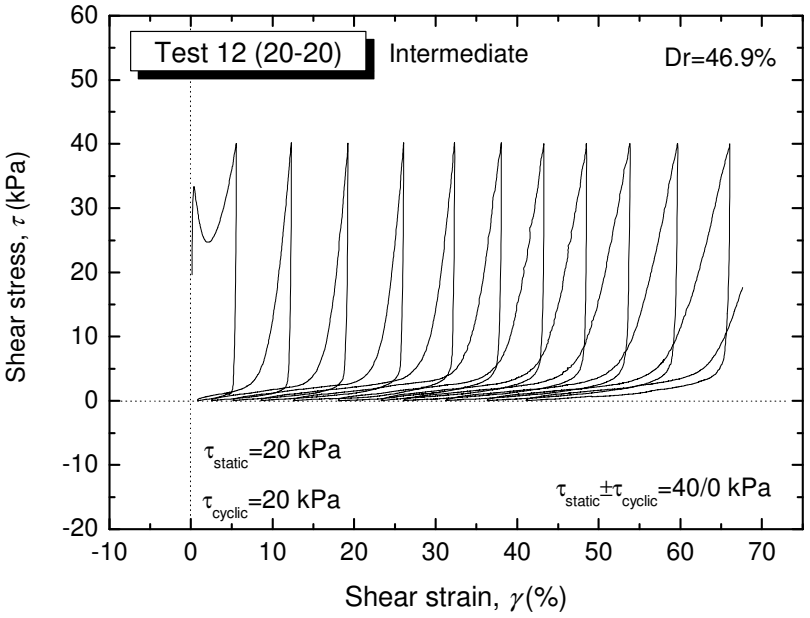

Fig. 4.3: Typical results of intermediate loading tests:
(a) Effective stress path; and (b) Stress-strain relationship.

(a)

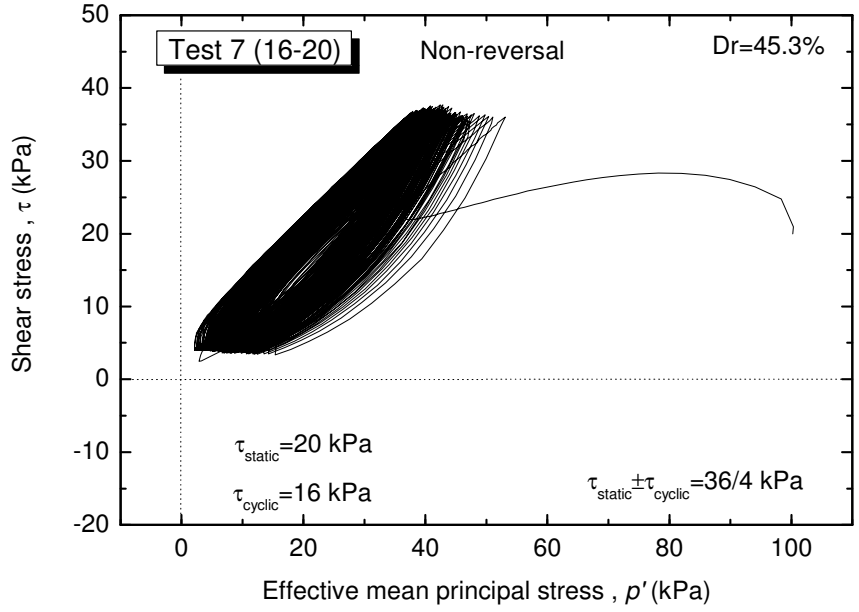

(b)

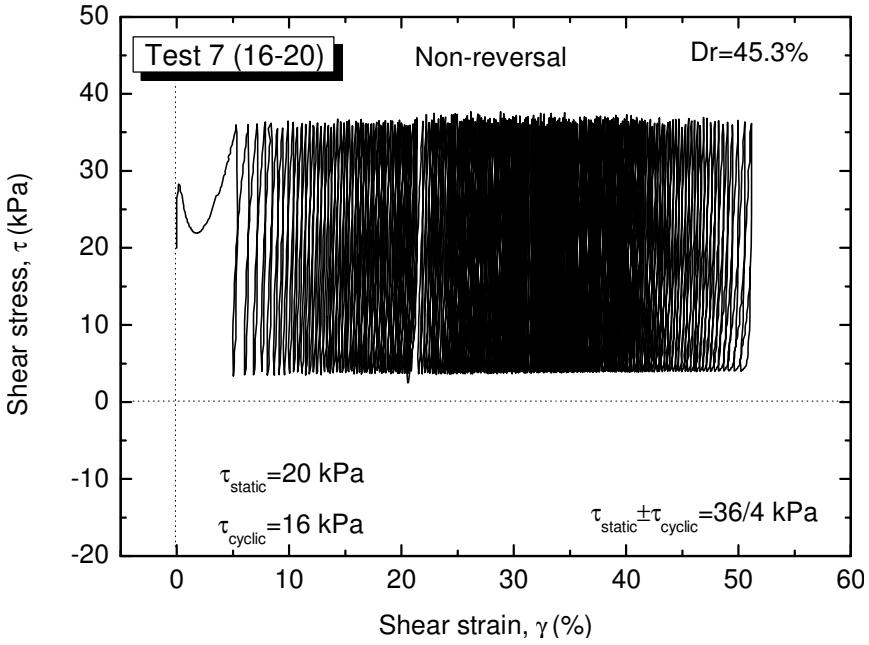

Fig. 4.4: Typical results of non-reversal loading tests:
(a) Effective stress path; and (b) Stress-strain relationship.

4.3 Failure characteristics

It is recognized from post-earthquake field investigations and many laboratory tests that soils susceptible to liquefaction consist mainly of saturated, uniform grain size distributions, deposited in loose states. However, the fact that a soil is susceptible to liquefaction does not guarantee that liquefaction will actually initiate during an earthquake event.

It is also recognized that the stress conditions (confining pressure, cyclic shear and initial static shear stresses) play an important role in the liquefaction behavior of soil, the type of failure mechanism and the mode of development of soil deformation, especially in the case of slopes of sandy deposits.

Many studies on the liquefaction of sand, including the current one, show that under non-reversal stress conditions (see section 4.2), saturated loose sand most likely will not experience liquefaction. However, this does not mean that sand is very resistant against seismic loading, in fact, a significant magnitude of combined static and cyclic shear stresses may cause failure of soil even though liquefaction does not take place.

In view of the above, it is definitely important not only to have a clear understanding of the liquefaction mechanisms, but also to carry out in depth investigation on the effects of static shear on the failure modes of saturated sandy soil during undrained shearing.

4.3.1 Failure behavior of sand in undrained cyclic torsional shear tests

As seen in section 4.2, the failure behavior of sand can be correlated with the degree of reversal stress. In this study, similarly to the results presented by Hyodo et al. (1991), in the case of reversal and intermediate loading patterns, failure of the specimen was induced by full liquefaction; on the other hand, in the case of non-reversal loading, residual deformation brought the specimens to failure.

However, for a comprehensive understanding of failure behavior of sand, in addition to the degree of stress reversal, other factors should be taken into account.

Therefore, in this study, the observed failure mechanisms were analyzed in terms of the difference in the effective stress paths and the modes of development of shear strain during both monotonic and cyclic undrained torsional shear loading. Hence, three types of failure could be identified:

$$\begin{cases} \text{Liquefaction} \begin{cases} \text{Cyclic liquefaction failure } (LQ) \\ \text{Rapid flow liquefaction failure } (RF) \end{cases} \\ \text{Residual deformation failure } (RD) \end{cases}$$

4.3.2 Cyclic Liquefaction Failure

In some cyclic tests, the shear stress reached a maximum value (τ_{max}) which was lower than the peak stress during undrained monotonic loading (τ_{peak}); in addition, the minimum shear stress value was negative ($\tau_{min} < 0$). Under these stress conditions (i.e., reversal stress), while undergoing several tens of cycles, due to the excess pore water pressure generation, the effective mean principal stress progressively decreased and the stress state moved toward the failure envelope and finally reached the full liquefaction state ($p' = 0$). Then, in the post liquefaction process, large deformations were developed. Fig 4.5 shows typical test results of cyclic liquefaction failure (LQ).

4.3.3 Rapid Flow Liquefaction Failure

In other tests, the shear stress reached a maximum value which was higher than the peak stress during undrained monotonic loading ($\tau_{max} > \tau_{peak}$), while due to stress reversal or intermediate conditions the minimum shear stress value was negative ($\tau_{min} < 0$) or zero ($\tau_{min} < 0$), respectively. As a result, liquefaction took place mostly in-between the first cycle of loading (few cycles for intermediate tests) and a rapid development of residual strain was observed. Typical test results of rapid flow liquefaction failure (RF) are shown in Fig. 4.6 and Fig. 4.7 for reversal and intermediate loading cases, respectively.

4.3.4 Residual Deformation Failure

In some tests the shear stress reached a maximum value which was higher than the peak stress during undrained monotonic loading ($\tau_{max} > \tau_{peak}$), as well as the minimum shear stress value was positive ($\tau_{min} > 0$). Under these stress conditions (i.e., non-reversal stress),

during cyclic loading large deformations were achieved rapidly, while in general liquefaction was not reached even after applying many tens of cycles. As a result, residual deformation brought the sample to failure. Fig. 4.8 illustrates typical tests results of residual deformation failure (RD).

It should be noted that, in Test 6 (16-17), in which the degree of reversal loading was just lower than zero (i.e., R^* = -0.03, non-reversal), full liquefaction ($p'=0$) took place after applying 13 cycles, as shown in Fig. 4.8. However, at the cycle at which liquefaction was achieved, the shear strain already exceeded 20%. As a result, the failure behavior of this specimen was associated with the large residual deformation, while the liquefaction was not the main cause of specimen failure.

In chapter 5, the simulation results confirmed that, although the amount of the non-reversal stress is only 1 kPa, liquefaction does not take place; therefore, the liquefaction behavior observed in laboratory for Test 6 (16-17) can be associated with technical limitations in conducting accurate correction for membrane force and/or stress control.

4.3.5 Flow Liquefaction Surface

Kramer (1996) showed that the initiation of the flow liquefaction failure can be determined by looking at the effective stress path and it depends on the level of initial confining pressure. The behavior of five loose sand specimens isotropically consolidated to the same void ratio at different initial effective confining pressure was compared, and the stress conditions required to initiate flow liquefaction failure could be established (Fig. 4.10). Flow liquefaction was initiated at the peak of the stress paths. The boundary described by the locus of these points was termed the flow liquefaction surface (FLS). Hence, it is recognized that flow liquefaction begins when the stress path crosses the FLS during undrained monotonic or cyclic shear loading.

In the test results presented in this study, the initial effective confining pressure was not changed; however, by taking the effects of initial static shear into consideration, a FLS with similar features to the one described by Kramer (1996) could be defined.

Flow liquefaction behavior was observed in the tests in which the stress path exceeds the point of peak stress before the cyclic shearing. In Fig. 4.11 the response of three saturated loose Toyoura sand specimens under the same conditions of initial void ratio and confining pressure by varying the initial static shear stress level are examined.

It can be seen that the stress at peak state increases with an increase of the initial static shear stress level; in accordance with the results presented by Kramer (1996) this represents the stress condition required to initiate the flow liquefaction failure.

As a result, drawing a line passing through these points, a boundary with the meaning of FLS could be defined for specimens under the same void ratio and initial confining pressure, but varying the effect of initial static shear stress, as shown in Fig. 4.11.

(a)

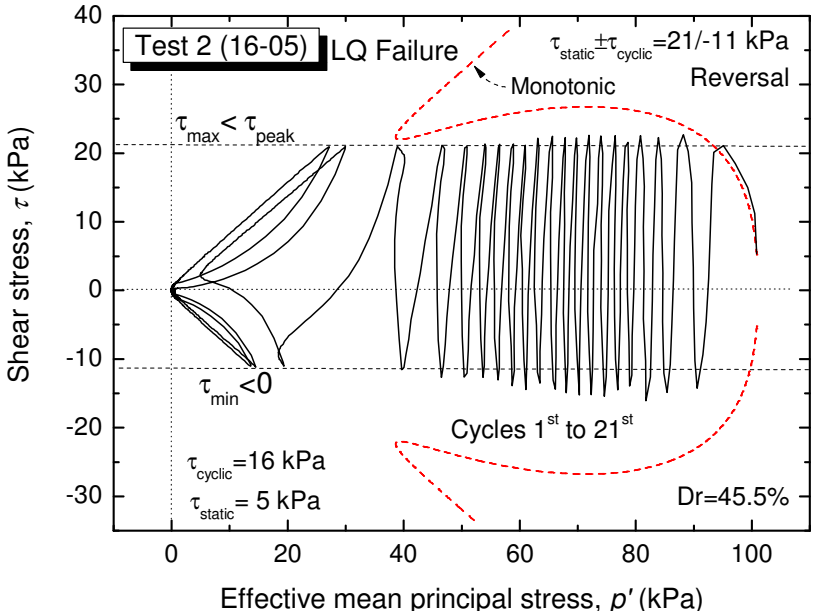

(b)

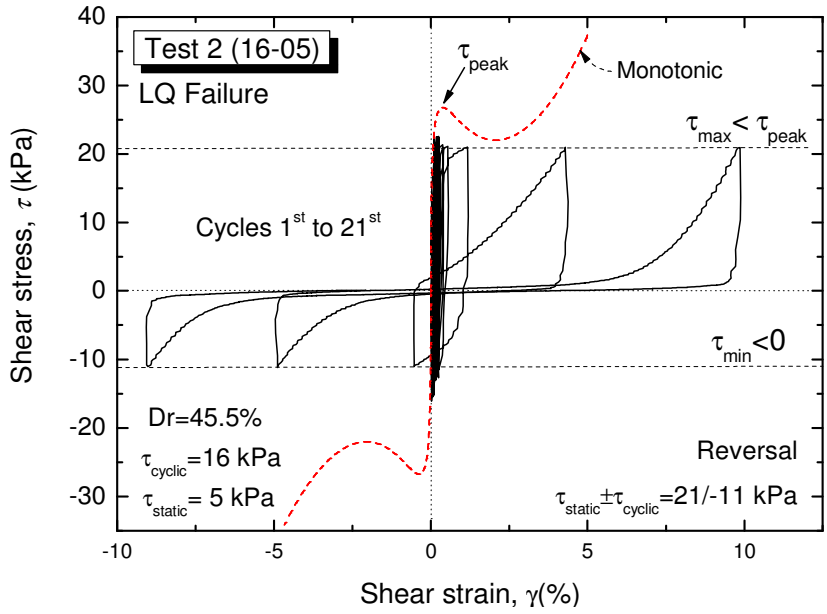

Fig. 4.5: Typical cyclic liquefaction failure (LQ) behavior:
(a) Effective stress path; and (b) Stress-strain relationship
(refer to Fig. 4.2 for the complete test results)

(a)

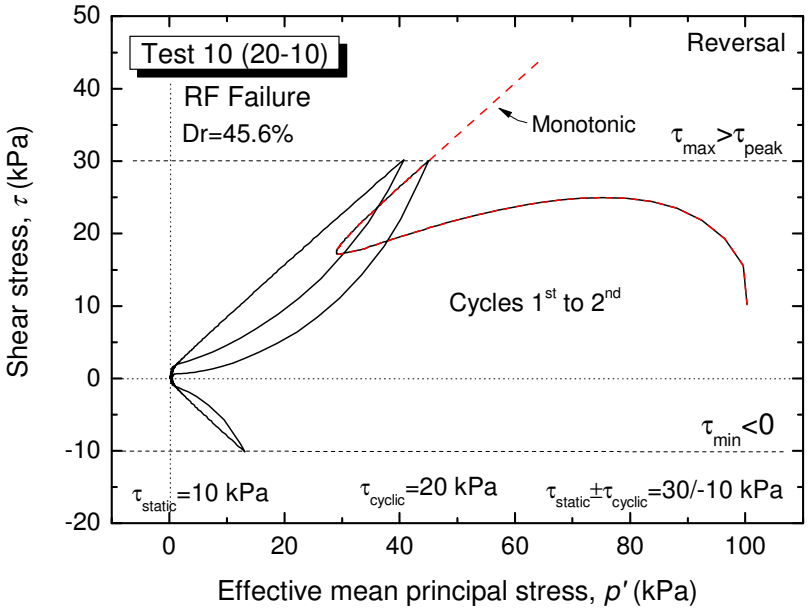

(b)

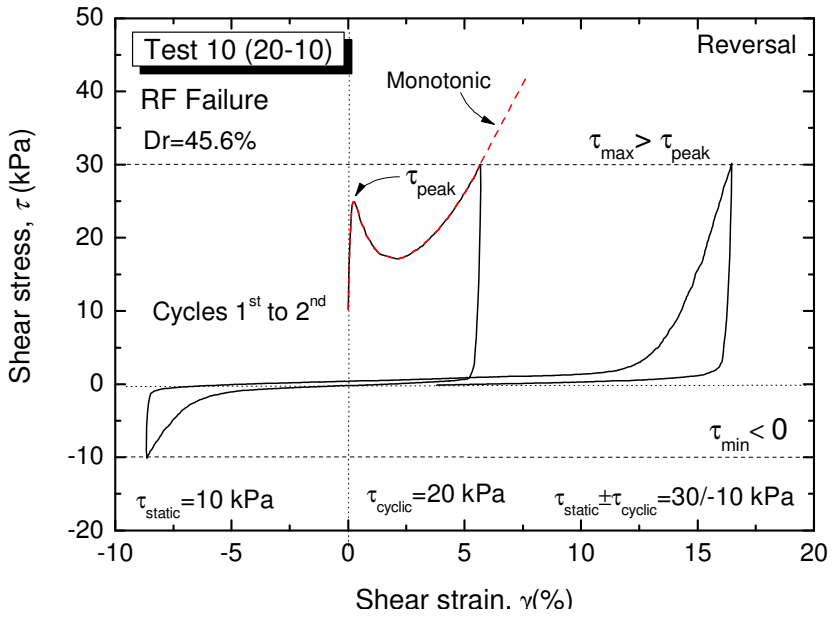

Fig. 4.6: Typical rapid flow liquefaction failure (RF) behavior for reversal tests: (a) Effective stress path; and (b) Stress-strain relationship.

(a)

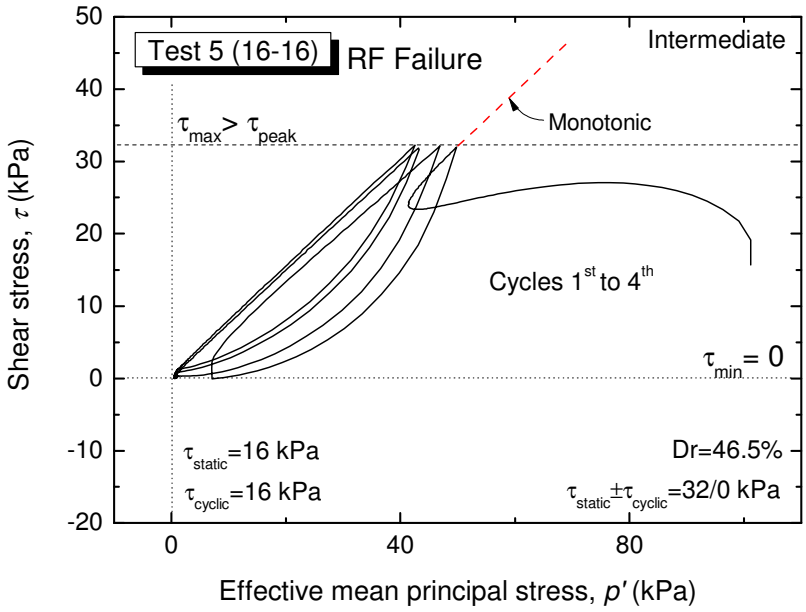

(b)

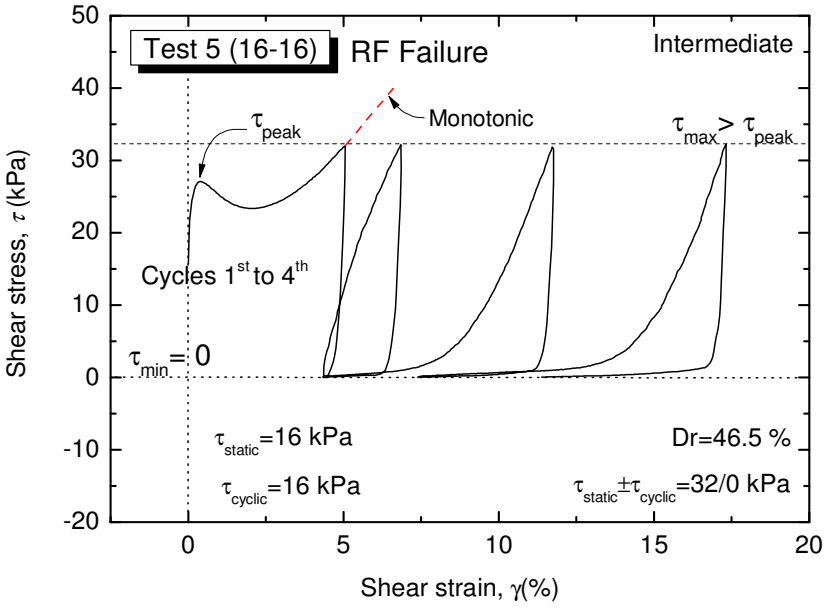

Fig. 4.7: Typical rapid flow liquefaction failure (RF) behavior for intermediate tests:
(a) Effective stress path; and (b) Stress-strain relationship
(refer to Fig. 4.21 for the complete test results)

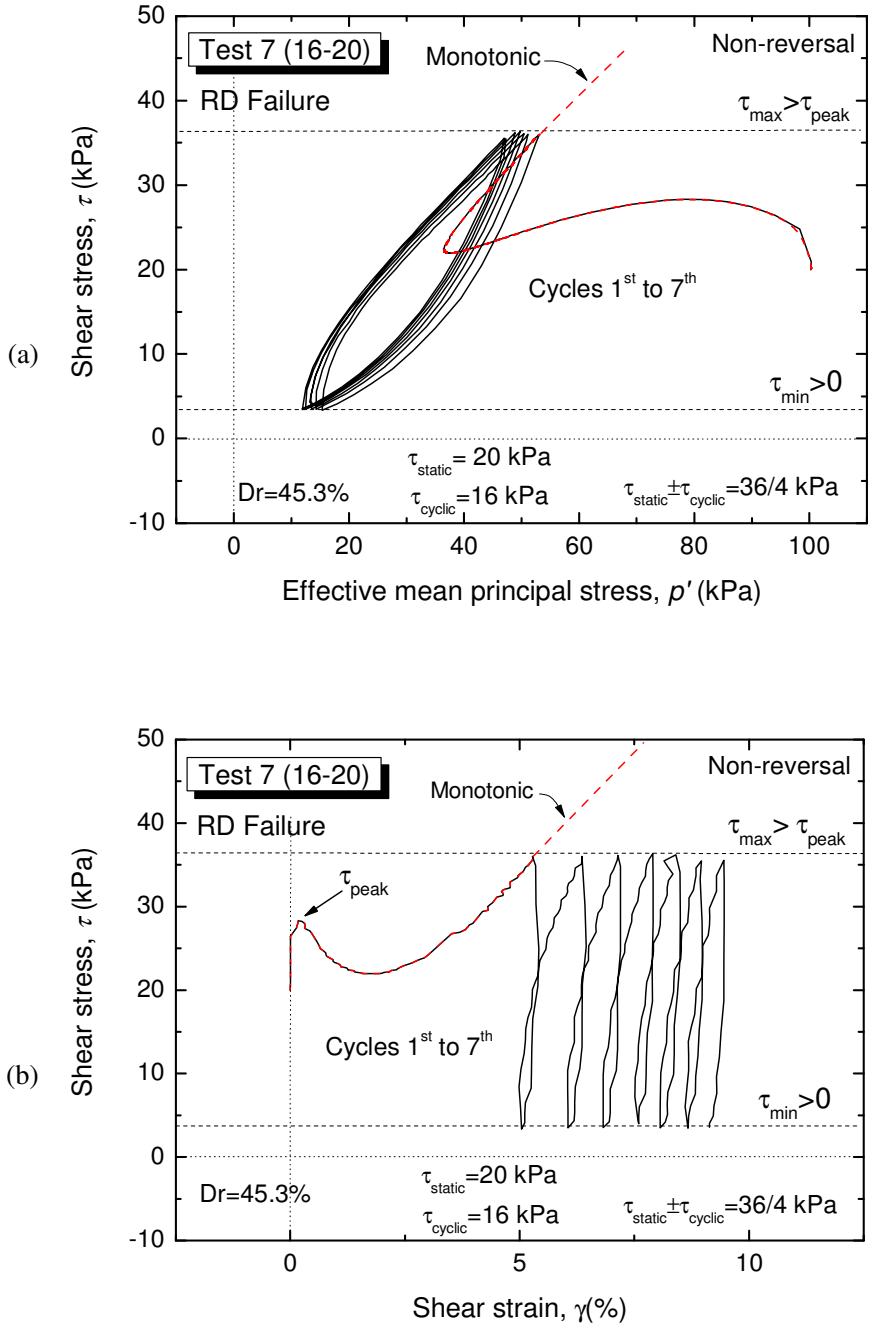

Fig. 4.8: Typical residual deformation failure (RD) behavior:
(a) Effective stress path; and (b) Stress-strain relationship
(refer to Fig. 4.4 for the complete test results)

(a)

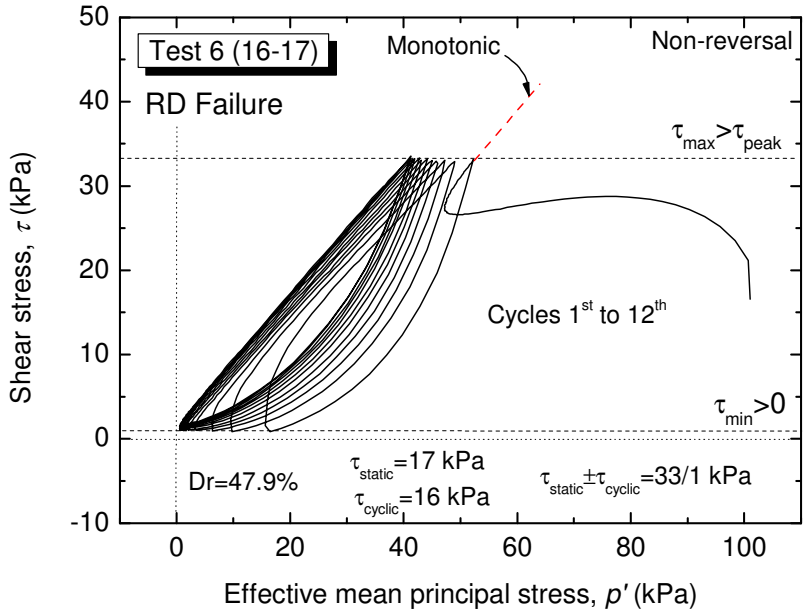

(b)

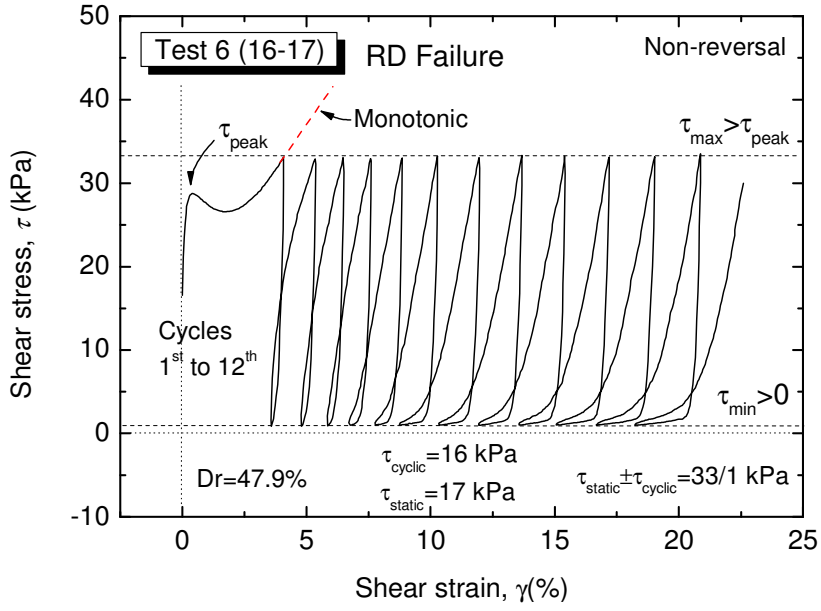

Fig. 4.9: Results of Test 6 (16-17): (a) Effective stress path; and (b) Stress-strain relationship. In liquefaction was not the main cause of specimen failure, therefore the specimen failure was associated with a large level of residual deformation (RD).

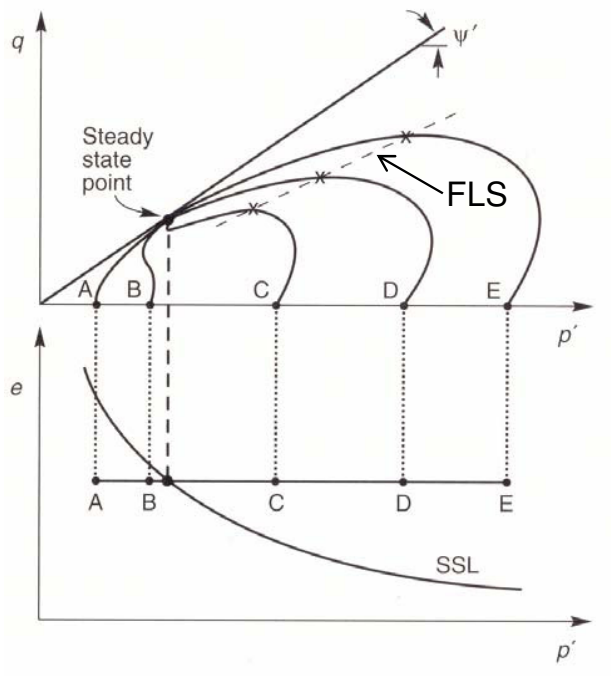

Fig. 4.10: Flow liquefaction surface (FLS) as defined by Kramer (1996).

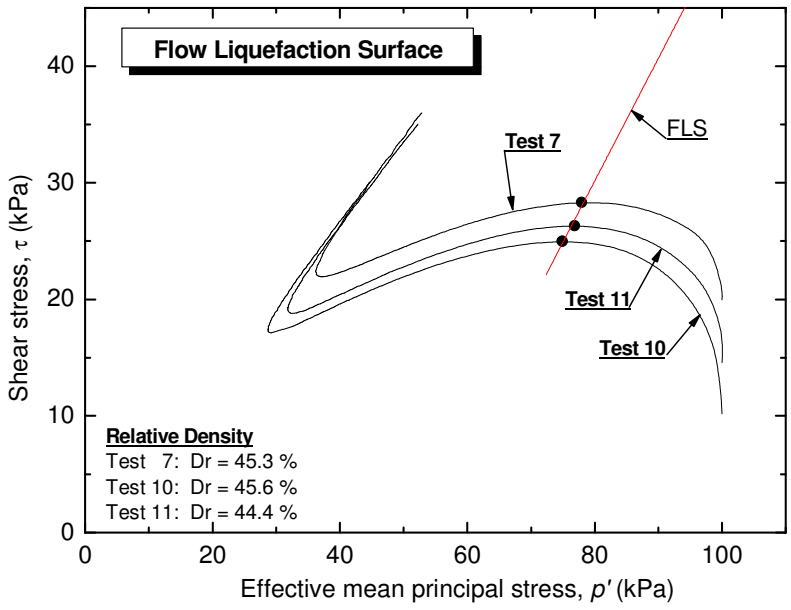

Fig. 4.11: Flow liquefaction surface (FLS) as defined in the current study by considering the effects of initial static shear stress.

4.4 Resistance to liquefaction and cyclic strain accumulation

Usually, the resistance to liquefaction or cyclic strain accumulation is expressed by the cyclic stress ratio ($CRS = \tau_{cyclic} / p'_0$) required to develop a specific amount of deformation from the initial configuration of the specimen or during cyclic loading (i.e., single or double amplitude shear strain).

However, in many cases, it can be seen that cyclic stress ratio is not a sufficient single parameter to describe the effects of initial static shear on the resistance to liquefaction or cyclic strain accumulation. Therefore, in this study, to address this issue, the liquefaction resistance curves were described in terms of both the cyclic stress ratio (CSR) and the static stress ratio ($SSR = \tau_{static} / p'_0$), as listed in Table 4.2.

To describe the resistance to liquefaction, double amplitude shear strain (γ_{DA}) and/or single amplitude shear strain at the maximum shear stress state ($\gamma_{SA, \tau = \tau max}$) are typically used. However, as schematically shown in Fig. 4.12, in using initial static shear, the stress conditions become non-symmetric with respect to the zero stress state; as a result γ_{DA} is not well representative of the strain accumulation during cyclic loading. Therefore, in the current study, the resistance to liquefaction (or more strictly, resistance to cyclic strain accumulation) was evaluated in terms of number of cycles required to develop a specific amount of single amplitude shear strain (γ_{SA}), which in this study was referred as the residual deformation (γ_{RS}), to be in accordance with the strain parameter used in section 4.5 to examine the effects of initial static shear on the deformation properties of sand.

Fig. 4.13 shows the resistance to liquefaction in terms of relationships between either the CSR or SSR and the number of cycles required to achieve the full liquefaction state of $p'=0$ (N_L). It can be seen that in the plot CSR - N_L, the resistance to liquefaction decreases with an increase in the initial static shear. On the contrary, the plot SSR - N_L more clearly revealed that at lower levels of SSR the number of cycles required to achieve $p'=0$ decreases with SSR. Then, additional/sudden drop in liquefaction resistance occurs when higher SSR is employed. Such change can be associated with a change in the failure behavior from LQ to RF. Moreover, the resistance to liquefaction increases for the specimen which shows a RD failure; this additional change in liquefaction behavior can be explained with the fact that RD does not allow liquefaction to occur, as described in

the section 4.3. It should also be noted that, as show in previous studies, the resistance against strain accumulation decreases with an increase in CSR.

In accordance with the latter consideration, the resistance to liquefaction expressed in terms of $p'=0$ cannot be representative of the tests in which the full liquefaction was not achieved. Therefore, to address this issue, the resistance to liquefaction (or more strictly, resistance to cyclic strain accumulation) was evaluated in terms of number of cycles required to develop a specific amount of residual shear strain γ_{RS}.

Fig. 4.14 through Fig. 4.17 show the resistance to cyclic strain accumulation in terms of the relationship between either the *CSR* or *SSR* and the number of cycles required to develop a γ_{RS} of 5 % (N_5), 10 % (N_{10}), 20 % (N_{20}) and 50 % (N_{50}), respectively. Similarly to the liquefaction resistance, the resistance to strain accumulation can either increase or decrease depending on the level of initial static shear stress and the failure mechanisms.

As shown in Fig. 4.14, the number of cycles to develop γ_{RS} of 5 % decreases with an increase in the initial static shear. In addition, the observed drop in resistance to strain accumulation can be associated with the change in failure mode from LQ to RF.

On the contrary, Fig. 15, Fig. 16 and Fig. 17 show that, the number of cycles to achieve a specific amount of 10 %, 20% and 50 % shear strain, first decreases and then increases with increasing the static shear stress. Similarly to the case of liquefaction resistance, the two-phase change in strain accumulation behavior can be associated with a two-phase change in failure behavior, from LQ to RF and from RF to RD.

It should be noted that, the results presented in Fig. 4.17 represents one of the goal of this study. In fact, they can help to understand the liquefaction-induced extremely large deformation behavior of slopes of sandy deposits that was observed during past large large-magnitude earthquakes, as explained later in chapter 6.

In conclusion, these tests results show that the presence of initial static shear does not always lead to an increase in the resistances against liquefaction and strain accumulation. They can either increase or decrease depending on the magnitude of the combined shear stress and the type of loading (i.e., degree of reversal stress), and the failure behaviors.

Table 4.2 Liquefaction, strain accumulation and failure characteristics.

	Test	*SSR=* τ_{static}/p'_0	*CSR=* τ_{cyclic}/p'_0	N_L *(p'=0)*	N_5 *(γ_{RS}=5%)*	N_{10} *(γ_{RS}=10%)*	N_{20} *(γ_{RS}=20%)*	N_{50} *(γ_{RS}= 50%)*	*Type of failure*
1	(16-00)	0.00	0.16	34	35	36	38	48	LQ
2	(16-05)	0.05	0.16	20	20	23	26	33	LQ
3	(16-10)	0.10	0.16	10	9	11	13	20	LQ
4	(16-15)	0.15	0.16	2	1	3	4	8	RF
5	(16-16)	0.16	0.16	3	0.8	3	5	13	RF
6	(16-17)	0.17	0.16	12	0.6	4	13	30	RD
7	(16-20)	0.20	0.16	No Liq.	0.2	8	46	202	RD
8	(20-00)	0.00	0.20	3	3	3	7	18	LQ
9	(20-05)	0.05	0.20	2	2	3	5	14	LQ
10	(20-10)	0.10	0.20	0.5	0.2	2	2.5	8	RF
11	(20-15)	0.15	0.20	0.5	0.2	2	2.5	7.5	RF
12	(20-20)	0.20	0.20	0.5	0.15	2	3	9	RF

LQ: cyclic liquefaction failure; RF: rapid flow liquefaction failure; RD: residual deformation failure

p'_0 = initial effective mean principal stress (=100 kPa)

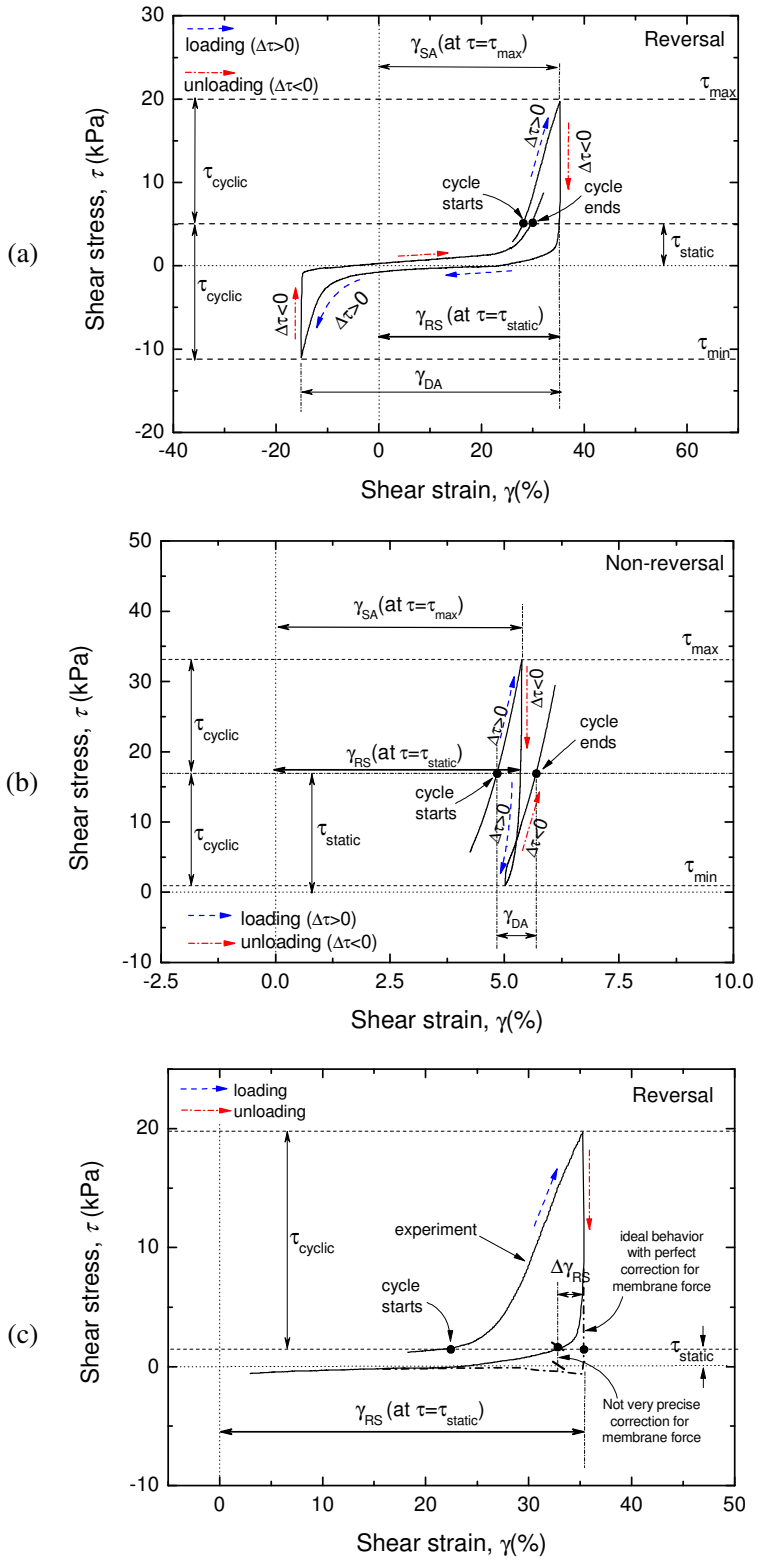

Fig. 4.12: Schematic definition of γ_{DA}, γ_{SA}*(at* τ=τ_{max}*)* and γ_{RS}*(at* τ=τ_{static}*)*: (a) reversal tests; (b) non-reversal tests; and (c) reversal tests with static shear very small (refer to section 4.5 for the description of the latter figure)

(a)

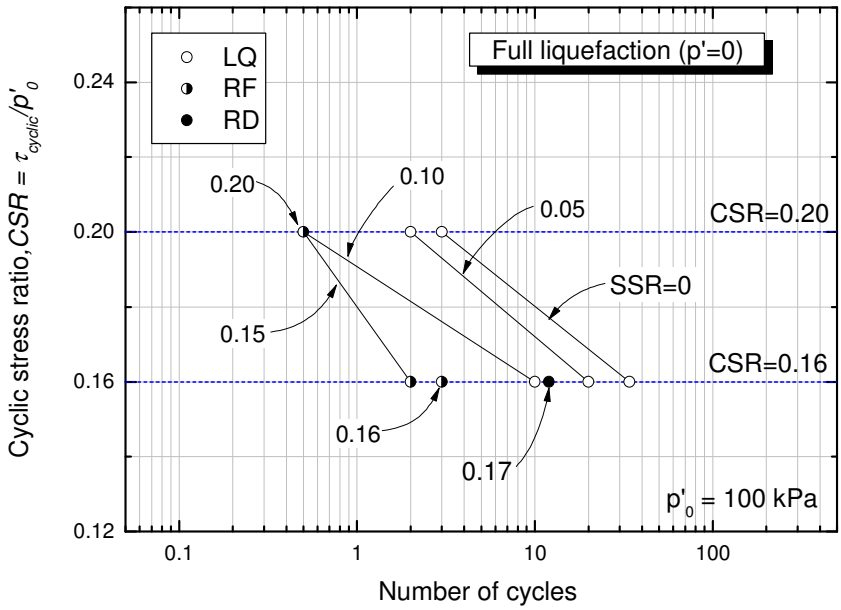

(b)

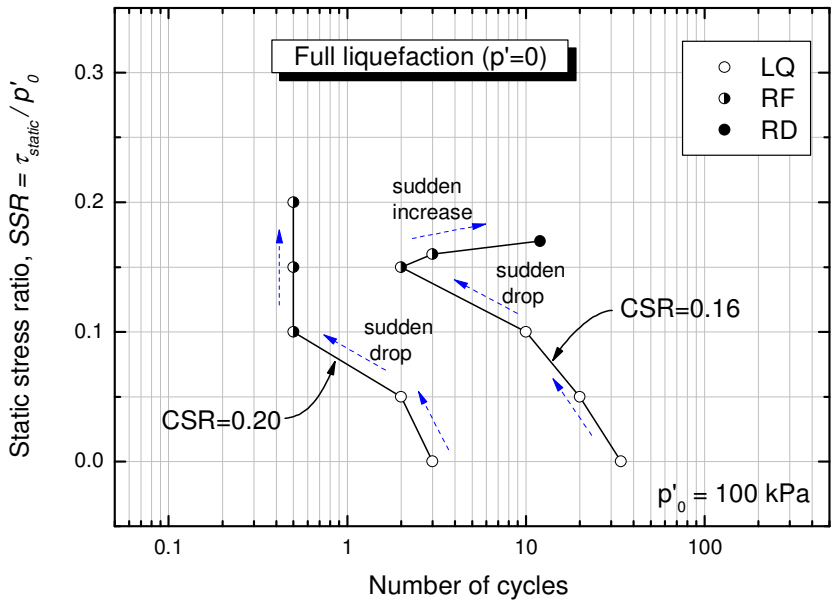

Fig. 4.13: Liquefaction resistance curves in terms of :

(a) CSR vs. Number of cycles to achieve full liquefaction (*p'=0*); and

(b) SSR vs. Number of cycles to achieve full liquefaction (*p'=0*)

(a)

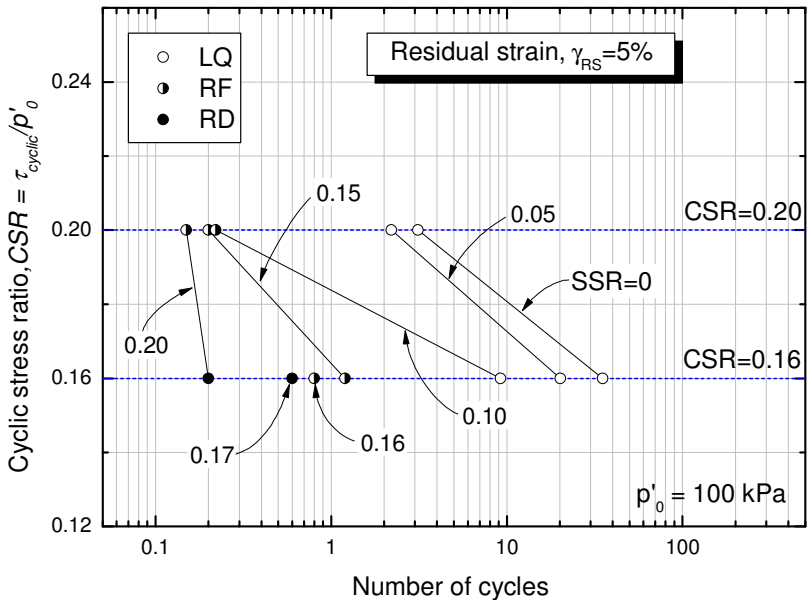

(b)

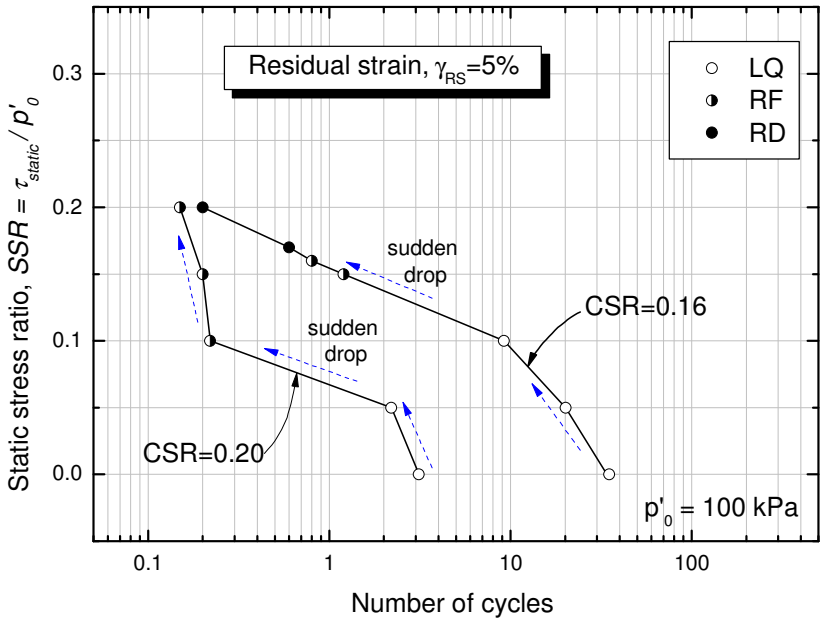

Fig. 4.14: Strain accumulation resistance curves in terms of :

(a) CSR vs. Number of cycles to cause γ_{RS} = 5%; and

(b) SSR vs. Number of cycles to cause γ_{RS} = 5%

(a)

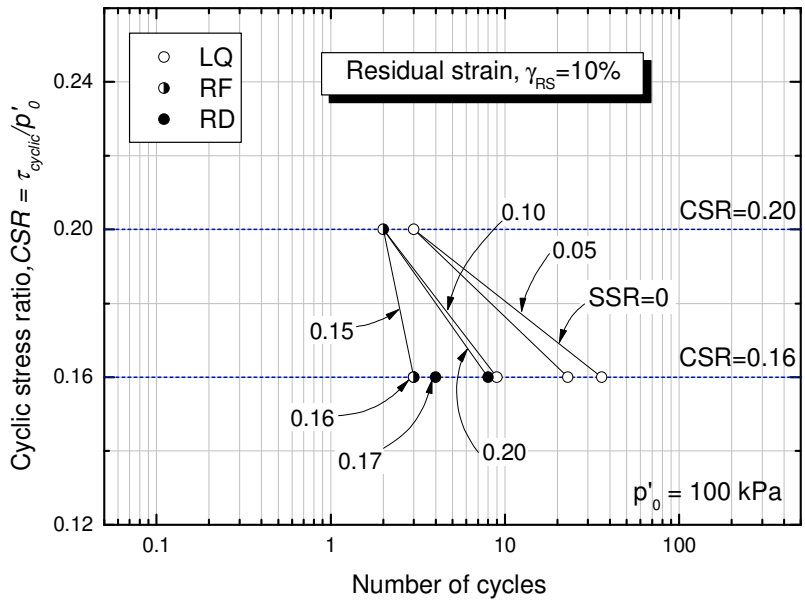

(b)

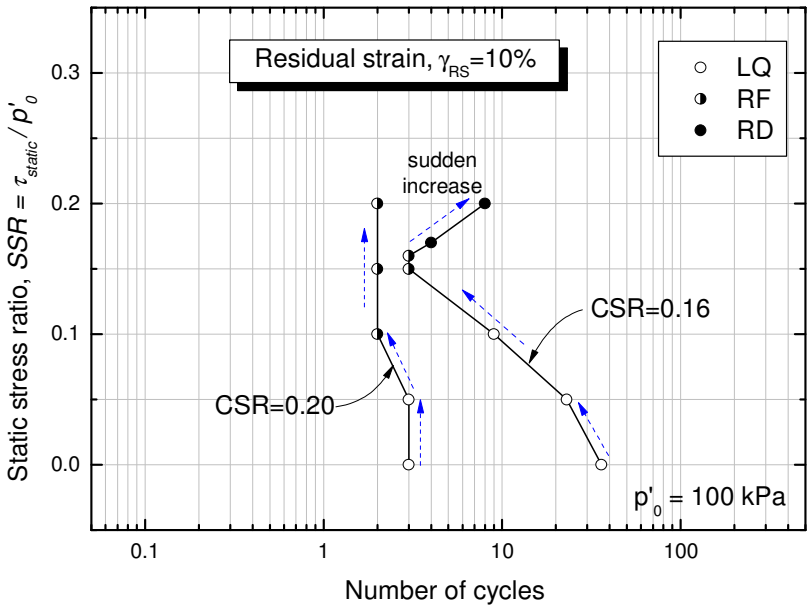

Fig. 4.15: Strain accumulation resistance curves in terms of:

(a) CSR vs. Number of cycles to cause γ_{RS} = 10 %; and

(b) SSR vs. Number of cycles to cause γ_{RS} = 10 %

(a)

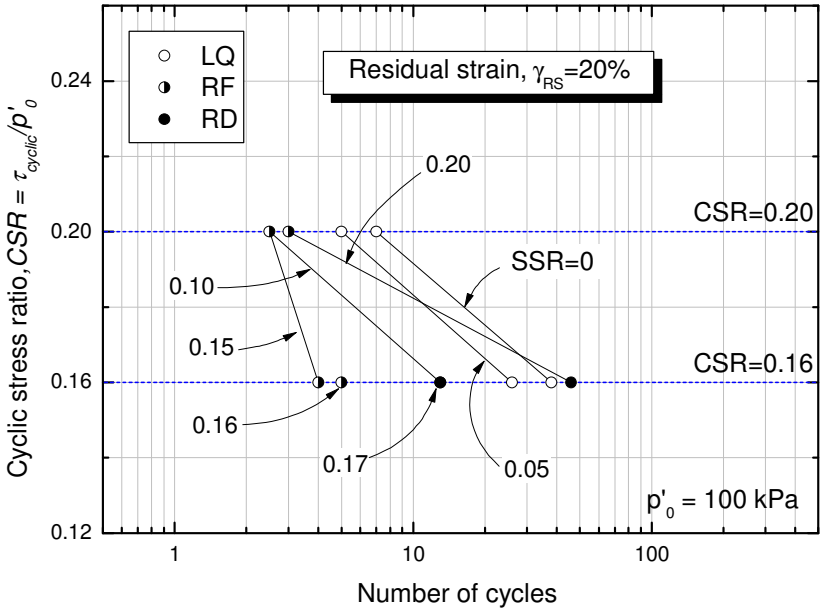

(b)

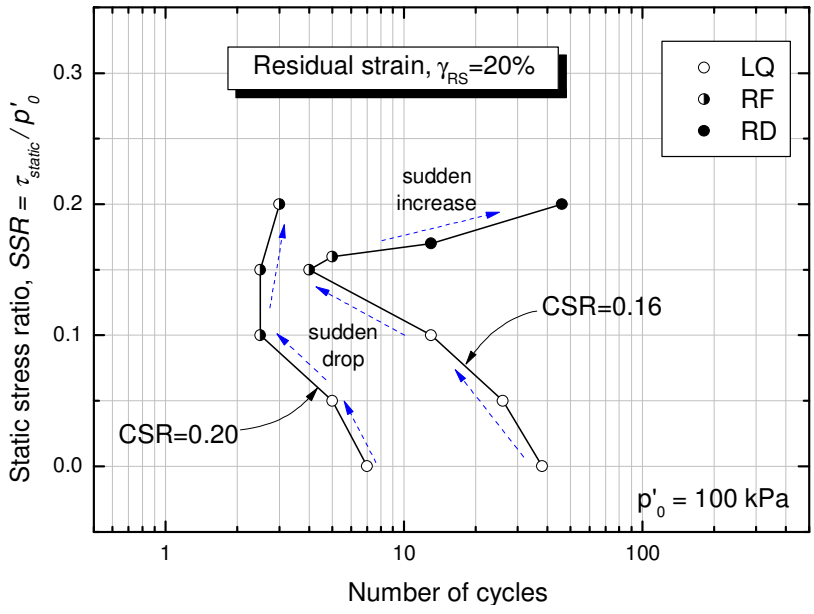

Fig. 4.16: Strain accumulation resistance curves in terms of:

(a) CSR vs. Number of cycles to cause γ_{RS} = 20 %; and

(b) SSR vs. Number of cycles to cause γ_{RS} = 20 %

(a)

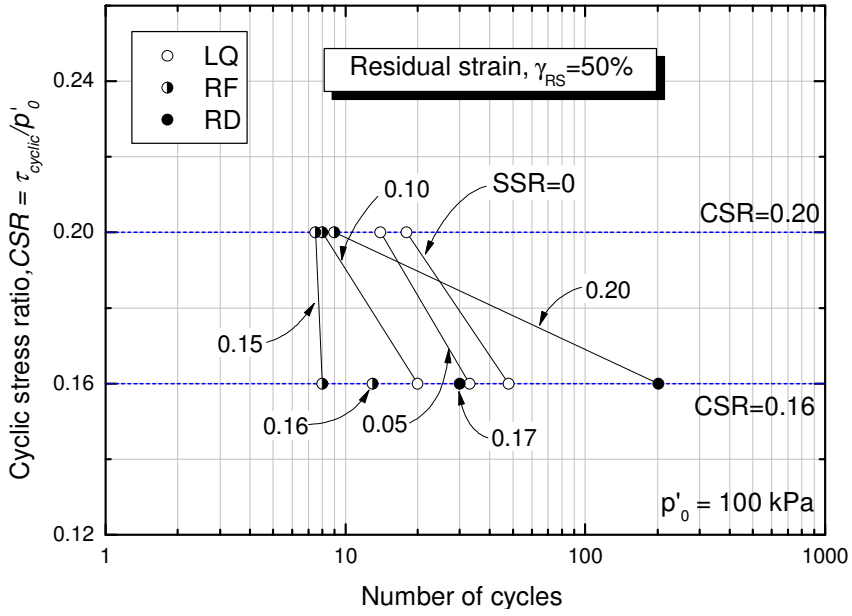

(b)

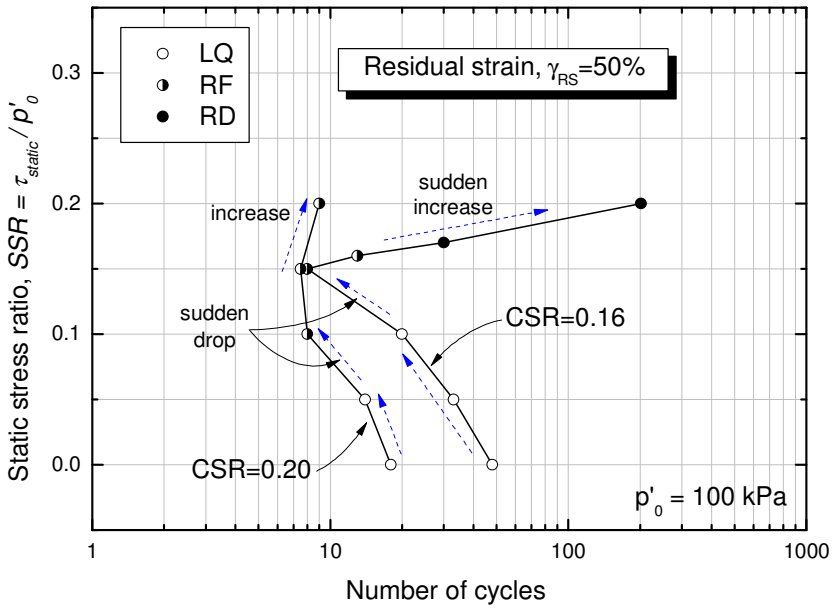

Fig. 4.17: Strain accumulation resistance curves in terms of:

(a) CSR vs. Number of cycles to cause γ_{RS} = 50%; and

(b) SSR vs. Number of cycles to cause γ_{RS} = 50%

4.5 Development of residual deformation due to cyclic shearing

In the current study, to examine the effects of initial static shear on the deformation properties of saturated loose sand in undrained cyclic torsional shear tests, the residual deformation (γ_{RS}), measured in terms of shear strain at the moment when the stress state recovered the initial value of static shear stress during the unloading stage of each cycle (i.e., at $\tau=\tau_{static}, d\tau < 0$), was employed. The definition of the γ_{RS} (at $\tau=\tau_{static}, d\tau < 0$) is shown in Fig. 4.12 .

It should be noted that, in the case in which the employed initial static shear was very small (i.e., $\tau_{static} \approx 0$), due to not a very precise correction of the membrane force at very large strain level, the residual strain γ_{RS} (at $\tau=\tau_{static}$) could not be properly defined. Hence, in such a case, it was defined by assuming an ideal behavior of specimen with a perfect correction for membrane force as show in Fig. 4.12 (c).

Based on the failure behavior of each specimen, three types of mechanisms of residual strain development could be identified, as shown in Fig. 4.18.

Fig 4.18 (a) summarizes the residual deformation behavior of specimens showing cyclic liquefaction failure behavior (LQ). In these tests, full liquefaction state ($p'=0$) was achieved after applying several cycles of loading; then, a sudden development of residual deformation took place.

Fig. 4.18 (b) illustrates the behavior of specimens characterized by rapid flow liquefaction failure mode (RF). In this case, during the first cycle, full liquefaction and deformation of a few percent were achieved. In addition, in most of the tests, deformation exceeding 50% was reached in less than 10 cycles.

Fig. 4.18 (c) shows the case of residual deformation failure (RD). These tests show that, extremely large deformation could be reached after applying a large number of cycles of loading, even in the case in which liquefaction did not take place.

(a)

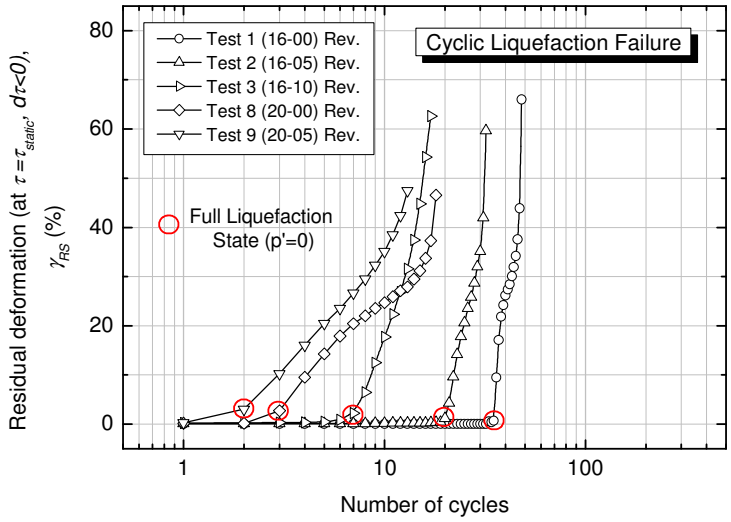

(b)

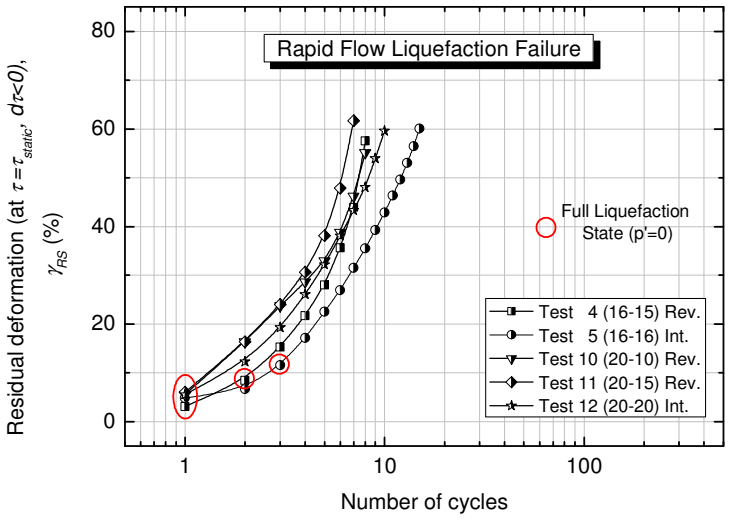

(c)

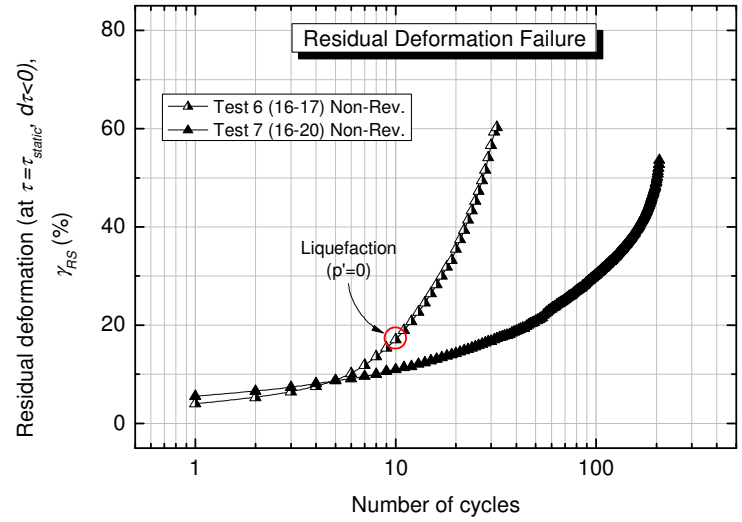

Fig. 4.18: Development of residual deformation during the cyclic loading:
(a) LQ failure behavior; (b) RF failure behavior; and (c) RD failure behavior.

4.6 Specimen deformation and strain localization

In torsional shear tests on hollow cylindrical specimens, a higher strain level can be achieved by increasing the amount of torsional displacement that is applied to the specimen through rotating the top cap.

In the computation of average stresses (see section 2.5), it is assumed that the shear strain is uniformly distributed throughout the height of the specimen, as shown in Fig. 4.19(a).

However, as already explained in section 2.3, the actual deformation behavior of hollow cylindrical specimens in torsional shear tests is affected by many factors, such as end restraint and bedding errors. Yet, by using appropriate geometric properties, one can define an area which is free from the effects of end restraint and bedding errors, as shown in Fig. 4.19(b). This can be true with respect to a range of small to moderate strain, at which the deformation of specimen can still be considered uniform.

On the contrary, at a large strain level, specimen deformation behavior is not uniform, as shown schematically in Fig. 4.19(c). To this regard, several factors should be considered, such as the use of non-rigid boundary (i.e., membranes), large extent of torsional deformation, the effects of liquefaction on the deformation response of soil, the strain localization (i.e., formation of shear band), etc.

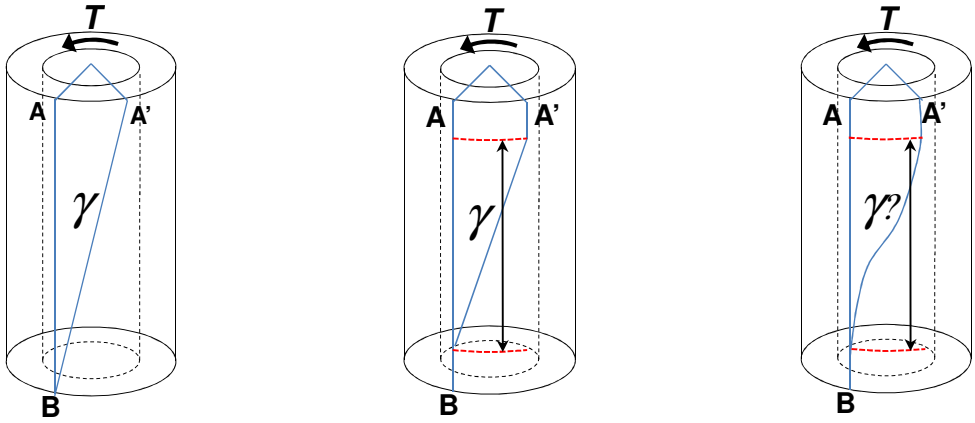

Fig. 4.19: Specimen deformation behavior: (a) Uniform deformation; (b) Uniform deformation within the area free from the effect of end restraint; and (c) Non-uniform deformation

4.6.1 Visual observation of specimen deformation

In the present study, using the torque loading device that was modified for enlarging the effective range of torsional displacement, the deformation properties of Toyoura sand were studied up to single amplitude shear strain exceeding 50%. Non-uniform deformation or strain localization was observed at higher strain levels.

By visual observation, an attempt was made to evaluate the limiting state of uniform deformation of the specimens, and to investigate the effects of initial static shear on it.

Herein, three types of specimen deformation were analyzed for reversal, intermediate and non-reversal loading conditions.

Reversal loading test results

Fig. 4.20 shows typical deformation at several states of the specimen under reversal loading conditions:

i. At state 1 (γ= 12 %), the deformation was almost uniform except for the regions close to the pedestal and the top cap that are affected by the end restraint; the outer membrane appeared slightly wrinkled;
ii. At state 2 (γ= 22 %), the outer membrane was visibly wrinkled; in the region near the top cap the deformation of the specimen started to localize due probably to water film formation;
iii. At state 3 (γ= 31 %), the localization of specimen deformation developed clearly in the upper part of the specimen. On the other hand, in the bottom part the uniformity of the specimen deformation is maintained even though many wrinkle appear; and
iv. At state 4 (γ= 54 %), the specimen was almost twisted near the top cap.

Intermediate loading test results

Fig. 4.21 illustrates typical deformation at several states of the specimen under intermediate loading conditions:

i. At state 1 (γ= 11 %), the deformation was almost uniform except for the regions close to the pedestal and the top cap that were affected by the end restraint;
ii. At state 2 (γ= 23 %), the outer membrane was extensively wrinkled. However, it should be noted that, the type of wrinkle observed in this tests can have a different meaning with respect to the one observed in the reversal tests described above; in

fact, in this tests, the specimen deformation pattern before and after each wrinkle is shift in correspondence of each wrinkle. This behavior suggest that, the formation of many shear bands took place into the specimen, and several parts of the specimen moved independently each other with different extent of deformation;

iii. At state 3 (γ= 39 %), the specimen reduced its diameter at several locations, as evidenced by the red arrows, due to probably the formation of shear bands; and

iv. Finally, at state 4 (γ= 64 %), the specimen was completely twisted.

Non-reversal loading test results

Fig. 4.22 shows typical deformation at several states of the specimen performed under non-reversal loading conditions:

i. At state 1 (γ= 21 %) the deformation was rather uniform except for the zones near the top cap and pedestal due to the effect of end restraint;

ii. At state 2 (γ= 25 %) the outer membrane was wrinkled at several locations due to local drainage;

iii. At state 3 (γ= 50 %) the membrane was extensively wrinkled from the bottom to the top; and

iv. At state 4 (γ= 0 %, after test), when the zero shear strain state was recovered while keeping undrained condition, formation of a spiral shear band could be observed (red dotted lines).

(a)

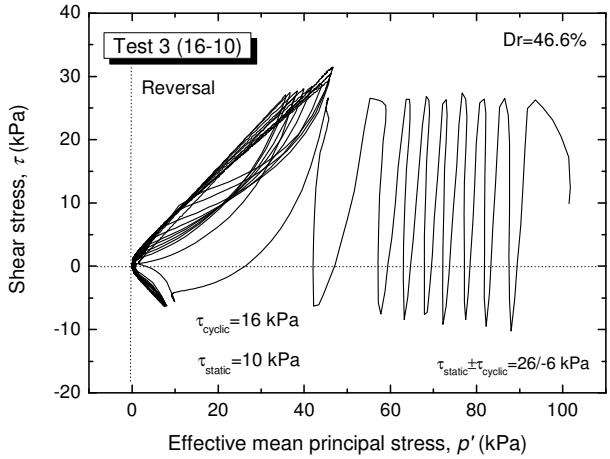

(b)

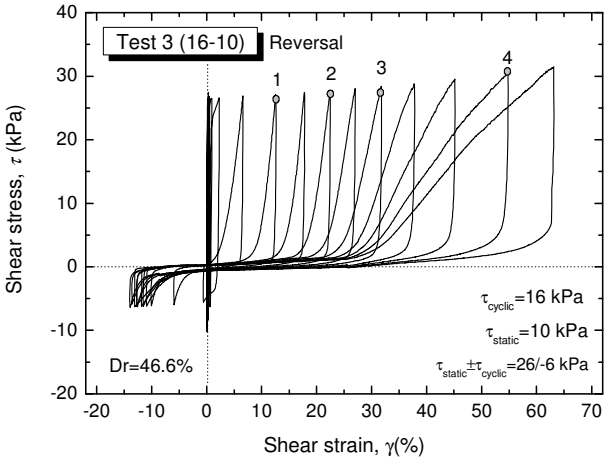

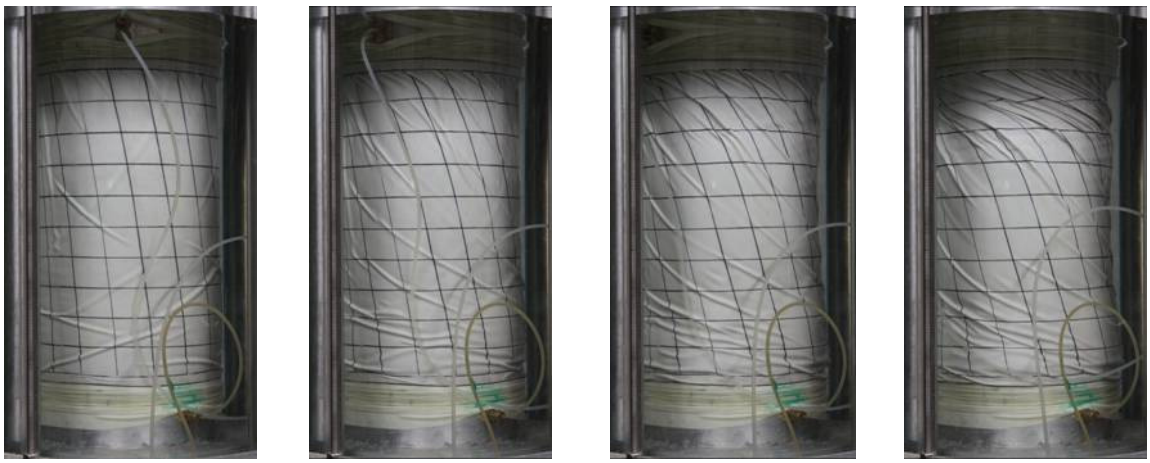

(c-1) State 1 (γ = 12 %) (c-2) State 2 (γ = 22 %) (c-3) State 3 (γ = 31%) (c-4) State 4 (γ = 54%)

Fig. 4.20: Typical specimen deformation for reversal loading tests:
(a) effective stress path; (b) stress-strain relationship; and (c) specimen deformation

(a)

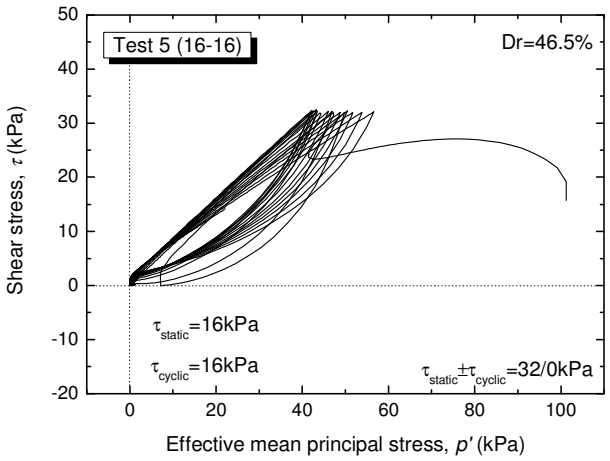

(b)

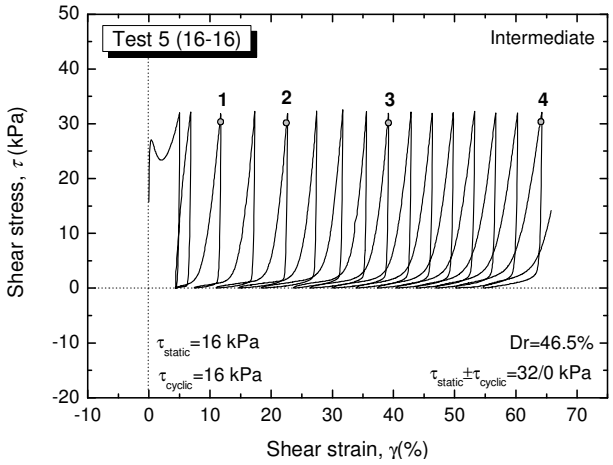

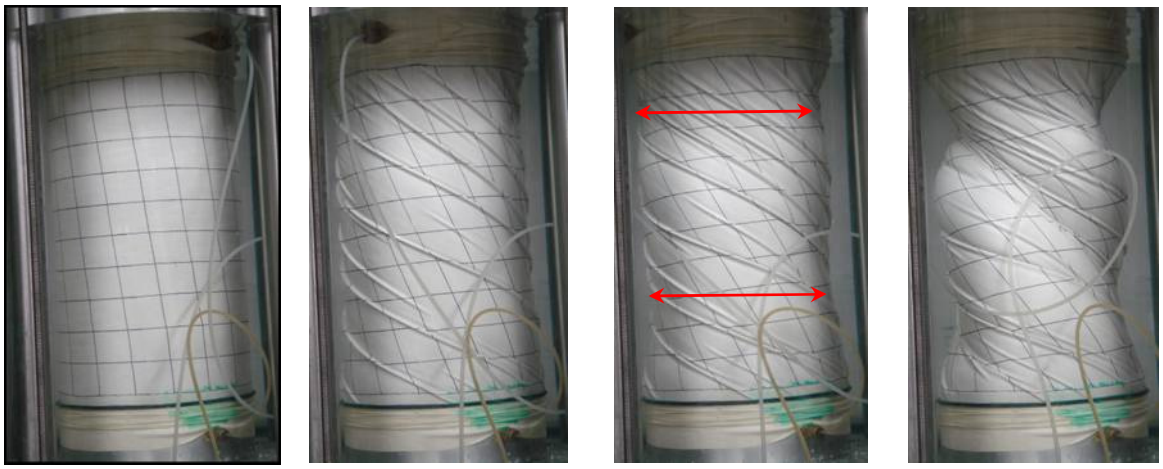

(c-1) State 1 (γ = 11 %) (c-2) State 2 (γ = 23 %) (c-3) State 3 (γ = 39%) (c-4) State 4 (γ = 64%)

Fig. 4.21: Typical specimen deformation for intermediate loading tests:
(a) effective stress path; (b) stress-strain relationship; and (c) specimen deformation

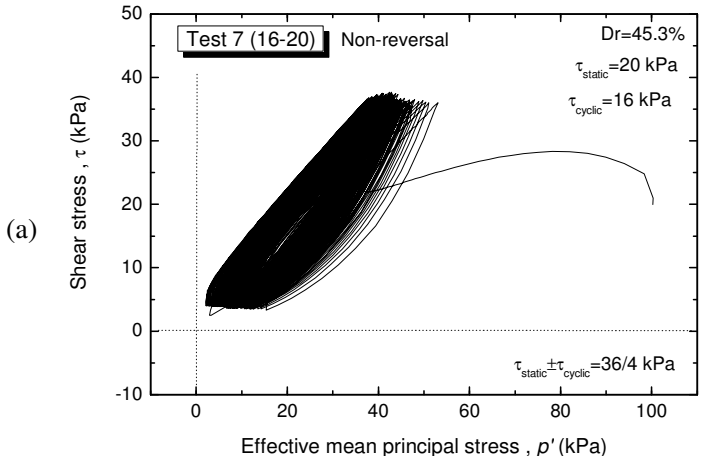

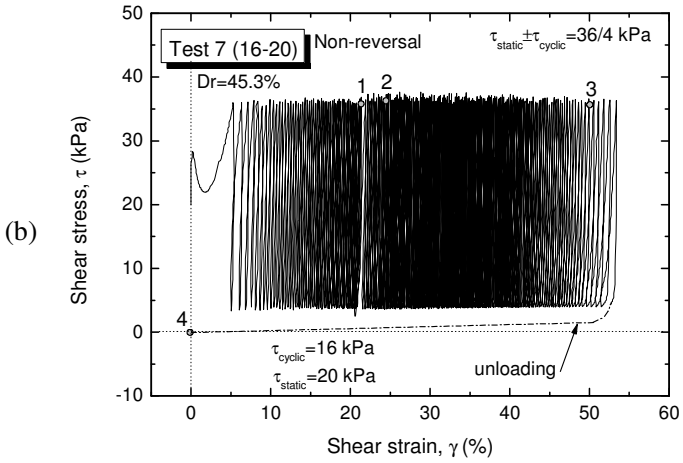

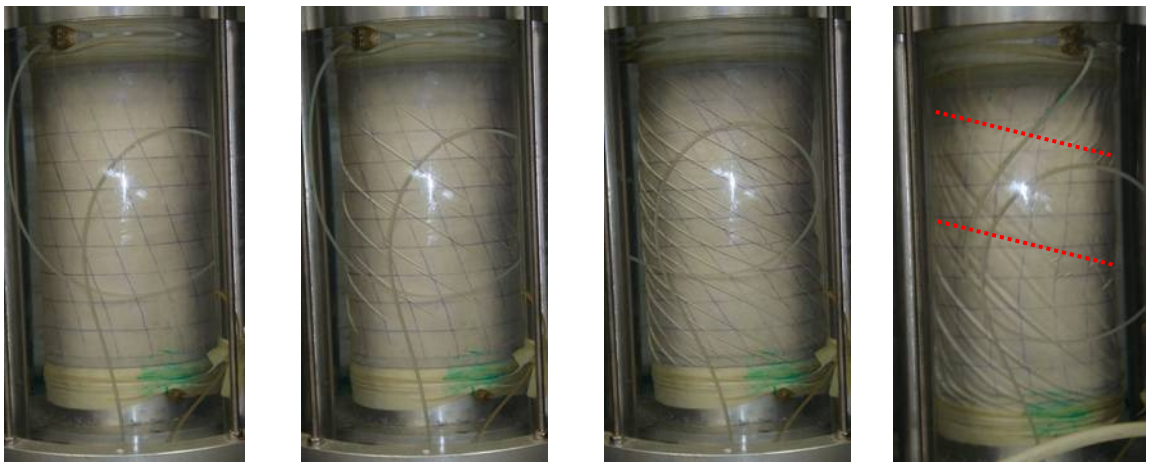

(c-1) State 1 (γ = 21%) (c-2) State 2 (γ = 25 %) (c-3) State 3 (γ = 50 %) (c-4) State 4 (γ = 0 %, after test)

Fig. 4.22: Typical specimen deformation for non-reversal loading tests:
(a) effective stress path; (b) stress-strain relationship; and (c) specimen deformation

4.6.2 Strain localization during cyclic loading

Kiyota et al. (2008) performed undrained cyclic torsional shear tests on saturated Toyoura sand, similar to those presented in this study, but without applying any initial static shear. In their tests the initiation of strain localization could not be clearly defined on the basis of visual observation, therefore, they defined it based on the change in the response of the deviator stress q $(= \sigma_v' - \sigma_h')$ which was measured during the undrained cyclic torsional shear loading while preventing any vertical displacement of the top cap.

Tatsuoka et al. (1986) performed drained monotonic torsional shear tests on hollow cylindrical specimens, while keeping the σ_v' and σ_h' constant. They reported that the vertical strain was accumulated on the extension side due to the mobilization of positive dilatancy, and it was reduced suddenly when the shear band was formed in the specimen.

The latter behavior that was observed during drained monotonic torsional shear tests is consistent with the change in deviator stress observed in undrained torsional shear tests; therefore, Kiyota et al. (2008) considered the state at which the amplitude of q decreases as the limiting state to initiate formation of shear band and thus strain localization. Furthermore, it was accompanied with an increase in the shear increment of single amplitude shear strain $(\Delta\gamma_{SA})$.

As a result, these features imply that the stress-strain characteristics of the specimen were changed by the formation of shear band and the initiation of strain localization in the specimen.

In this study, non-uniform specimen deformations were observed at higher strain levels. However, similarly to Kiyota et al. (2008), the initiation of strain localization could not be clearly defined on the basis of visual observation. To address this issue and evaluate the effects of initial static shear on the specimen deformation behavior, the attempt made by Kiyota et al. (2008) was employed. Therefore, from the analysis of deviator stress responses and stress-strain relationships, as typically shown in Fig. 4.23 through Fig. 4.26, the following two states were defined:

i) State A: the state at which q suddenly decreases; and

ii) State B: the state at which a change in the strain accumulation properties was observed.

The evaluated values of shear strain at state A and state B, respectively, are shown in Fig. 4.27 and Fig. 4.28. They were measured in terms of half of the double amplitude shear strain ($\gamma_{DA}/2$), as employed by Kiyota et al. (2008), and residual shear strain (γ_{RS}) which in this study was used to describe the effects of static shear on the deformation behavior (see Fig. 4.12 for the definition of γ_{DA} and γ_{RS}).

In Fig. 4.27 and Fig. 4.28, it can be seen that the greater the static shear stress (τ_{static}) the lower the $\gamma_{DA}/2$; in addition, a sudden drop in the value of $\gamma_{DA}/2$ is observed in case of the intermediate and non-reversal loading tests. On the other hand, γ_{RS} is rather constant whilst increasing the static shear stress level; however, in the case of intermediate and non-reversal tests, a sudden increase in γ_{RS} value can be observed.

In view of the above considerations, in this study, the shear strain required to cause the specimen strain localization was defined in terms of residual shear strain $\gamma_{RS.}$ Therefore, based on the response of the specimens subjected to reversal loading conditions, it was defined:
(i) $\gamma^{A}_{RS,avg} \cong 23$ %, which represents the state at which q suddenly decreases (state A);
(ii) $\gamma^{B}_{RS,avg} \cong 28$ %, which corresponds to the state at which a change in strain accumulation takes place (state B).

As mentioned above, the drop in q implies that the stress-strain characteristics of the specimen were changed by the formation of shear band and the initiation of strain localization in the specimen. In this study, in several cases, state A was not easy to define (e.g., when the change in the deviator stress amplitude was not unique as evidenced in Fig. 4.23 by the two red arrows) and thus different evaluations may be given among different researchers.

On the contrary, the change in stress accumulation at state B is a result of the specimen strain localization (i.e., formation of shear band). However, in this study, it could be unequivocally evaluated in all the tests.

The above observation suggests that, even if slightly over-estimated, the limiting state to initiate the strain localization in the specimen can be defined in terms of γ^{B}_{RS} which is a clear evidence of formation of shear band and can be clearly determined.

In addition, by analyzing the deviator stress responses, in this study, it was noted that after achieving state B the deviator stress becomes negative ($q < 0$) in the case of reversal tests, as shown in Fig. 4.23 (a) and Fig. 4.24 (a). This peculiar behavior would be associated with the full development of the shear band in the specimen; this aspect will be investigated later in section 4.7.

The latter behavior was not observed in case of intermediate and non-reversal tests as typically shown in Fig. 4.25 and 4.26.

In Fig. 4.26 a sudden drop of q can be observed; it may be the evidence of the formation of a shear band into the specimen. However, from the pictures took before and after this change in q response, as illustrated in Fig. 4.22 (c-1) and Fig. 4.22 (c-2), respectively, it cannot be seen any shear band.

Finally, as shown in Fig. 4.29, to have a comprehensive understanding, the value of $\gamma^{A}_{RS,avg}$ and $\gamma^{B}_{RS,avg}$ are shown in the plot of the residual deformation γ_{RS} vs. number of cycles with respect to reversal loading tests.

In Fig. 4.29, it is clear that the increment of single amplitude shear strain during each cycle decreases before reaching $\gamma^{B}_{RS,avg}$ and then increases with the number of cycles.

(a)

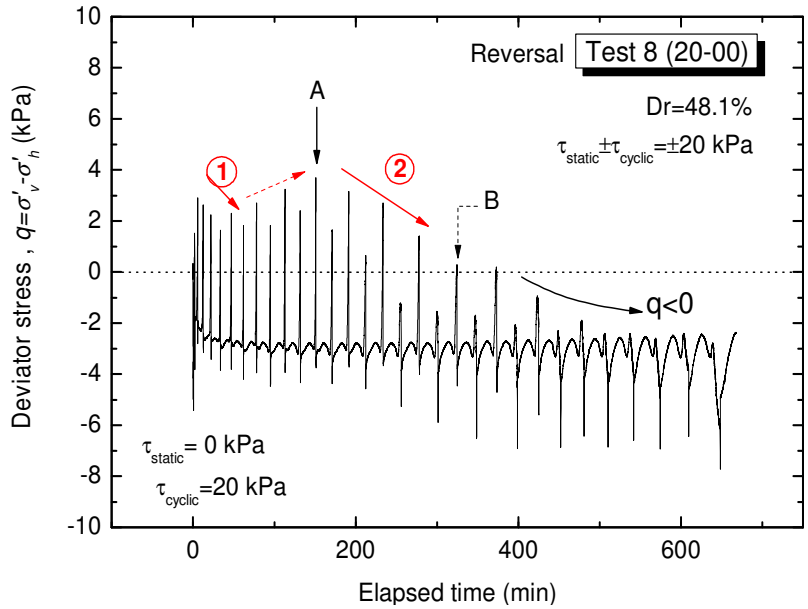

(b)

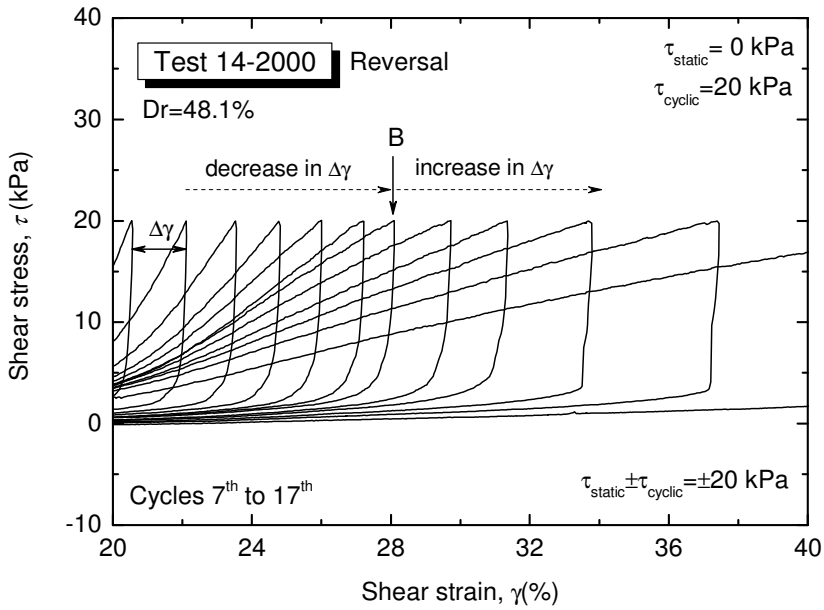

Fig. 4.23: Reversal loading Test 8 (20-00): (a) Time history of deviator stress; and (b) Change in shear strain accumulation during cyclic loading

(a)

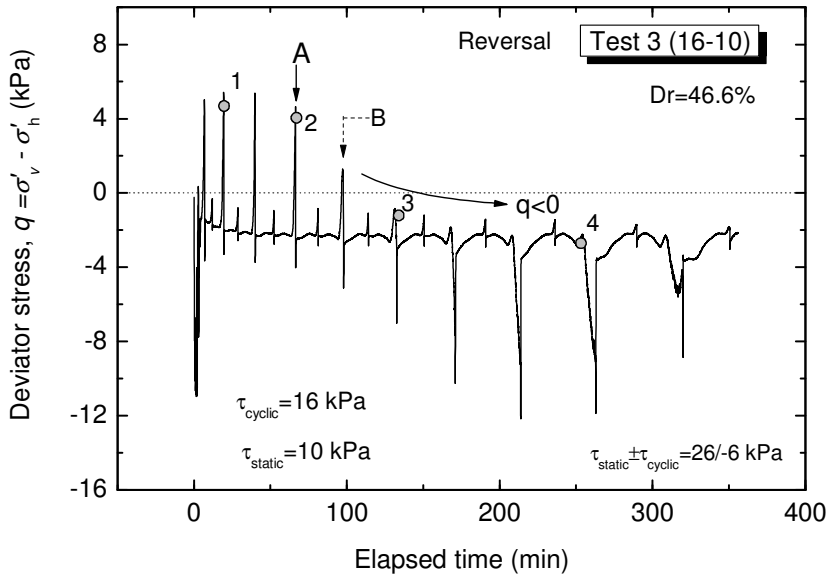

(b)

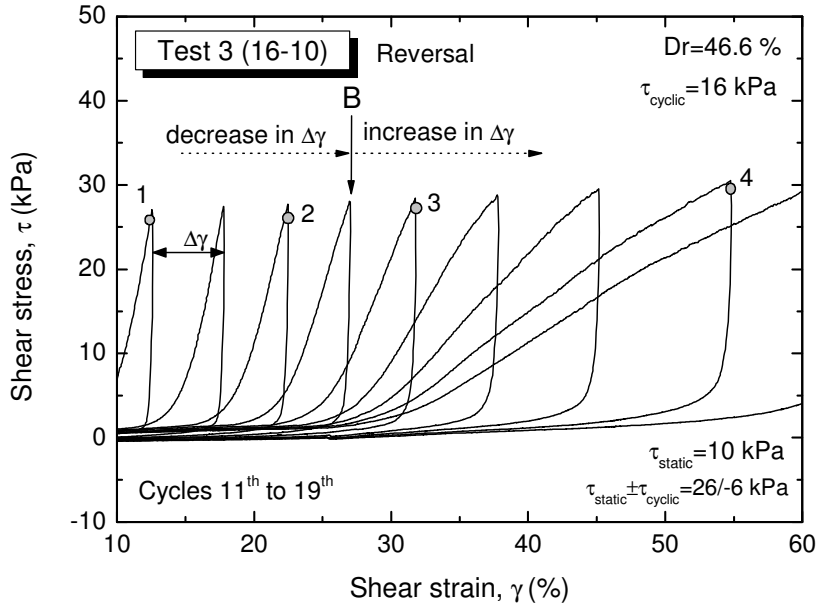

Fig. 4.24: Reversal loading Test 3 (16-10): (a) Time history of deviator stress; and (b) Change in shear strain accumulation during cyclic loading (refer to Fig. 4.20 for specimen deformation at states 1 through 4)

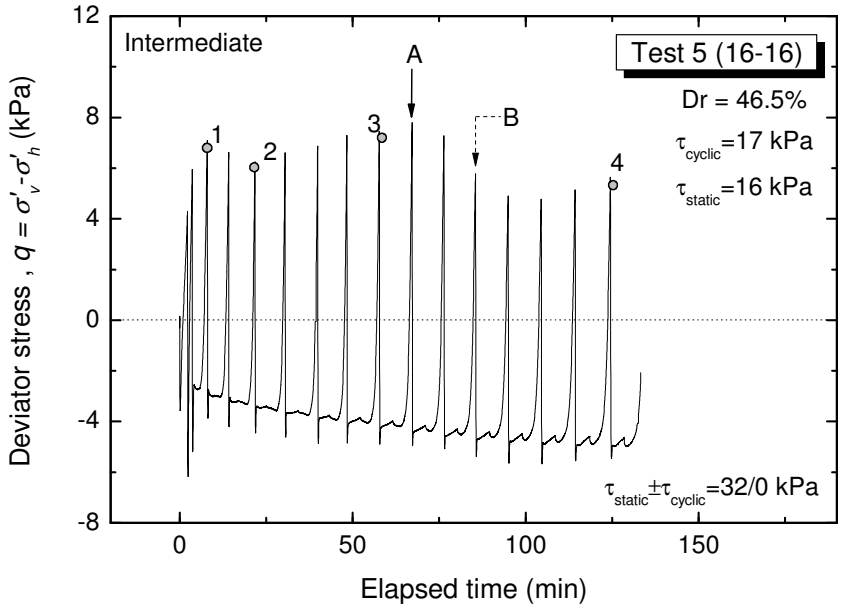

Fig. 4.25: Time history of deviator stress for intermediate loading Test 5 (16-16).
(refer to Fig. 4.21 for specimen deformation at states 1 through 4)

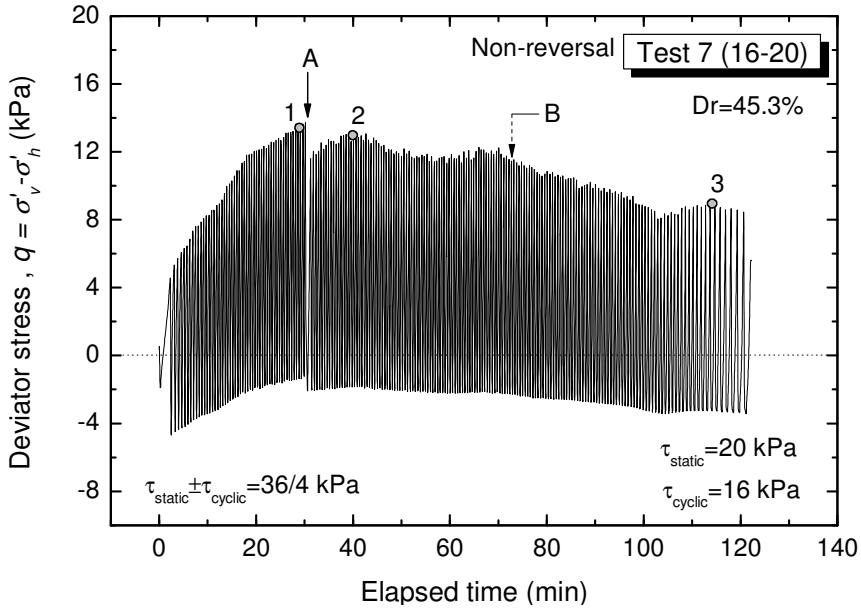

Fig. 4.26: Time history of deviator stress for non-reversal loading Test 7 (16-20).
(refer to Fig. 4.22 for specimen deformation at states 1 through 3)

(a)

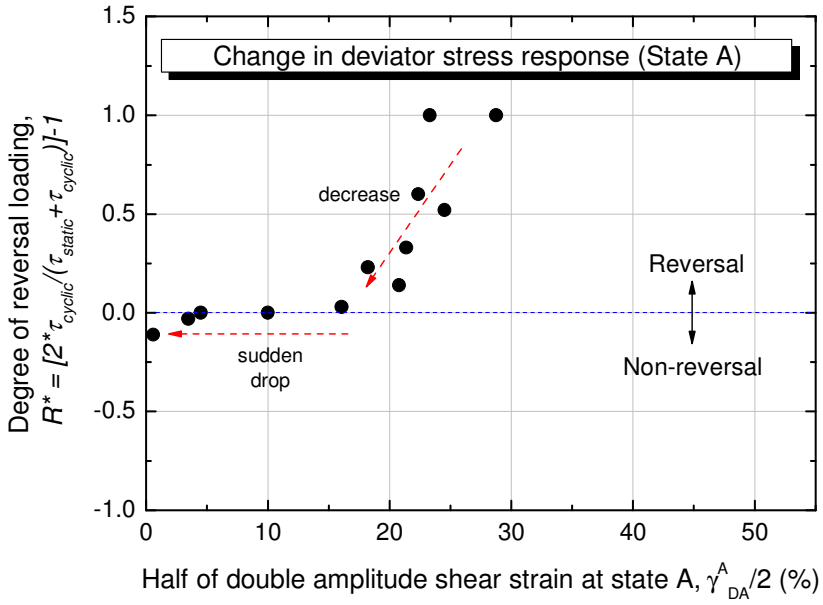

(b)

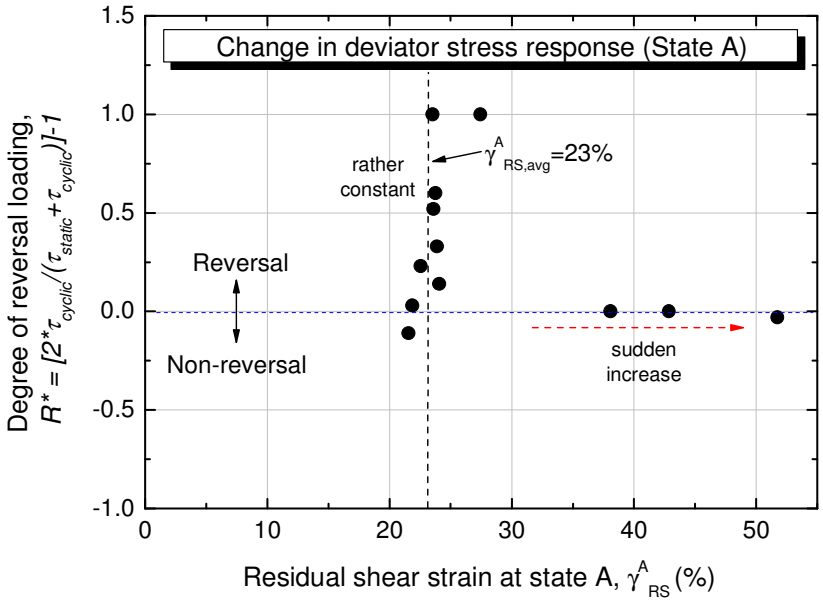

Fig. 4.27: Change in deviator stress response (state A) evaluated in terms of: (a) Half of double amplitude shear strain; and (b) Residual shear strain

(a)

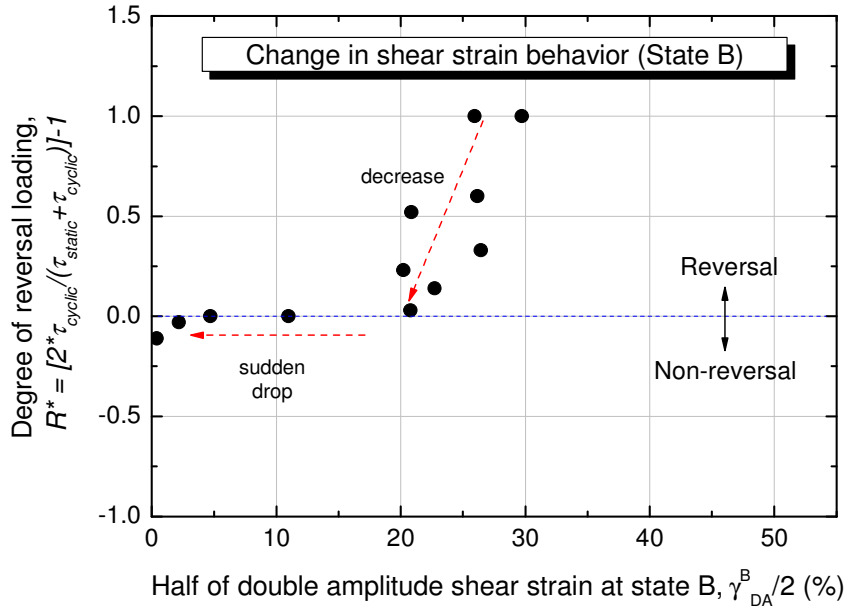

(b)

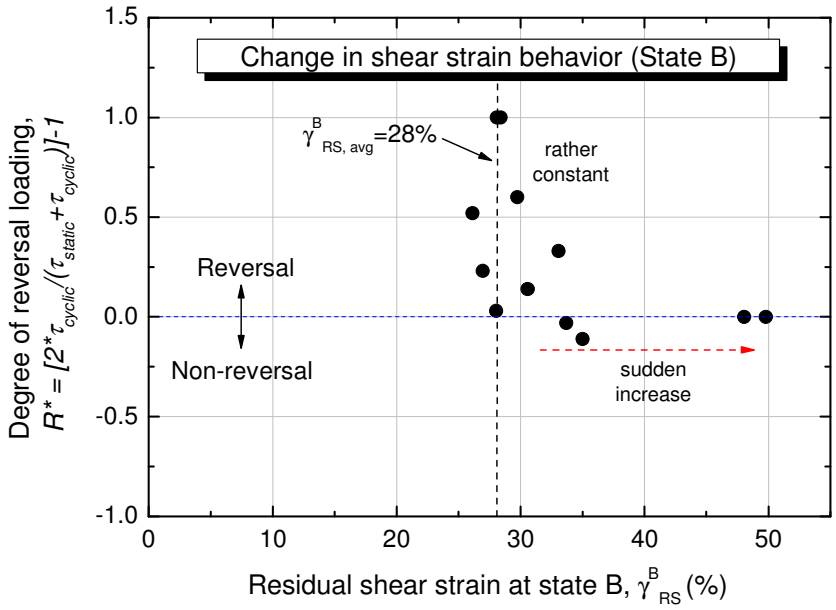

Fig. 4.28: Change in shear strain behavior evaluated in terms of: (a) Half of double amplitude shear strain; and (b) Residual shear strain

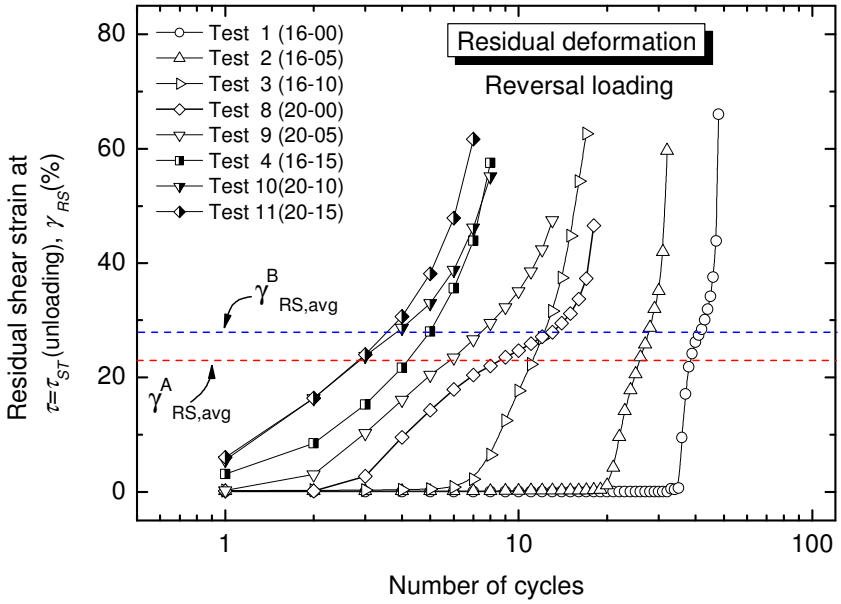

Fig. 4.29: Limiting shear strain to initiate the strain localization with respect to reversal loading tests

4.7 Strain softening at large strain levels

In this study, the limiting value of residual strain to initiate the strain localization of the specimen (i.e., formation of shear band) was defined as the one which induced a change in the behavior of strain accumulation. In addition, it was observed that the strain softening would be accompanied by negative values of deviator stress.

In order to confirm the validity of the method employed in this study to define the limiting value of residual strain to initiate the strain localization of the specimen, and to better understand the influence of static shear stress on such strain softening behavior of sand at large strain levels, the relationship between the modified shear stress and the modified current effective mean principal stress $(\tau-\Delta\tau)/(p'+\Delta p')$ introduced by Koseki et al. (2005) was employed.

4.7.1 Strain softening by employing the modified stress-strain relationship

Koseki et al. (2005) carried out a series of undrained torsional shear tests in order to investigate the liquefaction properties of Toyoura sand under low confining stress. The test results revealed that the effective stress path did not pass through the origin ($\tau = p' = 0$). They reported that this behavior is possibly affected by the following factors: (i) the effect of interlocking among sand particles that could be mobilized even under zero effective stress states; (ii) errors in the measured deviator stress q which could cause apparently non-zero values of p'; and (iii) the viscous interaction between pore water and the surface of sand grains, as pointed out by Towhata and Gallage (2003) among others. Therefore, in the attempts made by Koseki et al. (2005), an apparent increase in effective stress state ($\Delta p'$) and the shift in shear stress ($\Delta\tau$) were introduced to correct for the effects of mobilization of shear resistance under extremely low effective stress states.

Fig. 4.30 (a) shows a typical close-up around the origin of the effective stress path and the evaluation of $\Delta\tau$ and $\Delta p'$ as obtained in this study for the tests in which no initial static shear was employed (e.g., Test 8).

On the other hand, Fig. 4.30 (b) and Fig. 4.31 (a) show the relationships between the current shear stress ratio with/without correction for the above $\Delta\tau$ and $\Delta p'$, and the plastic shear strain γ^p in Tests 8, respectively. The plastic shear component was evaluated by

subtracting from the total strain component the elastic one evaluated by employing the quasi-elastic model developed at IIS, University of Tokyo (Hong Nam, 2004), as explained later in detail in chapter 5.

In the case without correction of $\Delta\tau$ and $\Delta p'$ (i.e., $\Delta\tau=0$, $\Delta p'=0$) as shown in Fig. 4.30 (b), the stress ratio totally fluctuated and occasionally became extremely large due to division by zero (i.e., $p'=0$ at full liquefaction state).

On the contrary, in the case with correction of $\Delta\tau$ and $\Delta p'$, as shown in Fig. 4.31 (a), such unstable behavior disappeared and the peak stress states that were followed by strain softening were observed at shear strain level (γ^{peak}) of about ± 19 %.

A parametric study on the sensitivity of the correction factor $\Delta\tau$ and $\Delta p'$ is presented in appendix A.

In Fig. 4.31 (a), the shear strain necessary to induce a change in strain accumulation (γ^{B}_{RS}), as defined in section 4.6, is also shown for comparison. Therefore, γ^{peak} can be considered as the state at which strain localization in the specimen begins.

Fig. 4.31 (b) represents a close-up of the modified stress-strain relationship in Fig. 4.31(a). The peak stress state was followed by strain softening until it enters into the residual stress state. It can be seen that γ^{B}_{RS} corresponds well with the end of strain softening and the beginning of residual stress state (intersection point of the two broken lines).

In section 4.6, the limiting value of residual strain to initiate the strain localization of the specimen (i.e., formation of shear band) was defined as the one which induced a change in the behavior of strain accumulation, and it was accompanied by negative values of deviator stress. In addition, as mentioned above, it was observed that γ^{B}_{RS} corresponds well to the state at which strain softening ends and the residual stress state begins. These features imply that γ^{B}_{RS} is the state at which the shear band is fully developed in the specimen.

Therefore, the limiting value of shear strain to initiate the strain localization might be evaluated in terms of strain softening behavior by defining the γ^{B}_{RS} or employing the relationship between the modified stress ratio and the plastic shear strain.

(a)

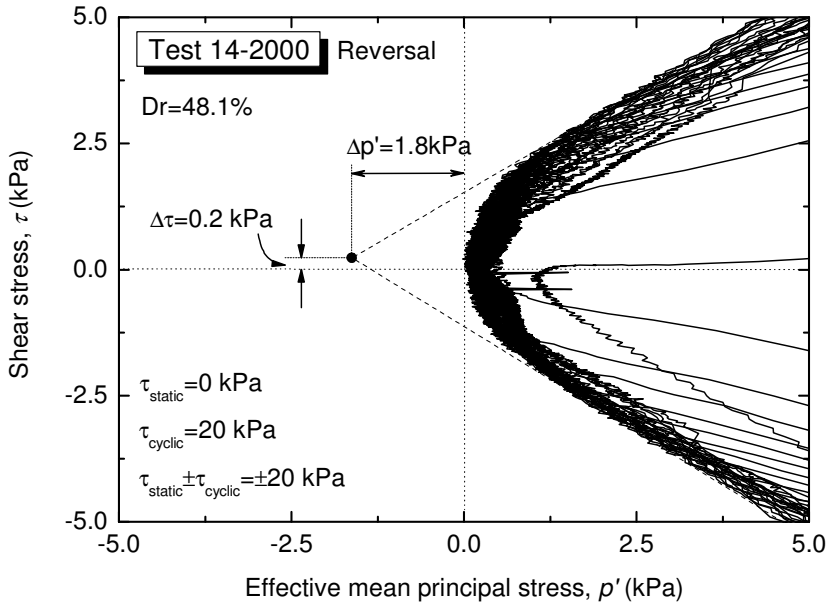

(b)

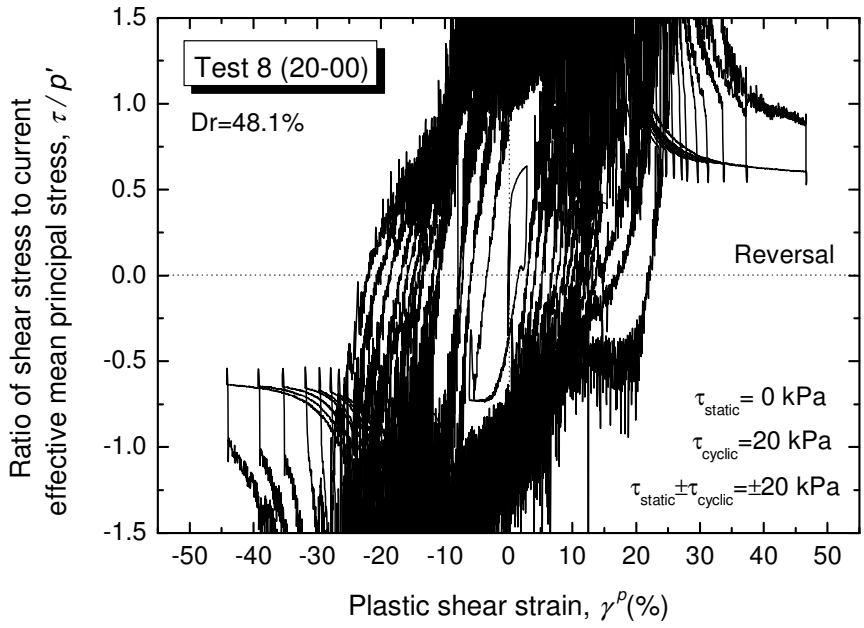

Fig. 4.30: Typical result of reversal loading test without initial static shear (Test 8): (a) Close-up around the origin of the effective stress path and the evaluation of $\Delta\tau$ and $\Delta p'$; and (b) Stress-strain relationship without correction for $\Delta\tau$ and $\Delta p'$

(a)

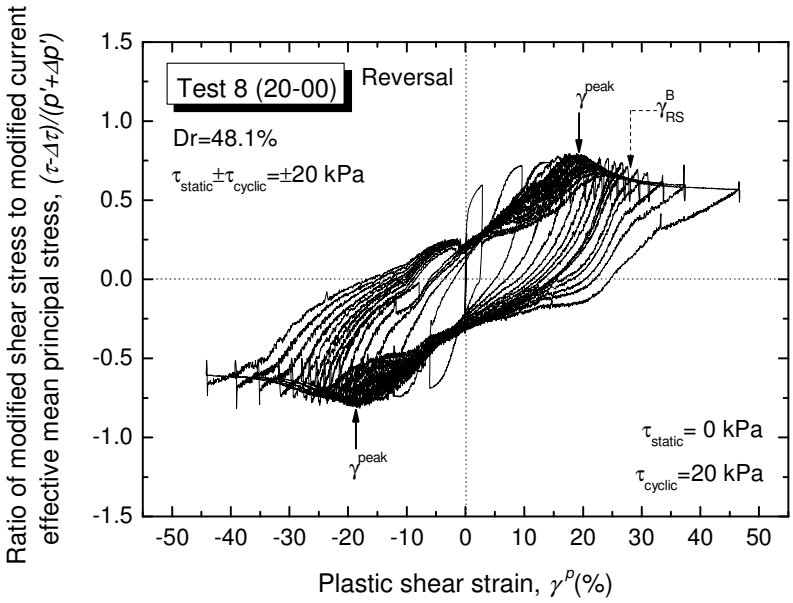

(b)

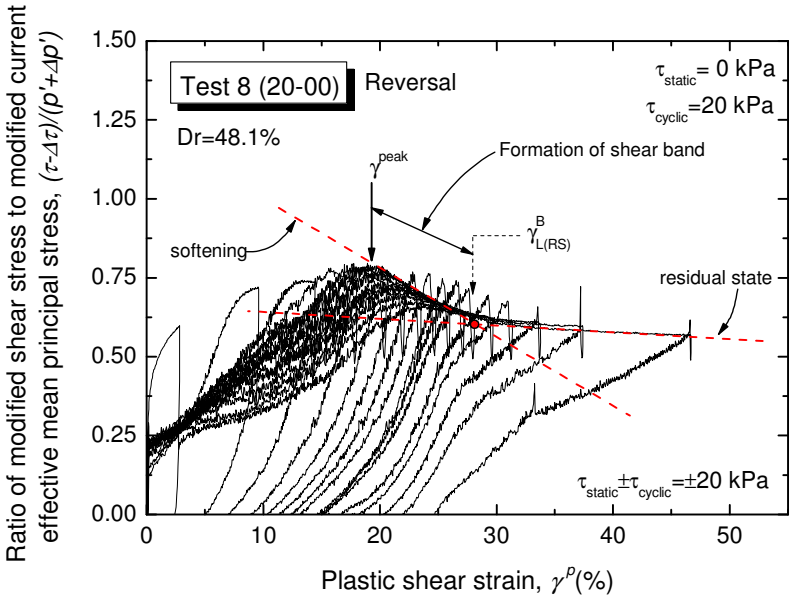

Fig. 4.31: Typical result of fully reversal loading test (τ_{static} = 0): (a) Modified stress-strain relationship (i.e., after correcting for $\Delta\tau$ and $\Delta p'$); and (b) Close-up of modified stress-strain relationship

4.7.2 Effect of static shear on the strain softening properties

The influence of static shear stress on such strain softening behavior of sand undergoing large strain levels is examined in terms of the relationship between the modified shear stress $(\tau-\Delta\tau)/(p'+\Delta p')$ and the plastic shear strain with respect to residual, intermediate and non-reversal loading conditions.

Fig. 4.32 shows the typical relationship between the modified stress ratio and the plastic shear strain in case of reversal loading test in which initial static shear was applied before the undrained cyclic shearing (e.g., Test 3). Similarly to Test 8 (see Fig. 4.31) in which no initial static shear was employed, in Tests 3 the peak stress state was followed by strain softening until it enters into the residual stress state.

Fig. 4.33 represents the close-up around the origin of the effective stress path and the evaluation of $\Delta\tau$ and $\Delta p'$ in the case of intermediate loading test 5. In this case the correction of $\Delta\tau$ was set equal to zero $(\Delta\tau = 0)$ due to the non-reversal loading conditions.

Fig. 4.34 shows the typical stress-strain relationship with/without the correction of $\Delta\tau$ and $\Delta p'$ in case of intermediate loading test (e.g., Test5). As shown in Fig. 4.34(b) the peak state cannot be clearly defined as in the case of reversal loading tests. In fact, the peak stress states moves progressively with the number of cycles. However, a strain softening can be observed after each peak stress state.

Fig. 4.35 shows the typical modified stress-strain relationship in case of non-reversal test (e.g., Test 7). In this test liquefaction was not achieved therefore the correction of $\Delta\tau$ and $\Delta p'$ was set to be equal to zero (i.e., $\Delta\tau=0, \Delta p'=0$). The close-up of the modified stress-strain relationship in Fig. 4.35(b) shows that similarly to the intermediate loading test results in Fig. 4.34(b) the stress peak state moves progressively with the number of cycles.

In addition, it should be noted that, progressively the amplitude of the stress-strain relationship increases with the number of cycles due to a decrease of the effective mean principal stress (p') with the number of cycles (see Fig. 4.4(a) for the effective stress path).

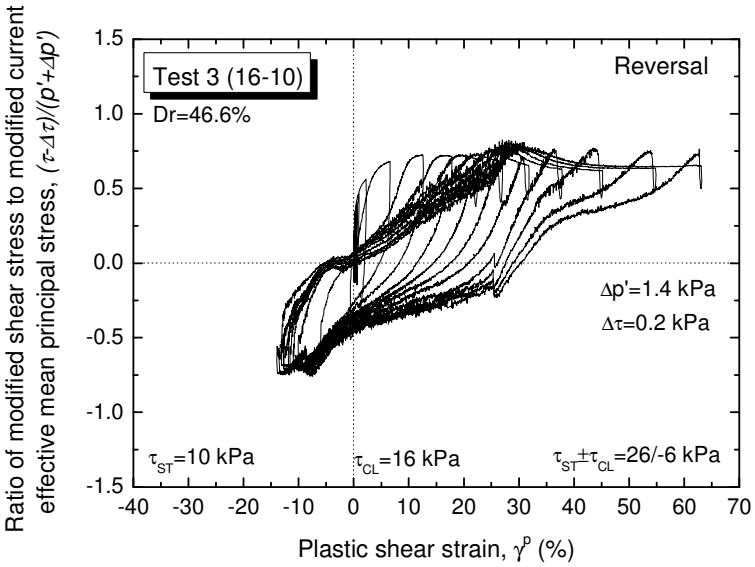

Fig. 4.32: Typical modified stress-strain relationship in reversal loading test with initial static shear (Test 3)

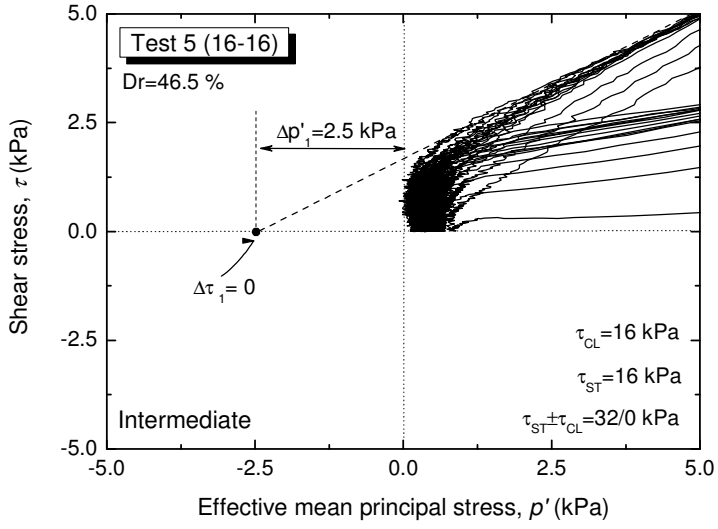

Fig. 4.33: Close-up around the origin of effective stress path and the definition of $\Delta\tau$ and $\Delta p'$ in intermediate loading test (Test 5)

(a)

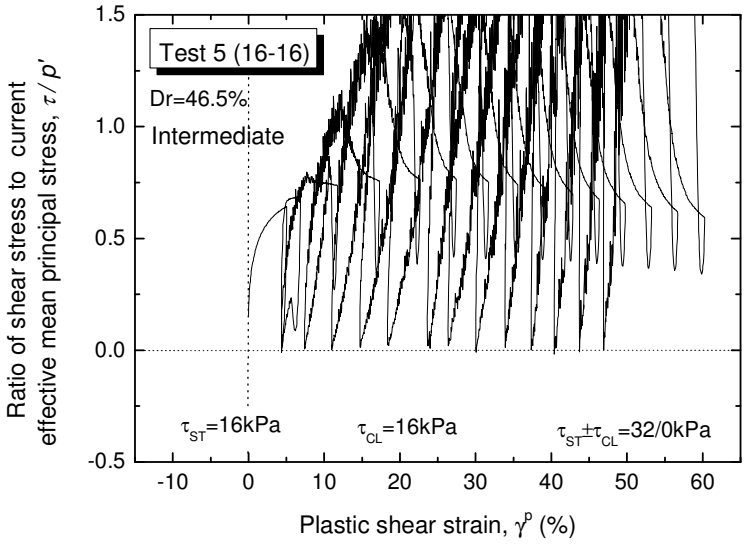

(b)

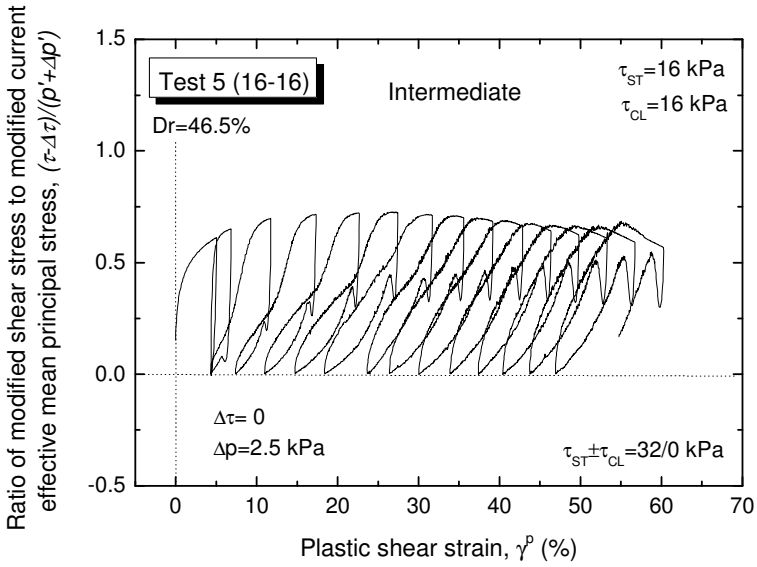

Fig. 4.34: Typical modified stress-strain relationship in intermediate loading test (Test 5): (a) Stress-strain relationship; and (b) Modified stress-strain relationship

(a)

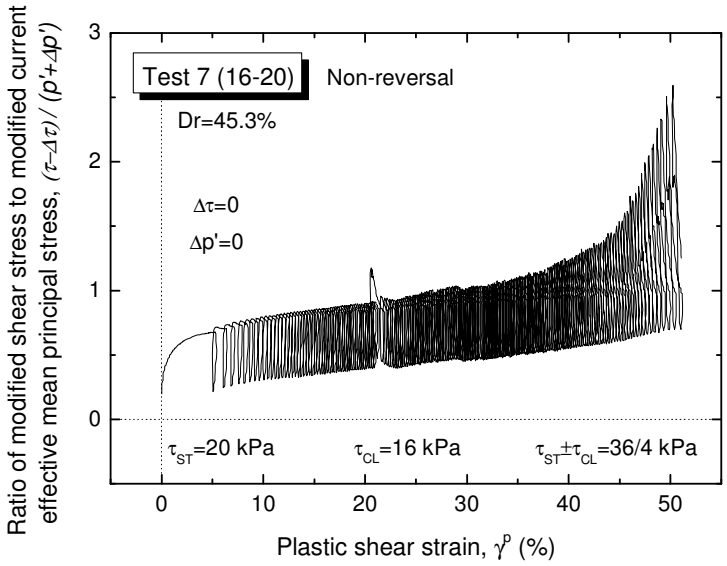

(b)

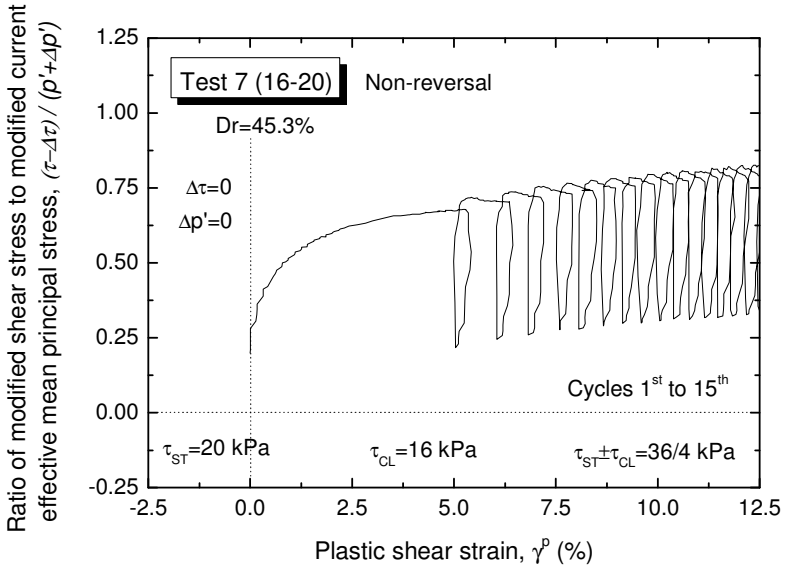

Fig. 4.35: Typical result of non-reversal loading test (Test 7): (a) Modified stress-strain relationship; and (b) Close-up of modified stress-strain relationship. In this test liquefaction was not achieved therefore the correction of $\Delta\tau$ and $\Delta p'$ was set equal to zero (i.e., $\Delta\tau=0$, $\Delta p'=0$)

4.8 Correction for membrane force

As Koseki et al. (2007) among others pointed out, in torsional shear tests on hollow cylindrical specimen, due to the presence of inner and outer membranes, the effect of membrane force cannot be neglected.

Furthermore, it becomes significantly important when shear strain reaches extremely high level as Kiyota et al. (2008) indicated.

Usually, the membrane force has been corrected based on the linear elasticity theory, which uses the Young's modulus of the membrane. The theoretical apparent shear stress (τ_m) induced by the inner and the outer membranes can be evaluated as:

$$\tau_m = \frac{t_m E_m \left(r_o^3 + r_i^3\right)\theta}{\left(r_o^3 - r_i^3\right)H} \tag{4.4}$$

where

r_o = outer radius of the specimen;

r_i = inner radius of the specimen;

t_m = thickness of membrane;

E_m = Young's modulus of membrane;

H = height of specimen;

θ = rotation angle detected by potentiometer.

In this study, in order to confirm the validity of Eq. (4.4) in correcting the effect of membrane force, a special test was performed by filling with water the area between the inner and outer membranes (Fig. 4.36) and shearing it cyclically under undrained condition up to double amplitude shear strain (γ_{DA}) of 100% (Fig. 4.40).

Preparation of the water specimen did not require a special technique; however, it was carried out with precaution in order to avoid any curvature of the specimen wall.

First the membranes were placed and the top cap attached to the load cell shaft. Then, water was allowed to flow within the empty space between the membranes in a similar manner to the saturation process in case of the soil specimens. At the same time the cell chamber was filled with water while maintaining throughout the same level of the water

within the membranes. Consequently, due to the self-balanced water pressure acting on both faces of each membrane the verticality of the membranes was guaranteed.

After, the obtained hollow cylindrical water specimen (Fig. 4.36) was sheared under undrained conditions whilst preventing any vertical displacement of the top cap. The shear loading was reversed when the single amplitude shear strain reached a target value of 2%, 5%, 10%, 20%, 30%, 40% and 50%.

Fig. 4.32 through Fig. 4.35 show the specimen deformation at several states as numbered 1 through 4. In the same figures, both the experimental and the theoretical relationships between shear strain (γ) and apparent shear stress (τ_m) that is induced by the membranes due to torsional deformation are depicted.

As shown in Fig. 4.37, at state 1 (γ= 5%) the water specimen deformation was nearly uniform, and the measured stress-strain relationship could be described by that which is assumed in the theory.

On the other hand, at state 2 (γ= 20%) and at state 3 (γ = 40%) in Fig. 4.38 and Fig. 4.39 respectively, the outer membrane appeared extensively wrinkled. In both cases, the measured stress-strain relationships were almost linear, but they clearly differed from the theoretical one.

At extremely large strains level (state 4, γ= 50%), the water specimen was almost twisted near the top cap; the experimental stress-strain relationship became non-linear (Fig. 4.40).

Therefore, from this tests, it is clear that the deviation of the actual membrane deformation from the uniform one that is assumed in the theory became larger with an increase in the strain levels; for this reason, in this study, the shear stress was corrected for the effect of membrane force by employing the polynomial approximation of the measured relationship between shear strain (γ) and the apparent shear stress (τ_m) as shown in Fig. 4.40.

Since the water specimen was sheared while preventing any vertical displacement of the top cap, apparent deviator stresses (q_m) induced by the extension of the membranes was observed. In Fig. 4.41, the measured relationship between the apparent deviator stress and the shear strain for the cycles of loading with γ_{DA}=10% and the one with γ_{DA}=100% are compared.

In Fig. 4.42, in order to confirm the validity of the membrane force obtained experimentally, the torsional deformation of the water specimen was compared with the deformation of sandy specimens subjected to reversal, intermediate and non-reversal loading whilst achieving levels of shear strain of about 20%, 30%, 40% and 50%.

The torsional deformation of the water specimen appeared to be suitable with the one observed for the sandy specimens up to a strain of about 30%; in fact, by exceeding this level of strain either the water or sand specimens exhibit non-uniform deformation which is extremely different from each other hence it becomes not so easy to make a comparison.

Fig. 4.36: Water specimen before undrained shearing (γ=0%)

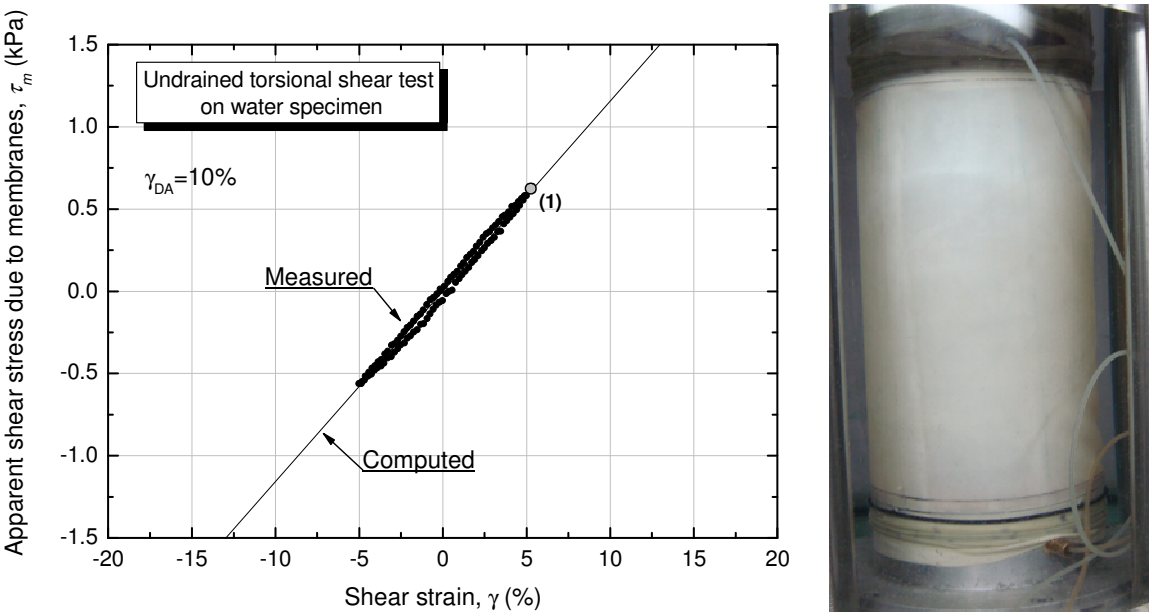

(a) (b)

Fig. 4.37: (a) Relationships between γ - τ_m on the range of γ_{DA}= 10%; and
(b) Specimen deformation at state 1 (γ= 5%)

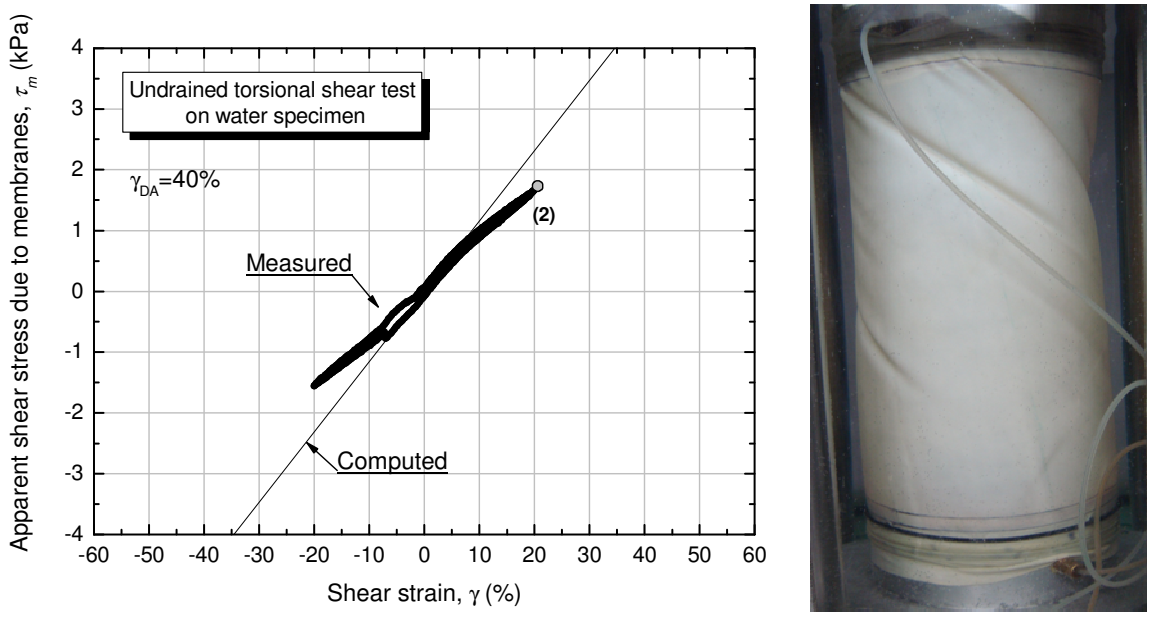

(a) (b)

Fig. 4.38: (a) Relationships between γ - τ_m on the range of γ_{DA}= 40%; and (b) Specimen deformation at state 2 (γ = 20%)

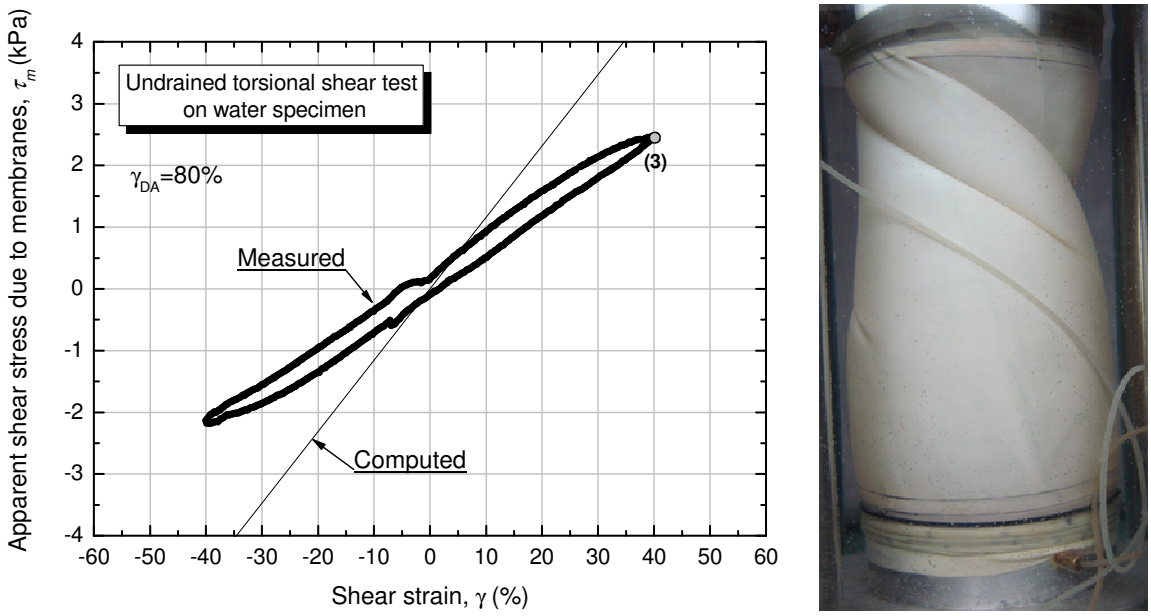

(a) (b)

Fig. 4.39: (a) Relationships between γ - τ_m on the range of γ_{DA}= 80%; and (b) Specimen deformation at state 3 (γ = 40%)

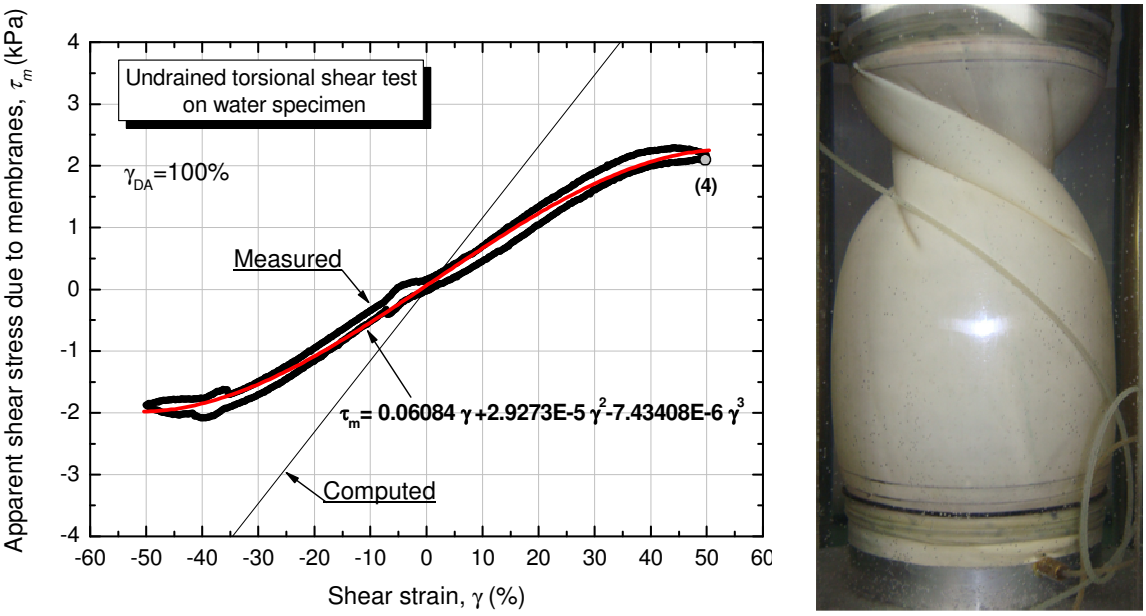

(a) (b)

Fig. 4.40: (a) Relationships between γ - τ_m on the range of γ_{DA}= 100%; and (b) Specimen deformation at state 4 (γ = 50%)

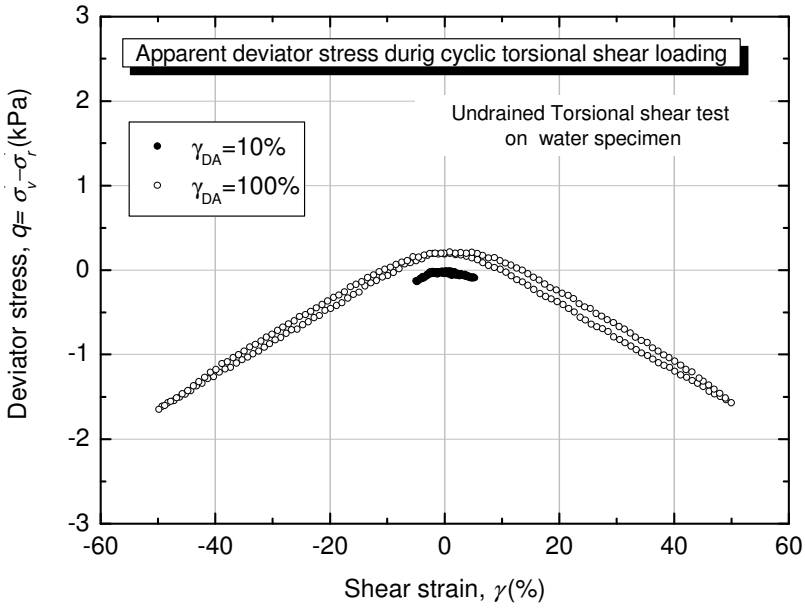

Fig. 4.41: Apparent deviator stress during undrained cyclic torsional shear loading on water specimen

(a) Water specimen performed for calibrating the membrane force

(a-1) γ = 20% (a-2) γ = 30% (a-3) γ = 40% (a-4) γ = 50%

(b) Sandy specimen subjected to reversal loading in the Test 3 (16-10)

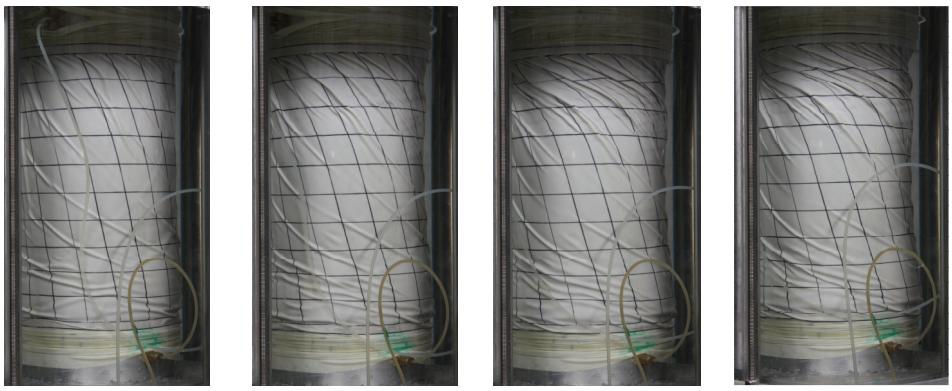

(b-1) γ = 22% (b-2) γ = 31% (b-3) γ = 45% (b-4) γ = 54%

(c) Sandy specimen subjected to intermediate loading in the Test 5 (16-16)

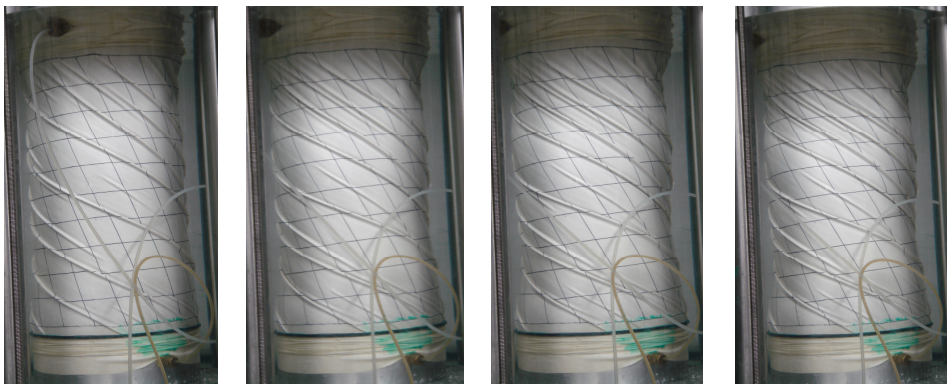

(c-1) γ = 23% (c-2) γ = 32% (c-3) γ = 39% (c-4) γ = 55%

(d) Sandy specimen subjected to non-reversal loading in the Test 7 (16-20)

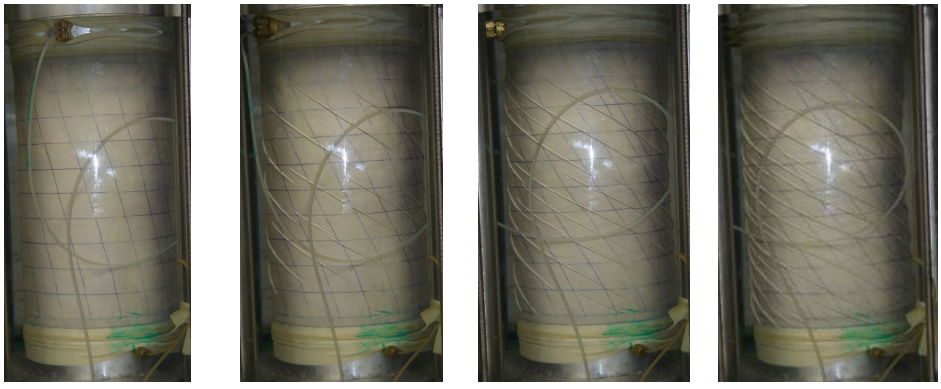

(d-1) γ = 20% (d-2) γ = 30% (d-3) γ = 40% (d-4) γ = 50%

Fig. 4.42: Comparison of the obtained torsional deformation of water and soil specimens

4.9 Summary

In order to investigate the effects of initial shear stress on the large deformation properties of loose sand, a series of undrained cyclic torsional shear tests were performed on saturated Toyoura sand specimens up to single amplitude of shear strain of about 50 % under various combinations of static and subsequent cyclic shear stresses. The following conclusion can be drawn from the above study:

(i) Depending on the relative magnitude of initial static shear and the cyclic shear stresses, the cyclic loading paths could be classified into three groups: stress reversal, intermediate and non-reversal. To better define the degree of reversal (R^*) a new formulation was also proposed.

(ii) From the study of failure mechanisms, based on the difference in the effective stress path and the modes of development of shear strain during both monotonic and cyclic undrained torsional shear loading, the observed types of failure could be distinguished into three types: cyclic liquefaction (LQ), rapid flow liquefaction (RF) and residual deformation (RD) failures.

In case of stress reversal and intermediate loadings, failure was associated with full liquefaction, followed by extremely large deformation in the post-liquefaction process. On the other hand, in the case of non-reversal loading, it was found that residual deformation brought the specimen to failure (i.e., formation of spiral shear band) although liquefaction did not occur.

(iii) The test results show that the presence of initial static shear does not always lead to an increase in the resistance to liquefaction and strain accumulation; in fact, both can either increase or decrease by increasing the static shear depending on the magnitude of the combined shear stress, the type of loading and the failure behavior.

It should be noted that, by the current study, for the fist time the effects of initial static shear on the resistance of sand against cyclic shear accumulation of 50% could be investigated and described.

(iv) The mechanisms of residual strain development clearly depend on the failure

behavior of sands.

In the case of LQ failure, full liquefaction state (*p'=0*) was achieved after applying several cycles of loading followed by a sudden development of residual deformation.

In this case of RF failure, during the first cycle, full liquefaction and deformation of a few percent was achieved; in addition, in most of the tests, deformation exceeding 50% was reached in less than 10 cycles.

In the case of RD failure, extremely large deformation could be reached after applying a large number of cycles of loading, even in the case in which liquefaction did not take place.

(v) In this study, the deformation properties of Toyoura sands were investigated up to single amplitude shear strain exceeding 50 %. Non-uniform specimen deformations were observed at higher strain levels.

Even though three types of specimen deformation could be observed for reversal, intermediate and non-reversal loading conditions, the initiation of strain localization could not be clearly defined on the basis of visual observation.

To address this issue and evaluate the effects of initial static shear on the specimen deformation behavior, the deviator stress response and the change in stress-strain relationship during cyclic loading were investigated. It was confirmed that a drop in deviator stress implies that the stress-strain characteristics of the specimen were changed by the formation of shear band and the initiation of strain localization in the specimen. However, in several cases, the change in the deviator stress amplitude could not be easily determined. Therefore, even if slightly over-estimated, the limiting value of residual strain to initiate the strain localization of the specimen (i.e., formation of shear band) was defined as the one which induced a change in strain accumulation γ^{B}_{RS}.

(vi) The limiting value of strain to initiate the strain localization of the specimen was measured in terms of half of the double amplitude ($\gamma_{DA}/2$), as used in previous studies, and residual shear strain (γ_{RS}) which in this study was used to describe the effects of initial static shear on the deformation behavior. On the basis of reversal loading tests results it was found that the greater is the initial static shear the lower $\gamma_{DA}/2$; on the other hand, γ_{RS} was rather constant whilst increasing the static shear stress level. These features suggested that to define the limiting value of strain to initiate the strain localization of the

specimen, γ_{RS} was much more appropriate than $\gamma_{DA}/2$.

(vii) By employing the relationship between the modified stress ratio $(\tau-\Delta\tau)/(p'+\Delta p')$ and the plastic shear strain γ^p, the peak stress states that were followed by strain softening were clearly observed in the case of reversal loading tests. The correspondent strain at peak stress state (γ^{peak}) can be considered as the state at which strain localization in the specimen (i.e., formation of shear band) begins.

In additions, it was observed that $\gamma^B_{L(RS)}$ corresponds well to the state at which strain softening ends and the residual stress state begins. These features imply that $\gamma^B_{L(RS)}$ is the state at which the shear band is fully developed in the specimen.

(viii) In torsional shear tests on hollow cylindrical specimens, due to the presence of inner and outer membranes, the effect of membrane force cannot be neglected. Furthermore, it becomes significantly important when shear strain reaches extremely high level.

In this study, by performing a special test on a water specimen which was cyclically sheared under undrained condition up to double amplitude shear strain (γ_{DA}) of 100%, it was observed that the deviation of the actual membrane deformation from the uniform one that is assumed in the theory became larger with an increase in the strain levels; for this reason, the measured shear stress was corrected for the effect of membrane force by employing a polynomial approximation of the measured relationship between shear strain (γ) and the apparent shear stress (τ_m).

In order to confirm the validity of the membrane force obtained experimentally, the torsional deformation of the water specimen was compared with the deformation of sandy specimens subjected to reversal, intermediate and non-reversal loading. The torsional deformation of the water specimen appeared to be suitable with the one observed for the sandy specimens up to a strain of about 30%.

4.10 References

1. Castro, G. (1975): "Liquefaction and cyclic mobility of saturated sand", Journal of Geotechnical Engineering Division, ASCE, 101 (GT6), 551-569
2. Castro, G. and Poulus, S. J. (1977): "Factors affecting liquefaction and cyclic mobility", Journal of Geotechnical Engineering Division, ASCE, 103 (GT6), 501-516
3. Chiaro, G., Kiyota, T., De Silva, L.I.N., Sato, T., and Koseki, J. (2009): "Extremely large post-liquefaction deformations of saturated sand under cyclic torsional shear loading", Proc. of Earthquake Geotechnical Engineering Satellite Conference, 17th International Conference on Soil Mechanics and Geotechnical Engineering, Alexandria, Egypt
4. Hong Nam, N. (2004): "Locally measured quasi-elastic properties of Toyoura sand in cyclic triaxial and torsional loadings", Ph.D. thesis, Dep. of Civil Engineering, University of Tokyo, Japan
5. Hyodo, M., Murata, H., Yasufuku, N. and Fujii, T. (1991): "Undrained cyclic shear strength and residual shear strain of saturated sand by cyclic triaxial tests", Soils and Foundations, 31 (3), 60-76
6. Hyodo, M., Tanimizu, H., Yasufuku, N. and Murata, H. (1994): "Undrained cyclic and monotonic triaxial behavior of saturated loose sand", Soils and Foundations, 34 (1), 19-32
7. Kiyota, T. (2007); "Liquefaction strength and small strain properties of in-situ frozen and reconstituted sandy soils, PhD thesis, Dep. of Civil Engineering, University of Tokyo, Japan
8. Kiyota, T., Sato, T., Koseki, J., and Mohammad, A.M. (2008): "Behavior of liquefied sands under extremely large strain levels in cyclic torsional shear tests", Soils and Foundations, 48 (5), 727-739
9. Koseki, J., Kiyota, T., Sato, T. and Mohammad, A.M. (2007): "Undrained cyclic torsional shear tests on sand up to extremely large strain levels", International Workshop on Earthquake Hazard and Mitigation, Guwahati, India, 257-263
10. Koseki, J., Yoshida, T. and Sato, T. (2005): "Liquefaction properties of Toyoura sand in cyclic torsional shear tests under low confining stress", Soils and Foundations, 45 (5), 103-113
11. Kramer, S. L. (1996): "Geotechnical Earthquake Engineering", Prentice Hall, New Jersey

12. Tatsuoka, F., Muramatsu, M. and Sasaki, T. (1982): "Cyclic undrained stress-strain behavior of dense sand by torsional simple shear test", Soils and Foundations, 22 (2), 55-69

13. Tatsuoka, F., Sonoda, S., Hara, K., Fukushima, S. and Pradhan, T. B. S. (1986): "Failure and deformation of sand in torsional shear", Soils and Foundations, 26 (4), 79-97

14. Towhata. I. and Callage, C. P. K. (2003): "Rate-dependency of sand under low effective stress as observed in laboratory shear tests", Proc. 8th US-Japan Workshop on Earthquake Resistance Design of Lifeline Facilities and Countermeasures against Liquefaction, paper-II, Tokyo, 437-448

15. Vaid, Y. P. and Chern, J.C. (1983): "Effects of static shear on resistance to liquefaction", Soils and Foundations, 23 (1), 47-60

16. Vaid, Y. P. and Finn, W.D.L. (1979): "Static shear and liquefaction potential", Journal of Geotechnical Engineering Division, ASCE, 105 (GT10), 1233-1246

17. Yoshimi, Y. and Oh-oka, H. (1975): "Influence of degree of shear stress reversal on the liquefaction potential of saturated sand", Soils and Foundations, 15 (3), 27-40

CHAPTER 5

Modeling the effects of initial static shear on the undrained cyclic behavior of sand

5.1 Introduction

To simulate the behavior of saturated sand under undrained cyclic loading which leads to liquefaction and large cyclic shear strain development, an elasto-plastic constitutive model which can describe both monotonic and cyclic torsional shear behaviors of saturated sand under drained or undrained condition was developed at IIS (Institute of Industrial Science), University of Tokyo.

It is noteworthy that the motivation of the current study comes from the successful attempts as above described in simulating the liquefaction behavior of sand as well the cyclic large deformation behavior. However, no attempt has been made so far to model the undrained behavior of sand by considering the effect of static shear. Therefore, the objectives of the present study were set by aiming at modeling the cyclic undrained torsional shear behavior of saturated sand with initial static shear ultimately.

This chapter entails the attempt to modify the above mentioned model in order to simulate the undrained cyclic behavior of loose Toyoura sand with initial static shear subjected to undrained cyclic torsional shear loading.

Therefore, the original elasto-plastic model developed at IIS and the modifications made in the current study to take the effects of initial static shear into account are presented.

The satisfactory simulation results, in terms of effective stress path and stress-strain relationship, are presented in this chapter and compared with the experimental observations. Resistance against liquefaction and shear strain accumulation, failure behaviors and the mode of development of residual shear strain during cyclic loading obtained by simulation are also shown.

5.2 Modeling of quasi-elastic deformation properties using IIS Model (Hong Nam, 2004)

Modeling of irreversible stress-strain relationships and stress-dilatancy properties of soils demands accurate modeling of elastic strain components as well. In fact, irreversible strain components can be evaluated by subtracting the elastic strain components from the total one.

Recently, Hong Nam (2004) proposed a new hypo-elastic model called "IIS model" to simulate the inherent and stress induced anisotropies of sand with rotation of the principal stress directions. On the basis of empirical rules on quasi-elastic deformation properties and coordinate transformation, this model is capable of taking into account the damage to quasi-elastic deformation properties at higher stress ratios as well. The elements of the compliance matrix were experimentally evaluated by employing local deformation measurements in hollow cylindrical Toyoura sand specimens and compared with the model predictions.

5.2.1 Basic formulation

The elastic response of soil is stress-path dependent (i.e., hypo-elastic behavior), therefore it can be modeled by applying Hooke's law of elasticity.

When working with a three-dimensional stress state, a 4th order tensor M_{ijkl} containing 81 elastic coefficients must be defined to link the stress increment tensor $d\sigma'_{kl}$ with the engineering strain increment tensor $d\varepsilon^{e}_{ij}$ as expressed in Eq. (5.1):

$$d\varepsilon^{e}_{ij} = M_{ijkl}\ d\sigma'_{kl} \tag{5.1}$$

Both stress and strain increment tensors can be represented by a second order (3×3) matrix as shown below. *i* and *j* stand for axial, radial and circumferential axes (z, r and θ, respectively). These axes are referred to as material axes in the IIS model.

$$d\sigma'_{ij} = \begin{Bmatrix} d\sigma'_{zz} & d\sigma'_{zr} & d\sigma'_{z\theta} \\ d\sigma'_{rz} & d\sigma'_{rr} & d\sigma'_{r\theta} \\ d\sigma'_{\theta z} & d\sigma'_{\theta r} & d\sigma'_{\theta\theta} \end{Bmatrix} = \begin{Bmatrix} d\sigma'_{z} & d\tau_{zr} & d\tau_{z\theta} \\ d\tau_{rz} & d\sigma'_{r} & d\tau_{r\theta} \\ d\tau_{\theta z} & d\tau_{\theta r} & d\sigma'_{\theta} \end{Bmatrix} \tag{5.2}$$

$$d\varepsilon_{ij}^{e} = \begin{Bmatrix} d\varepsilon_{zz}^{e} & d\varepsilon_{zr}^{e} & d\varepsilon_{z\theta}^{e} \\ d\varepsilon_{rz}^{e} & d\varepsilon_{rr}^{e} & d\varepsilon_{r\theta}^{e} \\ d\varepsilon_{\theta z}^{e} & d\varepsilon_{\theta r}^{e} & d\varepsilon_{\theta\theta}^{e} \end{Bmatrix} = \begin{Bmatrix} d\varepsilon_{z}^{e} & d\gamma_{zr}^{e} & d\gamma_{z\theta}^{e} \\ d\gamma_{rz}^{e} & d\varepsilon_{r}^{e} & d\gamma_{r\theta}^{e} \\ d\gamma_{\theta z}^{e} & d\gamma_{\theta r}^{e} & d\varepsilon_{\theta}^{e} \end{Bmatrix} \tag{5.3}$$

Stress symmetry ($M_{ijkl} = M_{jikl}$) and strain symmetry ($M_{ijkl} = M_{ijlk}$) reduce the number of elastic coefficients to 36, which can be represented by a (6×6) matrix. In addition, it reduces the number of stress and strain parameters to 6 each, which can be represented by (6×1) matrices, as shown in Eq. (5.4):

$$\begin{Bmatrix} d\varepsilon_{z}^{e} \\ d\varepsilon_{r}^{e} \\ d\varepsilon_{\theta}^{e} \\ d\gamma_{zr}^{e} \\ d\gamma_{r\theta}^{e} \\ d\gamma_{\theta z}^{e} \end{Bmatrix} = \begin{bmatrix} M_{11} & M_{12} & M_{13} & M_{14} & M_{15} & M_{16} \\ M_{21} & M_{22} & M_{23} & M_{24} & M_{25} & M_{26} \\ M_{31} & M_{32} & M_{33} & M_{34} & M_{35} & M_{36} \\ M_{41} & M_{42} & M_{43} & M_{44} & M_{45} & M_{46} \\ M_{51} & M_{52} & M_{53} & M_{54} & M_{55} & M_{56} \\ M_{61} & M_{62} & M_{63} & M_{64} & M_{65} & M_{66} \end{bmatrix} \begin{Bmatrix} d\sigma_{z}' \\ d\sigma_{r}' \\ d\sigma_{\theta}' \\ d\tau_{zr} \\ d\tau_{r\theta} \\ d\tau_{\theta z} \end{Bmatrix} \tag{5.4}$$

In short, Eq. (5.4) can be written as

$$\{d\varepsilon\}^{e} = [M]\{d\sigma'\} \tag{5.5}$$

Before the material is subjected to rotation of the principal stress directions (i.e., isotropic stress state), material axes (z, r, θ) coincides with the principal stress axes (ξ, ρ, η). After the rotation of the principal stress directions took place (refer to Fig. 5.1), Hooke's law can be applied to the stress-strain relationship in principal stress axes as follows:

$$\{\overline{d\varepsilon}\}^{e} = [\overline{M}]\{\overline{d\sigma'}\} \tag{5.6}$$

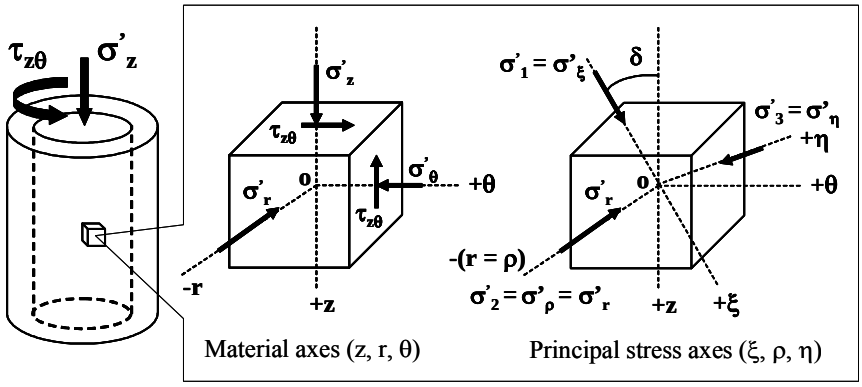

Fig. 5.1: Coordinate systems in IIS model (HongNam, 2004)

Transformations of effective stress and elastic strain increment tensors can be written in the matrix form as follows:

$$\left\{\overline{d\sigma'}\right\}=[T_\sigma]\left\{d\sigma'\right\} \tag{5.7}$$

$$\left\{\overline{d\varepsilon}\right\}^e=[T_\sigma]\left\{d\varepsilon\right\}^e \tag{5.8}$$

where the transformation matrix $[T_\sigma]$ is

$$[T_\sigma]=\begin{bmatrix} \cos^2\delta & 0 & \sin^2\delta & 0 & 0 & \sin 2\delta \\ 0 & 1 & 0 & 0 & 0 & 0 \\ \sin^2\delta & 0 & \cos^2\delta & 0 & 0 & -\sin 2\delta \\ 0 & 0 & 0 & \cos\delta & \sin\delta & 0 \\ 0 & 0 & 0 & -\sin\delta & \cos\delta & 0 \\ -\dfrac{\sin 2\delta}{2} & 0 & \dfrac{\sin 2\delta}{2} & 0 & 0 & \cos 2\delta \end{bmatrix} \tag{5.9}$$

in which the rotation angle of principal stress axis δ can be evaluated as

$$\delta=(1/2)\ \arctan[2\tau_{z\theta}/(\sigma'_z-\sigma'_\theta)] \tag{5.10}$$

It is assumed that the transformation matrices for stress and strain increments are the same. In addition, it should be noted that, the transformation matrix has the following property: $[T_\sigma]^{-1}=[T_\sigma]^T$.

By substituting Eq. (5.5) and Eq. (5.6) into Eq. (5.8), the following expression is obtained

$$\left[\overline{M}\right]\left\{\overline{d\sigma'}\right\}=[T_\sigma]\left[M\right]\left\{d\sigma'\right\} \tag{5.11}$$

Then, replacing Eq. (5.7) into Eq. (5.11) yields

$$\left[\overline{M}\right][T_\sigma]\left\{d\sigma'\right\}=[T_\sigma]\left[M\right]\left\{d\sigma'\right\} \tag{5.12}$$

Finally, canceling out $\left\{d\sigma'\right\}$ in Eq. (5.12) the following equation is obtained

$$\left[M\right]=[T_\sigma]^T\left[\overline{M}\right][T_\sigma] \tag{5.13}$$

$[\overline{M}]$ is the compliance matrix of the principal stress axes, which can be obtained using the cross anisotropic hypo-elastic model proposed by Tatsuoka et al., (1999):

$$\left[\overline{M}\right]=\begin{bmatrix} \frac{1}{E_\xi} & \frac{-\nu_{\rho\xi}}{E_\rho} & \frac{-\nu_{\eta\xi}}{E_\eta} & 0 & 0 & -\frac{\alpha_{1o}}{E_{zo}} \\ \frac{-\nu_{\xi\rho}}{E_\xi} & \frac{1}{E_\rho} & \frac{-\nu_{\eta\rho}}{E_\eta} & 0 & 0 & -\frac{\alpha_{2o}}{E_{zo}} \\ \frac{-\nu_{\xi\eta}}{E_\xi} & \frac{-\nu_{\rho\eta}}{E_\rho} & \frac{1}{E_\eta} & 0 & 0 & -\frac{\alpha_{3o}}{E_{zo}} \\ 0 & 0 & 0 & \frac{1}{G_{\xi\rho}} & 0 & 0 \\ 0 & 0 & 0 & 0 & \frac{1}{G_{\rho\eta}} & 0 \\ -\frac{\alpha_{1o}}{E_{zo}} & -\frac{\alpha_{2o}}{E_{zo}} & -\frac{\alpha_{3o}}{E_{zo}} & 0 & 0 & \frac{1}{G_{\eta\xi}} \end{bmatrix} \tag{5.14}$$

Young's modulus E_i, shear modulus G_{ij} and Poisson's ratio ν_{ij} can be evaluated by employing the following empirical rules (i and j stand for ξ, ρ, η):

$$E_i = \frac{f(e)}{f(e_o)}\frac{E_{io}}{\sigma'^{\,m}_{o}}\sigma'^{\,m}_{i}\,(1-C_E k_n^2) \tag{5.15}$$

$$G_{ij} = \frac{f(e)}{f(e_o)}\frac{G_{ijo}}{\sigma'^{\,n}_{o}}(\sigma'_i\,\sigma'_j)^{n/2}(1-C_G k_n^2) \tag{5.16}$$

$$\nu_{ij} = \nu_{ijo}\left(\sigma'_i/\sigma'_j\right)^k \tag{5.17}$$

where

- e = current void ratio;
- $f(e)= (2.17 - e)^2/(1+ e)$, void ratio function (Hardin and Richart, 1963);
- m, n, k = material parameters to model stress induced anisotropy;
- σ'_i = effective principal stresses in ξ, ρ, η directions;
- σ'_o = reference effective stress.
- Effect of damage on the soil structure during the shearing is taken into account by using the factor k_n, and the two correction factors C_E and C_G for the degradation of Young's and shear moduli, respectively. C_E and C_G are determined by fitting the Eq. (5.15) and Eq. (5.16) to experimental data for Young's and shear moduli, respectively;
- $k_n=(\sigma'_1/\sigma'_3 -1)/[(\sigma'_1/\sigma'_3)_{max} -1]$, as proposed by Yu and Richart (1984);
- $(\sigma'_1/\sigma'_3)_{max}$ = principal stress ratio at failure (i.e., peak principal stress ratio).

In Eq. (5.14), α_{1o}, α_{2o} and α_{3o} denote the three coupling coefficients for the effect of loading. E_{io}, G_{ijo}, ν_{ijo} and these three coupling coefficients can be formulated by applying Eq. (5.13) at the initial isotropic stress state as described below.

At the isotropic stress state, the material is assumed to be cross-anisotropic in the material axes (z, r, θ) where z being the symmetrical axis and (r, θ) being the plane of isotropy. Stress-strain incremental relationship in these axes can be expressed by the following equation (the subscript 'o' stands for the isotropic reference state):

$$[d\varepsilon^e_{zo}\ d\varepsilon^e_{ro}\ d\varepsilon^e_{\theta o}\ d\gamma^e_{zro}\ d\gamma^e_{r\theta o}\ d\gamma^e_{\theta zo}]^T = [M_o][d\sigma'_{zo}\ d\sigma'_{ro}\ d\sigma'_{\theta o}\ d\tau_{zro}\ d\tau_{r\theta o}\ d\tau_{\theta zo}]^T \qquad (5.18)$$

where

$$[M_o]=\begin{bmatrix} \frac{1}{E_{zo}} & \frac{-\nu_{z\theta o}}{E_{zo}} & \frac{-\nu_{z\theta o}}{E_{zo}} & 0 & 0 & 0 \\ \frac{-\nu_{z\theta o}}{E_{zo}} & \frac{1}{E_{\theta o}} & \frac{-\nu_{\theta ro}}{E_{\theta o}} & 0 & 0 & 0 \\ \frac{-\nu_{z\theta o}}{E_{zo}} & \frac{-\nu_{\theta ro}}{E_{\theta o}} & \frac{1}{E_{\theta o}} & 0 & 0 & 0 \\ 0 & 0 & 0 & \frac{1}{G_{z\theta o}} & 0 & 0 \\ 0 & 0 & 0 & 0 & \frac{2(1+\nu_{\theta ro})}{E_{\theta o}} & 0 \\ 0 & 0 & 0 & 0 & 0 & \frac{1}{G_{z\theta o}} \end{bmatrix} \qquad (5.19)$$

in which

$$\begin{aligned} \nu_{\theta ro} &= \nu_o \\ E_{zo} &= aE_{\theta o} = aE_o \end{aligned} \qquad (5.20)$$

In Eq. (5.20), the parameter 'a' represents the inherent anisotropy of the material.

Stress-strain incremental relationship written in the principal stress axes (ξ, ρ, η; $\rho \equiv r$ and ξ axis making a δ angle relative to z axis) is shown below:

$$[d\varepsilon^e_{\xi o}\ d\varepsilon^e_{\rho o}\ d\varepsilon^e_{\eta o}\ d\gamma^e_{\xi\rho o}\ d\gamma^e_{\rho\eta o}\ d\gamma^e_{\eta\xi o}]^T = [\overline{M_o}][d\sigma'_{\xi o}\ d\sigma'_{\rho o}\ d\sigma'_{\eta o}\ d\tau_{\xi\rho o}\ d\tau_{\rho\eta o}\ d\tau_{\eta\xi o}]^T \qquad (5.21)$$

where

$$\left[\overline{M_o}\right]=\begin{bmatrix} \frac{1}{E_{\xi o}} & \frac{-\nu_{\rho\xi o}}{E_{\rho o}} & \frac{-\nu_{\eta\xi o}}{E_{\eta o}} & 0 & 0 & -\frac{\alpha_{1o}}{E_{zo}} \\ \frac{-\nu_{\xi\rho o}}{E_{\xi o}} & \frac{1}{E_{\rho o}} & \frac{-\nu_{\eta\rho o}}{E_{\eta o}} & 0 & 0 & -\frac{\alpha_{2o}}{E_{zo}} \\ \frac{-\nu_{\xi\eta o}}{E_{\xi o}} & \frac{-\nu_{\rho\eta o}}{E_{\rho o}} & \frac{1}{E_{\eta o}} & 0 & 0 & -\frac{\alpha_{3o}}{E_{zo}} \\ 0 & 0 & 0 & \frac{1}{G_{\xi\rho o}} & 0 & 0 \\ 0 & 0 & 0 & 0 & \frac{1}{G_{\rho\eta o}} & 0 \\ -\frac{\alpha_{1o}}{E_{zo}} & -\frac{\alpha_{2o}}{E_{zo}} & -\frac{\alpha_{3o}}{E_{zo}} & 0 & 0 & \frac{1}{G_{\eta\xi o}} \end{bmatrix} \tag{5.22}$$

Coefficients of $[\overline{M_o}]$ can be evaluated by transforming stress and strain incremental tensors using Eq. (5.13) as shown below

$$[\overline{M_o}] = [T_\sigma]^{-T}[M_o][T_\sigma]^{-1} \tag{5.23}$$

In order to evaluate all the coefficients of $[\overline{M_o}]$, it is necessary to experimentally determine all the elements in $[M_o]$. However, due to technical difficulties in accurately measuring $E_{\theta o}$ and $\nu_{\theta ro}$ in the hollow cylindrical specimen, two assumptions proposed by Tatsuoka et al. (1999) were used as depicted below:

$$\begin{aligned} &\nu_{z\theta o} = \sqrt{a}\ \nu_o \\ &\nu_{\xi\eta o}(at\ \delta = 45^o) = \nu_o \end{aligned} \tag{5.24}$$

Therefore, from Eq. (5.23), it can be evaluated

$$G_{z\theta o} = \frac{E_{zo}(\sqrt{a} - \nu_{z\theta o})}{(\sqrt{a} + \nu_{z\theta o})(1 + a - 2\nu_{z\theta o})} \tag{5.25}$$

As a result, five independent parameters E_{zo}, $\nu_{z\theta o}$, $G_{z\theta o,}$ $E_{\theta o}$ and $\nu_{\theta ro}$ in $[M_o]$ can be reduced to three independent parameters, namely a, E_o and ν_o, which can be determined from the measured values of E_{zo}, $\nu_{z\theta o}$ and $G_{z\theta,}$ at isotropic stress state by using Eq. (5.25), Eq. (5.20) and Eq. (5.24), respectively. In short, IIS model includes nine material parameters, namely, E_o, ν_o, a, m, n, k, C_E, C_G and $(\sigma'_1/\sigma'_3)_{\max}$.

Flow chart of calculation in IIS model

1. Determine E_{zo}, $\nu_{z\theta o}$, $G_{z\theta o}$, m, n, k, C_E, C_G and $(\sigma'_1/\sigma'_3)_{max}$ experimentally and calculate a, E_o and v_o using Eq. (5.25), (5.20) and (5.24), respectively;
2. Evaluate the coefficients of $[M_o]$ and calculate the elements of $[\overline{M_o}]$ using Eq. (5.23);
3. Determine the elements in $[\overline{M}]$ using the Eq. (5.15), Eq. (5.16) and Eq. (5.17);
4. Finally, determine the elements in [M] using Eq. (5.13), which are hypo-elastic deformation properties of the geomaterial in the material axes (z , r , θ) (e.g., M_{11} = $1/E_z$, $M_{66} = 1/G_{z\theta}$, $\nu_{z\theta} = M_{31}/M_{11}$, $\nu_{zr} = M_{21}/M_{11}$).

5.2.2 Evaluation of elastic strain components using IIS model

After the compliance matrix in the material axes [M] is fully determined, elastic strain increment components ($d\varepsilon_z^e, d\varepsilon_r^e, d\varepsilon_\theta^e, d\gamma_{z\theta}^e$) can be evaluated by using Eq. (5.4) as follows:

$$d\varepsilon_z^e = M_{11}d\sigma_z^{'} + M_{12}d\sigma_r^{'} + M_{13}d\sigma_\theta^{'} + M_{14}d\tau_{zr} + M_{15}d\tau_{r\theta} + M_{16}d\tau_{z\theta} \quad (5.26)$$

$$d\varepsilon_r^e = M_{21}d\sigma_z^{'} + M_{22}d\sigma_r^{'} + M_{23}d\sigma_\theta^{'} + M_{24}d\tau_{zr} + M_{25}d\tau_{r\theta} + M_{26}d\tau_{z\theta} \quad (5.27)$$

$$d\varepsilon_\theta^e = M_{31}d\sigma_z^{'} + M_{32}d\sigma_r^{'} + M_{33}d\sigma_\theta^{'} + M_{34}d\tau_{zr} + M_{35}d\tau_{r\theta} + M_{36}d\tau_{z\theta} \quad (5.28)$$

$$d\gamma_{z\theta}^e = M_{61}d\sigma_z^{'} + M_{62}d\sigma_r^{'} + M_{63}d\sigma_\theta^{'} + M_{64}d\tau_{zr} + M_{65}d\tau_{r\theta} + M_{66}d\tau_{z\theta} \quad (5.29)$$

If axial, radial and circumferential stresses (σ'_z, σ'_r, σ'_θ,) are kept constant during torsional shear loading (i.e., isotropic torsional shear, ITS), only $\tau_{z\theta}$ is varying. Therefore, in such a case Eq. (5.26), Eq. (5.27), Eq. (5.28) and Eq. (5.29) can be simplified as follows:

$$d\varepsilon_z^e = M_{16} d\tau_{z\theta} \tag{5.30}$$

$$d\varepsilon_r^e = M_{26} d\tau_{z\theta} \tag{5.31}$$

$$d\varepsilon_\theta^e = M_{36} d\tau_{z\theta} \tag{5.32}$$

$$d\gamma_{z\theta}^e = M_{66} d\tau_{z\theta} \tag{5.33}$$

Consequently, total elastic strain components can be evaluated by numerically integrating the above equations. Then, the total elastic volumetric strain can be obtained as follows:

$$\varepsilon_{vol}^e = \varepsilon_z^e + \varepsilon_r^e + \varepsilon_\theta^e \tag{5.34}$$

Finally, the irreversible strain components are evaluated by subtracting the elastic strain components from total strains. Note that, the time effects are not considered in the current study. Therefore, plastic strain components are taken as equal to the irreversible strain components.

5.2.3 Selection of quasi-elastic parameters for IIS model

For both drained and undrained loading conditions, the IIS model parameters for evaluating γ^e were selected as shown below:

E_{zo} = 174 MPa at σ'_o = 100 kPa for Toyoura sand specimen with Dr = 50.4%, $\nu_{z\theta o}$= 0.18, a = 0.7, m = 0.520, n = 0.508, k = 0.3, $C_E = C_G = 0$ (assuming no damage to elastic properties). It should be noted that, E_{zo} for sand specimens with different densities can be evaluated by assuming that the value of $E_{zo}/f(e)$ at the same stress level is similar among different densities.

5.3 Modeling the stress-strain relationship of sand under cyclic torsional shear

Soils are frequently subjected to large cyclic loadings due to traffic loads, sea waves, earthquakes, excavations and fillings, and subsequent construction of civil engineering structures. Therefore, in order to design economical structures with adequate safety and to analyze the performance of the existing structures that might be subjected to the loading conditions as described above, it is necessary to reasonably predict the behavior of soils under the cyclic loading conditions.

5.3.1 Modeling of skeleton curve

It is well known that the stress-strain relationship of soil subjected to drained or undrained loading conditions is highly nonlinear; yet, it can be represented by a form of a hyperbola as shown in the generalized form in Eq. (5.35)

$$Y = \frac{X}{\frac{1}{C_1} + \frac{X}{C_2}} \tag{5.35}$$

where, Y and X are normalized stress and strain parameters, respectively:

Y = Stress parameter/Maximum value of stress parameter

X = Strain parameter/Reference strain

and

Reference strain = Maximum value of stress parameter/Initial elastic stiffness

The stress and strain parameters are selected depending on the type of loading such as plane strain, triaxial or torsional shear.

C_1 and C_2 are coefficients of correlation. C_1 is the value of Y at $X = 0$, and C_2 is the value of Y at $X = \infty$. They have the following physical meaning:

C_1 = Initial stiffness/Initial elastic stiffness

C_2 = Normalized peak strength (= 1.0)

In order to obtain a better degree of fitting with the experimental data under the framework of the hyperbolic equation as shown in Eq. (5.35), various models are made

available by assuming different values for C_1 and C_2 to model the stress-strain relationships for wide range of strain as briefed below.

Original hyperbolic equation (C_1 and C_2 are constants)

The original hyperbolic equation assumes both C_1 and C_2 in Eq. (5.35) are constants throughout the loading and equal to 1.0. Therefore, only two parameters with clear physical meanings, namely initial stiffness and peak strength, which can be determined in a straight forward manner in the laboratory, are required for the modeling. Hyperbolic equations with constant values for C_1 and C_2 (not necessarily equal to 1.0) were employed by some researchers to model the stress-strain relationship of soil.

Kondner (1963) is widely regarded as the premier in using the hyperbolic equation to model the stress-strain relationship of soil, in which the behavior of clay under drained triaxial loadings were modeled by using a hyperbolic equation with constant values for C_1 and C_2. However, it was later found that the simulation using the original hyperbolic equation as proposed by Kondner is not in total agreement with the actual test data particularly at small strains.

Therefore, in order to obtain a better degree of fitting with the experimental data, models have been proposed with coefficients of correlation that are functions of the strain.

Generalized hyperbolic equation (GHE) (C_1 and C_2 are functions of strain)

Tatsuoka and Shibuya (1991) proposed a hyperbolic equation that has coefficients of correlation C_1 and C_2, which are functions of strain to simulate the stress-strain relations for a wide range of strain as shown in Eq. (5.36) , Eq. (5.37) and Eq. (5.38).

$$Y = \frac{X}{\frac{1}{C_1(X)} + \frac{X}{C_2(X)}} \tag{5.36}$$

$$C_1(X) = \frac{C_1(0) + C_1(\infty)}{2} + \frac{C_1(0) - C_1(\infty)}{2} \cos\left(\frac{\pi}{\left(\frac{\alpha'}{X}\right)^{m_t} + 1} \right) \tag{5.37}$$

$$C_2(X) = \frac{C_2(0) + C_2(\infty)}{2} + \frac{C_2(0) - C_2(\infty)}{2} \cos\left(\frac{\pi}{\left(\frac{\beta'}{X}\right)^{n_t} + 1} \right) \tag{5.38}$$

where, $C_1(0)$, $C_1(\infty)$, $C_2(0)$, $C_2(\infty)$, α' and β', m_t and n_t are parameters to be determined from a monotonic loading curve, which will be explained in section 5.3.2.

This equation is known as the Generalized Hyperbolic Equation (GHE). It has been verified that GHE can efefctively simulate the full stress-strain relationships of a wide range of geomaterials under different types of loadings.

5.3.1.1 Selection of GHE parameters

In the current study, normalized stress and strain parameters for modeling the stress-strain relationship of sand subjected to torsional shear loading are selected by following the procedure proposed by Hong Nam (2004):

- *Normalized drained backbone curve*

$$X = \frac{\gamma^p}{\gamma_{ref}} \tag{5.39}$$

$$Y = \frac{\tau}{\tau_{\max}} \tag{5.40}$$

$$\gamma_{ref} = \frac{\tau_{\max}}{G_{\max}} \tag{5.41}$$

in which

- $\gamma^e = \gamma - \gamma^p$, where γ^e and γ^p symbolizes the elastic and plastic strains, respectively. γ^e is evaluated by employing the IIS model (Hong Nam, 2004) as described in section 5.2. Note that the viscous effects such as creep and ageing are neglected in the current study;
- γ_{ref} = reference shear strain;
- τ_{max} and G_{max} = peak shear stress and initial shear modulus, respectively.

G_{max} value for loose specimen was set as 80 MPa while referring to the experimental results of De Silva (2008).

In the current study, specimens with relative densities of Dr = 50.6 % was subjected to monotonic drained torsional shear loading while preventing any vertical displacement of the top cap, in order to investigate the effects of initial static shear on the stress-strain relationship and compare it with the undrained stress-strain relationship.

The typical test results are presented in Fig. 5.2 and Fig. 5.3. A clear peak stress (τ_{max} = 77.5 kPa) can be observed in the stress-strain relationship shown in Fig. 5.2(a). It should be noted that, the change in effective mean principal stress (p') during the drained sharing, as shown in Fig. 5.2(b), can be associated with a change in vertical stress (σ_v') due to the torsional displacement applied on the specimen whilst the vertical strain was maintained constraint (i.e., ε_z = 0%). Fig. 5.2(c) shows the τ/p' vs. γ^p relationship. In addition, in Fig. 5.3 typical changes in volumetric strain, void ratio and relative density observed for loose sand during the shear loading are presented.

- *Normalized undrained backbone curve*

$$X = \frac{\gamma^p}{\gamma_{ref}} \tag{5.42}$$

$$Y = \frac{(\tau / p')}{(\tau / p')_{\max}} \tag{5.43}$$

$$\gamma_{z\theta r} = \frac{(\tau / p')_{\max}}{(G_0 / p'_0)} \tag{5.44}$$

in which

- $\gamma^e = \gamma - \gamma^p$, where γ^e and γ^p symbolizes the elastic and plastic strains, respectively. γ^e is evaluated by employing the IIS model (Hong Nam, 2004) as described in section 5.2. Note that the viscous effects such as creep and ageing are neglected in the current study;
- γ_{ref} = reference shear strain;
- p' = current effective mean principal stress;
- p'_0 = initial effective mean principal stress (=100 kPa);
- $(\tau / p')_{max}$ = peak shear stress in the plot τ / p' vs. γ^p
- G_0 = initial shear modulus; G_0 = 80 MPa was used in this study.

In the current study, a specimen with relative densities of Dr = 46.5 % was subjected to monotonic undrained torsional shear loading while preventing any vertical displacement of the top cap. The typical tests results are shown in Fig. 5.4, where a peak shear stress ratio $(\tau/p')_{max}$ = 0.65 could be observed. It should be noted that, the stress-strain relationship $(\tau\text{-}\gamma^p)$ shown in Fig. 5.4(a), became hyperbolic in shape once it was expressed in terms of $\tau/p'\text{-}\gamma$ relationship as shown in and Fig.5.4(c).

5.3.1.2 GHE model for stress-strain relationship in torsional shear tests

Since the stress-strain relationships during torsional shear loadings should be symmetrical in negative and positive shear (i.e., clockwise and anti-clockwise) directions, GHE parameters in one direction are enough to model the backbone curves in both negative and positive shear directions. Therefore, Eq. (5.36) can be rewritten as follows in order that it becomes an odd function.

$$Y = \frac{X}{\dfrac{1}{C_1(X)} + \dfrac{|X|}{C_2(X)}} \tag{5.45}$$

Where

$$C_1(X) = \frac{C_1(0)+C_1(\infty)}{2} + \frac{C_1(0)-C_1(\infty)}{2}\cos\left(\frac{\pi}{\left|\dfrac{\alpha'}{X}\right|^{m_t}+1}\right) \tag{5.46}$$

$$C_2(X) = \frac{C_2(0)+C_2(\infty)}{2} + \frac{C_2(0)-C_2(\infty)}{2}\cos\left(\frac{\pi}{\left|\dfrac{\beta'}{X}\right|^{n_t}+1}\right) \tag{5.47}$$

The procedure for evaluation of $C_1(0)$, $C_1(\infty)$, $C_2(0)$, $C_2(\infty)$, α' and β' for the plane strain compression (PSC) tests, proposed by Tatsuoka and Shibuya (1991b), is illustrated in Fig. 5.5. Note that in PSC test, it is assumed that $m_t = n_t = 1$.

$C_1(0)$ and $C_2(0)$ can be obtained by being fitted into the initial part of Y/X versus Y relationship, while $C_1(\infty)$ and $C_2(\infty)$ can be evaluated by being fitted into the end region of the Y/X versus Y relationship, as shown in Fig. 5.5.

$C_1(X=1)$ and $C_2(X=1)$ can be evaluated as shown in Fig. 5.5 by drawing a tangential

line to the intersection point of Y/X versus Y and $X=1$ relationships.

Then the two remaining parameters α' and β' can be determined by substituting the already evaluated $C_1(0)$, $C_1(\infty)$, $C_2(0)$, $C_2(\infty)$, $C_1(X=1)$ and $C_2(X=1)$ into the Eq. (5.46) and Eq. (5.47), respectively.

5.3.1.3 Simulation of two-phase (drained + undrained) backbone curve using GHE model

In this study, for each test both drained and undrained loading conditions were employed. In fact, a specific amount of initial static shear was achieved by applying monotonic drained torsional shear loading; subsequently, the cyclic behavior of sand with static shear was investigated under undrained loading conditions.

The above procedure was employed to evaluate the GHE parameters of the Toyoura sand specimen subjected to drained and undrained monotonic torsional shear loadings. Fig. 5.6 shows typical evaluation of GHE parameter for drained test 15 (D2).

In PSC test, it is assumed that $m_t = n_t = 1$. However, it was observed that in assuming $m_t = n_t = 1$, the simulation of torsional shear backbone curves does not match well with the experimental results. Therefore both of m_t and n_t values were determined to be as by trial and error in the current study.

In Fig. 5.7, it can be seen that the GHE model can efficiently simulate the stress-strain relationships of sand subjected to drained torsional shear loading up to the peak shear stress state, even in the case in which the vertical strain is constraint (i.e., $\varepsilon_z = 0\%$). It should be noted that, this drained test was performed in order to investigate the effects of initial static shear on the stress-strain relationship and compare it with the undrained stress-strain relationship.

In Fig. 5.8, comparison of normalized stress (Y) and strain (X) relationships for loose drained and undrained specimens is shown. The normalized backbone curves show a similar tendency at the initial stage of shearing and at the peak state; in-between these two states, the curves differ from each other and the undrained stress level is greater than the drained one. This behavior was confirmed by comparing these tests results with the results obtained by other tests, as shown in Fig. 5.9. This behavior cannot be attributed

totally to the change in density, as typically shown in Fig. 5.3, but it is probably due to the constraint of vertical strain. However, further investigations are necessary to clarify the latter considerations.

In Fig. 5.8, the close-up around the initial stage of shearing shows that the behavior of drained and undrained specimens is in agreement with each other. The range of stress shown in the close-up corresponds to the range of initial shear stress employed in this study (i.e., $\{(\tau_{static}/p'_0)/(\tau_{static}/p')_{max}\} < 0.35$ in all the tests).

In view of the latter observed behavior, in this study, it was attempted to model the entire two-phase monotonic loading curve (drained loading followed by undrained one), by employing the GHE parameters obtained for the undrained curve, in order to maintain the continuity of strain development during the change of loading from drained to undrained. The effect of drained shear loading was taken into consideration for describing the stress path (i.e., p' was assumed to be constant ($p'=p'_0$) during the drained shear loading) as explained later in this chapter.

The comparison between the experimental two-phase (drained + undrained) backbone curve obtained for the Test 4 (16-15) and its simulation using GHE model are shown in Fig. 5.10.

It can be seen that the a single set of GHE parameters obtained from undrained test can well simulate the two-phase backbone curve (drained + undrained) of sand subjected to torsional shear loading while preventing any vertical displacement of the top cap (i.e., $\varepsilon_z = 0\%$).

(a)

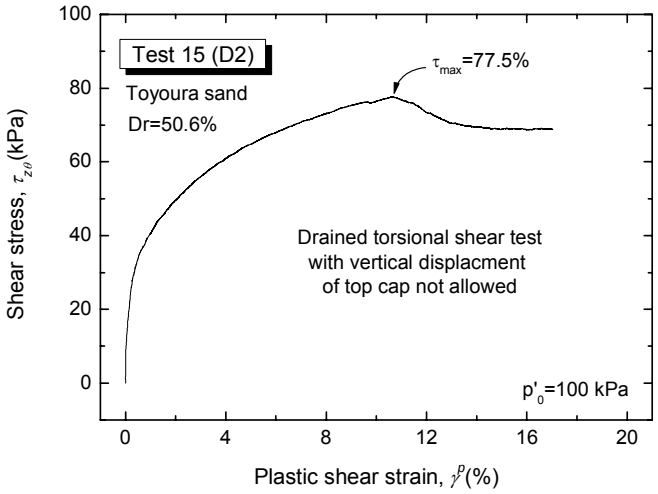

(b)

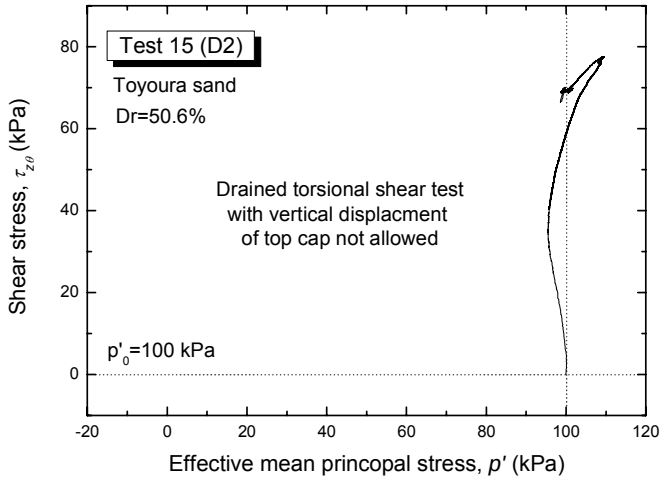

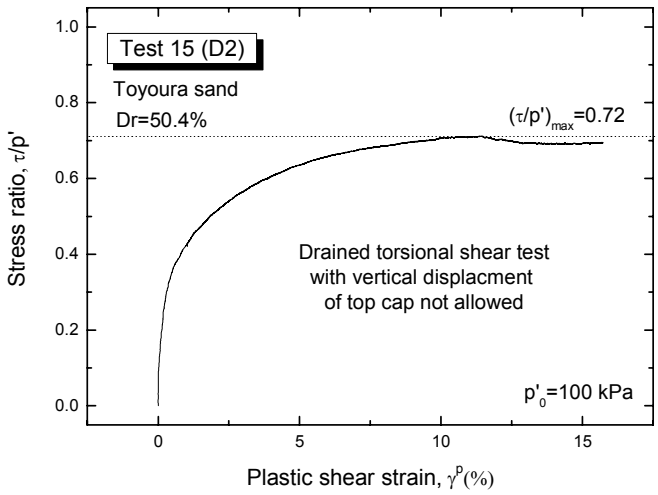

Fig. 5.2: Typical results of monotonic drained torsional shear test
in which the vertical displacement of top cap was not permitted:
(a) Stress-strain relationship; (b) Effective stress path; and (c) τ/p' vs. γ^p relationship

(a)

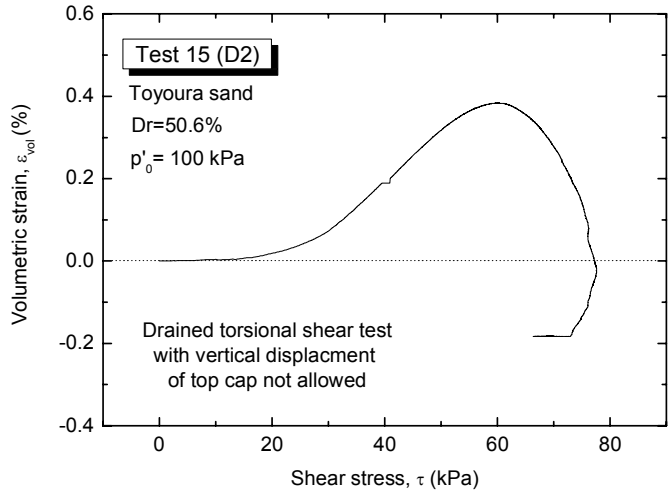

(b)

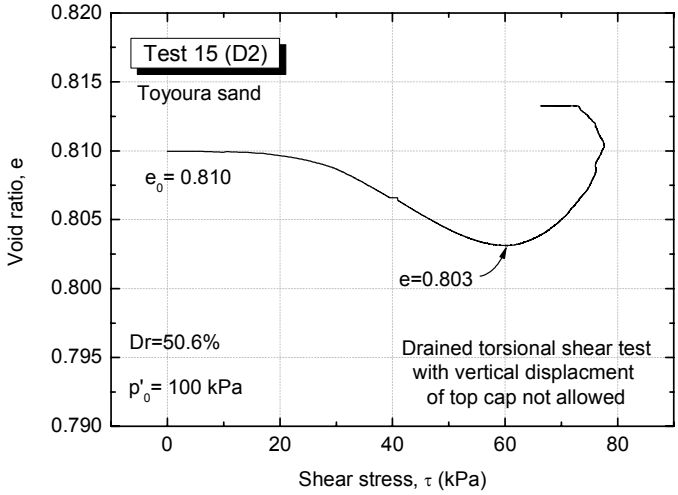

(c)

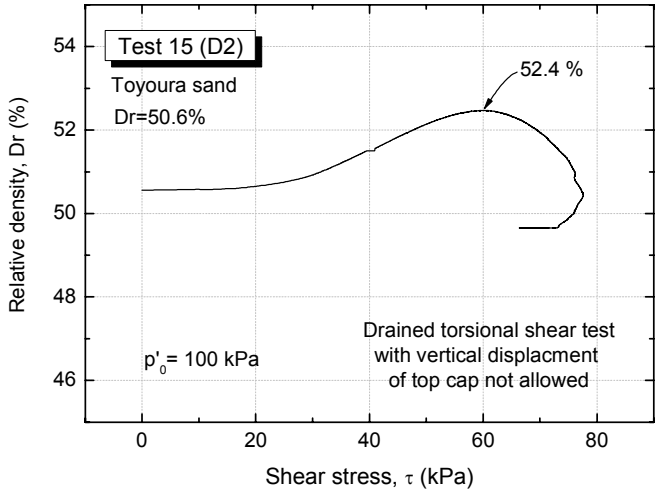

Fig. 5.3: Typical results of monotonic drained torsional shear test
in which the vertical displacement of top cap was not permitted:
(a) Volumetric strain change ; (b) Void ratio change; and (c) Relative density change

(a)

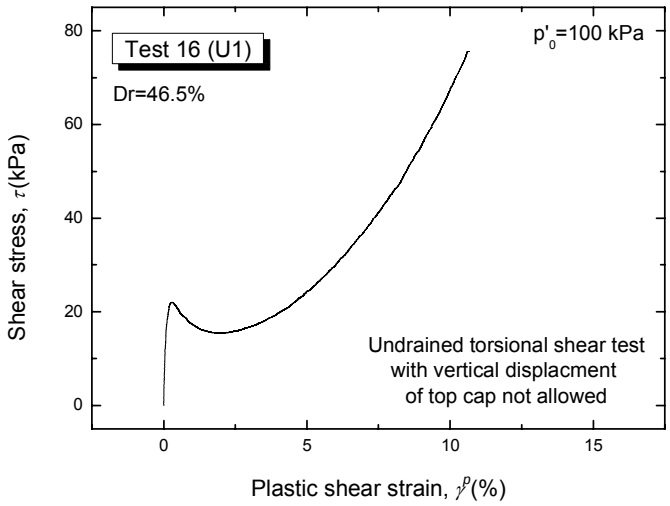

(b)

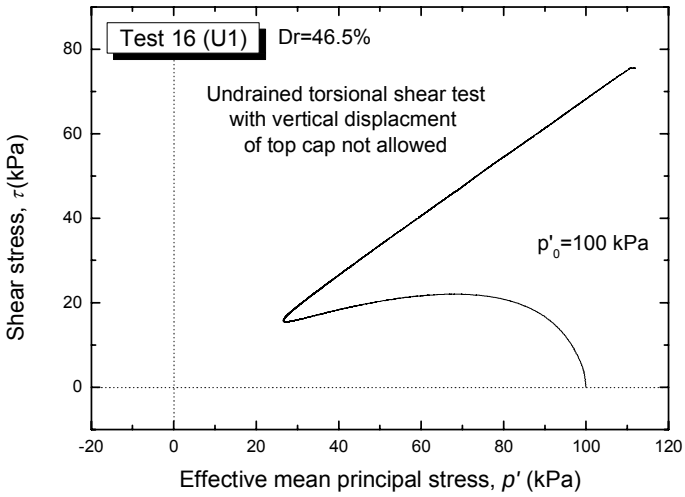

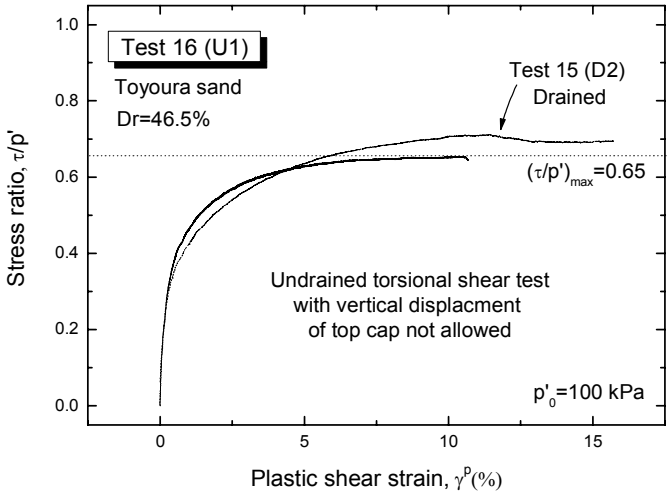

Fig. 5.4: Typical results of monotonic undrained torsional shear test
in which the vertical displacement of top cap was not permitted:
(a) Stress-strain relationship; (b) Effective stress path; and (c) τ/p' vs. γ^p relationship

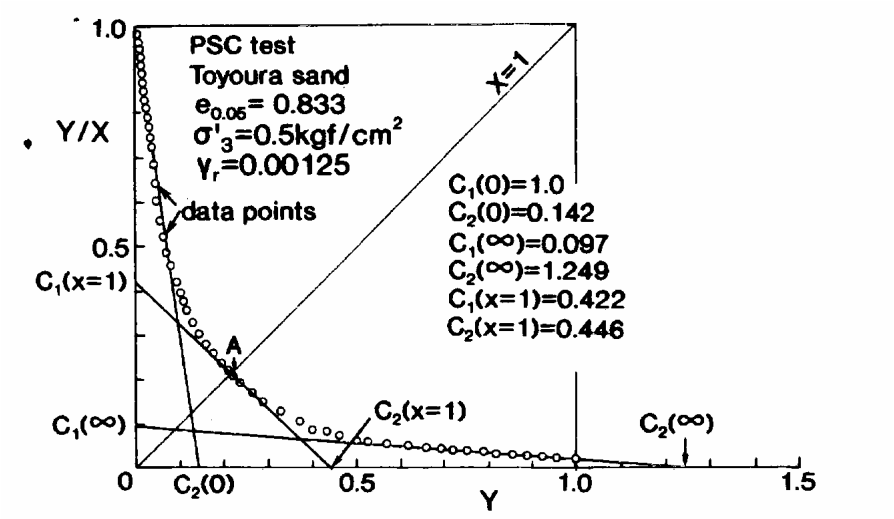

Fig. 5.5: Typical evaluation of the parameters $C_1(X)$ and $C_2(X)$ in the generalized hyperbolic equation (GHE) (Tatsuoka and Shibuya, 1991b)

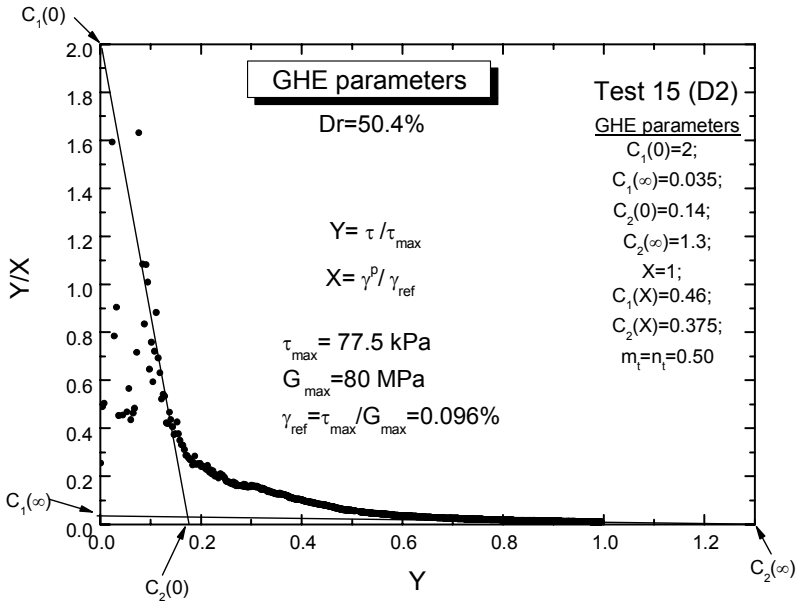

Fig. 5.6: Evaluation of the GHE parameters for Test 15 (D2)

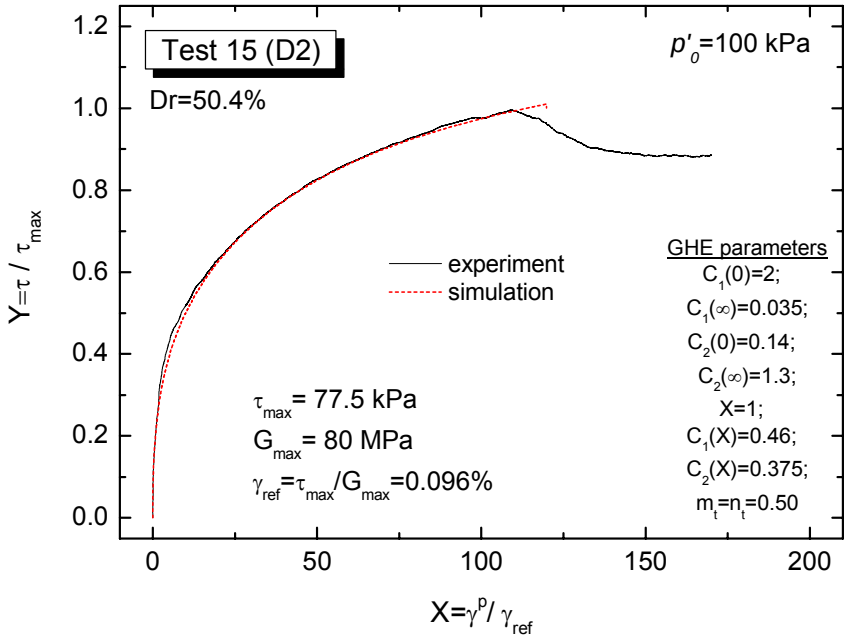

Fig. 5.7: Typical simulation of drained backbone curve for Test 15 (D2)

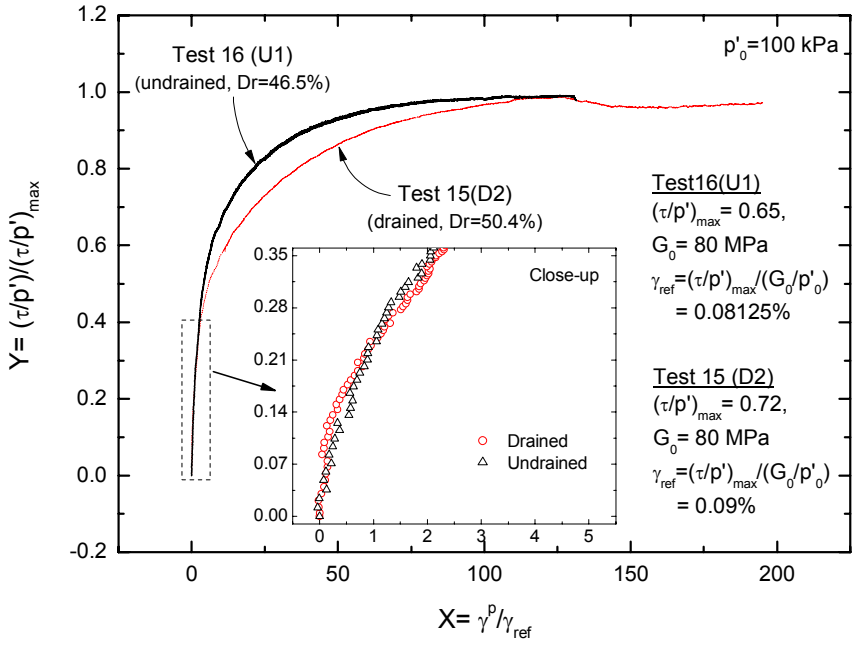

Fig. 5.8: Comparison of *X*-*Y* relationships for drained and undrained tests on loose sand.

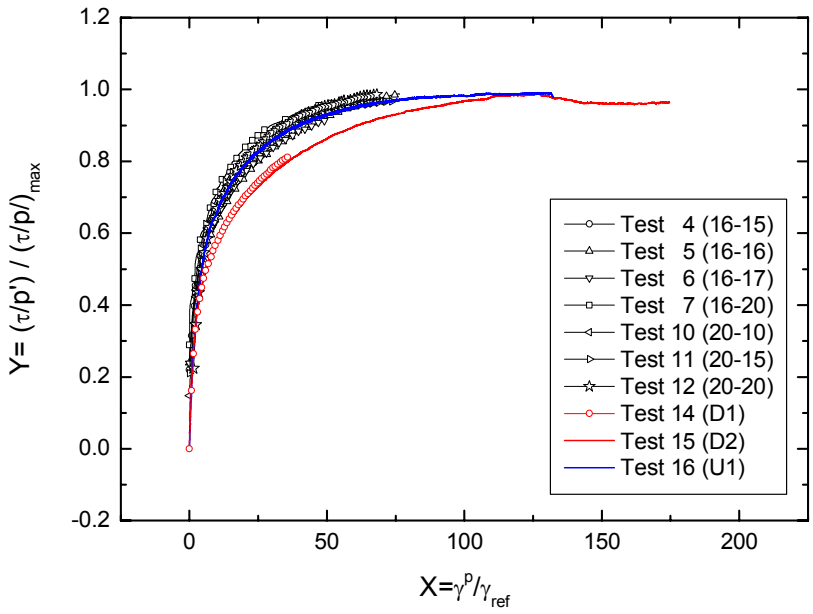

Fig. 5.9: Results and comparisons of *X-Y* relationships for several drained and undrained tests on loose sand

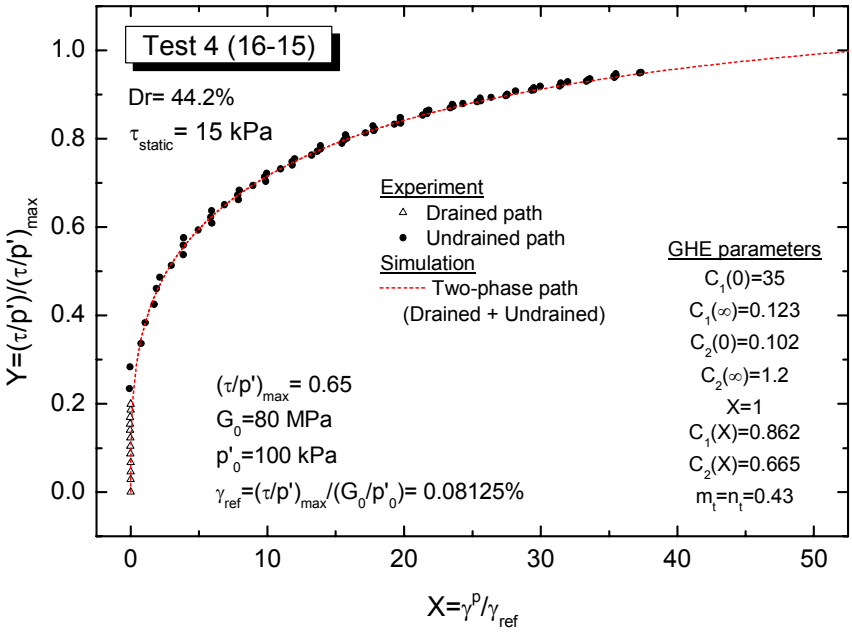

Fig. 5.10: Typical simulation of two-phase (drained + undrained) backbone for Test 6 (16-15)

5.3.2 Modeling the subsequent cyclic loading curves

5.3.2.1 Masing's second rule

The cyclic behavior can be modeled by employing the well-known Masing's 2nd rule (Masing, 1926; Ohsaki, 1980), as schematically shown in Fig. 5.11. It states that if the backbone curve can be simulated by an odd function $Y = f(X)$, where ($f(-X) = -f(X)$), the hysteretic unloading curve passing the initial point A having the coordinate of (X_A, Y_A) can be obtained by

$$\frac{Y - Y_A}{2} = f\left(\frac{X - X_A}{2}\right) \tag{5.48}$$

If the backbone curve is simulated by the GHE model, Eq. (5.48) yields

$$Y = Y_A + \frac{(X - X_A)}{\frac{1}{C_1} + \frac{|X - X_A|}{2C_2}} \tag{5.49}$$

where, C_1 and C_2 are evaluated from Eq. (5.46) and Eq. (5.47), respectively.

It is a known fact that the soil subjected to cyclic loading does not necessarily follow the original Masing's rule (Pyke, 1979; Tatsuoka et al., 1997), therefore, several modified versions of Masing's rules have been proposed.

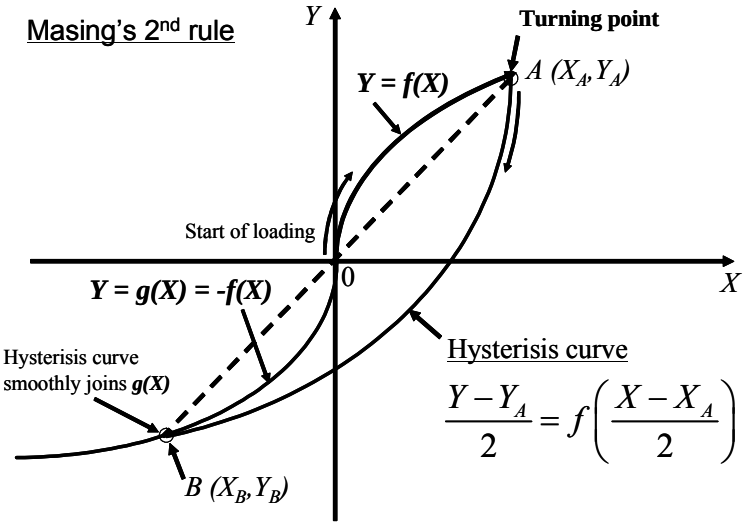

Fig. 5.11: Modeling of hysteresis curve using Masing's 2nd rule (De Silva, 2008)

5.3.2.2 Proportional rule

In order to consider the non-symmetry of the backbone curves in the compression and the extension sides of PSC loading, the proportional rule has been proposed by Tatsuoka et al. (2003).

Suppose that the backbone curve in the compression side is represented by the equation $Y = f(X)$ and in the extension side it is represented by the equation $Y = g(X)$, Eq. (5.48) can be rewritten as

$$\frac{Y - Y_A}{n_p} = h\left(\frac{X - X_A}{n_p}\right) \tag{5.50}$$

$$n_p = -(Y_A - Y_B)/Y_B \quad \text{or} \quad n_p = -(X_A - X_B)/X_B \tag{5.51}$$

where, (X_A, Y_A) is the turning point A.

- $h(X) = g(X)$ for unloading and $h(X) = f(X)$ for reloading, respectively
- n_p denotes the proportional parameter.

The location of points A and B and the schematic illustration of the proportional rule are shown in Fig. 5.12. In general, $n_p > 2$, and it changes during cyclic loading. Note that when $f(X) = -g(X)$ as in the case with the Masing's rule discussed in section 5.3.2.1, the n_p value to be used is always equal to 2.

If the backbone curve is simulated by the GHE model, the hysteretic curve is obtained by:

$$Y = Y_A + \frac{(X - X_A)}{\dfrac{1}{C_1\left(\dfrac{X - X_A}{n_p}\right)} + \dfrac{\left|X - X_A\right|}{n_p C_2\left(\dfrac{X - X_A}{n_p}\right)}} \tag{5.52}$$

5.3.2.3 External and internal rules

The proportional rule can be separated into two sub-rules namely external and internal rules depending on the strain level of the current turning point and previous strain histories (Masuda, 1998; Masuda et al., 1999).

The external rule and internal rule are basically the same, but vary in the way of deriving the proportional parameter n_p. In order to decide the type of rule to be applied,

two limiting strain levels, referred to as the maximum and minimum strains (X_{max} and X_{min}, respectively), are defined each time the stress direction is reversed. If the turning occurs at or out of this strain range, then the external rule is applied. Otherwise, when the turning point occurs within the limit, the internal rule is applied as shown schematically in Fig. 5.13.

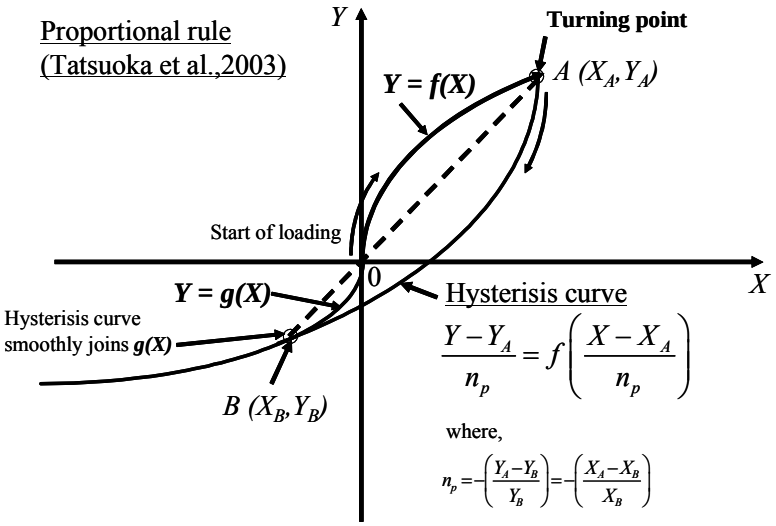

Fig. 5.12: Schematic illustration of the proportional rule (De Silva, 2008)

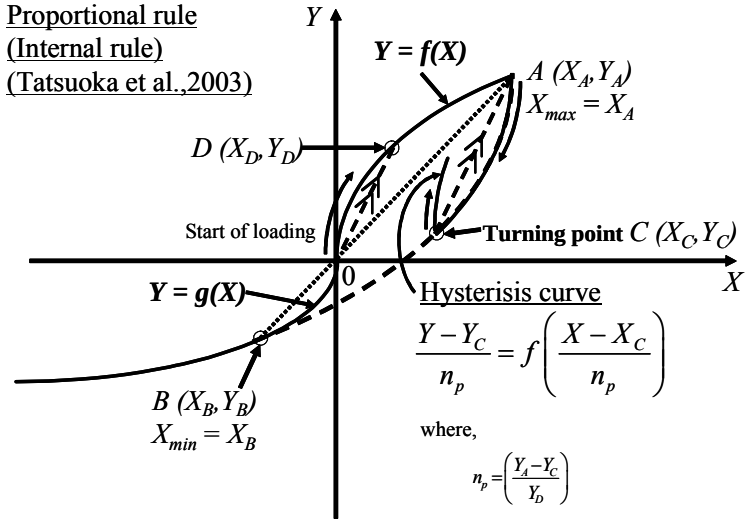

Fig. 5.13: Schematic illustration of the internal rule (De Silva, 2008)

5.3.2.4 Drag rule

Tatsuoka et al., (1997) reported that the stress-strain relationships of soils are significantly influenced by cyclic strain hardening, damage by straining etc., which are caused by the rearrangement of the particles during cyclic loading, and suggested that additional rules are required to model these features to account for behaviors under more general stress conditions. In this regard, a conceptual approach by applying a horizontal shift to the basic skeleton curves (i.e., dragging the basic skeleton curve) along the *X*-axis (strain parameter axis) in the opposite direction to its loading direction was implemented for dense Toyoura sand under plane strain condition (Masuda, 1998; Tatsuoka et al., 2003). The concept of dragging is schematically illustrated in Fig. 5.14.

Note that the idea of dragging the basic skeleton curve arose mainly based on the experimental evidence. It was assumed that the amount of drag, β applied to one basic skeleton curve in one loading direction is a function of the plastic shear strain accumulated in the opposite loading direction (Masuda, 1998; Balakrishnaiyer, 2000; Tatsuoka et al., 2003). The same approach was employed to model the cyclic stress-strain relationships of Toyoura sand under drained cyclic torsional shear loading condition (Hong Nam, 2004).

The formula for dragged backbone curve can be written as follows

$$Y = \frac{(X-\beta)}{\frac{1}{C_1(X-\beta)} + \frac{|X-\beta|}{C_2(X-\beta)}} \tag{5.53}$$

where, β denotes the amount of drag. In the current study, the following drag function proposed by HongNam (2004) is employed (see Fig. 5.15 for its schematic illustration):

$$\beta = \frac{X'}{\frac{1}{D_1} + \frac{X'}{D_2}} \tag{5.54}$$

where D_1 and D_2 are constants, which can be determined by trial and error based on the experimental data.

D_1 and D_2 have the following physical meanings:

D_2 = maximum amount of drag

D_1 = a fitting parameter, which is equivalent to the initial gradient of the drag function.

$$X' = \sum \Delta X \tag{5.55}$$

where ΔX denotes the increment of normalized plastic strains in one direction (positive or negative directions).

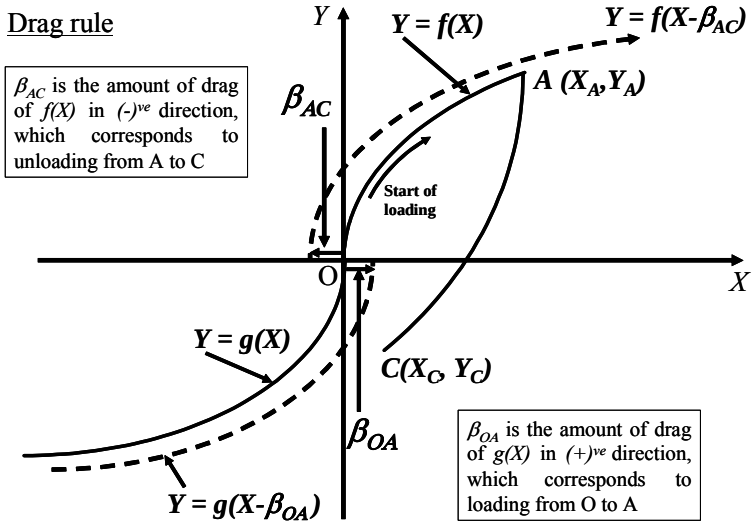

Fig. 5.14: Schematic illustration of the concept of dragging (De Silva, 2008)

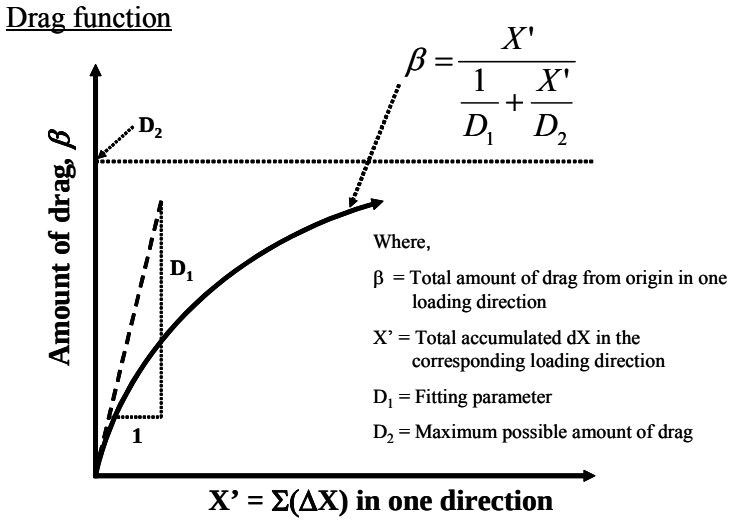

Fig. 5.15: Assumed drag function by Hong Nam (2004)

5.3.2.5 Damage and hardening parameters

In view of the shortcomings of the Masing's rule with drag, two conceptual modification factors, which take into account the hardening behavior and damage to plastic stiffness, were introduced by De Silva (2008) with the aim of reasonably simulating the stress-strain relationships of sand subjected to large cyclic torsional shear loading, while maintaining the continuity in the simulation.

As described in section 5.3.1, the two parameters $C_1(X=0)$ and $C_2(X=\infty)$ in the general hyperbolic equation represent the initial stiffness and the peak strength, respectively. Therefore, the damage that occurred to the plastic stiffness could be obtained by multiplying $C_1(X)$ with an appropriate damage factor D, and the hardening could be obtained by multiplying $C_2(X)$ with a hardening factor S.

Therefore, the hysteresis curve starting from a point A can be obtained as follows by modifying Eq. (5.49)

$$Y = Y_A + \frac{X - X_A}{\dfrac{1}{C_1\left(\dfrac{X - X_A}{n_p}\right) \times D} + \dfrac{|X - X_A|}{n_p \times C_2\left(\dfrac{X - X_A}{n_p}\right) \times S}} \tag{5.56}$$

In order to maintain the continuity, the dragged backbone curve, which is in the same direction as the curve to be modeled, should be modified as follows in order to determine the proportional parameter n_p for external and internal rules

$$Y = \frac{(X - \beta)}{\dfrac{1}{C_1(X - \beta) \times D} + \dfrac{|X - \beta|}{C_2(X - \beta) \times S}} \tag{5.57}$$

Note that, in the method proposed by Tatsuoka et al. (2003), a unique backbone curve in either positive or negative direction was dragged (S and D is equal to 1.0) to apply the proportional rules. On the other hand, De Silva (2008), in order to consider the damage and hardening, proposed a backbone curve that changes with subsequent cyclic loading by means of drag.

Evaluation of the damage parameter D

In the study conducted by De Silva (2008), it was found that the plastic shear modulus can be expressed as an "S curve" of the total plastic strain accumulated between the

current and previous turning points as follows.

$$D = \frac{(1+e^{-0.8})(1-D_{ult})}{1+e^{\left\{\left(\sum|\Delta\gamma^{p}_{z\theta}|_{p}\right)-0.8\right\}}} + D_{ult} \tag{5.58}$$

where, D_{ult} is the minimum value of D and $\sum|\Delta\gamma^{p}_{z\theta}|_{p}$ is the total plastic strain accumulated between the current and previous turning points.

Evaluation of the hardening parameter S

De Silva (2008) assumed that the hardening parameter S can be expressed as a hyperbolic function of the total normalized plastic strain up to the current turning point as follows

$$S = 1 + \frac{\left(\sum|\Delta X|\right)_{\text{Upto current turing point}}}{\frac{D_2}{D_1} + \frac{\left(\sum|\Delta X|\right)_{\text{Upto current turing point}}}{(S_{ult}-1)}} \tag{5.59}$$

where, S_{ult} is the maximum value of S after applying an infinite number of cycles, and D_1 and D_2 are the parameters used in the drag function as shown in Eq. (5.54).

5.3.2.6 Simulation of the subsequent stress-strain relationship

In order to properly investigate the effects of drag, damage and hardening with cyclic loading, it is necessary to conduct a large number of experiments until failure with varying cyclic stress amplitude. Since this was out of the scope of this study, the parameters of drag (D_1 and D_2), damage (D_{ult}) and hardening (S_{ult}) were established by trial and error by referring to those employed by Hong Nam (2004) and De Silva (2008).

De Silva proposed two values of D_{ult} and two values of S_{ult}:

- D_{ult} = 0.2 for varying stress amplitude cyclic loadings, and D_{ult} = 0.6 for constant stress amplitude cyclic loadings;
- S_{ult} = 0.15 for varying stress amplitude cyclic loadings and S_{ult} = 1.35 for constant stress amplitude cyclic loadings.

Hong Nam (2004) proposed D_1 = 0.45 and D_2 = 3.13 for Toyoura sand (Dr_{ini} = 71 %) subjected to cyclic torsional shear loading starting from isotropic stress state ($\sigma'_z = \sigma'_r = \sigma'_\theta$ = 100 kPa) for the cases where there is no damage and hardening.

After introducing the damage and hardening factors, De Silva (2008) recommended D_1 = 0.15 and D_2 = 12 to simulate the stress-strain relationships using the extended Masing's rule with proportional rules.

In this study, by trial and error, the following parameters were set:

(i) *Drag*: D_1= 0.25 and D_2 = 12;

(ii) *Damage*: D_{ult} = 0.6 (constant stress amplitude cyclic loading);

(iii) *Hardening*: S_{ult} = 1.05.

In a similar manner to that of De Silva (2008), the damage parameter D was assumed to be equal to 1.0 (i.e., no damage) until the stress state first exceeds the yield stress of the material. The yield stress was taken as the stress state at which volumetric response of the material changed from contractive to dilative behavior (usually when $\tau/p' \approx 0.5$, the value 0.8 as shown in Eq. (5.58) corresponds to the γ^p value at which yielding occurs).

The comparison of experimental data with the simulation using (i) Masing's 2nd rule with proportional rule, (ii) Extended Masing's rule (i.e., Masing's rule with drag), and (iii) Extended Masing's rule with damage and hardening are shown in Fig 5.16 and Fig. 5.17.

Fig. 5.16(a) and Fig. 5.17(a) show that the simulation using Masing's 2nd rule with proportional rule is not consistent with the test results.

Fig. 5.16(b) and Fig. 5.17(b) show that the simulation results after introducing the dragging of the backbone curves into the cyclic loading. Due to the constant cyclic shear stress amplitude, effect of drag is not relevant. As a result, large deformation behavior as observed in the experiment cannot be well simulated by the application of drag only.

Fig. 5.16(c) and Fig. 5.17(b) show that the simulation results become consistent with the experimental data after introducing damage and hardening into the model, and the cyclic stress-strain relationship can be reasonably simulated up to strain level of 8 %.

It should be noted that, the development of shear strain during undrained cyclic loading is governed also by the stress-dilatancy relationship; hence, different simulations can be obtained when different stress-dilatancy models are used (refer to Fig. 5.27).

(a)

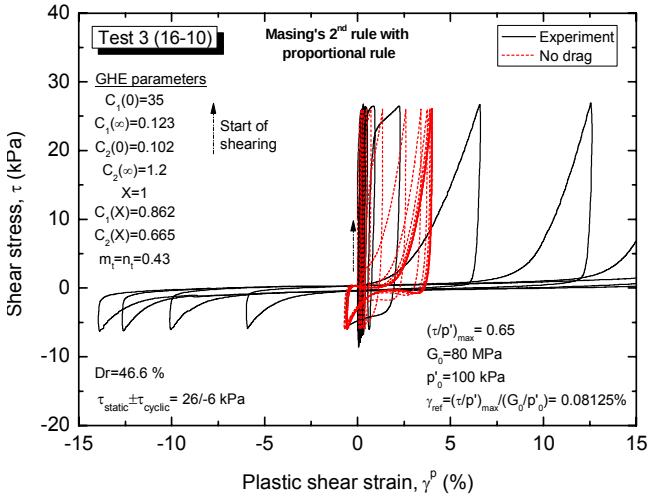

(b)

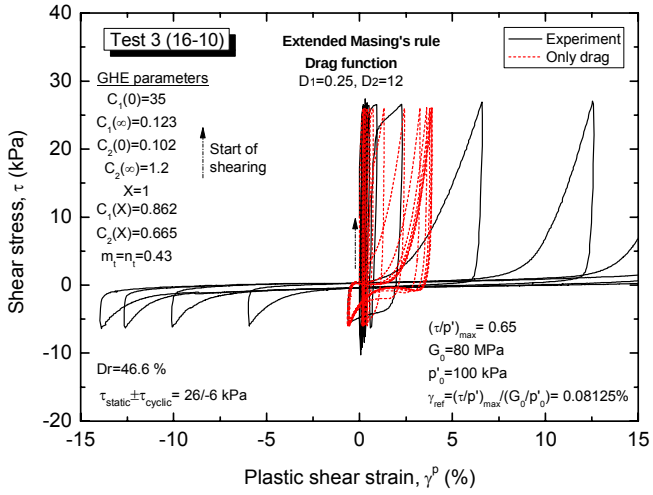

(c)

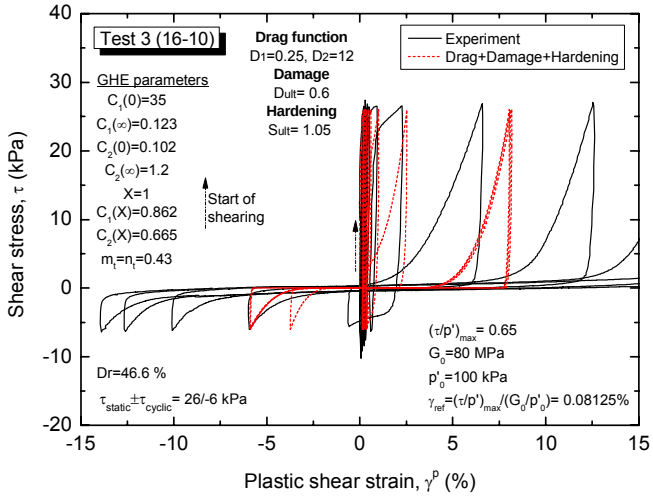

Fig. 5.16: Typical simulation for Test 3 (16-10) using: (a) Masing's 2nd rule with proportional rule; (b) Masing's rule with drag; and (c) Masing's rule with drag, damage and hardening

(a)

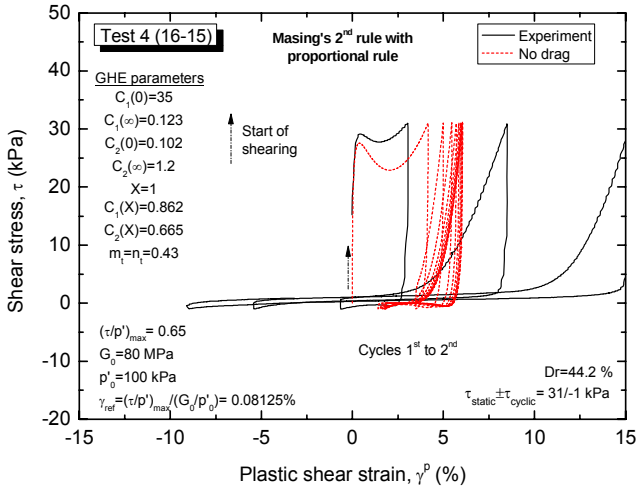

(b)

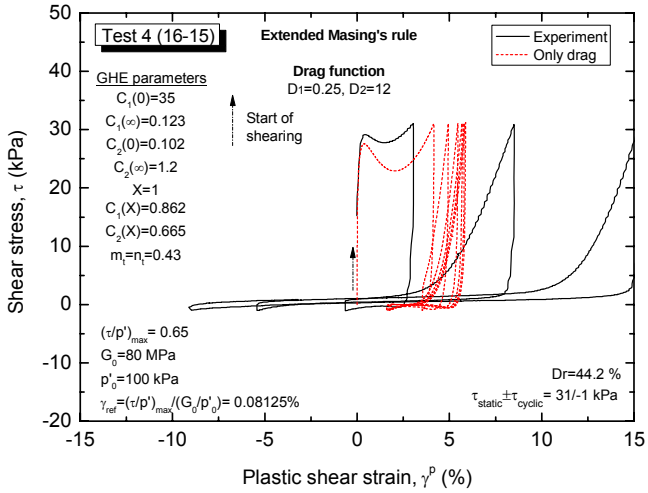

(c)

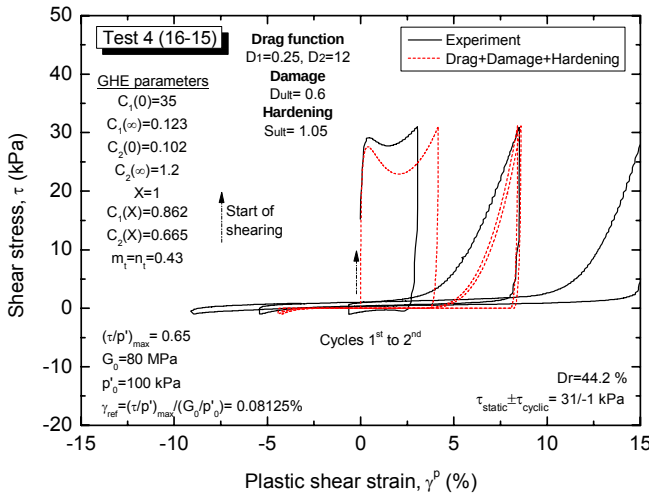

Fig. 5.17: Typical simulation for Test 4 (16-15) using: (a) Masing's 2nd rule with proportional rule; (b) Masing's rule with drag; and (c) Masing's rule with drag, damage and hardening

5.4 Stress-dilatancy relationship of sand in torsional shear tests

In order to describe the dilatancy behavior of soil, a relationship that deals with the ratio of plastic strain increments to stress ratio (i.e., a flow rule) is required in addition to the stress-strain relationship. This relationship is known as the stress-dilatancy relationship.

It should be noted that the theoretical stress-dilatancy relations, such as the Rowe's stress-dilatancy equations (refer to Appendix B), are derived only for either triaxial ($d\varepsilon_2 = d\varepsilon_3$ or $d\varepsilon_2 = d\varepsilon_1$) or plane strain (or simple shear) ($d\varepsilon_2 = 0$) loading conditions. On the other hand, Pradhan (1990) reported based on his experimental data on cyclic torsional shear loading of Toyoura sand that two unique empirical relationships of ($\tau_{z\theta}/p'$) versus ($-d\varepsilon^p_{vol}/d\gamma^p_{z\theta}$) for $d\tau_{z\theta} > 0$ and $d\tau_{z\theta} < 0$ could be derived for Toyoura sand subjected to cyclic torsional shear loadings. De Silva (2008) attempted to investigate the applicability of Rowe's stress-dilatancy relationships in case of torsional shear loading, as described in Appendix B. Nishimura (2002) employed an empirical stress-dilatancy relationship to model the drained and undrained cyclic behavior of sand by assuming a linear combination of ($\tau_{z\theta}/p'$) vs. ($-d\varepsilon^p_{vol}/d\gamma^p_{z\theta}$). In this study the bilinear stress-dilatancy relationship proposed by Nishimura (2002) was employed.

5.4.1 Empirical bi-linear stress-dilatancy equation for torsional shear loading

Nishimura (2002) employed an empirical linear combination of $\tau_{z\theta}/p'$ vs. $-d\varepsilon_{vol}{}^p/d\gamma^p$ to model the stress-dilatancy relationship of Toyoura sand subjected to cyclic torsional shear loading. He further showed that the stress-dilatancy relationships during virgin loading and subsequent cyclic loadings are different, hence he modeled them using different linear equations.

- For $d\gamma^p_{z\theta} > 0$

$$\frac{\tau_{z\theta}}{p'} = R_k\left(-\frac{d\varepsilon^p_{vol}}{d\gamma^p_{z\theta}}\right) + C \tag{5.60}$$

- For $d\gamma^p_{z\theta} < 0$

$$\frac{\tau_{z\theta}}{p'} = R_k\left(-\frac{d\varepsilon^p_{vol}}{d\gamma^p_{z\theta}}\right) - C \tag{5.61}$$

The previously mentioned stress-dilatancy relationship was successfully employed by De Silva (2008) to model the liquefaction behavior of dense Toyoura sand in cyclic torsional shear tests, as shown in Fig. 5.18.

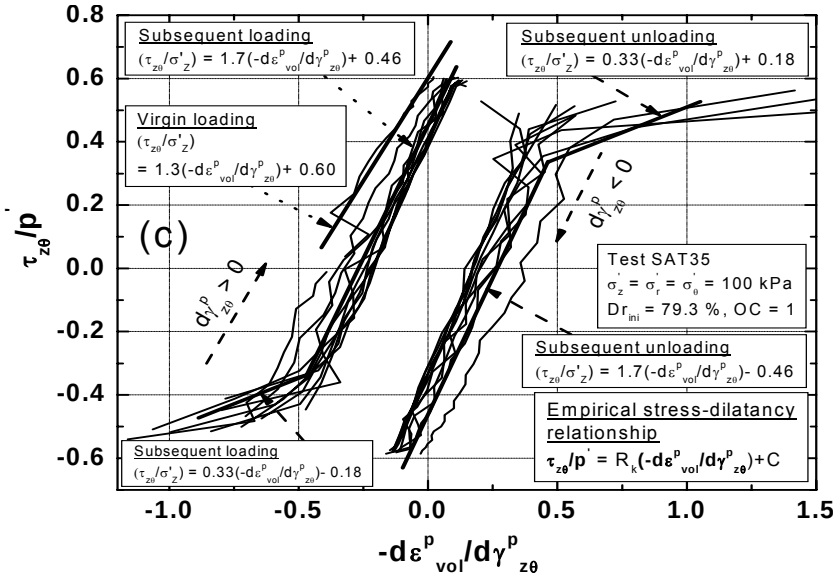

Fig. 5.18: Comparison of experimental data fro Test SAT35 and simulation results using the empirical relationship proposed by Nishimura (2002) (after De Silva, 2008)

However, in order to obtain a more realistic simulation of $\varepsilon^p{}_{vol}$, and to take the slight variations in the stress-dilatancy relationship during cyclic shearing into considerations, the above bilinear stress-dilatancy relationship was further modified by De Silva (2008) by introducing the damage factor D_m

$$\frac{\tau_{z\theta}}{p'} = (R_{\max} \times D_m) \times \left(-\frac{d\varepsilon^p_{vol}}{d\gamma^p_{z\theta}}\right) \pm \frac{C_{\min}}{D_m} \tag{5.62}$$

where

- D_m = the same as the damage parameter D in Eq. (5.58);
- R_{max} = the maximum value of R_k in Eq. (5.60) or Eq. (5.61);
- C_{min} = the minimum value of C in Eq. (5.60) or Eq. (5.61);

In addition, the following boundary conditions were specified for $R_{max} \times D_m$ value and C_{min}/D_m value by referring to the experimental data:

- $R_{max} \times D_m > 1.0$ (if $R_{max} \times D_m$ becomes less than 1.00, $R_{max} \times D_m = 1.00$ to be used)
- $C_{min}/D_m < 0.50$ (if C_{min}/D_m becomes greater than 0.50, $C_{min}/D_m = 0.50$ to be used)

5.4.2 Evaluation of the generation of excess pore water pressure

Although volumetric strain increment ($d\varepsilon_{vol}$) during undrained loading is equal to zero, it is considered to consist of two major components namely volumetric strain components due to dilatancy ($d\varepsilon^{d}_{vol}$) and consolidation/swelling ($d\varepsilon^{c}_{vol}$). The change of mean effective stress (p') during undrained loading causes the consolidation/swelling of specimen, while the change of shear stress causes the dilation of the specimen. As well, possible errors due to the effects of membrane penetration ($d\varepsilon^{MP}_{vol}$) and end restraint ($d\varepsilon^{ER}_{vol}$) should be considered. Therefore, the following equation can be written:

$$d\varepsilon_{vol} = d\varepsilon^{c}_{vol} + d\varepsilon^{d}_{vol} + (d\varepsilon^{ER}_{vol} - d\varepsilon^{MP}_{vol}) = 0 \tag{5.63}$$

However, it has been observed in previous studies (De Silva, 2008; among others) that the effects due to membrane penetration and end restraint are nearly counter-balanced to each other. Thus, Eq. (5.63) can be rewritten as

$$d\varepsilon_{vol} = d\varepsilon^{c}_{vol} + d\varepsilon^{d}_{vol} = 0 \tag{5.64}$$

Quasi-elastic bulk modulus is defined as follows:

$$K = \frac{dp'}{d\varepsilon^{c}_{vol}} \tag{5.65}$$

It can be also expressed as a unique function of the mean effective principal stress (p') as

$$K = \frac{f(e)}{f(e_o)} \frac{K_o}{(p'_o)^{m_k}} (p')^{m_k} \tag{5.66}$$

where

- K_o = bulk modulus at reference mean effective stress (p'_o);
- $f(e)$ and $f(e_o)$ = void ratio functions at current and reference stress states, respectively.
- m_k = coefficient to model the stress-state dependency of K.

By substituting Eq. (5.65) into Eq. (5.66), and considering that $f(e) = f(e_o)$ in undrained tests, the volumetric strain component due to consolidation ($d\varepsilon_{vol}^{c}$) can be defined as follows

$$d\varepsilon_{vol}^{c} = \frac{dp'}{K_o \left(\frac{p'}{p'_o} \right)^{m_k}} \tag{5.67}$$

Finally, by combining Eq. (5.64) with Eq. (5.67), the following equation to evaluate the change of mean effective stress (*dp'*) during undrained cyclic loading can be derived:

$$dp' = K_o \left(\frac{p'}{p'_o} \right)^{m_k} (-d\varepsilon_{vol}^{d}) \tag{5.68}$$

where $d\varepsilon_{vol}^{d}$ is the volumetric strain increment due to dilatancy.

Quasi-elastic bulk modulus (*K*) is usually indirectly evaluated by using *E* and ν with the main assumption that the soil is isotropic, which may not be true. However, the direct evaluation of *K* requires an accurate measurement of the volumetric change of the specimen at quasi-elastic strain range. De Silva (2008) attempted to directly evaluate *K* using a high sensitive electronic balance which is free from the effects of surface tension or meniscus force on the water retained into the beaker.

In this study, taking advantages of the tests results of previous studies where the high sensitive electronic balance was employed, the bulk modulus (*K*) for loose Toyoura sand specimens was determined empirically using the following procedure.

Eq. (5.66) shows that the bulk modulus (*K*) can be expressed as a unique function of the mean effective principal stress (*p'*). However, at $p'=p'_0$, the *K* value of a specimen having any density can be evaluated as a function of the K_0 and $f(e_0)$ which are the bulk modulus and the void ratio function at the reference effective principal stress (p'_0), respectively. Therefore, at $p'=p'_0$, Eq. (5.66) can be rewritten as

$$p' = p'_0 \quad \Rightarrow \quad K = \frac{f(e)}{f(e_0)} K_0 \tag{5.69}$$

Hence, by employing Eq. (5.69) while referring to a reference value of K_0 = 50 MPa at e_0 = 0.784 (i.e., $f(e_0)$ = 1.055), as evaluated experimentally by De Silva (2008), the bulk modulus of each specimen was determined as shown in Fig. 5.19.

Since K was found varying between 46 MPa and 48 MPa, a bulk modulus K = 47 MPa was selected to be used as K_0 in the model to simulate the stress-dilatancy relationships of all the specimens.

In addition, a coefficient m_k = 0.50, to model the stress-state dependency of K, was used in the current study, which is a typical value employed for loose Toyoura sand specimens.

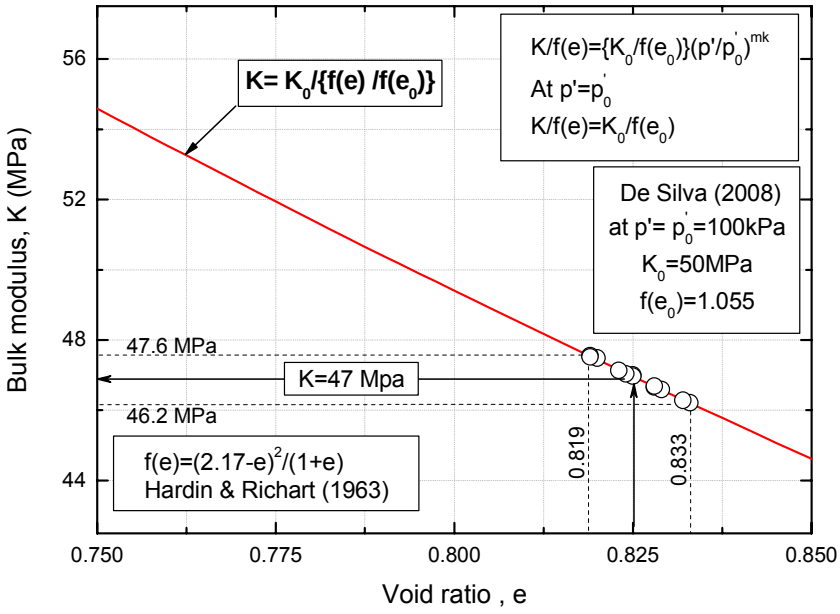

Fig. 5.19: Evaluation of bulk modulus for all the tests.

5.4.3 Modeling the initial static shear on the effective stress path

The presence of initial static shear widely affects the monotonic undrained behavior of sand as well as the subsequent cyclic liquefaction behavior (e.g., liquefaction resistance, failure behavior, mode of residual strain development, etc).

Under the same initial condition of void ratio and effective mean principal stress, the peak undrained strength of sand during monotonic shearing increases with the initial static shear stress as shown in Fig. 4.11.

In this study, the initial shear stress was simulated by a monotonic drained loading path before the undrained monotonic shearing, with the simplified assumption that no change of p' occurs (i.e., $p' = p'_0$ = constant). As a result, as shown in Fig. 5.20, an increase in the peak undrained strength of sand with the initial static shear was observed in the simulation results in a similar manner to that of the experimental observations.

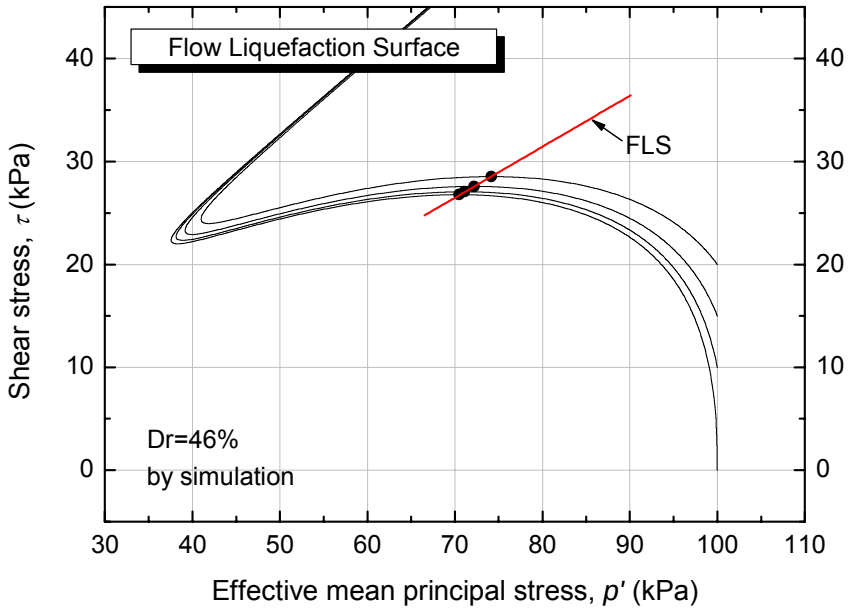

Fig. 5.20: Effects of static shear on the undrained peak strength (refer to Fig. 4.11 for the experimental observations).

5.4.4 Combined effects of over-consolidation and initial static shear

During undrained cyclic loadings, the effective mean principal stress (*p'*) decreases with number of cycles. It is assumed that the above reduction is associated with two mechanisms. Firstly, the soil is subjected to significant effects of over-consolidation until the stress state exceeds the phase transformation stress state for the first time (i.e., the first instance where the volumetric behavior changes from contractive to dilative (*dp'>0*); Ishihara (1975) defined this stress state as the phase transformation stress state). Then the soil will enter into the stage of cyclic mobility.

Effects of over-consolidation significantly alter the stress-dilatancy relationship until the stress state exceeds the phase transformation stress state of the material for the first time. After the stress state exceeds the phase transformation stress state for the first time, the stress-dilatancy relationship during cyclic torsional loading is modeled simply by the modified bilinear stress-dilatancy relationship as expressed in Eq. (5.62).

5.4.4.1 Over-consolidation boundary surface (Oka et al., 1999)

Oka et al. (1999) proposed the following stress-dilatancy equation to consider the effects of over-consolidation within a certain boundary.

$$\left(-\frac{d\varepsilon_{vol}^{p}}{d\gamma_{z\theta}^{p}}\right)=\frac{D_k}{R_k}\left(\frac{\tau_{z\theta}}{p'}-\frac{\tau_{z\theta}/p'}{\ln(p'_0/p')}\right) \qquad (d\tau_{z\theta}>0) \qquad (5.70)$$

where

$$D_k=\left[\frac{\tau_{z\theta}/p'}{C\ln(p'_0/p')}\right]^{1.5} \qquad (5.71)$$

The over-consolidation boundary surface to induce D_k = 1.0 is defined as follows:

$$C=\frac{\tau_{z\theta}/p'}{\ln(p'_0/p')} \qquad (5.72)$$

Therefore, when D_k=1.0, Eq. (5.70) can be rewritten as follows:

$$\left(-\frac{d\varepsilon_{vol}^{p}}{d\gamma_{z\theta}^{p}}\right)=\frac{1}{R_k}\left(\frac{\tau_{z\theta}}{p'}-C\right) \qquad (5.73)$$

The above equation is the same as the empirical bilinear stress-dilatancy relationship proposed by Nishimura (2002) in Eq. (5.60). Therefore, Eq. (5.70) meets Eq. (5.60) when D_k = 1.0, and the over-consolidation boundary surface to induce D_k = 1.0 can be defined by Eq. (5.72).

Rearranging the terms in Eq. (5.72) yields

$$\tau_{z\theta} = C \ln(p'_0 / p') \, p' \tag{5.74}$$

Note that whenever the stress state exceeds the phase transformation stress state for the first time, the effects of over-consolidation is assumed to have vanished and the modified bilinear stress-dilatancy relationship can be applied to evaluate $d\varepsilon^d_{vol}$.

Definition of over-consolidation boundary surface and phase transformation line is shown in Fig. 5.21.

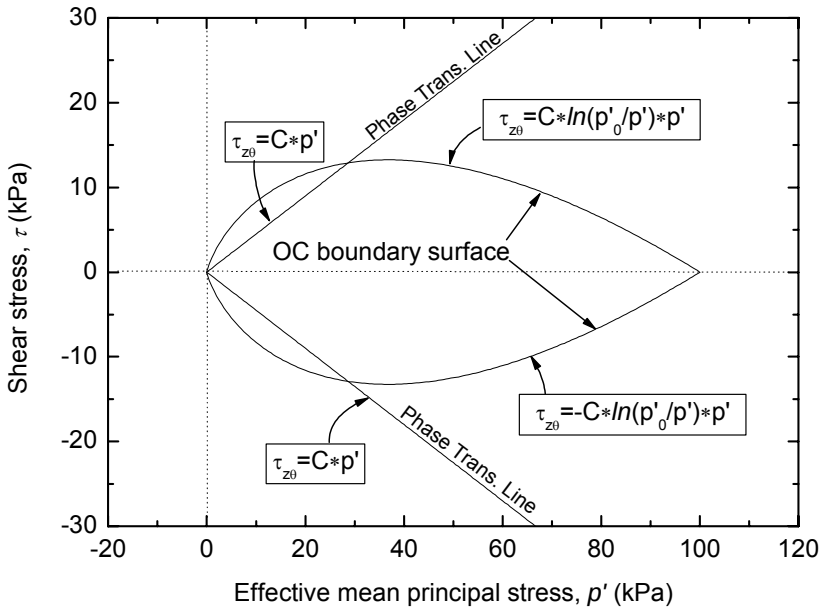

Fig. 5.21: Definition of OC boundary surface (Oka et al., 1999) and phase transformation line.

5.4.4.2 Modified over-consolidation boundary surface

A modified OC boundary surface which takes the effects of initials static shear into account is proposed in this study.

The OC boundary surface has been used in previous studies (e.g., Oka et al. (1999); among others) not only to define the region within which the specimen behaves as contractive while being affected by of over-consolidation, but also to control the shape of the plastic potential function (i.e., yield surface).

It is recognized that the yield surface expands in as such a way that the current stress state never exceeds it. In fact, under isotropic consolidation conditions it can shrink or extend horizontally if the soil is over-consolidated or normally consolidated, respectively. Under anisotropic consolidation conditions, due to the presence of deviator stress, it is assumed that the yield surface can rotate centered about the origin (*0; 0*) with respect to the axis of zero deviator stress state, since the stress state at the end of the consolidation process is different from the one under isotropic stress conditions. As a results, the shape and the location of yield surface changes according to the extent of deviator stress and the over-consolidation ratio.

In view of the above, the following stress-dilatancy equation, to consider the combined effects of over-consolidation and the initial static shear stress within a certain boundary, was proposed in this study:

$$\left(-\frac{d\varepsilon_{vol}^{p}}{d\gamma_{z\theta}^{p}}\right)=\frac{D_k}{R_k}\left(\frac{\tau_{z\theta}}{p'}-\frac{\frac{\tau_{z\theta}}{p'}-\frac{\tau_{static}}{p'_0}}{\ln(p'_0/p')}\right) \qquad (d\tau>0) \qquad (5.75)$$

where

$$D_k=\left[\frac{\frac{\tau_{z\theta}}{p'}-\frac{\tau_{static}}{p'_0}}{C\ln(p'_0/p')}\right]^{1.5} \qquad (5.76)$$

The over-consolidation boundary surface to induce $D_k = 1.0$ is defined as follows:

$$C = \frac{\frac{\tau_{z\theta}}{p'} - \frac{\tau_{static}}{p'_0}}{\ln(p'_0 / p')} \tag{5.77}$$

where τ_{static}/p'_0 is the inclination of the line which connects the point of coordinates (τ_{static}; p'_0) with the point of coordinates ($\tau = 0$; $p' = 0$). In fact it is assumed that due to the presence of initial static shear the OC boundary surface can rotate centered about the origin ($\tau = 0$; $p' = 0$) by a quantity of τ_{static}/p', as shown schematically in Fig. 5.22.

Therefore, when $D_k = 1.0$, Eq. (5.75) can be rewritten as follows:

$$\left(-\frac{d\varepsilon^p_{vol}}{d\gamma^p_{z\theta}}\right) = \frac{1}{R_k}\left(\frac{\tau_{z\theta}}{p'} - C\right) \tag{5.78}$$

which is the same as Eq. (5.60) proposed by Nishimura (2002). Therefore, Eq. (5.75) meets Eq. (5.60) when $D_k = 1.0$, and the modified over-consolidation boundary surface, which takes the initial static shear stress into account, can be defined by Eq. (5.77).

Note that, when $\tau_{static} = 0$ the modified OC boundary surface proposed in this study meets the OC boundary surface (Fig. 5.21) proposed by Oka et al. (1999).

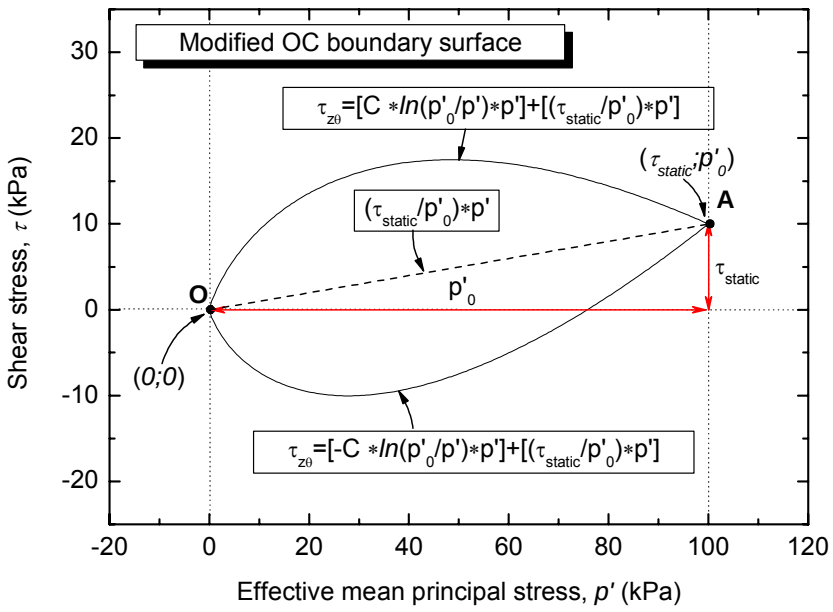

Fig. 5.22: Modified OC boundary surface as defined in this study.

5.4.5 Four-phase stress-dilatancy model employed in this study

In this study the empirical bi-linear stress-dilatancy relationship proposed by Nishimura (2002) and modified by De Silva (2008) was employed. However, further modifications were necessary to take into consideration the effects of initial static shear in modeling the tests results.

In a similar way to that of De Silva (2008), the stress path during undrained loading was divided into four sections namely:

(A) Virgin stress path;
(B) Stress path within the limits of phase transformation stress state;
(C) Stress path within the limits of modified over-consolidation boundary surface; and
(D) Stress path after exceeding the phase transformation stress state for the first time.

A typical simulation result using the four-phase stress-dilatancy model employed in the current study, with the parameter values as assigned below, is shown in Fig. 5.23. Different stress-dilatancy relationships were used for each section of the stress path to evaluate the volume change increment due to dilatancy.

(A) *Virgin stress path*

Previous studies (Nishimura, 2002; De Silva, 2008; among others) showed that the stress-dilatancy relationships during the virgin loading before the first reversal of loading direction and the subsequent cyclic loading are different from each other.

In this study the stress-dilatancy relationship during the virgin loading was modeled as follows (the coefficients R_k and C were set by trial and error)

Eq. (A) $$\frac{\tau_{z\theta}}{p'} = R_k \left(-\frac{d\varepsilon_{vol}^{p}}{d\gamma_{z\theta}^{p}} \right) + C \qquad (5.79)$$

$R_k = 1.7$ and $C = 0.595$ (set by trial and errors)

C is the $\tau_{z\theta}/p'$ value at zero dilatancy (phase transformation).

(B) *Stress path within the limits of phase transformation stress state*

The stress-dilatancy relationship above the OC boundary surface and below the phase transformation line was modeled as follows:

$$\text{Eq. (B)} \quad \left.\begin{array}{l} \left|\dfrac{\tau_{z\theta}}{p'}\right|^{\max} \le |C| \\ \& \\ \left|\dfrac{\tau_{z\theta}}{p'}\right| > \left|C\ln(p'_0/p')\right| \end{array}\right\} \Rightarrow \quad \frac{\tau_{z\theta}}{p'} = R_k\left(-\frac{d\varepsilon_{vol}^p}{d\gamma_{z\theta}^p}\right) \pm C \qquad (5.80)$$

R_k = 2.2 and C = 0.45 (as proposed by De Silva, 2008)

$\left|\dfrac{\tau_{z\theta}}{p'}\right|^{\max}$ is the maximum of $\left|\tau_{z\theta}/p'\right|$ applied to the specimen up to the current stress state.

C is the $\tau_{z\theta}/p'$ value at zero dilatancy (phase transformation).

(C) *Stress path within the limits of modified over-consolidation boundary surface*

The stress-dilatancy relationship within the OC boundary surface and below the phase transformation line was modeled as follows:

$$\text{Eq. (C)} \quad \left.\begin{array}{l} \left|\dfrac{\tau_{z\theta}}{p'}\right|^{\max} \le |C| \\ \& \\ \left|\dfrac{\tau_{z\theta}}{p'}\right| \le \left|C\ln(p'_0/p')\right| \end{array}\right\} \Rightarrow \quad \left(-\frac{d\varepsilon_{vol}^p}{d\gamma_{z\theta}^p}\right) = \frac{D_k}{R_k}\left(\frac{\tau_{z\theta}}{p'} - \frac{\dfrac{\tau_{z\theta}}{p'} - \dfrac{\tau_{static}}{p'_0}}{\ln(p'_0/p')}\right) \qquad (5.81)$$

$$D_k = \left[\frac{\dfrac{\tau_{z\theta}}{p'} - \dfrac{\tau_{static}}{p'_0}}{C\ln(p'_0/p')}\right]^{1.5}$$

R_k = 2.2 and C = 0.45 (as proposed by De Silva, 2008)

$\left|\dfrac{\tau_{z\theta}}{p'}\right|^{\max}$ is the maximum of $\left|\tau_{z\theta}/p'\right|$ applied to the specimen up to the current stress state.

C is the $\tau_{z\theta}/p'$ value at zero dilatancy (phase transformation).

(D) *Stress path after exceeding the phase transformation stress state for the first time*

The stress-dilatancy relationship above the phase transformation line was modeled as

Eq. (D1) $$\left|\frac{\tau_{z\theta}}{p'}\right|^{\max} > |C| \Rightarrow \quad \frac{\tau_{z\theta}}{p'} = (R_{\max} \times D_m) \times (-\frac{d\varepsilon_{vol}^{p}}{d\gamma_{z\theta}^{p}}) \pm \frac{C_{\min}}{D_m} \tag{5.82}$$

R_{max}= 2.2 and C_{min} = 0.36 (as proposed by De Silva, 2008)

$\left|\frac{\tau_{z\theta}}{p'}\right|^{\max}$ is the maximum of $|\tau_{z\theta} / p'|$ applied to the specimen up to the current stress state.

C is the $\tau_{z\theta}/p'$ value at zero dilatancy (phase transformation).

The stress-dilatancy after the reversal of the loading direction was modeled with another linear combination of $(\tau_{z\theta} / p')$ vs. $(-d\varepsilon_{vol}^{p} / d\gamma^{p})$ as follows:

Eq. (D2) $$\left|\frac{\tau_{z\theta}}{p'}\right|^{\max} > |C| \Rightarrow \quad \left(-\frac{d\varepsilon_{vol}^{p}}{d\gamma_{z\theta}^{p}}\right) = \frac{D_k}{R_k}\left(\frac{\tau_{z\theta}}{p'} - \frac{\tau_{z\theta} / p'}{\ln(p'_0 / p')}\right) \tag{5.83}$$

R_k = 0.33 and C = 0.18 (as proposed by De Silva, 2008)

$\left|\frac{\tau_{z\theta}}{p'}\right|^{\max}$ is the maximum of $|\tau_{z\theta} / p'|$ applied to the specimen up to the current stress state.

C is the $\tau_{z\theta}/p'$ value at zero dilatancy (phase transformation).

(a)

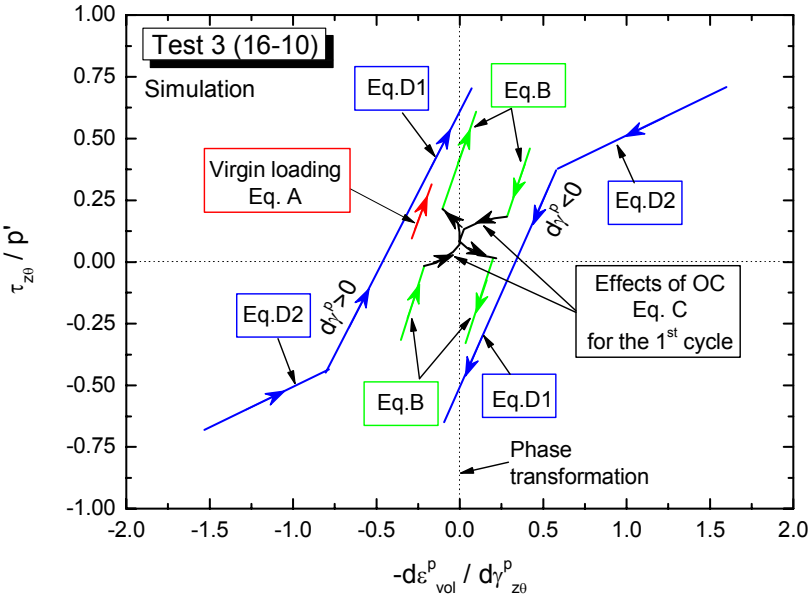

(b)

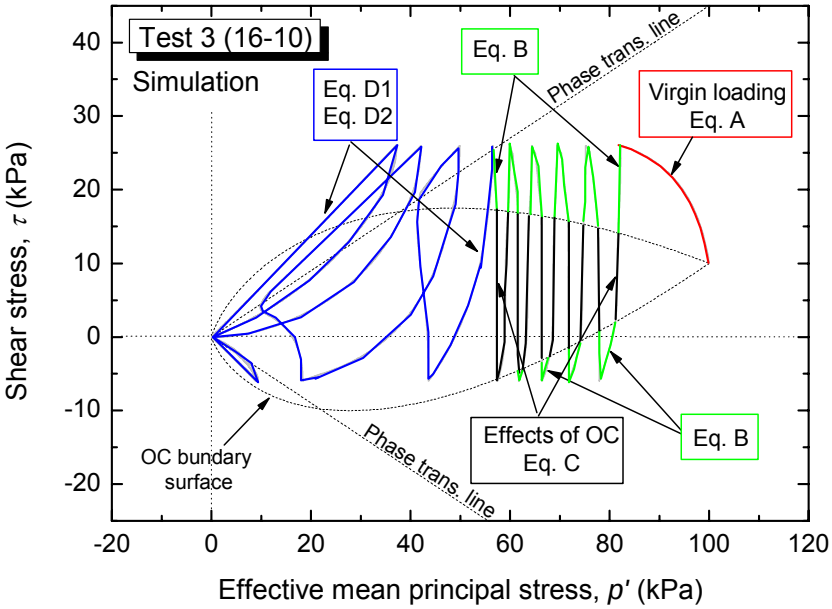

Fig. 5.23: Typical simulation result for Test 3 (10-16) using the four-phase stress-dilatancy model employed in the current study: (a) $\tau_{z\theta}$/p' vs. $d\varepsilon^p_{vol}$ / $d\gamma^p_{z\theta}$ relationship; and (b) Effective stress path.

5.4.6 Simulation of the effective stress path using the four-phase stress-dilatancy model

To simulate the cyclic stress path, the four-phase stress-dilatancy model described in section 5.4.5 and shown in Fig. 5.23(a) was used.

Fig. 5.24 shows the comparison of experimental data with the simulation results for Test 8 (20-00) in which no static shear was employed. The simulation of the virgin stress path using the empirical linear stress-dilatancy described by Eq. (5.79) is consistent with the test results.

Fig. 5.25 shows the comparison of experimental data with the simulation results for Test 12 (20-00), considering the cases with and without initial static shear stress. It can be seen that after the introduction of the drained loading path (i.e., initial static shear) in the model, the simulation of virgin stress path becomes consistent with the experimental data.

It should be noted that, in both cases the same stress-dilatancy relationship with coefficients R_k = 1.7 and C = 0.595, as described by Eq. (5.79), was employed; therefore, the use of a drained loading path makes it possible to use the model to describe the effects of initial static shear on the monotonic undrained behavior of sand.

Fig. 5.26 shows the comparison of experimental data with the simulation results for Test 3 (16-10) in terms of effective stress paths. In Fig. 5.26 the OC boundary surfaces and the phase transformation lines are also shown in aiding to understand which of the four stress-dilatancy relationships was used to model each part of the stress path.

In Fig. 5.26(a), experimental observations show that during the cyclic loading, p' progressively decreases at a rather constant dp' during both loading and unloading stages until it reaches for the first time the phase transformation line.

In Fig. 5.26(b), typical simulation results obtained without using the OC boundary surface are presented. They are not consistent with experimental data since p' decreases very quickly.

In Fig. 5.26(c), simulation results obtained using the OC boundary surface as defined by Oka et al. (1999) are presented. The simulation results are not consistent with the experimental data. In fact, p' mostly decreases in the region outside the OC boundary surface; as well, when the reversal of stress occurs within the OC boundary surface, no change in p' can be observed. It should be noted that, due to the presence of initial static

shear, the loading path is shifted vertically with respect to the axis of zero shear stress state ($\tau = 0$). On the contrary, the shape and the location of the OC boundary surface is the same irrespective of the level of static shear. This is the main reason why the simulation results are not consistent with the experimental data.

In Fig. 5.26(d), simulation results obtained using the modified OC boundary surface proposed in this study are presented. In this case, the OC boundary surface moves according with the extent of static shear. Simulation results are much more consistent with the test results.

Fig. 5.27 shows the comparison of experimental data with the simulation results for Test 3 (16-10) in terms of stress-strain relationships. It can be seen that using the modified OC boundary surface, the stress-strain relationship can be simulated qualitatively.

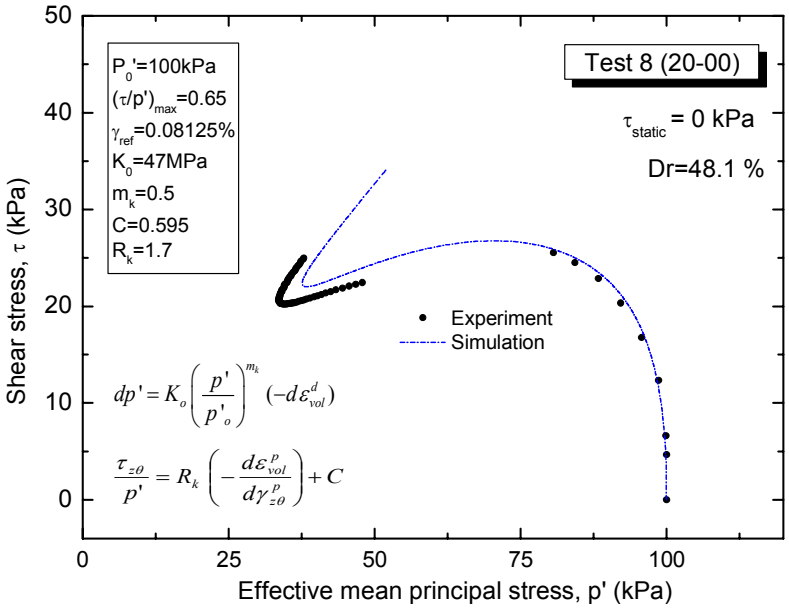

Fig. 5.24: Typical simulation of virgin stress path for Test 8 (20-00) in which no initial static shear was employed

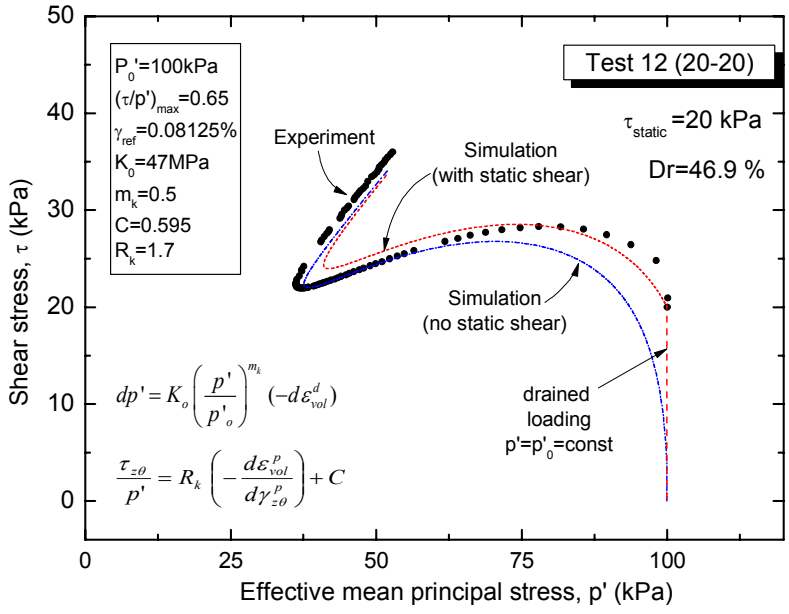

Fig. 5.25: Typical simulation of virgin stress path with/without initial static shear effects for Test 12 (20-20)

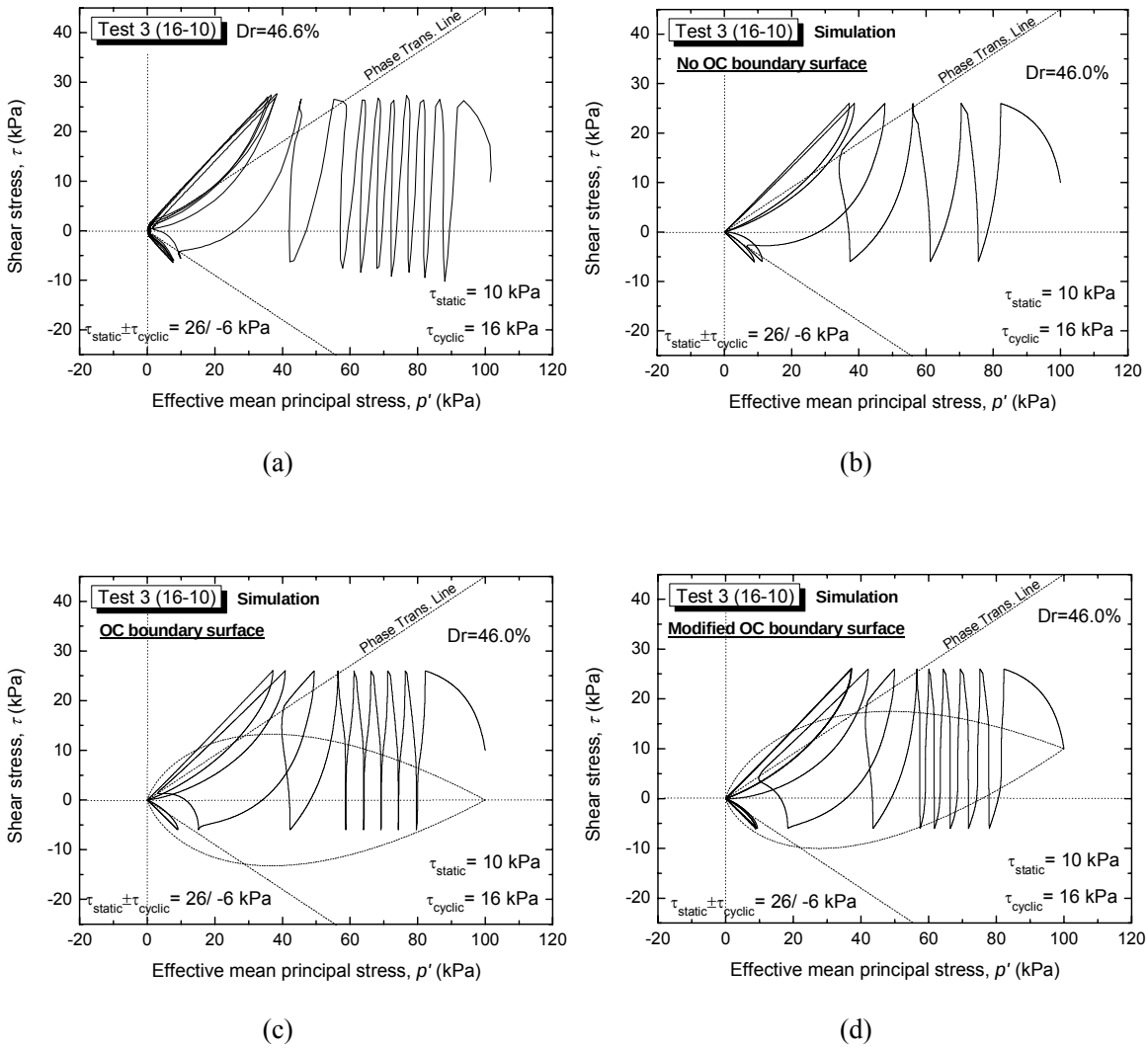

Fig. 5.26: Typical effective stress path for Test 3 (16-10): (a) Experimental observations; (b) Simulation without using the OC boundary surface; (c) Simulation using the OC boundary surface; and (d) Simulation using the modified OC boundary surface

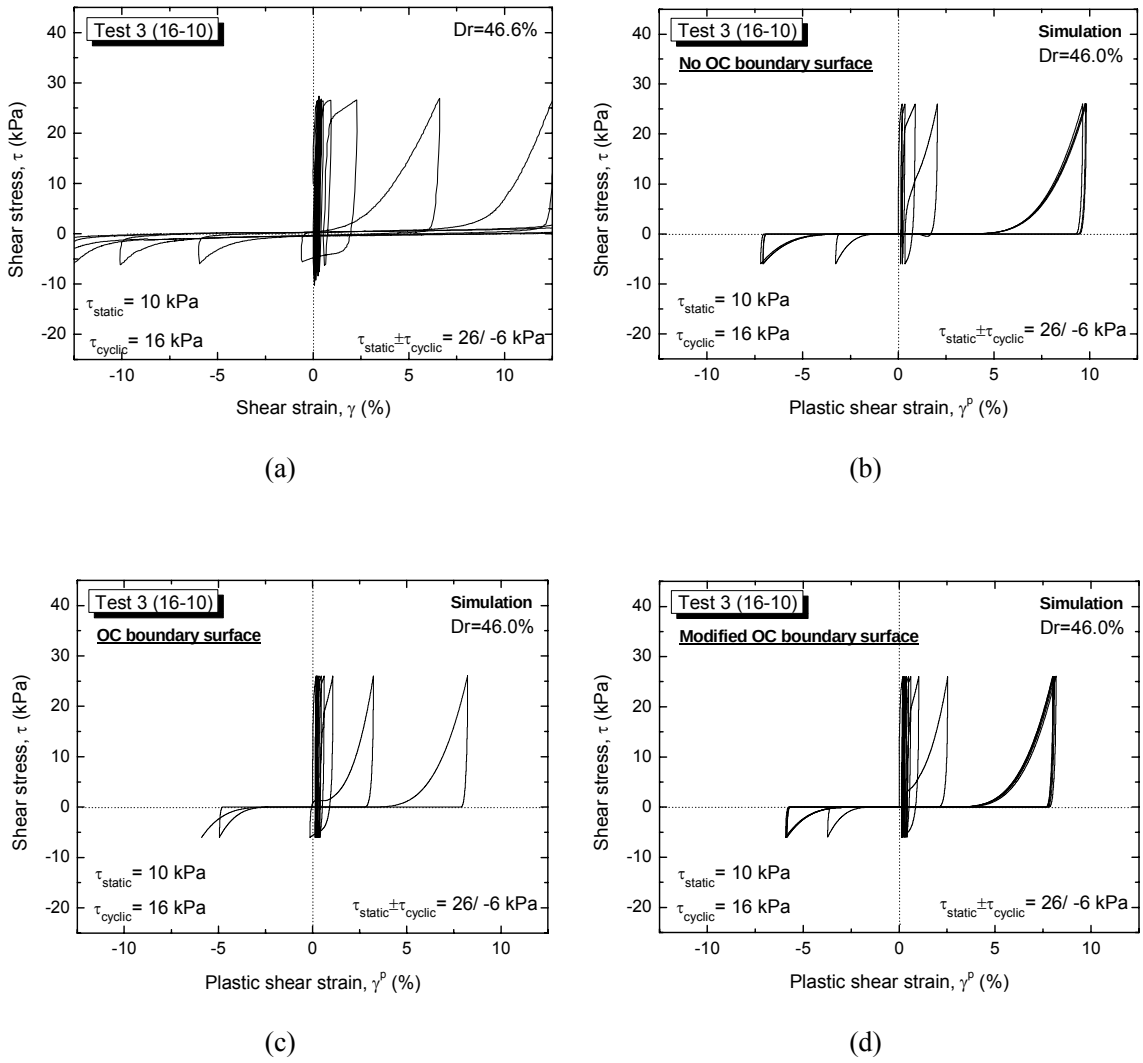

Fig. 5.27: Typical stress-strain relationship for Test 3 (16-10): (a) Experimental observations; (b) Simulation without using the OC boundary surface; (c) Simulation using the OC boundary surface; and (d) Simulation using the modified OC boundary surface

5.5 Simulation results of the liquefaction behavior of sand with initial static shear

5.5.1 Simulation results

The comparison of the experimental data with simulation results for all the tests, in terms of effective stress paths and stress-strain relationships, are presented hereafter in Fig. 5.28 through Fig. 5.39. It should noted that, the stress-strain relationships are shown in the shear strain range of ±12.5 % to better compare each of the experimental data with the simulation results.

It can be seen that the elasto-plastic constitutive model presented in this study is able to simulate the liquefaction behavior of loose sand under undrained cyclic torsional shear loading until the specimen enters into a full liquefaction state, as well during the cyclic mobility process. The development of large deformation up to 8% can be qualitatively simulated.

The simulation results also show that this model can simulate the liquefaction behavior of sand under general conditions of stress reversal, intermediate and non-reversal loadings by varying the initial static shear and the amplitude of cyclic shear stress (i.e., varying the degree of reversal loading, R^*).

5.5.2 Failure behaviors of sand

As mentioned in chapter 4, the degree of reversal stress is the main parameter used to describe the failure behavior of sand. However, for a comprehensive understanding of the failure behavior of sand the comparison between both monotonic and cyclic undrained behaviors is necessary.

The simulation results confirmed that the three types of failure defined in this study can be effectively simulated by employing the proposed model.

Fig. 5.40 shows typical simulation results of the cyclic liquefaction failure (LQ) behavior, in which full liquefaction ($p'=0$) is achieved after applying many cycles of loading. It should be noted that, LQ failure can only occur under reversal stress conditions.

On the other hand, Fig. 5.41 and Fig. 5.42 show the typical simulation results of rapid flow liquefaction failure (RF) behavior for reversal and intermediate loading cases,

respectively. In both of these cases, liquefaction and large deformation are achieved in-between the first cycle of loading.

Fig. 5.43 shows the typical simulation results of the residual deformation (RD) behavior in which liquefaction does not occur due to the non-reversal stress conditions. However, failure is achieved due to the development of large residual deformation.

In Fig. 5.44 the simulation results for Test 6 (16-17) are presented. They clearly show that even though the minimum value of non-reversal stress is just 1 kPa (i.e., τ_{min}=1 kPa, R^*= -0.03), liquefaction does not occur. On the contrary, the experimental observations show that liquefaction was achieved for Test 6 (16-17), as shown in Fig. 4.9. Therefore, these simulation results suggest that the technical limitations in conducting correction for membrane force and/or accurate control can be the reason why in the laboratory tests liquefaction was achieved even under non-reversal stress-conditions.

In addition, by numerical simulations, the following case in which either failure or liquefaction did not take place even after applying several tens of cycles could be defined when the maximum cyclic shear stress was lower than the monotonic peak stress $(\tau_{max} < \tau_{peak})$ as well as the minimum shear stress was positive $(\tau_{min} > 0)$, as typically shown in Fig. 5.45. This additional case hereafter is called No Failure-No Liquefaction (NN).

5.5.3 Development of residual deformation due to cyclic shearing

The mode of development of residual deformation obtained by the numerical simulation for the case of LQ failure, RF failure and RD failure behaviors is shown in Fig. 5.46. In a similar manner to that of the experimental results, to analyze the simulation results the residual deformation (γ_{RS}) during cyclic loading was measured in terms of shear strain at the moment when the stress state recovered the initial value of static shear stress (i.e., $\tau = \tau_{static}$, $d\tau < 0$) during the unloading stage of each cycle (as illustrated in Fig. 4.12).

In Fig 5.46(a), the residual deformation behavior of specimens showing cyclic liquefaction failure behavior (LQ) obtained by numerical simulations is compared with the experimental data. Simulation results are quite consistent with the experimental observations.

In Fig. 5.46(b) the behavior of specimens characterized by rapid flow liquefaction failure mode (RF) obtained by numerical simulations is compared with the experimental data. In this case also by numerical simulations, large deformation is achieved in a few cycles, but the amount of shear strain developed in the laboratory tests is larger than the one developed in the simulations by referring to the same the number of cycles.

Fig. 5.46(c) shows the case of residual deformation failure (RD). These tests confirmed that large deformation could be reached even in the case where liquefaction did not take place. Simulation results are consistent with the experimental observations.

These simulation results confirmed that three types of mode of development of residual deformation can be observed according to the above types of failure behavior of sand.

5.5.4 Resistance to cyclic strain accumulation

The resistance to liquefaction (or more strictly, resistance to cyclic strain accumulation) was evaluated in terms of the number of cycles required to develop a specific amount of residual shear strain γ_{RS} = 7.5 % ($N_{7.5}$), which corresponds to an axial strain (ε_a) of 5% in undrained Triaxial Compression (TC) tests.

Fig. 5.47 show the resistance to cyclic strain accumulation, in terms of relationship between either the cyclic stress ratio ($CSR = \tau_{cyclic} / p'_0$) or the static stress ratio ($SSR = \tau_{static} / p'_0$) and the number of cycles required to develop a γ_{RS} = 7.5 % ($N_{7.5}$), for all the simulation results which are listed in Table 5.1. It should be noted that, additional tests conditions were simulated to better describe the above mentioned relationships.

As already pointed out in chapter 4, the CSR is not a sufficient single parameter to describe the effects of initial static shear on the resistance against strain accumulation, as shown in Fig. 5.47 (a). Therefore, the simulation results are described also in terms of SSR as shown in Fig. 5.47(b).

It can be seen that, the resistance against strain accumulation can either increase or decrease depending on the level of initial static shear and cyclic shear stresses (i.e., the extent of reversal stress, R^*), in a similar manner to that of the experimental observations presented in chapter 4. A two-phase change in strain accumulation behavior can be observed; it was associated with a two-phase change in failure behavior from LQ to RF and from RF to RD.

Fig. 5.48 confirmed that, although the degree of reversal stress (R^*) can be used to describe the change in the strain accumulation, it is not a sufficient single parameter to describe the two-phase change in the strain behavior. On the contrary, the failure behavior can be used to describe clearly the two-phase strain accumulation behavior: the sudden drop in the resistance against strain accumulation can be associated with the two-phase change in the failure behavior from LQ to RF; on the other hand, the sudden increase in the resistance against strain accumulation can be associated with the two-phase change in the failure behavior from RF to RD.

Table 5.1 Strain accumulation parameters, type of loading and failure characteristics

Simulation	τ_{static} *(kPa)*	τ_{cyclic} *(kPa)*	*SSR*	*CSR*	*R**	$N_{7.5}$ *(γ_{RS}=7.5%)*	*Type of loading*	*Type of failure*
Test 1 (16-00)	0	16	0.000	0.160	1.00	33.5	Rev	LQ
Test 2 (16-05)	5	16	0.050	0.160	0.60	19.5	Rev	LQ
Test 3 (16-10	10	16	0.100	0.160	0.23	7.5	Rev	LQ
Test 4 (16-15)	15	16	0.150	0.160	0.03	1.5	Rev	RF
Test 5 (16-16)	16	16	0.160	0.160	0.00	1.5	Int	RF
Test 6 (16-17)	17	16	0.170	0.160	-0.03	3.5	N-Rev	RD
Test 7 (16-20)	20	16	0.200	0.160	-0.11	5.5	N-Rev	RD
S 16-02.5	2.5	16	0.025	0.160	0.73	23.5	Rev	LQ
S 16-07.5	7.5	16	0.075	0.160	0.36	13.5	Rev	LQ
S 16-12.5	12.5	16	0.125	0.160	0.12	1.5	Rev	RF
S 16-25	25	16	0.250	0.160	-0.22	6.5	N-Rev	RD
S 16-30	30	16	0.300	0.160	-0.30	7.5	N-Rev	RD
Test 8 (20-00)	0	20	0.000	0.200	1.00	6.5	Rev	LQ
Test 9 (20-05)	5	20	0.050	0.200	0.60	5.5	Rev	LQ
Test 10 (20-10	10	20	0.100	0.200	0.33	1.5	Rev	RF
Test 11 (20-15)	15	20	0.150	0.200	0.14	1.5	Rev	RF
Test 12 (20-20)	20	20	0.200	0.200	0.00	2.5	Int	RF
S 20-02.5	2.5	20	0.025	0.200	0.78	6.5	Rev	LQ
S 20-07.5	7.5	20	0.075	0.200	0.45	1.5	Rev	RF
S 20-17.5	17.5	20	0.125	0.200	0.07	1.5	Rev	RF
S 20-25	25	20	0.250	0.200	-0.11	3.5	N-Rev	RD
S 20-30	30	20	0.300	0.200	-0.20	4.5	N-Rev	RD

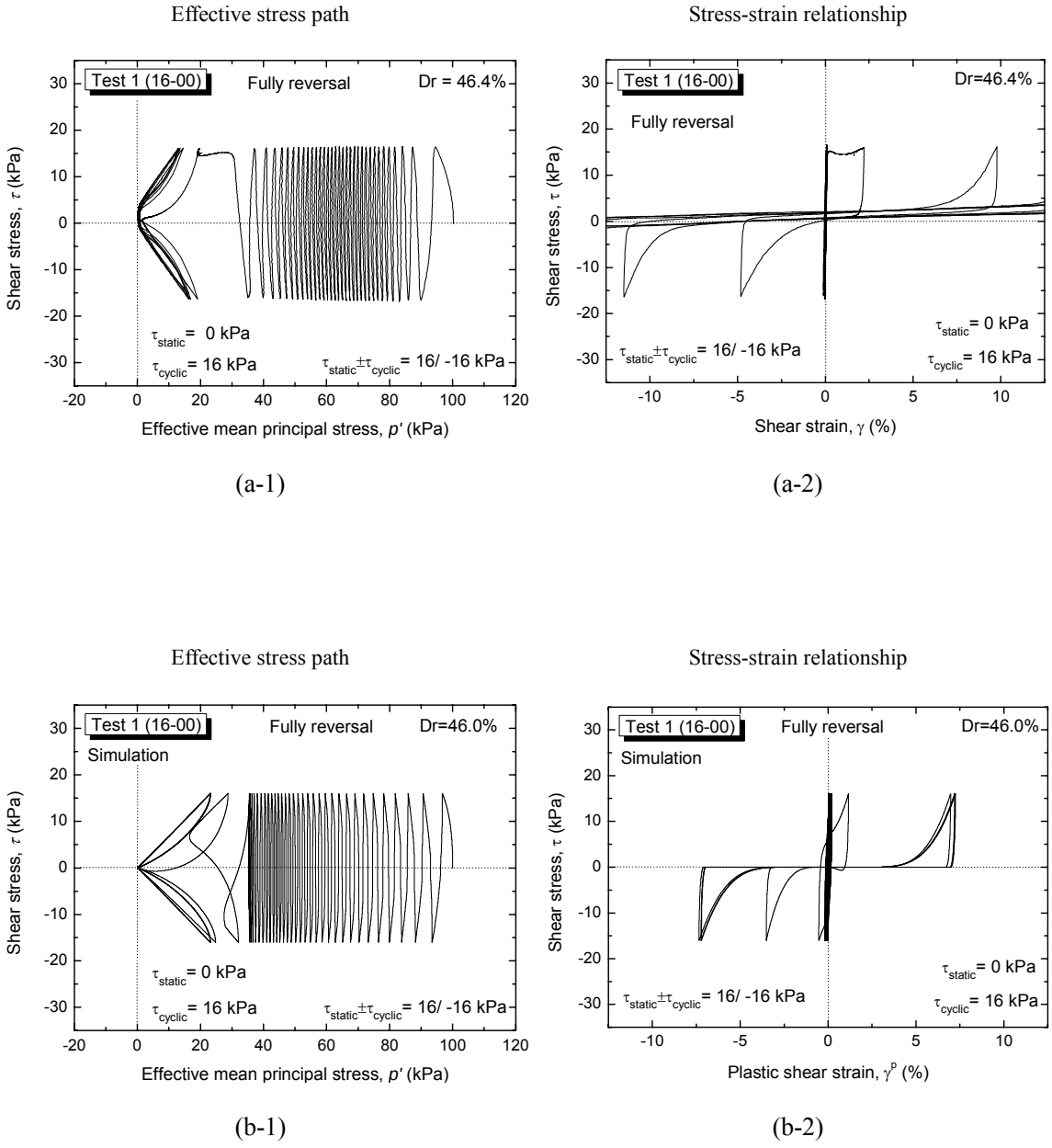

Fig. 5.28: Test 1 (16-00): (a) Experimental observations; and (b) Simulation results

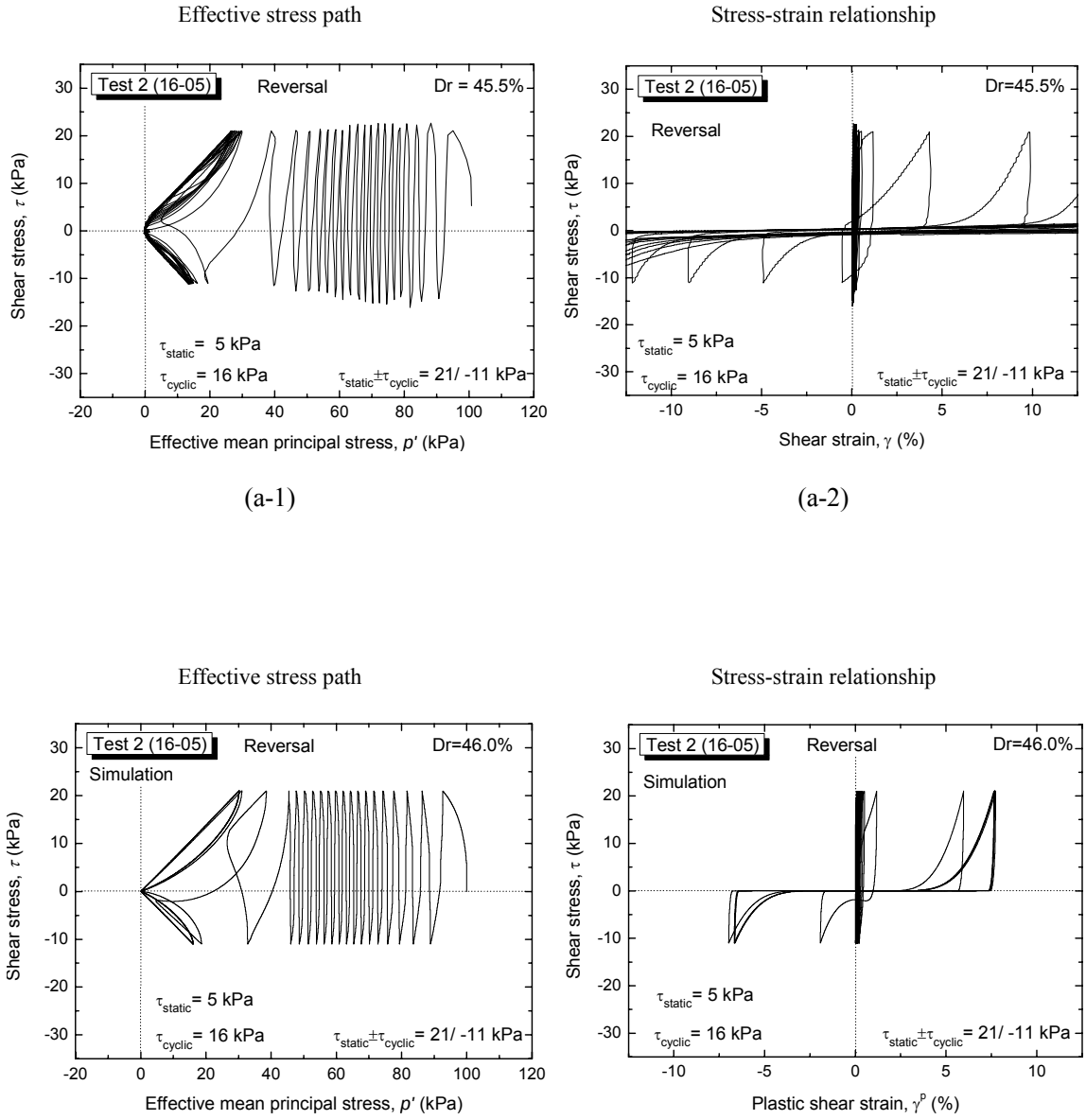

Fig. 5.29: Test 2 (16-05): (a) Experimental observations; and (b) Simulation results

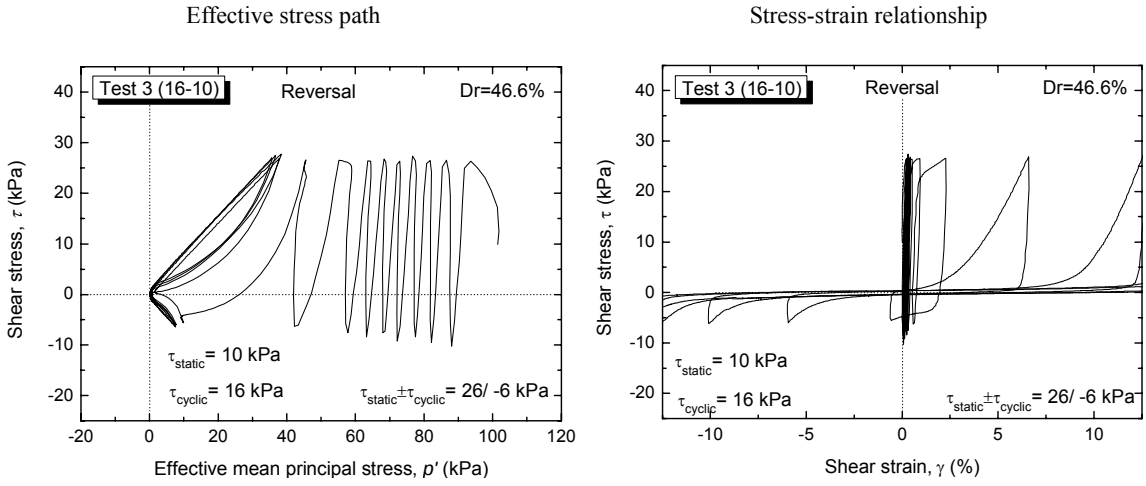

(a-1) (a-2)

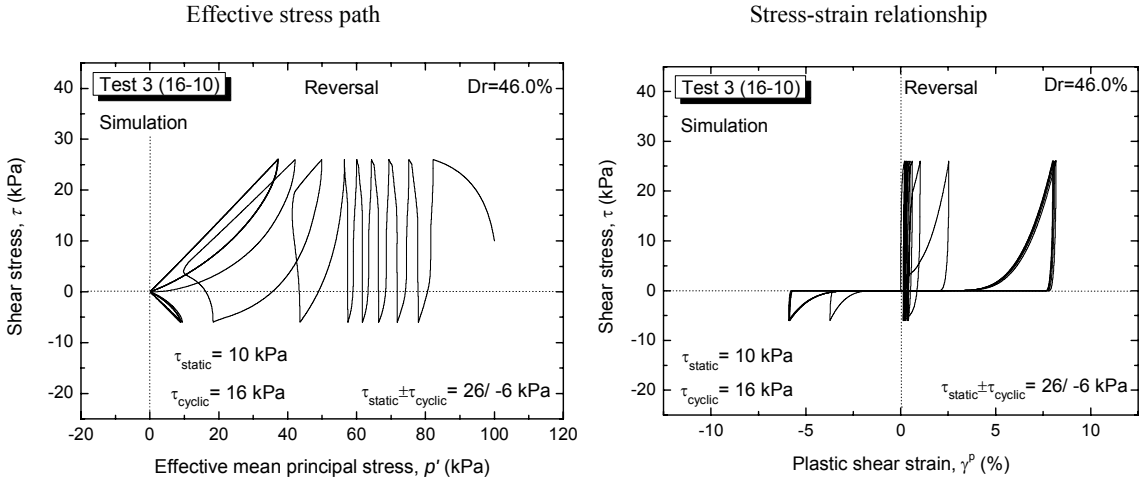

(b-1) (b-2)

Fig. 5.30: Test 3 (16-10): (a) Experimental observations; and (b) Simulation results

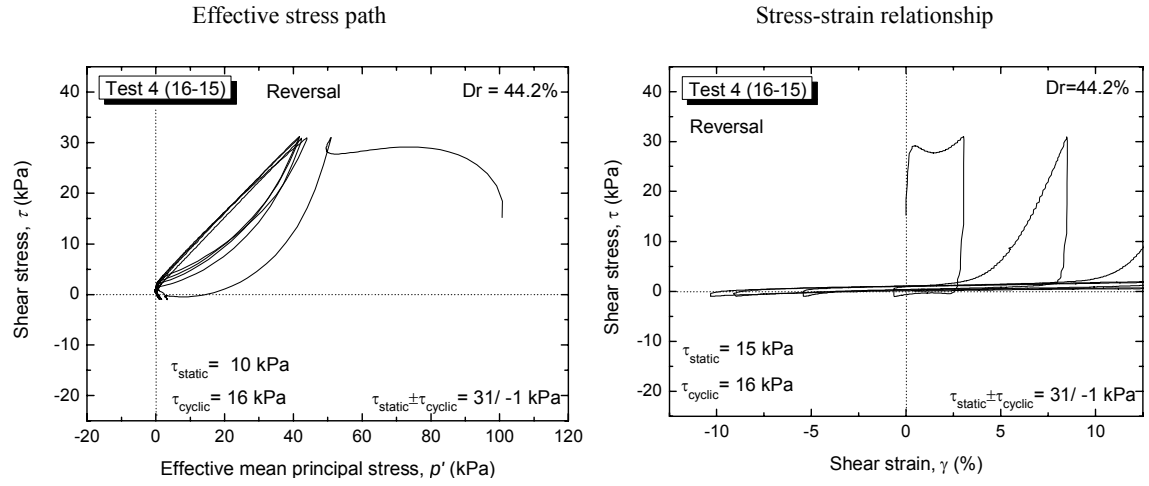

(a-1) (a-2)

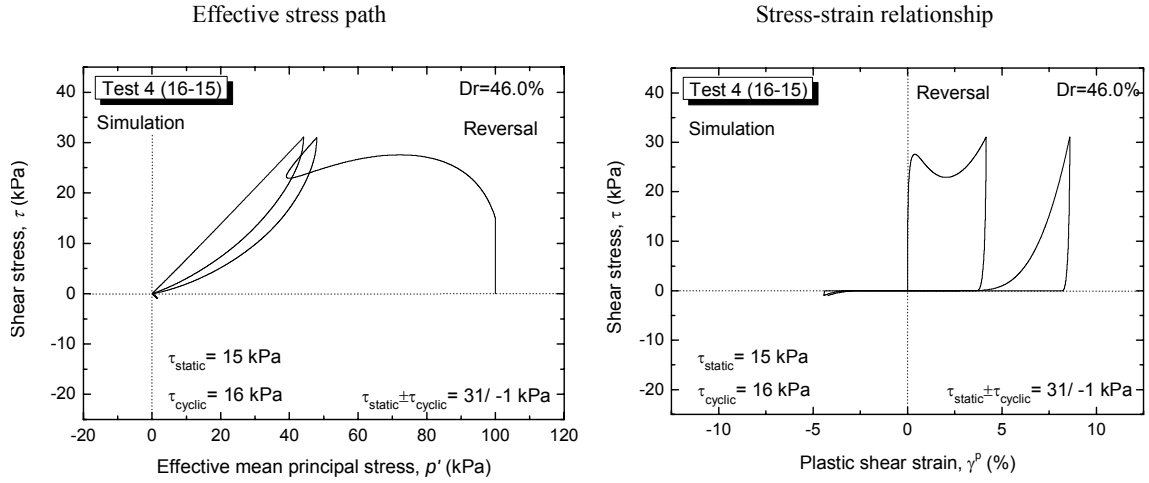

(b-1) (b-2)

Fig. 5.31: Test 4 (16-15): (a) Experimental observations; and (b) Simulation results

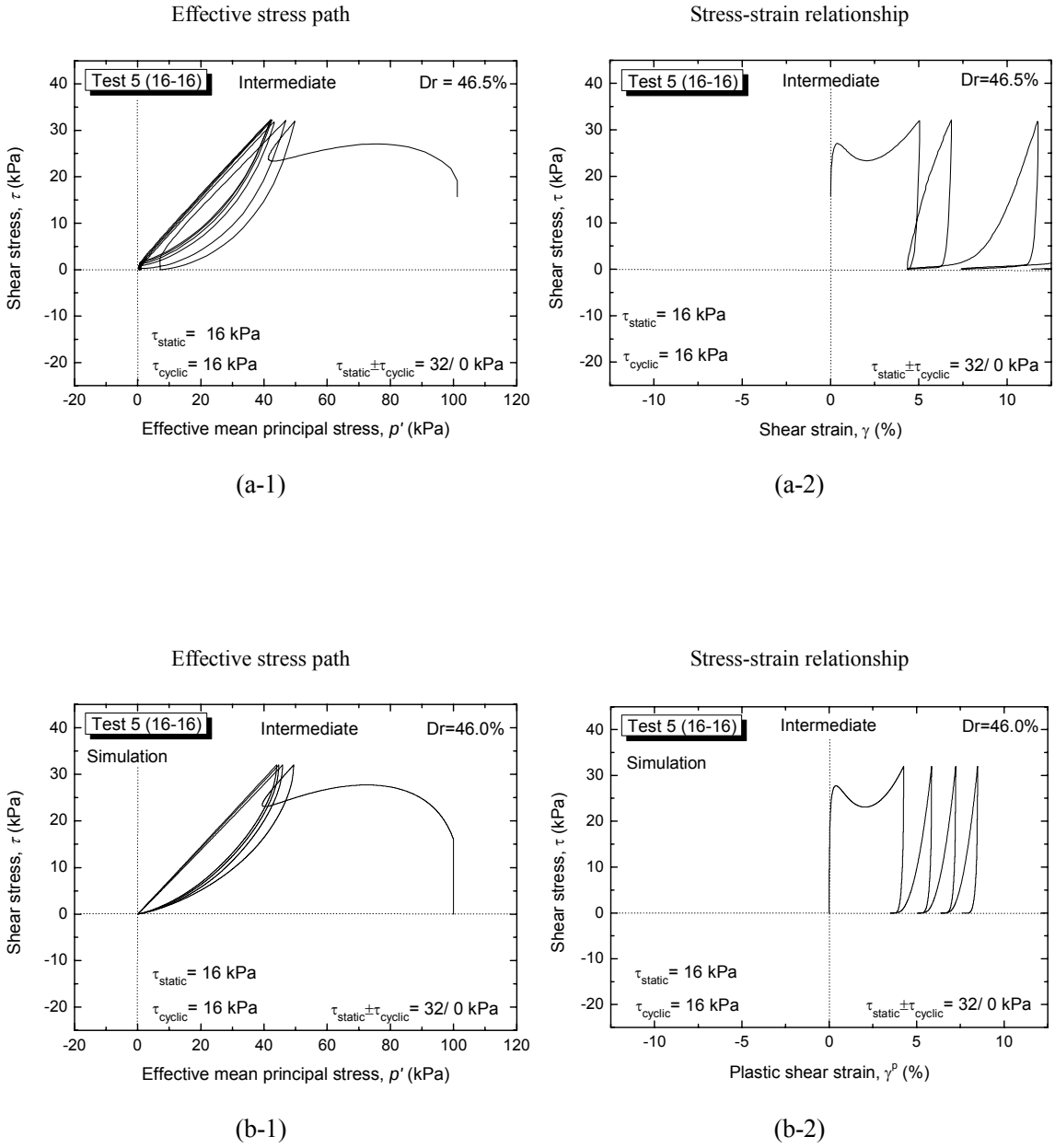

Fig. 5.32: Test 5 (16-16): (a) Experimental observations; and (b) Simulation results

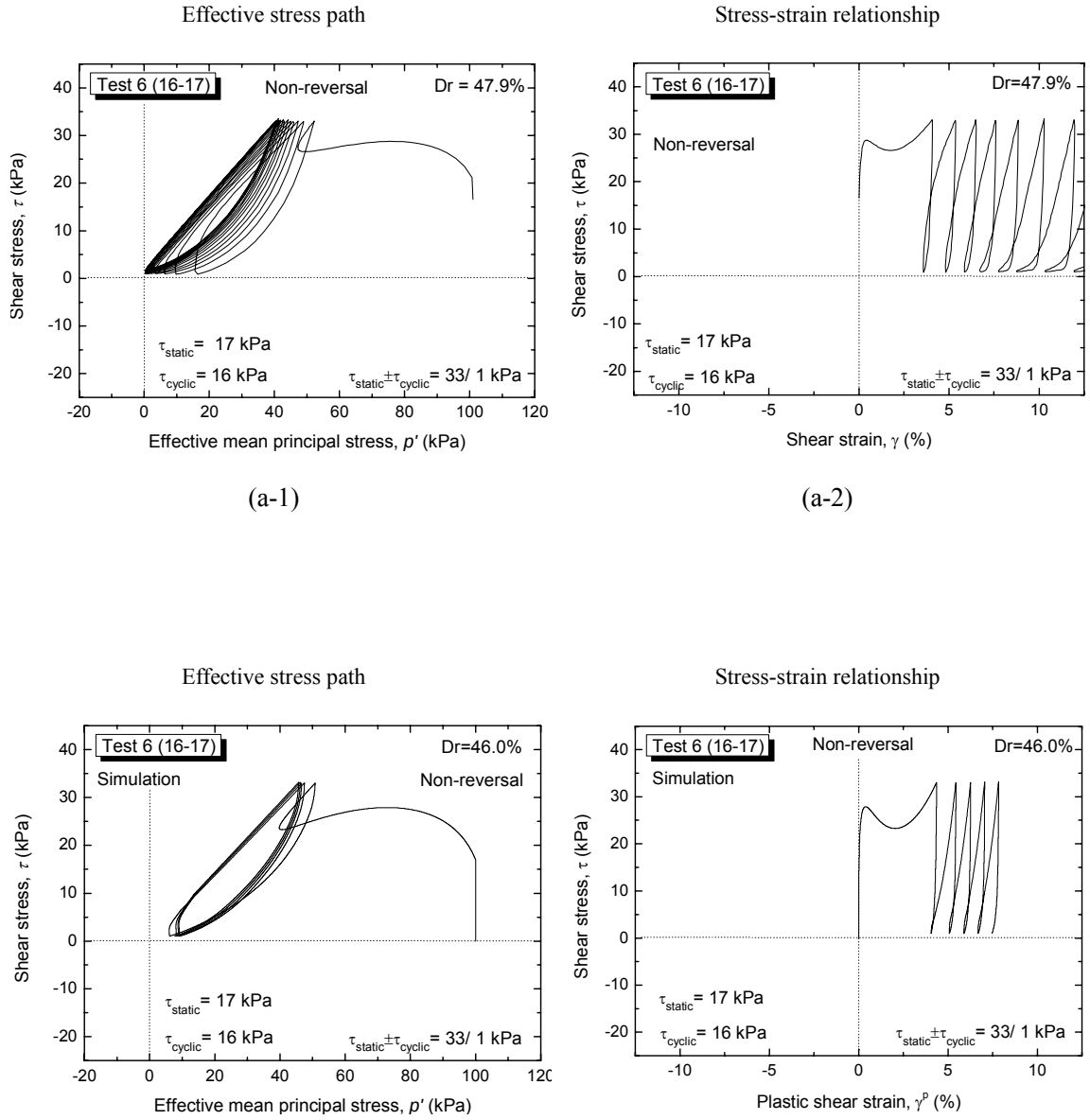

Fig. 5.33: Test 6 (16-17): (a) Experimental observations; and (b) Simulation results

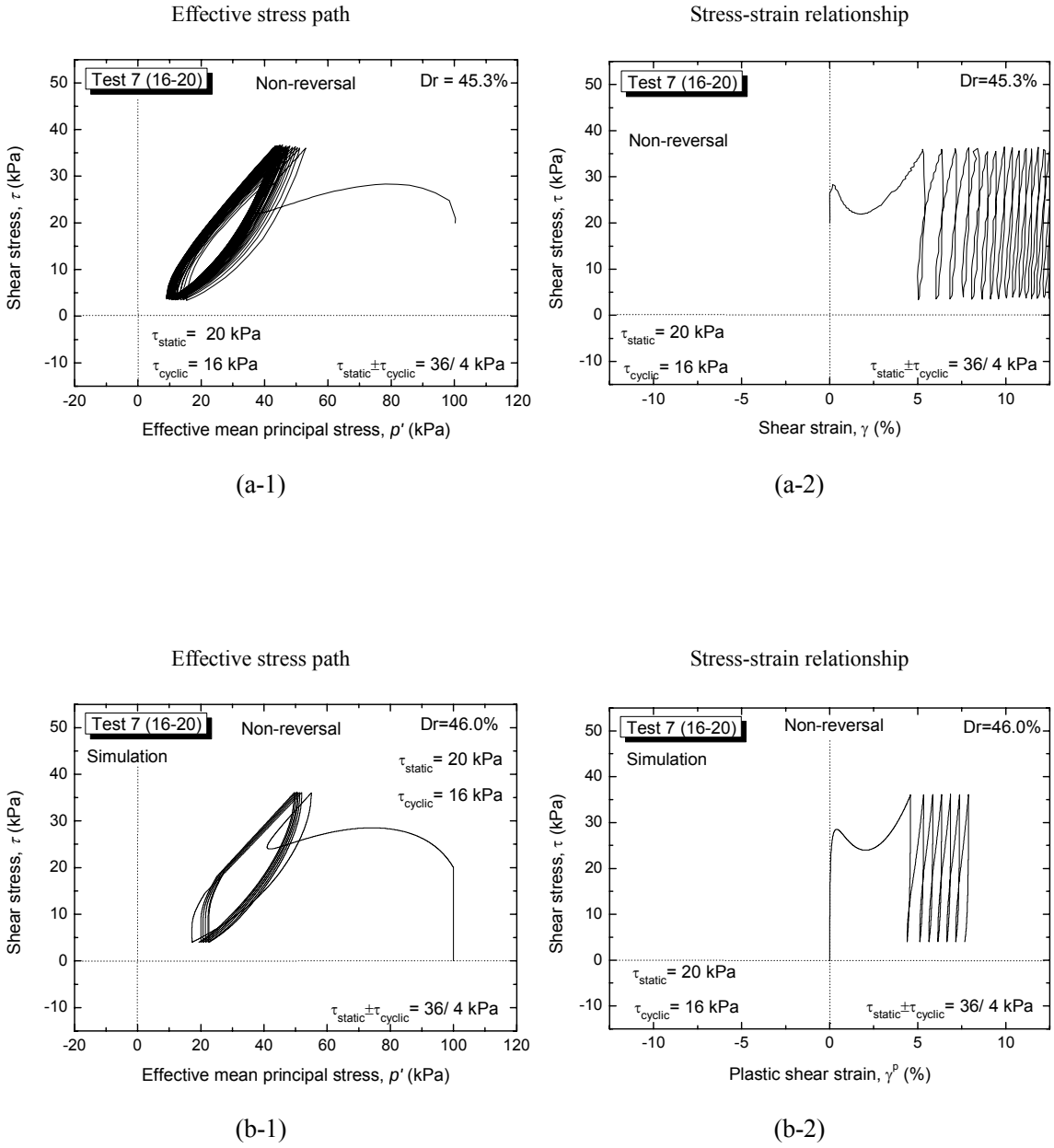

Fig. 5.34: Test 7 (16-20): (a) Experimental observations; and (b) Simulation results

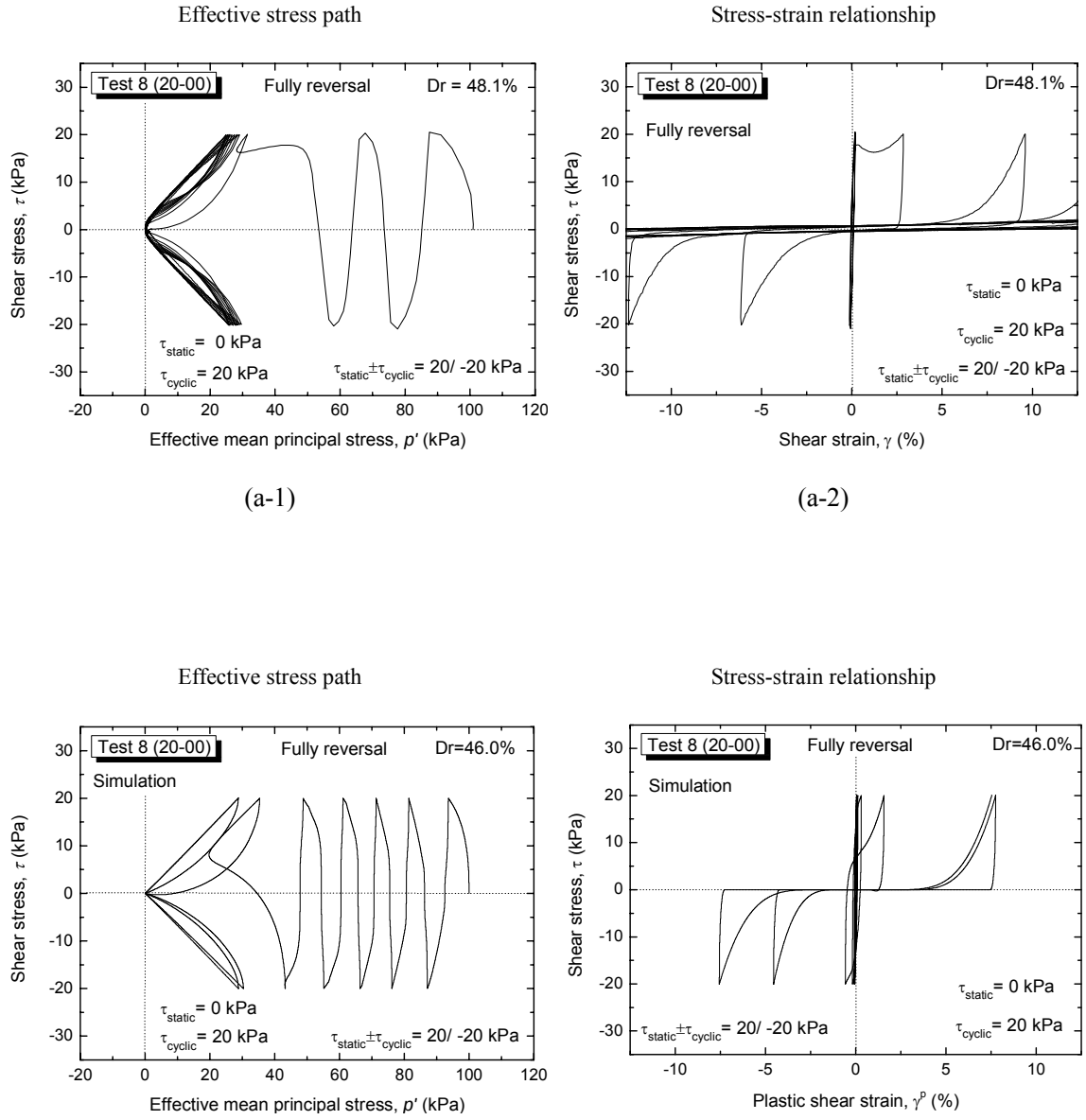

Fig. 5.35: Test 8 (20-00): (a) Experimental observations; and (b) Simulation results

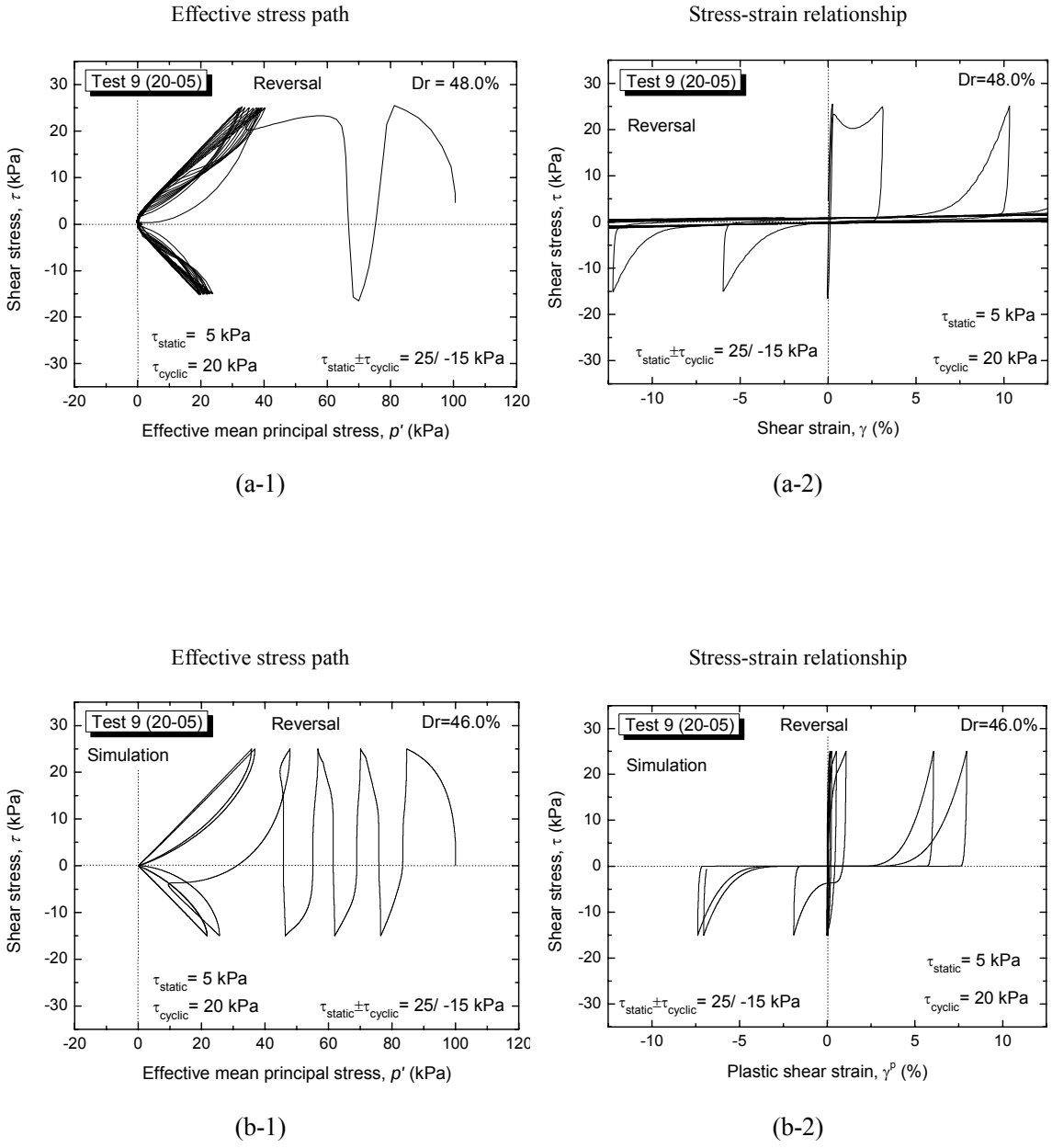

Fig. 5.36: Test 9 (20-05): (a) Experimental observations; and (b) Simulation results

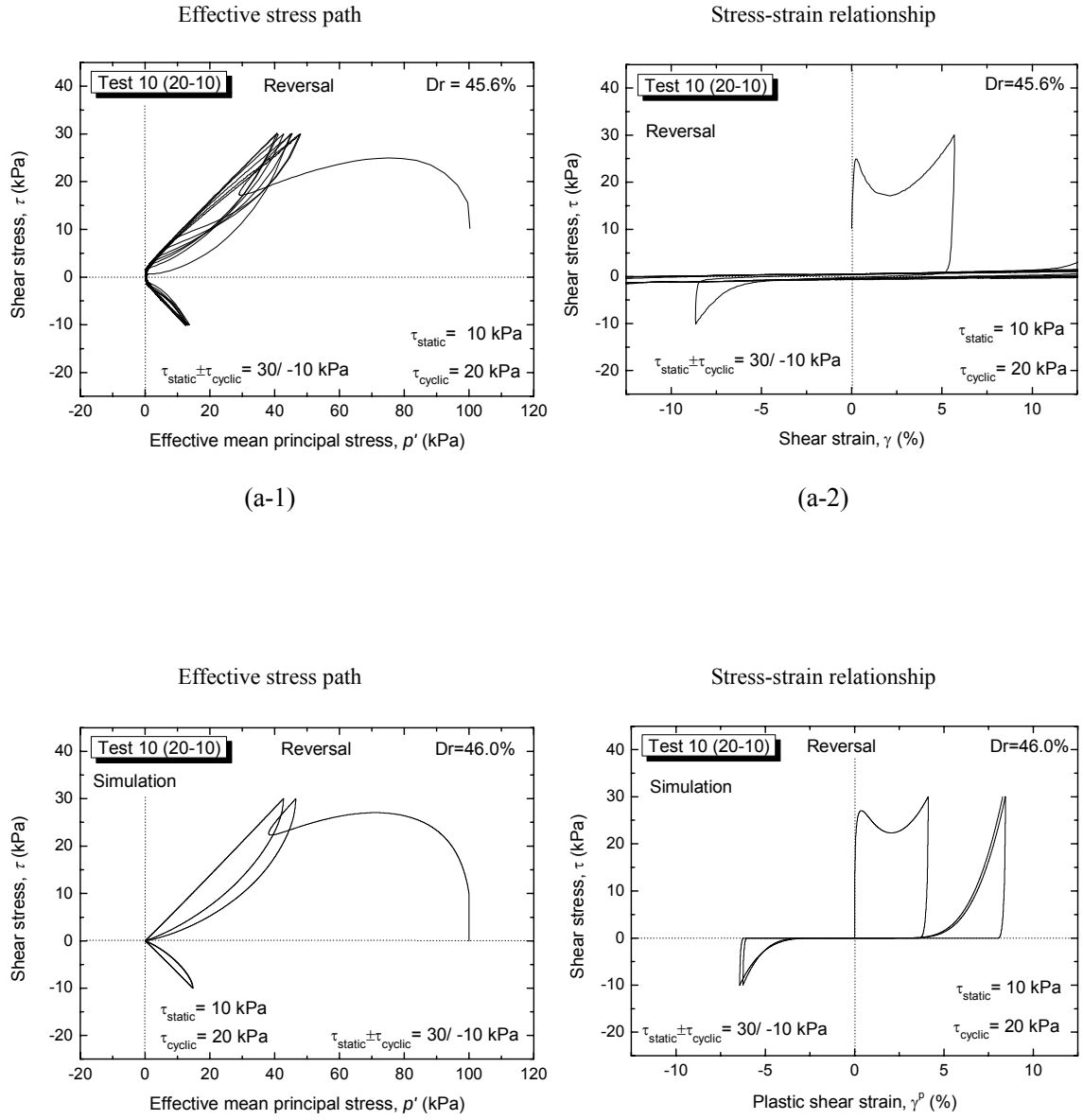

Fig. 5.37: Test 10 (20-10): (a) Experimental observations; and (b) Simulation results

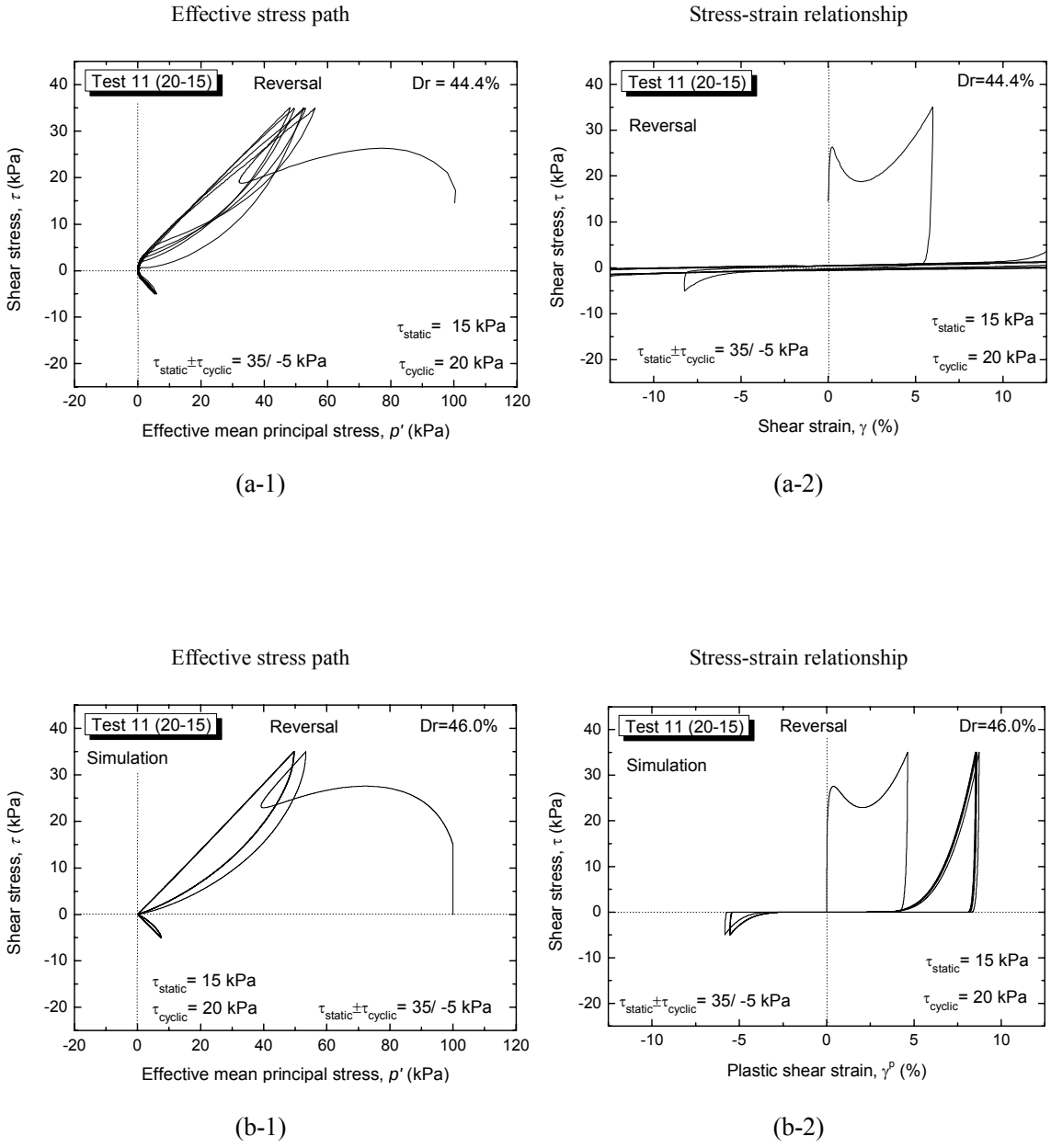

Fig. 5.38: Test 11 (20-15): (a) Experimental observations; and (b) Simulation results

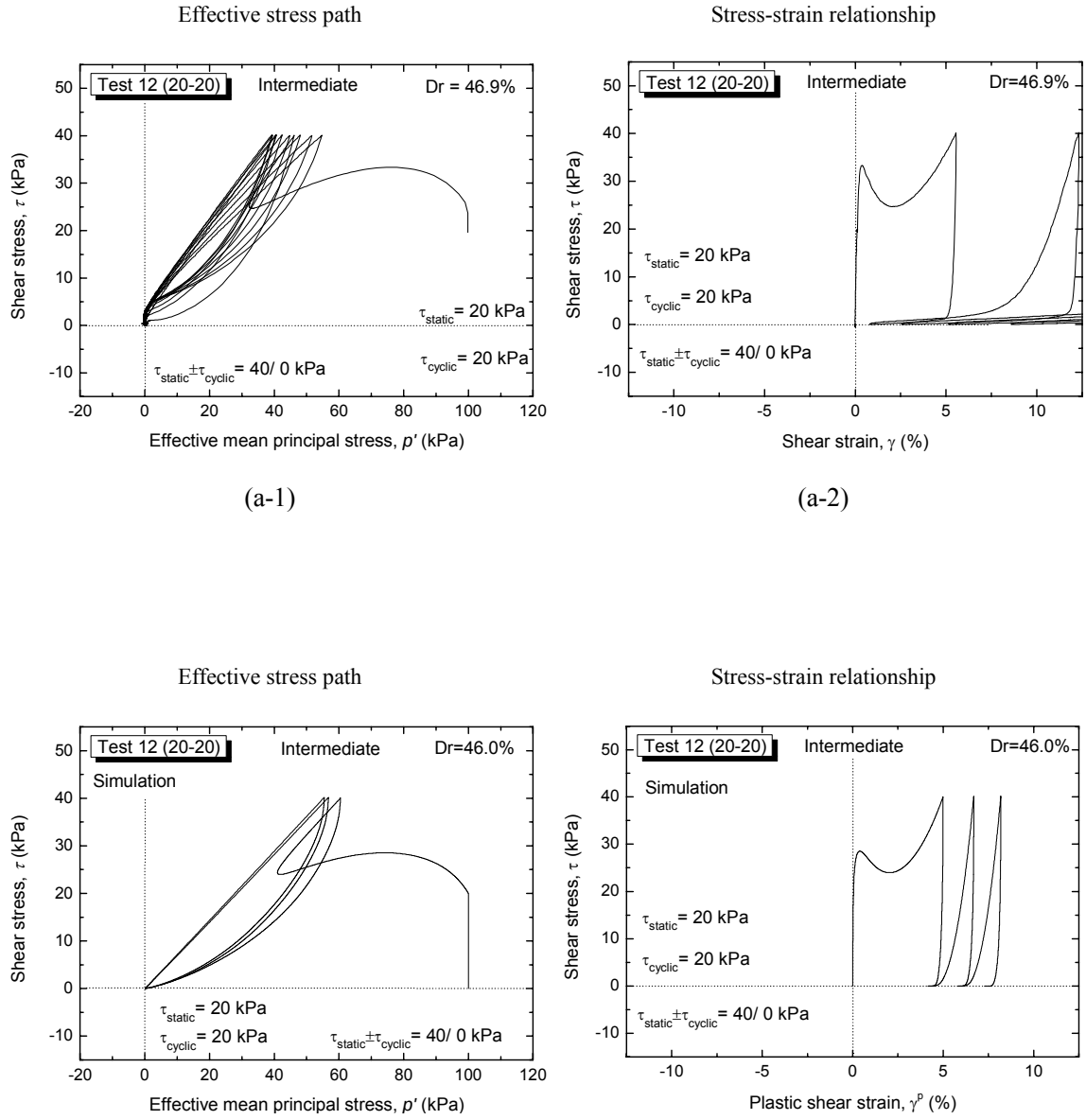

Fig. 5.39: Test 12 (20-20): (a) Experimental observations; and (b) Simulation results

(a)

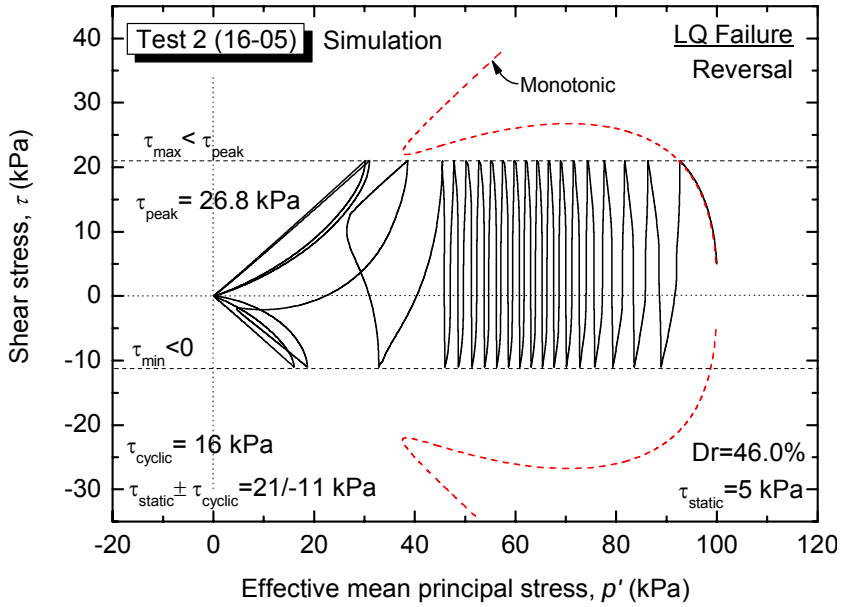

(b)

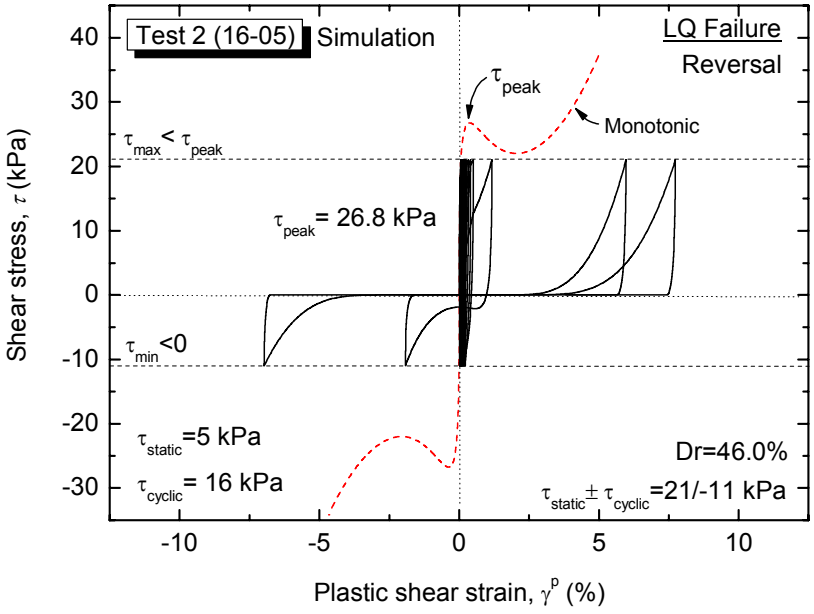

Fig. 5.40: Typical simulation of cyclic liquefaction failure (LQ) behavior: (a) Effective stress path; and (b) Stress-strain relationship

(a)

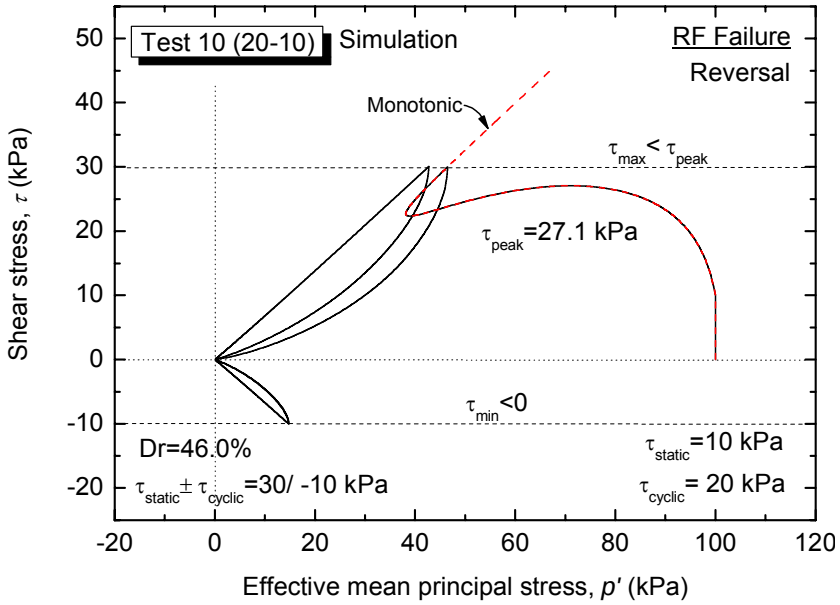

(b)

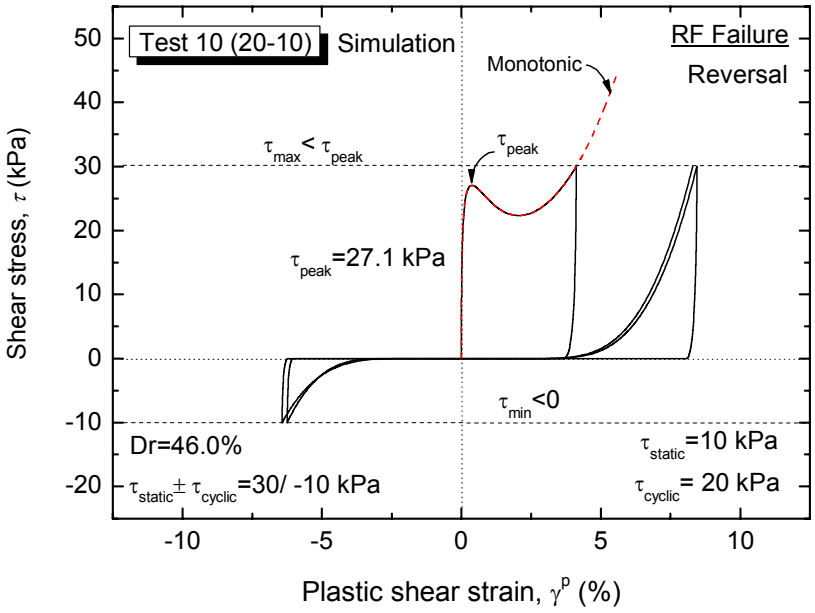

Fig. 5.41: Typical simulation of rapid flow liquefaction failure (RF) behavior for reversal tests: (a) Effective stress path; and (b) Stress-strain relationship

(a)

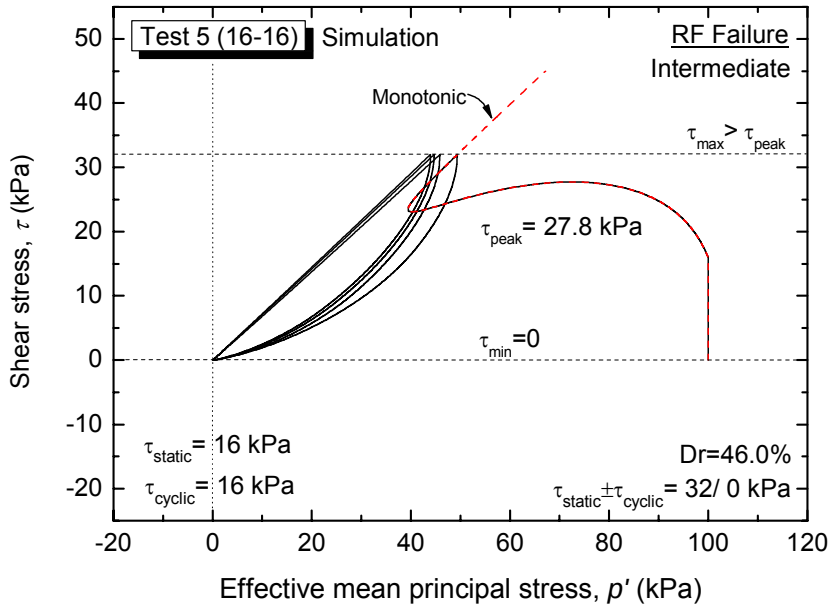

(b)

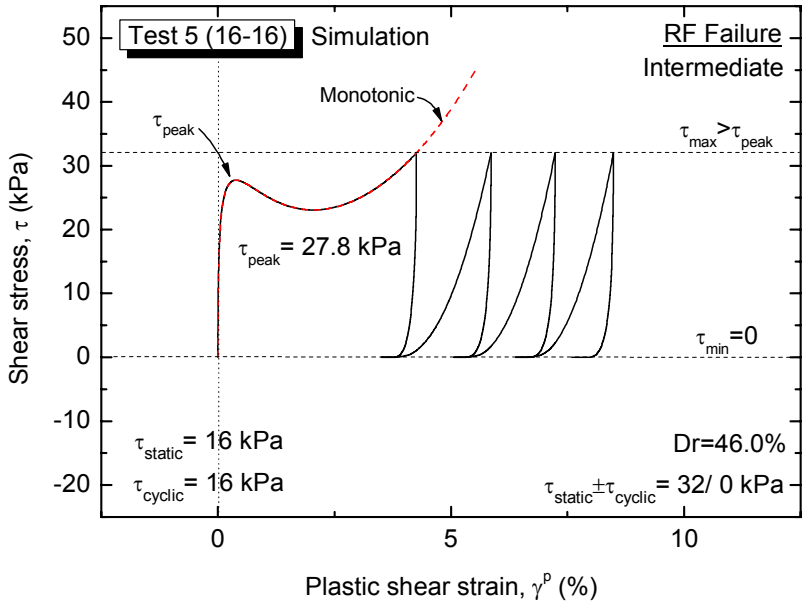

Fig. 5.42: Typical simulation of rapid flow liquefaction failure (RF) behavior for intermediate tests (e.g., Test 5): (a) Effective stress path; and (b) Stress-strain relationship

(a)

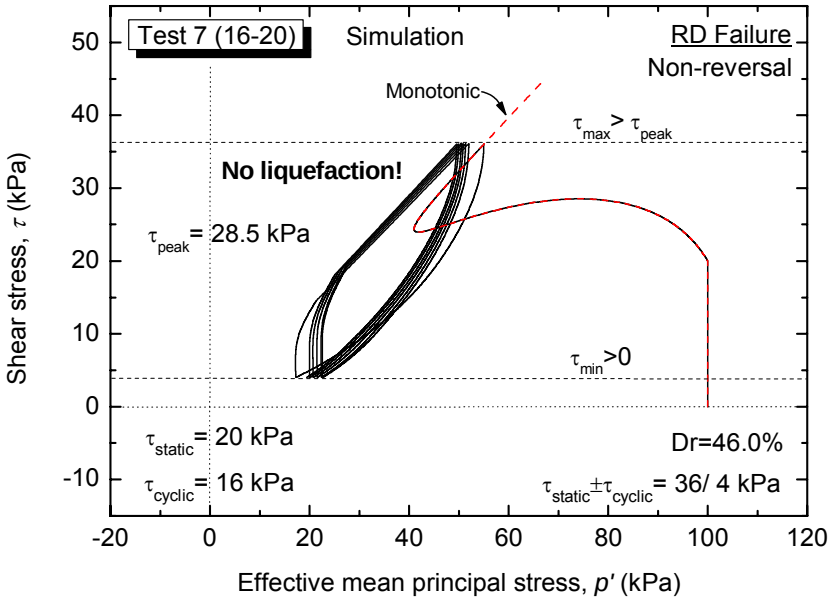

(b)

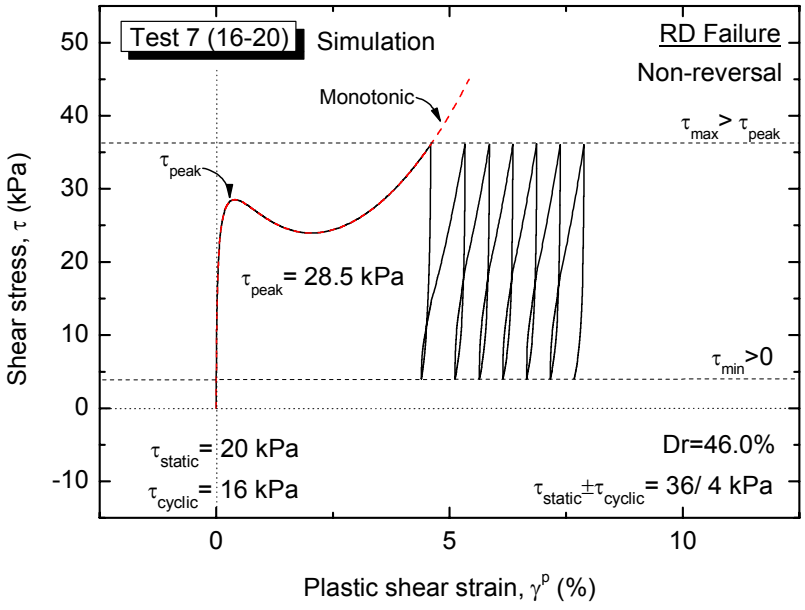

Fig. 5.43: Typical simulation of residual deformation (RD) behavior (e.g., Test 7): (a) Effective stress path; and (b) Stress-strain relationship

(a)

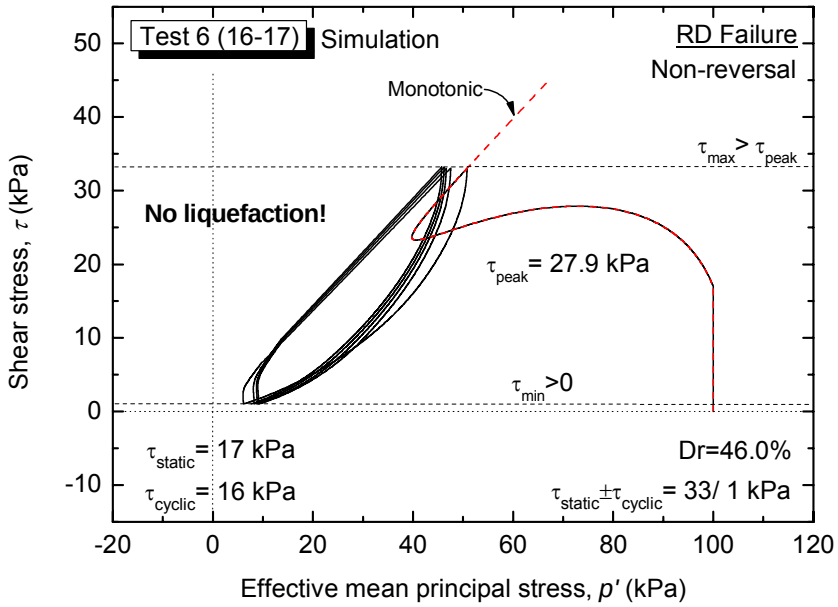

(b)

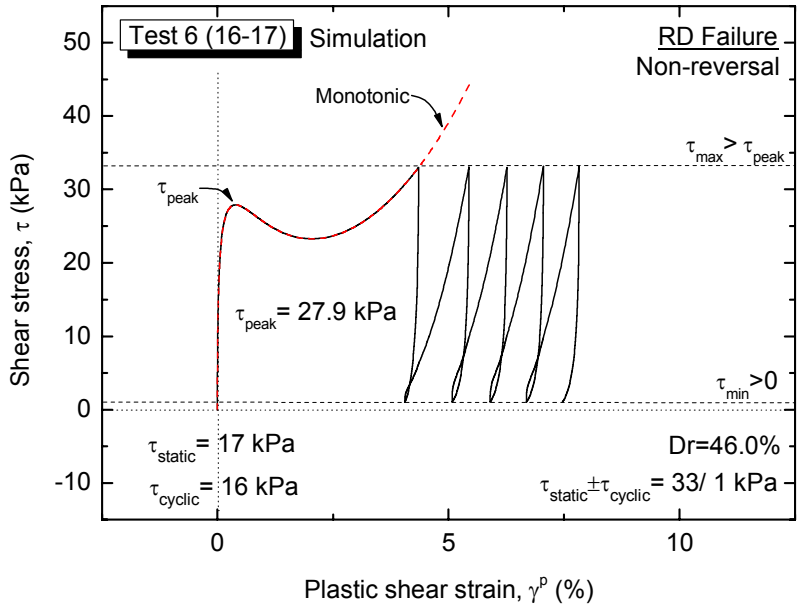

Fig. 5.44: Typical simulation of residual deformation (RD) behavior (e.g., Test 6): (a) Effective stress path; and (b) Stress-strain relationship

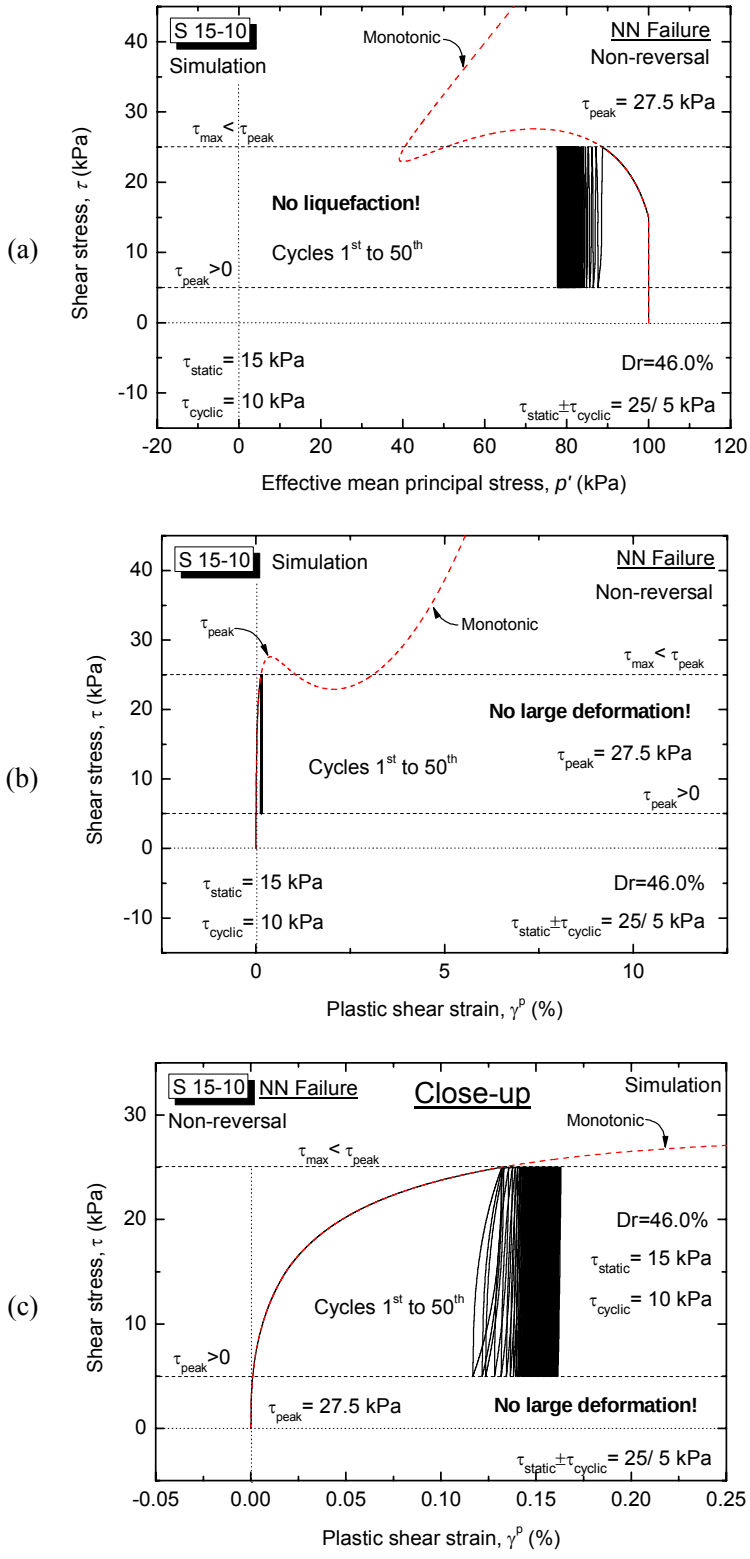

Fig. 5.45: Typical simulation of no liquefaction and no failure behavior (NN) (e.g., S 15-10): (a) Effective stress path; (b) Stress-strain relationship; and (c) Close-up of stress-strain relationship in Fig. 5.43(b)

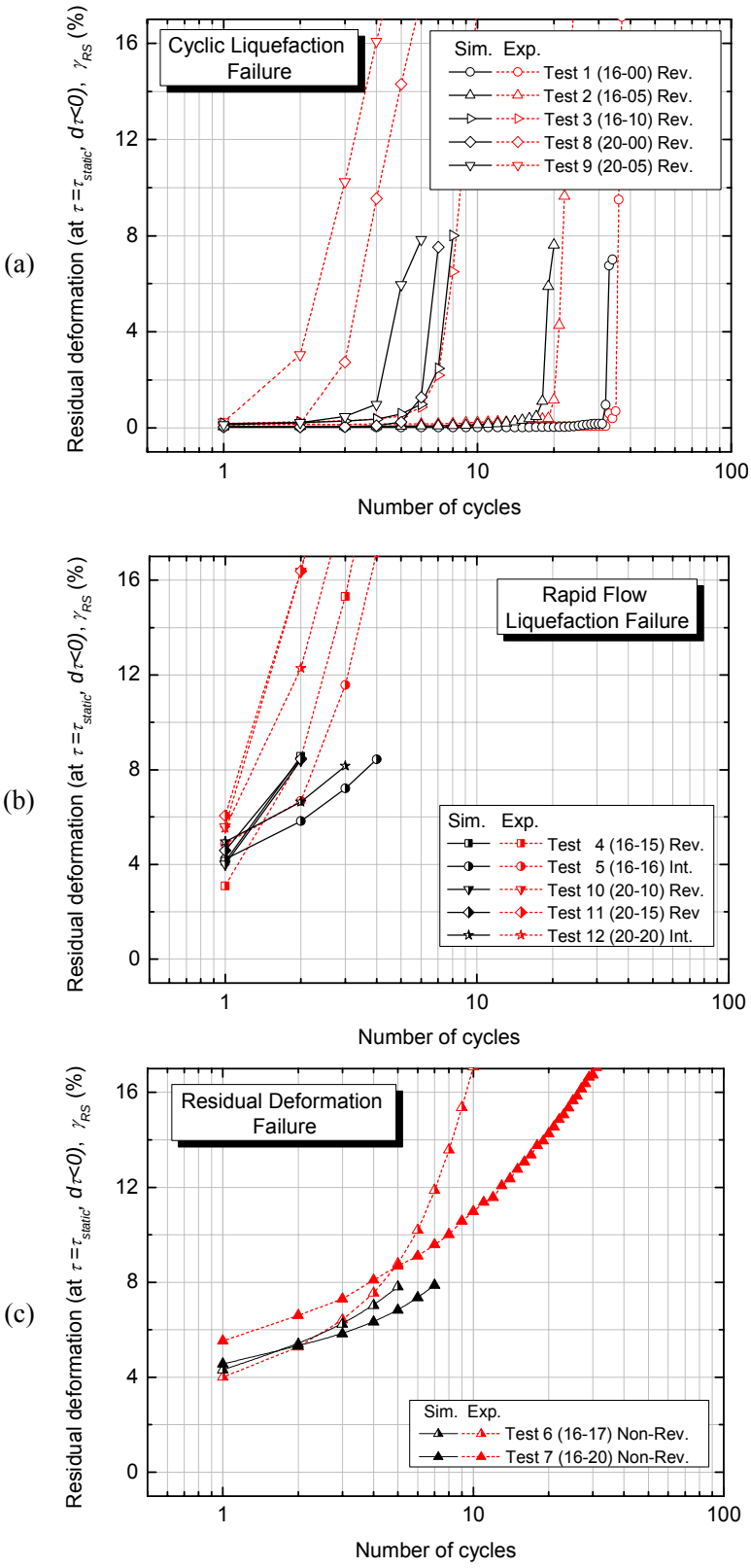

Fig. 5.46: Development of residual deformation during the cyclic loading: (a) LQ failure behavior; (b) RF failure behavior; and (c) RD failure behavior.

(a)

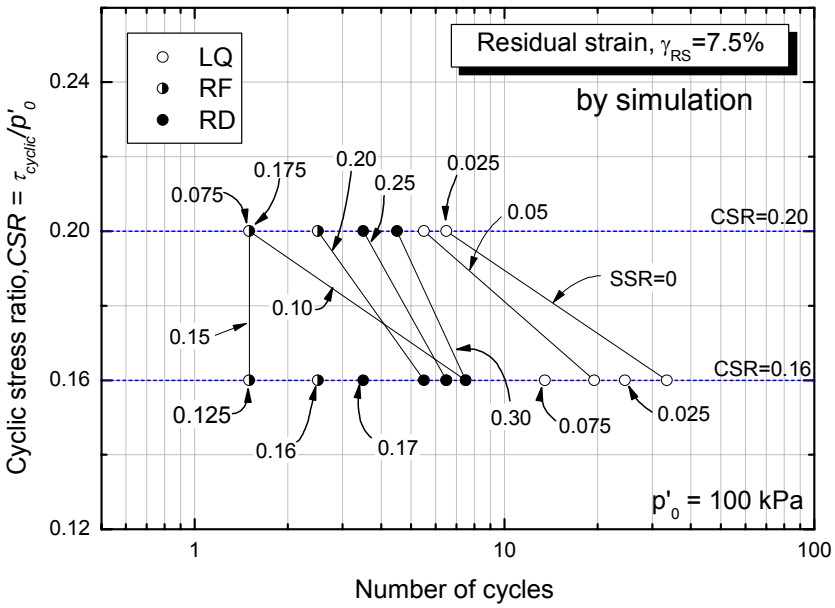

(b)

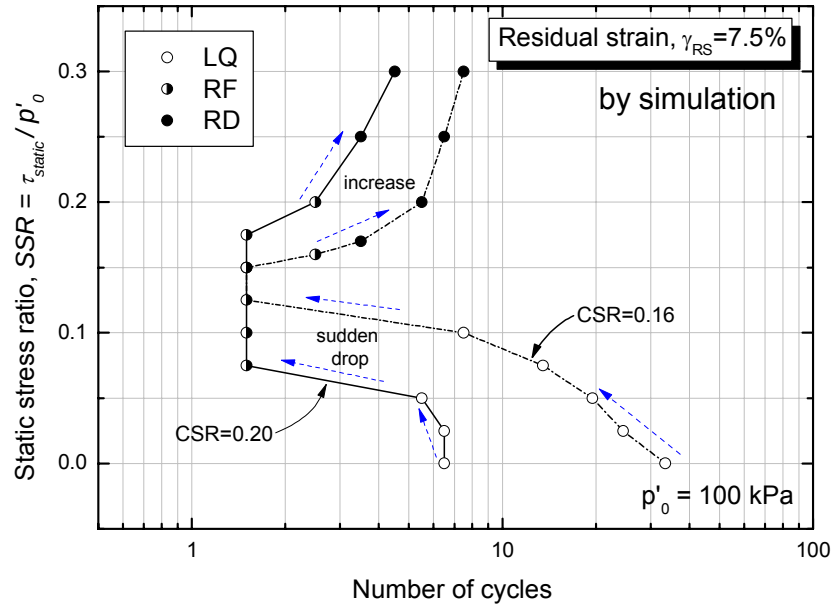

Fig. 5.47: Strain accumulation resistance curve in terms of :

(a) CSR vs. Number of cycles to cause γ_{RS} = 7.5%; and

(b) SSR vs. Number of cycles to cause γ_{RS} = 7.5%

(a)

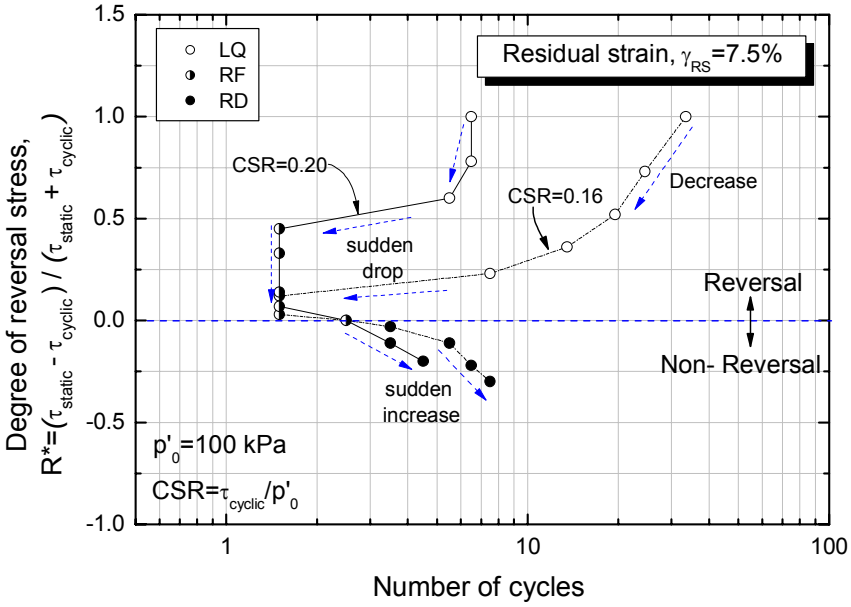

Fig. 5.48: Strain accumulation resistance curve in terms of Degree of reversal stress vs. Number of cycles to cause γ_{RS} = 7.5%

5.6 Summary

With the aim of simulating the behavior of saturated sand with initial static shear undergoing undrained cyclic loading which leads to liquefaction and large cyclic shear strain development, an elasto-plastic constitutive model which can describe both monotonic and cyclic torsional shear behaviors of saturated sand with initial static shear under drained or undrained condition was presented in this study.

To simulate drained and undrained large cyclic behavior of sand, the proposed model requires accurate evaluation of the irreversible strain component. Therefore, in this study, the quasi-elastic constitutive model, named IIS model (Hong Nam, 2004), was used to evaluate the elastic shear strain component. Consequently, in analyzing the hollow cylindrical torsional shear test data, the plastic shear strain components are obtained by subtracting from the measured total shear strain component the elastic one.

The presence of initial static shear stress was introduced in the model by means of a monotonic drained shear loading path before the undrained one.

The two-phase (drained followed by undrained) monotonic loading behavior which is defined in terms of shear stress vs. plastic shear strain relationship (i.e., skeleton curve) was simulated by employing the GHE model proposed by Tatsuoka and Shibuya (1991). Based on the experimentally obtained skeleton curves, the undrained cyclic shear loading behavior was modeled by using the extended Masing's rules whilst considering: (a) rearrangement of particles during cyclic loading (drag effect), (Tatsuoka et al., 2003; Hong Nam, 2004); (b) damage of plastic shear modulus at large level of shear stress (De Silva, 2008) and (c) hardening of the material during cyclic loading (De Silva, 2008).

In addition, in modeling the undrained cyclic shear behavior it was assumed that the total volumetric strain increment during the undrained loading, which consists of dilatancy and consolidation/swelling components, is equal to zero. An empirical four-phase stress-dilatancy relationship which varies with the amount of damage to the plastic shear modulus of the material (De Silva, 2008) was employed in order to model the accumulation of volumetric strain increment due to dilatancy and the generation of pore water pressure during the undrained cyclic torsional shear loading.

A modified OC boundary surface was proposed to introduce the combined effects of over-consolidation and initial static shear stress into the model.

Applicability of the proposed model was verified by simulating the experimental results that were conducted in order to study the effect of initial static shear stress on the undrained cyclic behavior of saturated Toyoura sand. The following satisfactory simulation results were obtained:

(i) The proposed model could simulate the behavior of loose saturated sand subjected to undrained torsional shear loading, under general conditions of stress reversal, intermediate and non-reversal loadings by varying the initial static shear and the amplitude of the subsequent cyclic shear stresses (i.e., varying the degree of reversal stress).

(ii) The liquefaction behavior of sand, described in terms of effective stress path, can be qualitatively modeled until the specimen enters into a full liquefaction state ($p'=0$), as well as during the cyclic mobility process. The stress-strain relationship revealed that the development of large deformation up to shear strain of 8% can be qualitatively modeled as well.

(iii) The simulation results of both monotonic and cyclic undrained behavior could be employed to evaluate the failure behavior of sand. Therefore, cyclic liquefaction (LQ), rapid flow liquefaction (RF) and residual deformation (RD) failures were simulated. As well, by conducting additional numerical simulations, the behavior called as no-liquefaction and no-failure (NN), in which either liquefaction or failure did not take place even after applying several tens of cycles, could be defined.

(iv) The simulations confirmed that three types of mode of development of residual deformation can be observed according to the above types of failure behavior of sand.

(v) It was confirmed also that even though the amount of non-reversal stress is only 1 kPa, liquefaction did not take place; as a consequence, liquefaction behavior observed in laboratory for Test 6 (16-17) can be associated with technical limitations in conducting accurate correction for membrane force and /or accurate stress control.

(vi) The resistance against strain accumulation can either increase or decrease depending

on the level of initial static shear and the amplitude of cyclic shear stress (i.e., extent of reversal stress). Much more stress conditions than the ones performed in the laboratory were simulated in order to define strain accumulation resistance curves with more details. A two-phase change in strain accumulation behavior was observed; it was associated with a two-phase change in the failure behavior from LQ to RF and from RF to RD.

5.7 References

1. Balakrishnayer, K. (2000): "Modeling of deformation characteristics of gravel subjected to large cyclic loading", Ph.D. thesis, Dep. of Civil Engineering, University of Tokyo, Japan
2. De Silva, L.I.N. (2008): "Deformation characteristics of sand subjected to cyclic drained and undrained torsional loadings and their modeling", Ph.D. thesis, Dep. of Civil Engineering, University of Tokyo, Japan
3. Hardin, B. O. and Richart Jr., F. E. (1963): "Elastic wave velocities in granular soils", Journal of Soil Mechanics and Foundation Division, ASCE, 89 (SM1), 33-65
4. Hong Nam, N. (2004): "Locally measured quasi-elastic properties of Toyoura sand in cyclic triaxial and torsional loadings", Ph.D. thesis, Dep. of Civil Engineering, University of Tokyo, Japan
5. Ishihara, K., Tatsuoka, F. and Yasuda, S. (1975): "Undrained deformation and liquefaction of sand under cyclic stresses", Soils and Foundations, 15 (1), 29-44
6. Konder, R. L. (1963): "Hyperbolic stress-strain response: cohesive soils", Journal of Soil Mechanics and Foundation Division, ASCE, 89 (SM1), 115-143
7. Masing, G. (1926): "Eiganspannungen und verfestigung beim messing" Proc. of 2nd International Conference of Applied Mechanics, Zurich, 332-335
8. Masuda, T. (1998): "Study on the effect of pre-load on the deformation of excavated ground", Ph.D. thesis, Dep. of Civil Engineering, University of Tokyo, Japan (in Japanese)
9. Masuda, T., Tatsuoka, F., Yamada, S. and Sato, T. (1999): "Stress-strain behavior of sand in plane strain compression, extension and cyclic loading tests", Soils and Foundations, 39 (5), 31-45
10. Nishimura, S. (2002): "Development of three dimensional stress-strain model of sand undergoing cyclic undrained loading and stress-axes rotation", M.Eng. thesis, Dept. of Civil Engineering, University of Tokyo, Japan
11. Ohsaki, Y. (1980): "Some notes on Masing law and non-linear response of soil deposits", Journal of the Faculty of Engineering, The University of Tokyo, XXXXV(4), 513-536
12. Oka, F., Yashima, A., Tateishi, Y., Taguchi, Y. and Yamashita, S. (1999): "A cyclic elasto-plastic constitutive model for sand considering a plastic-strain dependence of the shear modulus", Geotechnique, 49 (5), 661-680
13. Pradhan, T. B. S. (1990): "The behavior of sand subjected to monotonic and cyclic loadings", Ph.D. thesis, Dep. of Civil Engineering, University of Tokyo, Japan

14. Pyke, R. (1979): "Non-linear soil models for irregular cyclic loading", Journal of Geotechnical Engineering Division, ASCE, 105 (GT6), 715-726

15. Tatsuoka, F. and Shibuya, S. (1991): "Modeling of non-linear stress-strain relations of soil and rocks- Part 1: New equation", Seisan-Kenkyu, Journal of Institute of Industrial Science, University of Tokyo, 43 (10), 435-437

16. Tatsuoka, F., Jardine, R. J., Lo Presti, D., Di Benedetto, H. and Kodaka, T. (1997): "Characterizing the pre-failure deformation properties of geomaterials, Theme lecture for the plenary session No.1", Proc. of 14th International Conference on Soil Mechanics and Foundation Engineering, Hamburg, Vol. 4, 2129-2164

17. Tatsuoka, F., Masuda, T., Siddiquee, M. S. A. and Koseki, J. (2003): "Modeling the stress-strain relations of sand on cyclic plane strain loading", Journal of Geotechnical and Geoenvironmental Engineering, ASCE, 129 (6), 450-467

18. Yu, P. and Richart Jr., F. E. (1984): "Stress ratio effects on shear modulus of dry sands", Journal of Geotechnical Engineering, ASCE, 110 (3), 331-345

CHAPTER 6

A method for assessing the failure behavior of sand with initial static shear

6.1 Introduction

Soils that are susceptible to liquefaction consist substantially of saturated uniform grain size distributions deposited in loose states. However, the fact that a soil is susceptible to liquefaction does not guarantee that liquefaction will be actually initiated during an earthquake event.

It is also recognized that the stress conditions (confining pressure, cyclic shear and initial static shear stresses) play an important role in the liquefaction behavior of soil, the type of failure mechanism and the mode of development of soil deformation, especially in the case of slopes of sandy deposits.

Many studies on the liquefaction of sand, including the current one, show that under non-reversal stress conditions saturated loose sand most likely will not experience liquefaction. However, this does not mean that sand is very resistant against seismic loading; in fact, a significant magnitude of combined static and cyclic shear stresses may cause failure of soil even though liquefaction does not take place.

For these reasons, it is definitely important not only to have a clear understanding of the liquefaction mechanisms, but also to carry out in depth investigation on the effects of static shear on the failure modes of saturated sandy soil during undrained shearing.

In view of the above, in this chapter, a method to assess the failure behavior of sand specimens with initial static shear under undrained cyclic torsional shear loading is presented. Its applicability is investigated on a wide range of combinations of static and cyclic shear stresses on very loose, loose and dense sand by referring to: (i) the results of undrained cyclic torsional shear tests; and (ii) a number of single-element numerical simulations by employing the elasto-plastic constitutive model described in chapter 5.

Finally, on the basis of field data investigations from case histories of liquefaction-induced failure of sandy slopes during past earthquakes, the proposed method is used directly to compare the sand failure characteristics observed in the laboratory with the failure of slopes on site.

6.2 The four-zone CSR/MPSR vs. SSR/MPSR method

6.2.1 Failure behavior of sand in undrained torsional shear tests

In this study, based on the difference in the effective stress paths and the modes of development of shear strain during both monotonic and cyclic undrained torsional shear loading, three types of failure could be identified (refer to section 4.3 for their description):

$$\begin{cases} \begin{cases} \textit{Cyclic liquefaction failure } (LQ) \\ \textit{Rapid flow liquefaction failure } (RF) \end{cases} \textit{Liquefaction} \\ \textit{Residual deformation failure } (RD) \end{cases}$$

In addition, by numerical simulations, the case in which either failure or liquefaction did not take place even after applying several tens of cycles could be defined. This additional case was called No Liquefaction -No Failure (NN), as described in section 5.5.2.

To describe the liquefaction or cyclic strain accumulation behavior of sand during cyclic loading, two parameters referred to as cyclic stress ratio (*CSR*) and static stress ratio (*SSR*) were employed in this study:

$$CSR = \frac{\tau_{cyclic}}{p'_0} \tag{6.1}$$

$$SSR = \frac{\tau_{static}}{p'_0} \tag{6.2}$$

where

- τ_{cyclic} = cyclic shear stress;
- τ_{static} = static shear stress;
- p'_0 = initial effective mean principal stress.

Both the experimental observations and simulation results show that the liquefaction or strain accumulation resistances can either increase or decrease depending on the level of initial static shear and the amplitude of the cyclic shear stress (i.e., degree of reversal stress R^*). However, as described in section 4.4 and section 5.5.4, R^* is not a sufficient single parameter to describe the two-phase change in the cyclic strain accumulation behavior; on the contrary, the failure behavior can be effectively used to describe the two-phase strain accumulation resistance behavior.

6.2.2 Static and cyclic stress conditions

With the aim of gaining a better understanding of the failure mechanisms of saturated sand, the failure behaviors observed in the laboratory or obtained by numerical simulations were analyzed in terms of CSR-SSR relationship. In Fig. 6.1, all the LQ, RF and RD failure behaviors obtained by numerical simulation as listed in Table 5.1 are depicted; in addition, the NN behavior for Test S15-10 presented in Fig. 5.43 is also plotted. It can be seen that, for each of the four types of failure behavior, a specific region can be distinguished. This suggests that each failure behavior can be developed only under specific stress conditions.

In order to define the stress conditions required to produce each type of failure behavior, the following two boundary conditions were taken into consideration:

$$SSR = CSR \tag{6.3}$$

$$SSR + CSR = MPSR_0 \tag{6.4}$$

where $MPSR_0$ is the reference monotonic undrained peak stress ratio defined as follows:

$$MPSR_0 = \frac{\tau_{peak,0}}{p'_0} \tag{6.5}$$

$\tau_{peak,0}$ = the reference undrained peak strength referred to for the case at which $\tau_{static} = 0$ kPa (i.e., no static shear).

The boundary condition expressed by Eq. (6.3) is the stress reversal line. As shown in Fig. 6.2, the stress conditions that are necessary to obtain RD or NN failure behaviors, typically observed for the specimens subjected to non-reversal stress loading ($R^* < 0$),

are located above this line; on the other hand, the stress conditions that are necessary to obtain LQ or RF failure behaviors, typically observed for the specimens subjected to reversal stress loading $(R^* > 0)$, can be found below this line. In addition, the stress conditions that are necessary to obtain the RF failure of the specimens subjected to intermediate stress loading $(R^* = 0)$ are situated on this line itself.

The stress reversal line is also the boundary between liquefaction and no-liquefaction failure behavior; in fact, the test results and their simulation show that in order for liquefaction to take place the reversal of stress is necessary.

The boundary condition expressed by Eq. (6.4) is the line which defines the reference undrained peak strength ($\tau_{peak,0}$) during the monotonic loading for the test with τ_{static} = 0 kPa (e.g., $\tau_{peak,0}$ = 26.8 kPa obtained by simulation for Dr = 46 %, p'_0 =100 kPa and τ_{static} = 0 kPa).

As shown in Fig. 6.3, the stress conditions that are necessary to obtain RF or RD failure behaviors, which were observed in the tests where the maximum stress ($\tau_{max} = \tau_{cyclic} + \tau_{static}$) was higher than the peak strength ($\tau_{max} > \tau_{peak,0}$), can be found above the undrained peak strength line. On the other hand, the stress conditions necessary to obtain NN or LQ failure behaviors, which were observed in the tests where the maximum stress ($\tau_{max} = \tau_{cyclic} + \tau_{static}$) was lower than the peak strength ($\tau_{max} < \tau_{peak,0}$), can be found below the undrained peak strength line.

Using both of the boundary conditions mentioned above, the four-zone CRS-SSR relationship shown in Fig. 6.4 could be defined.

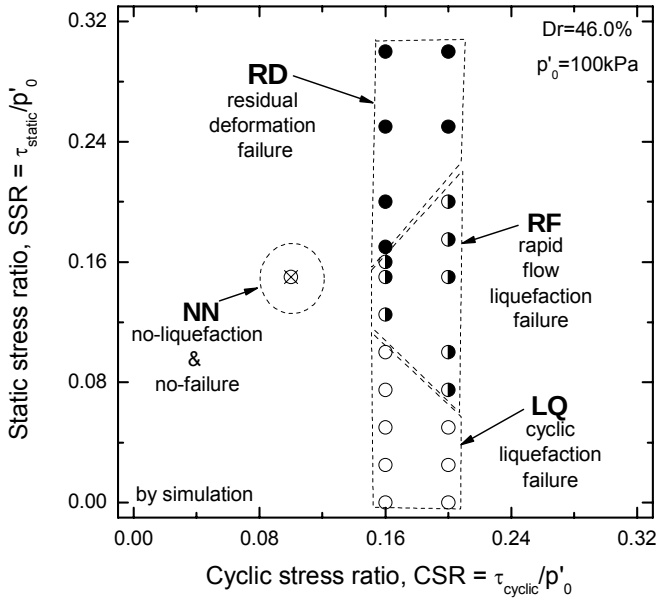

Fig. 6.1: Failure characteristics of sand expressed in terms of CSR-SSR relationship

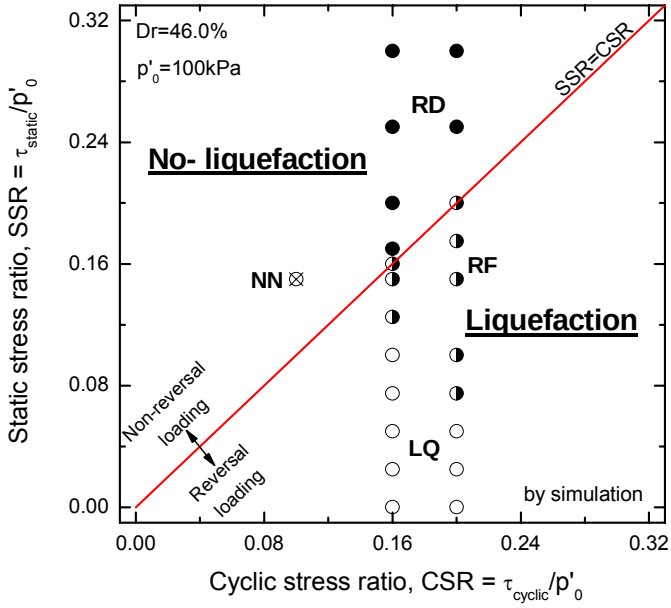

Fig. 6.2: Failure characteristics with respect to the reversal stress line and definition of liquefaction and no-liquefaction regions

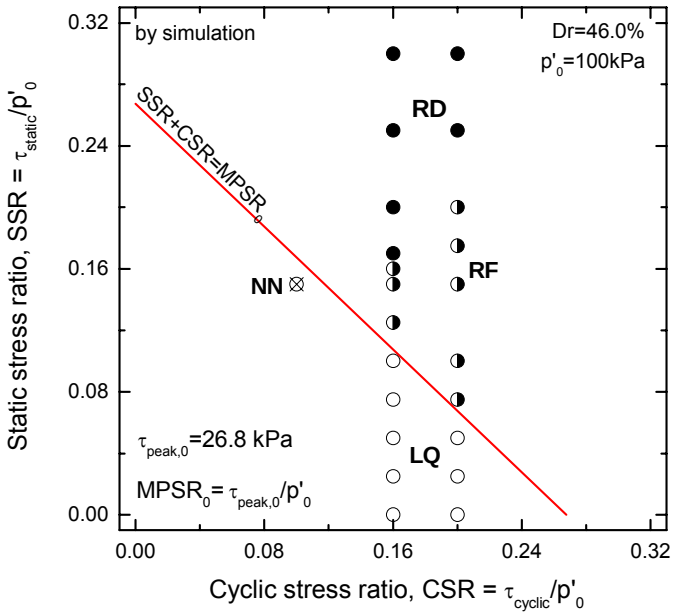

Fig. 6.3: Failure characteristics with respect to the monotonic undrained peak strength line

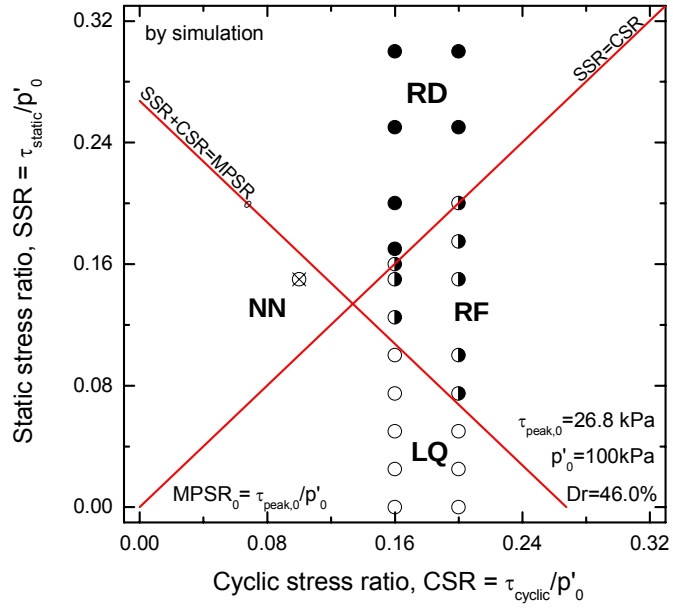

Fig. 6.4: The four-zone CSR-SSR method to predict/evaluate the failure characteristics of sand in undrained cyclic torsional shear tests

6.2.3. Effects of the relative density on the failure characteristics

In this study, the degree of reversal stress (R^*) and the undrained peak strength (τ_{peak}) have been recognized as the key parameters to evaluate the failure behavior of sand.

The degree of reversal stress (R^*) only depends on τ_{cyclic} and τ_{static}; in other words, it is independent from the initial effective confining pressure (p'_0) and the soil properties such as the relative density of the specimen (Dr).

On the contrary, $\tau_{peak,0}$ takes into account the strength of soil which depends on the soil properties (e.g., relative density, over-consolidation ratio, degree of saturation, fines content, etc) and the initial stress conditions (τ_{static} and p'_0).

Numerical simulation has the great advantage in that all the above mentioned conditions can be perfectly controlled, therefore $\tau_{peak,0}$ can be referred to as a constant value for given initial stress conditions and specimen density.

In contrast, it is very difficult if not impossible, to reproduce the same initial stress conditions and density of sand for different laboratory tests; as results, even a slight change in the test conditions produces a change in $\tau_{peak,0}$ value.

If the density of the specimens changes significantly (e.g., very loose, loose or dense), the failure behavior of sand with different densities can be assessed only by using different formats of the proposed four-zone CSR-SSR relationship, as typically shown in Fig. 6.5, Fig. 6.6 and Fig. 6.7.

Fig. 6.5 shows the comparison between the failure behaviors of very loose Toyoura sand specimens, which were performed by Kiyota (2007), and the prediction by the four-zone CSR-SSR relationship.

In Fig. 6.6, the comparison between the failure behaviors observed in this study for loose Toyoura sand specimens, and the prediction by the four-zone CSR-SSR relationship are illustrated.

In Fig. 6.7, the comparison between the failure behaviors of dense Toyoura sand specimens, which were performed by De Silva (2008), and the prediction by the four-zone CSR-SSR relationship can be seen.

The predictions obtained using the four-zone CSR-SSR method are consistent with the experimental data in all the cases. Therefore, the four-zone CSR-SSR relationship can be used to predict/evaluate individually the failure behavior of very loose, loose or dense sands; however, the failure behavior of the specimens with different degrees of relative density cannot be compared in a unique framework, since the undrained peak strength line changes with the relative density of the specimens.

In view of the above considerations and with the purpose of defining a unique framework for analyzing the failure behavior of sands irrespective of the relative density of specimens and other soil properties, the *SSR* and the *CSR* were normalized with respect to the $MPSR_0$ as follows:

$$\frac{CSR}{MPSR_0} = \frac{\tau_{cyclic} / p'_0}{\tau_{peak,0} / p'_0} \tag{6.6}$$

$$\frac{SSR}{MPSR_0} = \frac{\tau_{static} / p'_0}{\tau_{peak,0} / p'_0} \tag{6.7}$$

As a consequence, the two boundary conditions, defined in Eq. (6.3) and Eq. (6.4), were redefined as follows:

$$\frac{SSR}{MPSR_0} = \frac{CSR}{MPSR_0} \tag{6.8}$$

$$\frac{SSR}{MPSR_0} + \frac{CSR}{MPSR_0} = 1 \tag{6.9}$$

To confirm the applicability of this method, in Fig. 6.8 the failure behavior observed for very loose, loose and dense specimens (as listed in Table 6.1) are compared with respect to the four-zone $CSR/MPSR_0$ vs. $SSR/MPSR_0$ relationship. It can be seen that the proposed method can be effectively used to evaluate/predict the failure characteristics of specimens with different degrees of density in a unique framework.

Table 6.1: Very loose and dense Toyoura sand specimens from pervious studies

Test	*Dr (%)*	τ_{cyclic} *(kPa)*	τ_{static} *(kPa)*	$\tau_{peak,0}$ *(kPa)*	*CSR*	*SSR*	$MPSR_0$	*Type of Failure*	*No. cycles to p'=0*
Very loose Toyoura sand specimens (Kiyota, 2007)									
HcToy-6	25.4	17	0	(22)*	0.170	0.000	0.220	LQ	7.5
HcToy-7	26.6	27	0	22	0.270	0.000	0.220	RF	0.5
HcToy-8	26.6	11	0	(22)*	0.110	0.000	0.220	LQ	68.5
HcToy-11	26.7	25	0	22	0.250	0.000	0.220	RF	0.5
Dense Toyoura sand specimens (De Silva, 2008)									
Sat 28	74.6	30	0	(43)*	0.300	0.000	0.430	LQ	10
Sat 31	79.4	40	0	(43)*	0.400	0.000	0.430	LQ	9
Sat 32	75.2	60	0	43	0.600	0.000	0.430	RF	4
Sat 38	75.7	22	0	(43)*	0.220	0.000	0.430	LQ	60
(--)* It is assumed to be the same as the tests in which a clear τ_{peak} could be observed.									

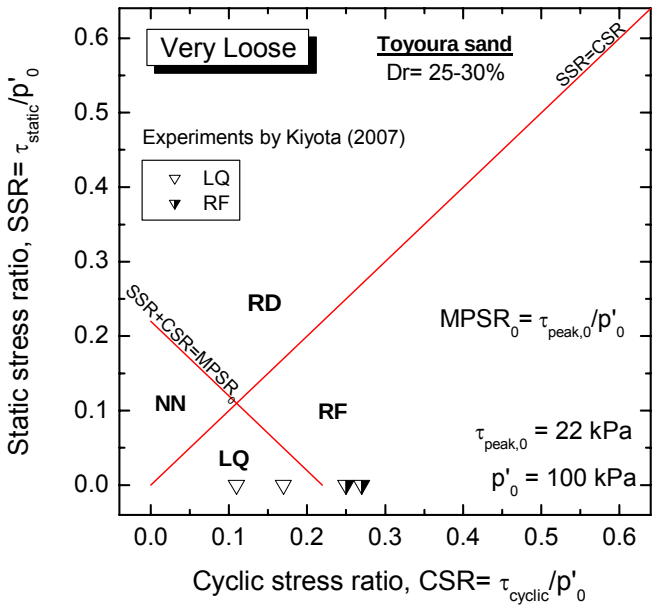

Fig. 6.5: Failure characteristics of very loose specimens evaluated by the CSR-SSR method

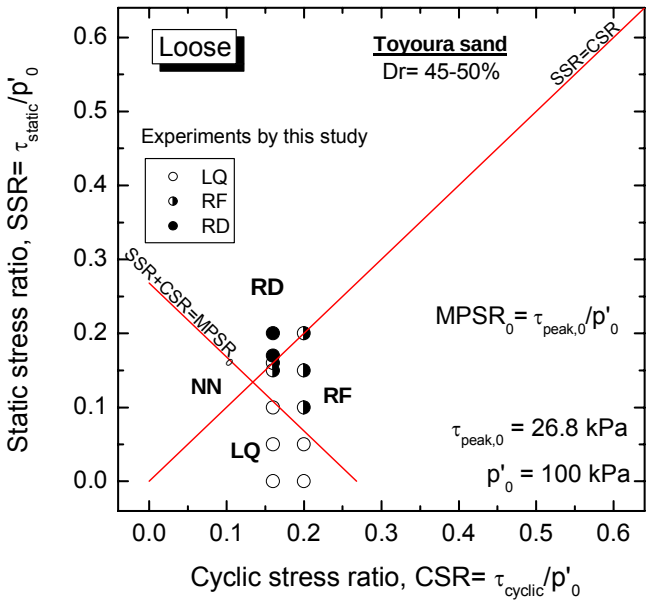

Fig. 6.6: Failure characteristics of loose specimens evaluated by the CSR-SSR method

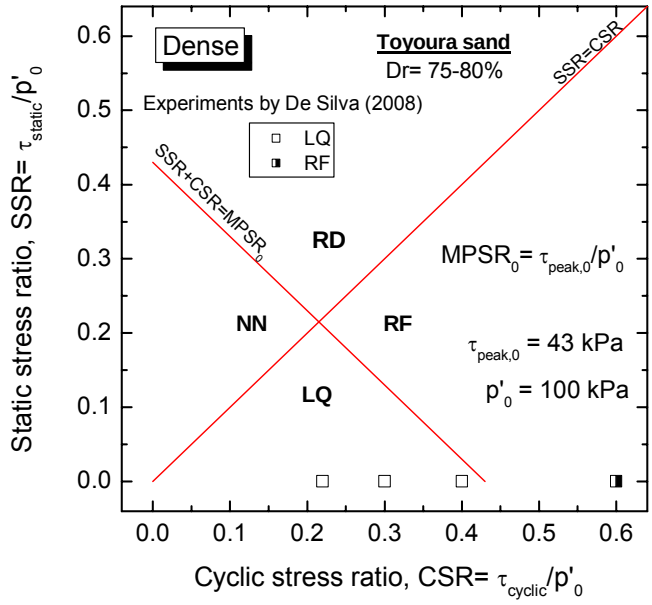

Fig. 6.7: Failure characteristics of dense specimens evaluated by the CSR-SSR method

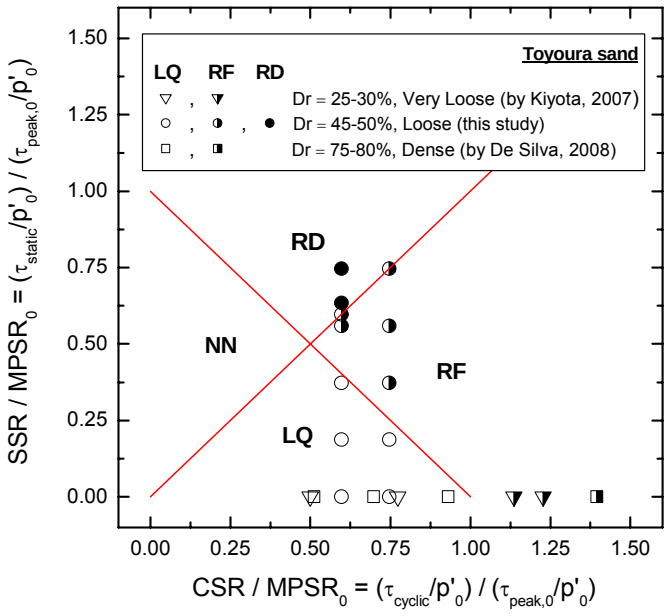

Fig. 6.8: Failure characteristics of very loose, loose and dense specimens evaluated by the $CSR/MPSR_0$ vs. $SSR/MPSR_0$ method

6.2.4 Effects of the initial static shear on the undrained peak strength

The presence of initial static shear widely affects the monotonic undrained behavior of sand as well as the cyclic undrained behavior (e.g., liquefaction resistance, mode of development of residual deformation, failure behavior, etc).

In Fig. 6.9 simulation results are compared with the predictions of the four-zone $CSR/MPSR_0$ vs. $SSR/MPSR_0$ method. It can be seen that due to the effects of the initial static shear on the undrained peak strength, the predictions are not consistent with the failure behavior observed by simulation, as evidenced by the dotted circles. However, it was observed that considering the actual value of τ_{peak} (blue line) which was obtained by simulation, the predictions become consistent with the simulation data.

In view of the above and with the aim of defining a unique framework for analyzing the failure behavior of sands irrespective of the relative density of the specimens, other soil properties and the effects of initial static shear, the *SSR* and the *CSR* were normalized with respect to the actual *MPSR* ($= \tau_{peak} / p'_0$) as follows:

$$\frac{CSR}{MPSR} = \frac{\tau_{cyclic} / p'_0}{\tau_{peak} / p'_0} \tag{6.11}$$

$$\frac{SSR}{MPSR} = \frac{\tau_{static} / p'_0}{\tau_{peak} / p'_0} \tag{6.12}$$

As a consequence, the two boundary conditions defined in Eq. (6.8) and Eq. (6.9) were redefined as follows:

$$\frac{SSR}{MPSR} = \frac{CSR}{MPSR} \tag{6.13}$$

$$\frac{SSR}{MPSR} + \frac{CSR}{MPSR} = 1 \tag{6.14}$$

In order to confirm the validity of the four-zone *CSR/MPSR* vs. *SSR/MPSR* method, the same simulation results used in Fig. 6.9 are plotted in Fig. 6.10. These simulation results are listed in Table 6.2. Hence, Fig. 6.10 shows that this method can be efficiently used to

evaluate/predict the failure characteristics of the specimens irrespective of the effects of initial static shear.

Table 6.2: Simulation results used to confirm the validity of the boundary conditions of the *CSR/MPSR* vs. *SSR/MPSR* method

Test	*Dr (%)*	τ_{cyclic} *(kPa)*	τ_{static} *(kPa)*	τ_{peak} *(kPa)*	$CSR = \tau_{cyclic}/p'_0$	$SSR = \tau_{static}/p'_0$	$MPRS = \tau_{peak}/p'$	*CSR/MPSR*	*SSR/MPSR*	*CSR/MPSR + SSR/MPSR*	*Type of failure*
S 26-00	46	26	0	26.8	0.260	0.000	0.268	0.970	0.000	0.970	LQ
S 18-08	46	18	8	26.9	0.180	0.080	0.269	0.669	0.297	0.966	LQ
S 19-07	46	19	7	26.9	0.190	0.070	0.269	0.706	0.260	0.966	LQ
S 12-12	46	12	12	27.1	0.120	0.120	0.271	0.443	0.443	0.886	LQ
S 16-15	46	16	15	27.6	0.160	0.150	0.276	0.580	0.543	1.123	RF
S 16-16	46	16	16	27.7	0.160	0.160	0.277	0.577	0.577	1.154	RF
S 24-24	46	24	24	29.7	0.240	0.240	0.297	0.808	0.808	1.616	RF
S 23-23	46	23	23	29.4	0.230	0.230	0.294	0.782	0.782	1.564	RF
S 26-01	46	26	1	26.8	0.260	0.010	0.268	0.970	0.037	1.007	RF
S 27-00	46	27	0	26.8	0.270	0.000	0.268	1.007	0.000	1.007	RF
S 19-08	46	19	8	26.9	0.190	0.080	0.269	0.706	0.297	1.003	RF
S 11-16	46	11	16	27.7	0.110	0.160	0.277	0.397	0.577	0.974	NN
S 06-23	46	06	23	29.4	0.060	0.230	0.294	0.204	0.782	0.986	NN
S 05-24	46	05	24	29.8	0.050	0.240	0.298	0.168	0.805	0.973	NN
S 12-13	46	12	13	27.2	0.120	0.130	0.272	0.441	0.478	0.919	NN
S 16-17	46	16	17	27.9	0.160	0.170	0.279	0.573	0.609	1.182	RD
S 12-16	46	12	16	27.7	0.120	0.160	0.277	0.433	0.578	1.011	RD
S 06-24	46	6	24	29.7	0.060	0.240	0.297	0.202	0.808	1.010	RD
S 23-24	46	23	24	29.7	0.230	0.240	0.297	0.774	0.808	1.582	RD
S 11-17	46	11	17	27.9	0.110	0.170	0.279	0.394	0.609	1.003	RD
$p'_0 = 100$ kPa											

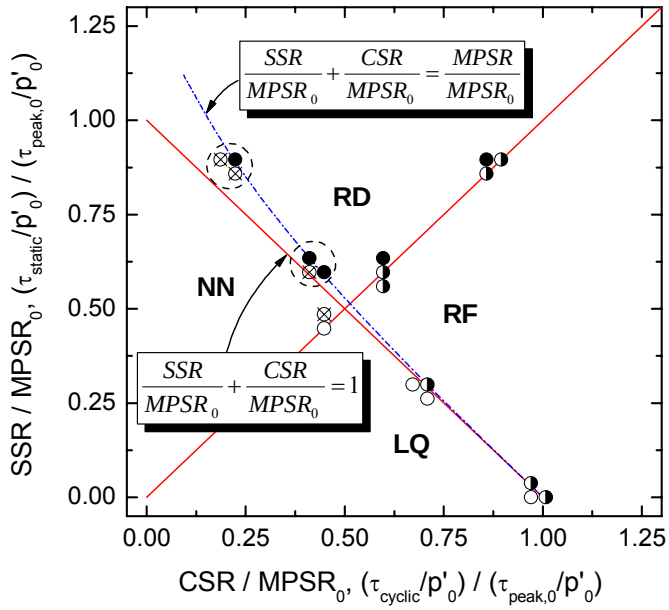

Fig. 6.9 Effects of static shear on the undrained peak strength described in terms of $CSR/MPSR_0$ vs. $SSR/MPSR_0$ relationship.

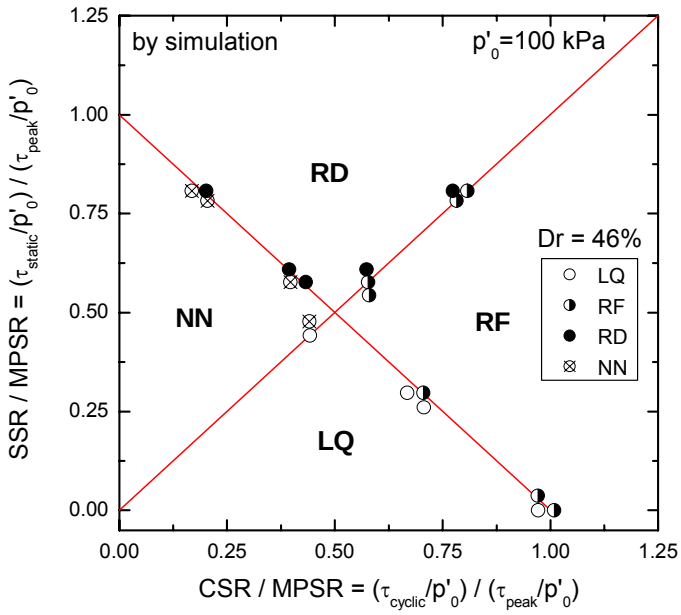

Fig. 6.10 Numerical simulations confirmed the applicability of the *CSR/MPSR* vs. *SSR/MPSR* method

6.2.5 Evaluation of MPSR for Toyoura sand specimens

It should be noted that, among the three stress parameters (*CSR*, *SSR* and *MPSR*) used to define the proposed *CSR/MPSR* vs. *SSR/MPSR* method, the *MPSR* is definitely the most important factor which directly leads the assessment of the failure behavior of sand.

MPSR could not be directly evaluate in many tests performed in this study; in fact, in the case of reversal loading tests the peak state was not achieved during the undrained cyclic loading, therefore in such a case, *MPSR* was evaluated by numerical simulations.

However, in most cases, when numerical simulation results are not available, additional monotonic tests are required to evaluate of the MPSR. For a practical point of view, to perform such undrained monotonic tests is very time consuming, and in addition the test conditions to be controlled are many (initial static shear, initial confining pressure, relative density/void ratio, etc) and the repetitively of tests results is not guaranteed.

As shown in Fig. 6.11, under the same conditions of initial effective confining pressure (p'_0), the undrained peak strength of sand during monotonic loading increases with the initial static shear as well as with the relative density.

In view of the above considerations, in this study an attempt was made to define a set of *MPRS* parameters for Toyoura sand, based on the experimental data and simulations results (Table 6.3). To address this issue, the effects of both the initial static shear and the void ratio/relative density on the change in *MPSR* were taken into account.

In Fig. 6.12 the effects of the initial static shear static on the undrained peak strength for very loose, loose and dense specimens are examined in terms of *SSR* vs. *MPSR* relationships. The experimental data are compared with the simulation results. It can be seen that numerical simulations are consistent with the experimental observations; however, the deviation of data is relevant.

The void ratio function $f(e_0)$ proposed by Hardin and Richart (1963) is usually employed for the evaluation and the comparison of small strain moduli (i.e., Young's modulus *E* and shear modulus *G*) of soil specimens having different density properties. In this study, with the aim of evaluating the effects of void ratio on the *MPSR* properties of Toyoura sand, it

was attempted to normalize the *MPSR* with the void ratio function $f(e_0)$.The results of this analysis are shown in Fig. 6.13. It can be seen that, after the normalization the range of *MPSR* parameter values becomes smaller. In addition, the MPSR parameter values obtained for very loose and loose specimens become unique. This suggests that the normalization is applicable within certain range of void ratio.

To verify the possibility of achieving the uniqueness of this curve, the power of the void ratio function $[f(e_0)]^n$ was used, as shown in Fig. 6.14. It was found that after normalizing the MPSR using $[f(e_0)]^n$ the MPSR values obtained by laboratory tests or by numerical simulations become rather unique, as a result a unique curve interpolating all the point could be drawn. The results of this analysis shown that in the case of saturated Toyoura sand, the *MPSR* parameter can be expressed as a function of the both the static stress ratio (SSR = τ_{static}/p'0) and the void ratio as follows:

$$MPSR = \left[0.27209 + 0.00324\exp(SSR/0.11403)\right]\left\{f(e_0)\right\}^{1.656} \qquad (6.10)$$

Where

- $f(e0)=(2.17-e_0)^2/(1+e_0)$, void ratio function proposed by Hardin and Richart (1963).

The typical *MPRS* parameter values obtained for Toyoura sand using Eq. (6.10) are listed in Table 6.4.

Table 6.3: Typical MPSR parameter values obtained by experiments or numerical simulations for very loose, loose and dense Toyoura sand specimens

Test	*SSR*	e_0	$f(e_0)$	*MPSR*	*Simulation*	*SSR*	e_0	$f(e_0)$	*MPSR*
HcToy-7*	0.00	0.896	0.856	0.220	M 00 L**	0.00	0.826	0.988	0.268
HcToy-11*	0.00	0.896	0.856	0.220	M 05 L**	0.05	0.826	0.988	0.268
Test 16(U1)**	0.00	0.828	0.991	0.240	M 10 L**	0.10	0.826	0.988	0.271
Test 10 (20-10)**	0.10	0.828	0.985	0.250	M 15 L**	0.15	0.826	0.988	0.276
Test 4(16-15)**	0.15	0.833	0.975	0.292	M 20 L**	0.20	0.826	0.988	0.285
Test 11(20-15)**	0.15	0.832	0.977	0.263	M 25 L**	0.25	0.826	0.988	0.301
Test 5 (16-16)**	0.16	0.825	0.991	0.271	M 30 L**	0.30	0.826	0.988	0.325
Test 6 (16-17)**	0.17	0.820	1.002	0.288	M 00 D**	0.00	0.678	1.327	0.433
Test 7 (16-20)**	0.20	0.827	0.987	0.283	M 05 D**	0.05	0.678	1.327	0.436
Test 12 (20-20)**	0.20	0.823	0.995	0.333	M 10 D**	0.10	0.678	1.327	0.439
SAT32***	0.00	0.691	1.294	0.450	M 15 D**	0.15	0.678	1.327	0.444
					M 20 D**	0.20	0.678	1.327	0.448
					M 25 D**	0.25	0.678	1.327	0.461
					M 30 D**	0.30	0.678	1.327	0.470

* by Kiyota (2007); ** this study; and *** by De Silva (2008)

Table 6.4: Typical MPSR parameter values calculated by Eq. (6.10) for very loose, loose and dense Toyoura sand specimens

e_{max} = 0.992; e_{min} = 0.632			*SSR*						
Dr (%)	e_0	$f(e_0)$	0.00	0.05	0.10	0.15	0.20	0.25	0.30
20	0.920	0.814	0.196	0.197	0.199	0.202	0.207	0.214	0.226
25	0.902	0.845	0.208	0.210	0.212	0.215	0.220	0.228	0.240
30	0.884	0.878	0.222	0.223	0.226	0.229	0.234	0.243	0.256
35	0.866	0.911	0.236	0.237	0.240	0.244	0.249	0.258	0.272
40	0.848	0.946	0.251	0.253	0.255	0.259	0.265	0.275	0.289
45	0.830	0.981	0.267	0.268	0.271	0.275	0.282	0.292	0.307
50	0.812	1.018	0.284	0.285	0.288	0.293	0.300	0.310	0.327
55	0.794	1.055	0.301	0.303	0.306	0.311	0.318	0.329	0.346
60	0.776	1.094	0.319	0.322	0.325	0.330	0.337	0.349	0.368
65	0.758	1.134	0.339	0.341	0.345	0.350	0.358	0.371	0.390
70	0.740	1.175	0.360	0.362	0.366	0.371	0.380	0.393	0.414
75	0.722	1.218	0.382	0.384	0.388	0.394	0.403	0.417	0.440
80	0.704	1.261	0.404	0.407	0.411	0.417	0.427	0.442	0.466
85	0.686	1.306	0.428	0.431	0.435	0.442	0.452	0.469	0.493
90	0.668	1.353	0.454	0.457	0.462	0.469	0.480	0.497	0.523

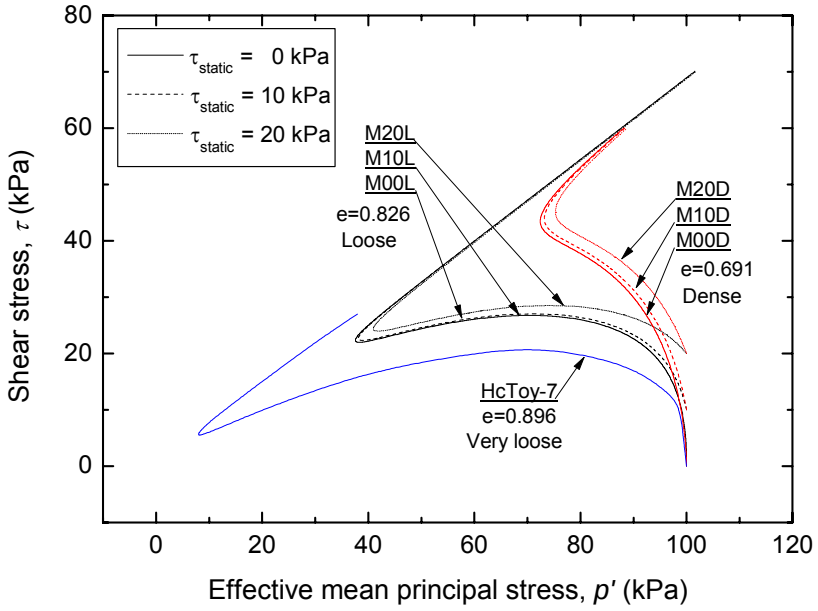

Fig. 6.11: Combined effects of both the initial static shear and the void ratio/relative density on the undrained peak strength

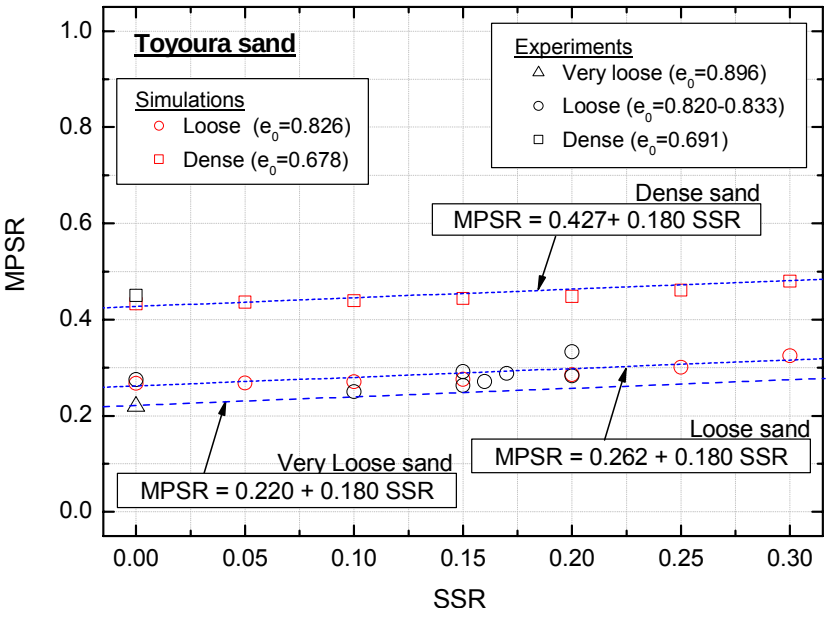

Fig. 6.12: Evaluation of MPS for Toyoura sand specimens considering the effects of initial static shear

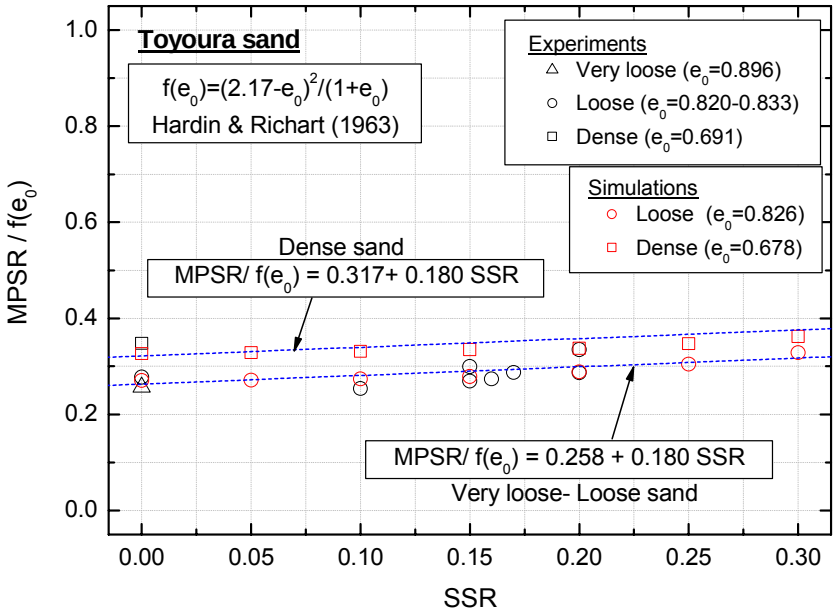

Fig. 6.13: Evaluation of MPSR for Toyoura sand specimens using the void ratio function $f(e_0)$

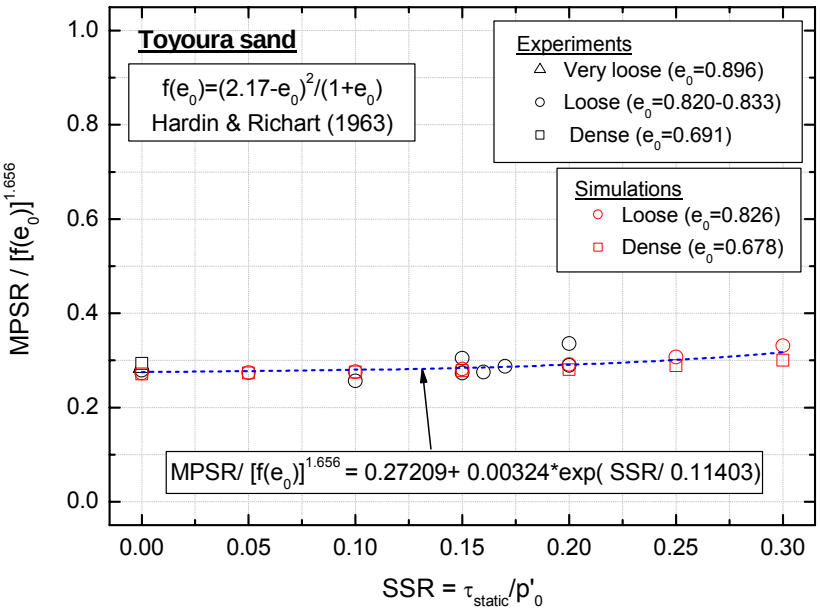

Fig. 6.14: Evaluation of MPSR for Toyoura sand specimens using the function[$f(e_0)$]$^{1.656}$

6.2.6 Number of cycles to define the liquefaction resistance

The fact that a soil is susceptible to liquefaction does not guarantee that liquefaction will be actually initiated during an earthquake event. In fact, it is recognized by past earthquake experiences that the number of cycles which characterizes an earthquake is less than 20-30 cycles. Therefore, liquefaction will be likely to occur only under stress conditions that require less than 30 cycles to achieve the full liquefaction state of $p'= 0$.

In this study, the resistance against liquefaction during cyclic loading is expressed in terms of relationships between either the *CSR* or *SSR* value and the number of cycles required to achieve the full liquefaction state of $p'= 0$, as shown in Fig. 4.13.

The tests results and numerical simulation show that in case of reversal tests in which the level of cyclic stress is very low, liquefaction occurs after applying even more than a hundred cycles. Therefore, under these stress conditions the probability that liquefaction takes place during an earthquake is very limited.

To take the limit of liquefaction into account, an additional boundary is introduced in the proposed four-zone CSR/MPSR vs. SSR/MPSR method as shown in Fig. 6.15. This boundary, which was defined by numerical simulations in this study, establishes whether liquefaction is achieved or not by applying 100 cycles.

In Fig. 6.16, the test results shown in Fig. 6.8 and the simulation results shown in Fig. 6.15 are plotted all together. It can be seen that, the CSR/MPSR vs. SSR/MPSR method can be effectively used to assess the failure characteristics of sandy specimens subjected to undrained cyclic torsional shear loading irrespective of the relative density, the effects of initial static shear and the limit of liquefaction resistance as well.

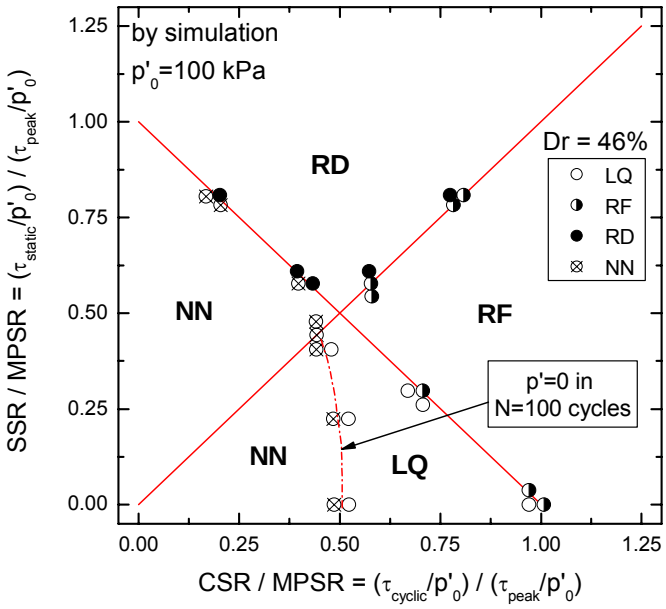

Fig. 6.15: Boundary conditions of the CSR/MPSR vs. SSR/MPSR method

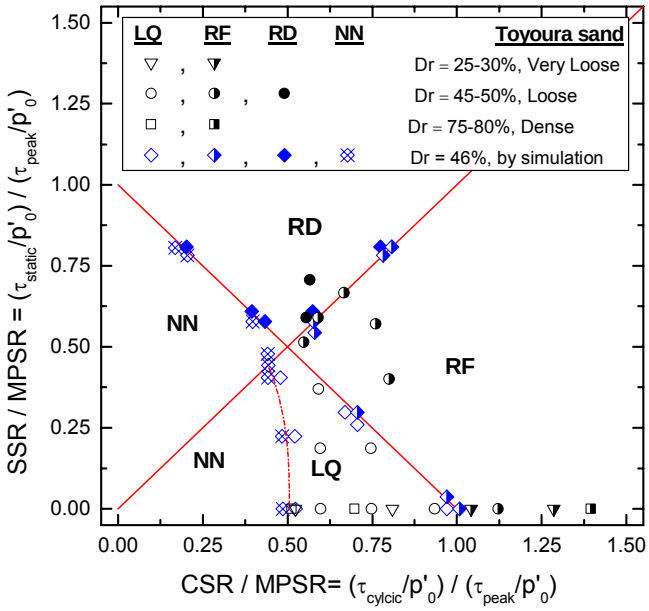

Fig. 6.16 Comparison of the failure characteristics of Toyoura sand specimens using the CSR/MPSR vs. SSR/MPSR method

6.2.7 Features of the four-zone CSR/MPSR vs. SSR/MPSR method

The four-zone CSR/MPSR vs. SSR/MPSR method presented in this study is a unique framework in which the failure behavior of saturated sand subjected to undrained cyclic torsional loading can be assessed irrespective of the degree of relative density of the specimens. This method is based on the rules described in Table 6.5.

The initial static shear stress and the cyclic shear stress, measured in terms of SSR/MPSR and CSR/MPSR, respectively, are compared with the stress reversal line and the undrained peak strength line, as schematically show in Fig. 6.17. Therefore, in accordance with the failure zone that these stress conditions correspond, the type of failure behavior of sand can be established.

The effects of relative density and the initial static shear on the failure behavior of sand are taken into consideration by means of the parameter MPSR, as mentioned previously in this chapter.

As well, the resistance against liquefaction of the investigated sand can be taken into account. In this study it was set as the boundary that establishes whether the liquefaction is achieved or not applying 100 cycles.

It should be noted that, the proposed method was used in this study to assess the failure behavior of sand subjected to cyclic undrained torsional shear loading, where the cyclic shear stress consists of a series of uniform stress cycles.

Its applicability to evaluate the failure behavior of sand under general loading conditions (e.g., cyclic triaxial loading) or under irregular stress cycles requires further investigations.

Table 6.5: The four-zone CSR/MPSR vs. SSR/MPSR method

	$\frac{SSR}{MPSR}+\frac{CSR}{MPSR}<1$ $(\tau_{static}+\tau_{cyclic}<\tau_{peak})$	$\frac{SSR}{MPSR}+\frac{CSR}{MPSR}\geq 1$ $(\tau_{static}+\tau_{cyclic}\geq\tau_{peak})$
$\frac{SSR}{MPSR}\leq\frac{CSR}{MPSR}$ ($R^*\geq 0$, reversal or intermediate)	LQ	RF
$\frac{SSR}{MPSR}>\frac{CSR}{MPSR}$ ($R^*<0$, non-reversal)	NN	RD
LQ = Cyclic liquefaction failure RF = Rapid flow liquefaction failure		NN = No-liquefaction & No-failure RD = Residual deformation failure
It should be noted that, the proposed method can be used to assess the failure behavior of sand subjected to cyclic undrained torsional shear loading, where the cyclic shear stress consists of a series of uniform stress cycles		

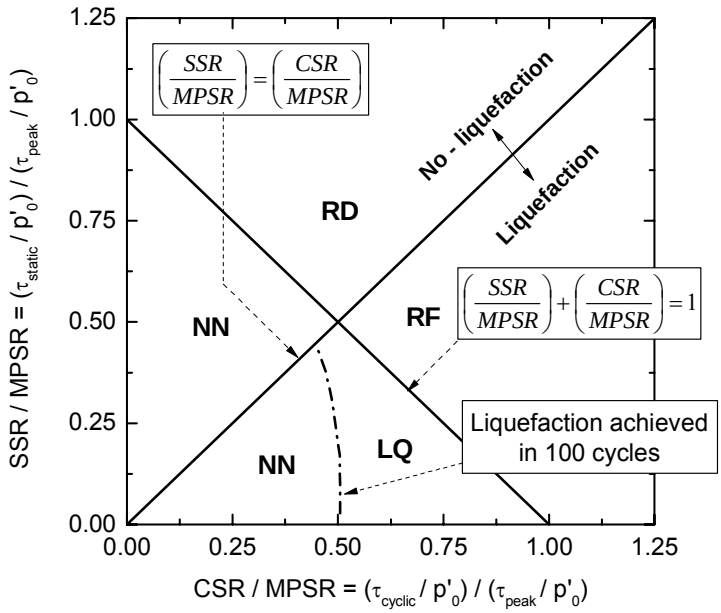

Fig. 6.17: The four-zone CSR/MPSR vs. SSR/MPSR method

6.3 Failure behavior of sand from field data interpretation

In this study, a series of torsional shear tests has been performed in order to better understand the behavior of sloped ground under cyclic undrained loading conditions. Different failure mechanisms were observed and two methods were proposed to assess the failure behavior of sand in undrained torsional shear tests.

With the aim of directly comparing the sand failure characteristics observed in the laboratory with the failure of slope on site, on the basis of the interpretation of field observations compiled by Hamada et al. (1994) as described in chapter 1, the cyclic stress ratio (*CSR*), the static stress ratio (*SSR*) and the relative density (*Dr*) of the natural levee of Ebigase area and Maeyama hill in Noshiro City are estimated under the considerations described hereafter.

6.3.1 Cyclic Stress Ratio due to an earthquake

To evaluate the cyclic stress ratio (*CSR*), it is assumed that there is a level ground surface, a soil column of unit width and length, and the water table is at the ground level. The soil column moves horizontally as a rigid body in response to the maximum horizontally acceleration (a_{max}) exerted by an earthquake at ground surface (Fig 6.18).

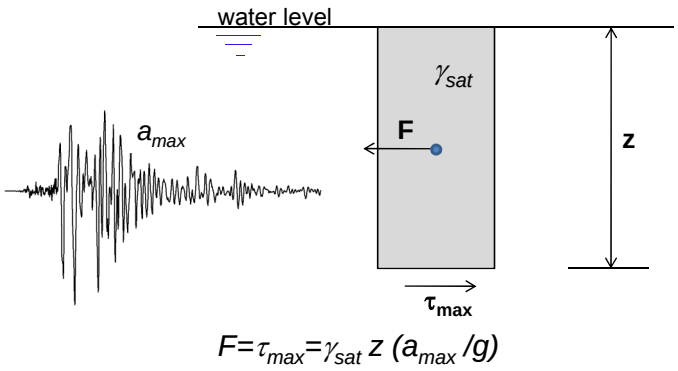

Fig. 6.18: Conditions assumed for the derivation of the cyclic stress ratio

Therefore, the horizontal earthquake force (*F)* acting on the soil column of unit width and length is:

$$F = m\,a = \frac{W}{g}a = \frac{\gamma_{sat}\ z}{g}a_{\max} = \sigma_v \frac{a_{\max}}{g} \qquad (6.15)$$

where:

F = horizontal earthquake-induced inertial force acting on a unit width and length of soil column;

m = total mass of soil column, which is equal to W/g;

W = total weight of soil column;

γ_{sat} = unit weight of saturated soil;

z = depth below ground surface of soil column;

a_{max} = the maximum horizontal acceleration at ground surface caused by the earthquake (i.e., peak ground acceleration);

g = gravitational acceleration;

σ_v = total vertical stress at bottom of soil column.

As shown in Fig. 6.18, by summing the forces in the horizontal direction the inertial force (F) acting on the rigid soil element is equal to the maximum shear force at the base of the soil element. Since the soil element is assumed to have a unit base width and length, the maximum shear force (F) is equal to the maximum shear stress (τ_{max}):

$$\tau_{\max} = F = \sigma_v \frac{a_{\max}}{g} = \gamma_{sat}\, z \frac{a_{\max}}{g} \tag{6.16}$$

In performing torsional shear tests, the effective mean principal stress (p') is the parameter used to evaluate the liquefaction behavior of sand or the generation of the pore water pressure (e.g., full liquefaction is referred to p'= 0). In general, the effective mean principal stress (p') acting on a soil element can be evaluated as follows:

$$p' = \frac{\sigma'_v + 2\,\sigma'_h}{3} = \frac{\sigma'_v + 2\,K_0\,\sigma'_v}{3} = \left(\frac{1 + 2\,K_0}{3}\right)\gamma' z \tag{6.17}$$

where

σ'_v and σ'_h = vertical and horizontal effective stresses, respectively;

K_0 = coefficient of earth pressure at rest.

γ' = unit weight of the saturated soil immersed in water or buoyant unit weight .

In accordance with the definition of *CSR* (= τ_{cyclic}/p'_0) used in this study in analyzing the torsional shear test results, in the current study the *CSR* on site considering the torsional shear stress conditions was formulated as follows:

$$\frac{\tau_{\max}}{p'} = \left(\frac{3}{1+2\,K_0}\right)\frac{\gamma_{sat}}{\gamma'}\frac{a_{\max}}{g} \tag{6.18}$$

The soil column does not act as a rigid body during the earthquake, but rather the soil is deformable. Seed and Idriss (1971) proposed a depth reduction factor r_d to consider such effect; hence, introducing the depth reduction factor into Eq. (6.18) yields

$$\frac{\tau_{\max}}{p'} = \left(\frac{3}{1+2\,K_0}\right) r_d \frac{\gamma_{sat}}{\gamma'}\frac{a_{\max}}{g} \tag{6.19}$$

In several design codes in Japan (e.g., RTRI, 1999; JRA, 2002) the linear relationship of r_d versus the depth proposed by Iwasaki et al. (1978) has been adopted:

$$r_d = 1 - 0.015\,z \qquad (z \text{ in meters}) \tag{6.20}$$

It should be noted that, r_d is a dimensionless parameter.

Seed et al. (1975) converted the typical irregular earthquake record to an equivalent series of uniform stress cycles by assuming the following relationship:

$$\tau_{cyclic} = 0.65\,\tau_{\max} \tag{6.21}$$

where τ_{cyclic} = uniform cyclic shear stress amplitude of the earthquake.

By substituting Eq. (6.20) and Eq. (6.21) into Eq. (6.19), the earthquake-induced cyclic stress ratio considering the torsional shear stress conditions, as proposed in this study, is formulated:

$$CSR = \frac{\tau_{cyclic}}{p'} = 0.65\left(\frac{3}{1+2\,K_0}\right)(1-0.015\,z)\frac{\gamma_{sat}}{\gamma'}\frac{a_{\max}}{g} \tag{6.22}$$

Finally, being $\gamma_{sat}/\gamma' \approx 2$, the following expression for CSR on site is obtained

$$CSR = \left(\frac{3.9}{1+2\,K_0}\right)(1-0.015\,z)\frac{a_{\max}}{g} \tag{6.23}$$

6.3.2 Static stress ratio due to gravity

To evaluate the static stress ratio the simplified assumptions that are commonly used to describe the stability of an infinite slope are adopted. It is assumed that:

- Soil is cohesionless and homogeneous;
- Failure is the results of shallow translational sliding and occurs in a single layer;
- The failure plane and the water table are parallel to the ground surface;
- The failure plane is of infinite length.

It is assumed that there is a sloped ground surface, a soil column of unit width and length, and the water table is located in-between the ground surface and the examined failure surface (Fig. 6.19).

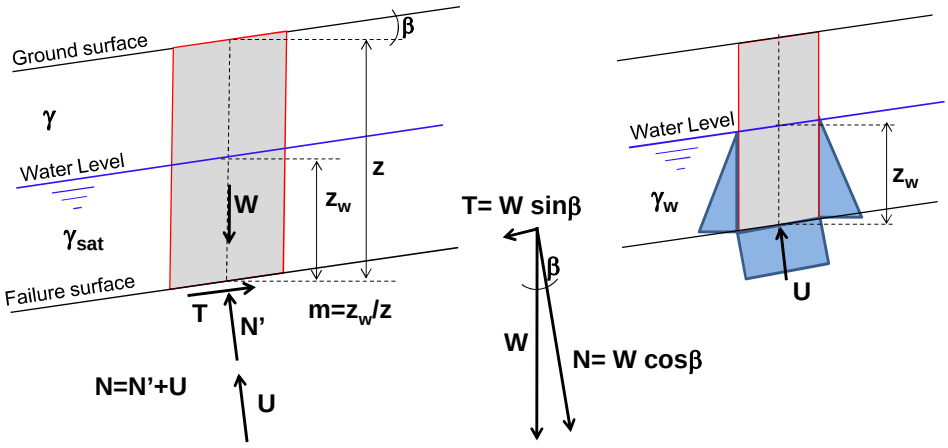

Fig. 6.19: Infinite slope conditions assumed for the derivation of the static stress ratio

By referring to the equilibrium of forces on a plane parallel to the slope at the bottom of soil column, the driving force T and total normal force N can be evaluated as:

$$T = W \sin\beta = \left[(1-m)\gamma + m\gamma_{sat}\right] z \sin\beta \tag{6.24}$$

$$N = W \cos\beta = \left[(1-m)\gamma + m\gamma_{sat}\right] z \cos\beta \tag{6.25}$$

where

W = total weight of saturated soil;

T = slope parallel component of gravity;

N = total normal component of gravity;

β = gradient of slope;

$m = z_w / z$, as defined in Fig. 6.19;

γ_{sat} = unit weight of saturated soil;
γ = unit weight of dry or partially saturated soil.

The pore water pressure (U) at the bottom of soil column can be evaluated as follows:

$$U = \gamma_w z_w = m\,\gamma_w\, z\cos\beta \tag{6.26}$$

Subsequently, in accordance to the well known principle of effective stress/force, the effective normal force N' can be defined as:

$$\begin{aligned} N' &= N - U = \left[(1-m)\gamma + m\gamma_{sat} - m\gamma_w\right] z\cos\beta \\ &= \left[(1-m)\gamma + m\gamma'\right] z\cos\beta \end{aligned} \tag{6.27}$$

where, γ' = unit weight of the saturated soil immersed in water (= γ_{sat} - γ_w) .

Considering that gravity component forces act on a surface having an area $A=1/\cos\beta$, the associated stress components result as:

$$\begin{aligned} \tau_{static} &= \frac{T}{A} = \frac{\left[(1-m)\gamma + m\gamma_{sat}\right] z\sin\beta}{1/\cos\beta} \\ &= \left[(1-m)\gamma + m\gamma_{sat}\right] z\sin\beta\cos\beta \end{aligned} \tag{6.28}$$

$$\begin{aligned} \sigma' &= \frac{N'}{A} = \frac{\left[(1-m)\gamma + m\gamma'\right] z\cos\beta}{1/\cos\beta} \\ &= \left[(1-m)\gamma + m\gamma'\right] z\cos^2\beta \end{aligned} \tag{6.29}$$

where,
τ_{static} = initial driving static shear stress; and
σ' = effective normal stress at bottom of soil column.

Moreover, by referring to Eq. (6.17), the effective mean principal stress (p') acting on a soil element of sloped ground can be evaluated as follows:

$$p' = \left(\frac{1+2K_0}{3}\right)\sigma' = \left(\frac{1+2K_0}{3}\right)\left[(1-m)\gamma + m\gamma'\right] z\cos^2\beta \tag{6.30}$$

Therefore, in this study, based on the above simplified assumptions on which generally infinite slope method relies, and considering the torsional shear conditions, the static stress ratio (*SSR*) induced by gravity on a saturated sloping ground is formulated as follows:

$$SSR = \frac{\tau_{static}}{p'} = \left(\frac{3}{1+2\,K_0} \right) \frac{\left[(1-m)\gamma + m\gamma_{sat} \right]}{\left[(1-m)\gamma + m\gamma' \right]} \tan\beta \tag{6.31}$$

It is recognized that due to the suction effects, the dry or partially saturated soil above the water table is often completely wet, therefore it can be assumed that $\gamma = \gamma_{sat}$. Under this conditions Eq. (6.31) can be simplified as follows:

$$\begin{aligned} SSR &= \left(\frac{3}{1+2\,K_0} \right) \frac{\gamma_{sat}}{\left(\gamma_{sat} - m\gamma_{sat} + m\gamma' \right)} \tan\beta \\ &= \left(\frac{3}{1+2\,K_0} \right) \frac{\tan\beta}{\left(1 - m + m\dfrac{\gamma'}{\gamma_{sat}} \right)} \end{aligned} \tag{6.32}$$

Finally, being $\gamma' / \gamma_{sat} \approx 0.5$, the following expression for SSR on site is obtained

$$SSR = \frac{3\tan\beta}{(1+2\,K_0)(1-0.5m)} \tag{6.33}$$

6.3.3 Relative density from the SPT data and undrained peak strength ratio

Terzaghi and Peck (1967) and Lambe and Whitman (1969) proposed correlations between *SPT N* value and relative density of clean sand which are summarized in Table 6.6; whereas, the correlations by Seed (1987) between *SPT* $(N_1)_{60}$ value (i.e., *SPT N* corrected from the effect of overburden pressure) and relative density of clean sand are listed in Table 6.7.

Idriss and Boulanger (2003) re-evaluated correlations between *SPT* $(N_1)_{60}$ value and relative density (*Dr*) for the purpose of liquefaction evaluations, and recommended the following expressions for clean sands:

$$Dr = \sqrt{\frac{(N_1)_{60}}{46}} \tag{6.34}$$

In general the resistance to liquefaction of a soil increases with the $(N_1)_{60}$ from the SPT. Based on the SPT and field performance data, Seed et al. (1985) concluded that there are three approximate potential damage ranges that can be identified, see Table 6.8.

As indicated in Table 6.7 and Table 6.8, sand with $(N_1)_{60}$ value below 20 is in a loose state; therefore it may be extensively damaged by liquefaction. On the other hand, sand with $(N_1)_{60}$ value over 30 is either a dense or very dense state; hence, liquefaction does not produce large deformations because of the dilatation tendency of the sand upon reversal of the cyclic shear stress. This is the reason why dense to very dense soils suffer no significant damage, as described in Table 6.8.

After estimating the relative density on site from the interpretation of field data, in the current study, the undrained peak strength ratio (MPSR) was evaluated by using Eq. (6.10) or referring to the value listed in Table 6.4, by assuming that the in-situ soil properties are similar to those used in this study (i.e., Toyoura sand).

Table 6.6: Correlation between SPT N value and density of clean sand (Terzaghi and Peck, 1967; Lambe and Whitman, 1969)

N	*Sand density*	*Relative density, Dr (%)*
0-4	Very loose condition	0-15
4-10	Loose condition	15-35
10-30	Medium condition	35-65
30-50	Dense condition	65-85
Over 50	Very dense condition	85-100

Table 6.7: Correlation between SPT $(N_1)_{60}$ value and density of sand (Seed, 1987)

$(N_1)_{60}$	*Sand density*	*Relative density, Dr (%)*
0-2	Very loose condition	0-15
2-5	Loose condition	15-35
5-20	Medium condition	35-65
20-35	Dense condition	65-85
Over 35	Very dense condition	85-100
$(N_1)_{60}$ = SPT N value corrected from the effect of overburden pressure, σ'_{v0} (in kPa) $(N_1)_{60}= (100/\sigma'_{v0})^{0.5} N_{60}$, and $N_{60}= 1.67 E_m C_b C_r N$		

Table 6.8: Potential liquefaction damage based on SPT data (Seed et al., 1985)

$(N_1)_{60}$	*Potential damage*
0-20	High
20-30	Intermediate
>30	No significant damage

6.3.4 Coefficient of earth pressure at rest (K_0)

The coefficient of earth pressure at rest is the ratio of the lateral to the vertical effective stresses in a soil consolidated under the condition of no lateral deformation, the stresses being principal stresses with no shear stress applied to the planes on which these stresses act" (Bishop,1958)

$$K_0 = \frac{\sigma_h'}{\sigma_v'} \tag{6.35}$$

where
σ_h' = horizontal principal effective stress; and
σ_v' = vertical principal effective stress.

The relationship between the coefficient of lateral earth pressure at rest (K_0) and the internal friction angle (ϕ'), proposed by Jaky (1944), is the most widely-used formula to estimate at-rest pressure in geotechnical engineering practice:

$$K_0 = 1 - \sin\phi' \tag{6.36}$$

For course soils, empirical correlation between the internal friction angle (ϕ') and the relative density *Dr* were proposed by Schmertmann (1978):

$$\phi' = 28 + 0.14\ Dr \quad \text{(Fine sand)} \tag{6.37}$$

$$\phi' = 31.5 + 0.115\ Dr \quad \text{(Medium sand)} \tag{6.38}$$

$$\phi' = 34.5 + 0.10\ Dr \quad \text{(Course sand)} \tag{6.39}$$

$$\phi' = 38 + 0.08\ Dr \quad \text{(Gravel)} \tag{6.40}$$

The same relationships are shown in Fig. 6.20 (refer to Table. 6.9. for the classification of course soil).

In this study, after estimating the relative density on site (*Dr*) from the interpretation of field data, with aim to evaluate the K_0 by means the Jaky's formula, the internal friction angle (ϕ') was evaluated as the average of the ones obtained using Eq.(6.37) and Eq. (6.38) for fine and medium sands respectively, assuming that the in-situ soil properties are similar to those used in this study (i.e., Toyoura sand).

Table 6.9: British Soil Classification System for course soil

Course soils	Gravel	course	20-60 mm
		medium	6-20 mm
		fine	2- 6mm
	Sand	course	0.6-2.0 mm
		medium	0.2-0.6 mm
		fine	0.06-0.2 mm

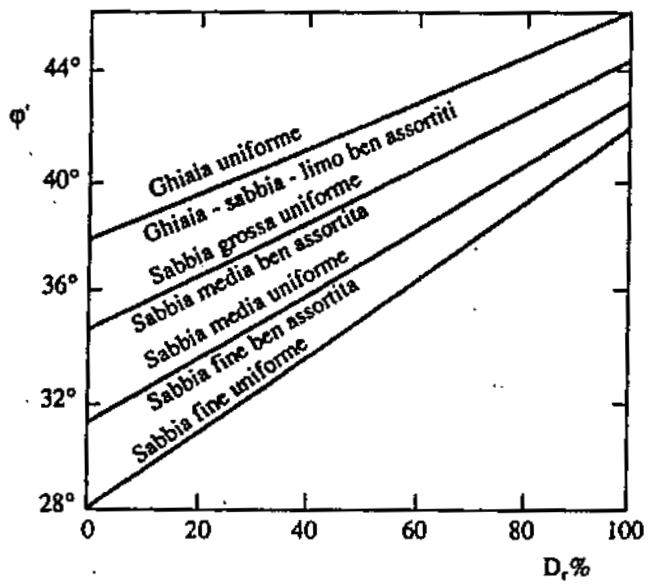

Legend:

- Ghiaia uniforme: uniform gravel
- Ghiaia-sabbia-limo ben assortiti: well graded gravel, sand and silt
- Sabbia grossa uniforme: uniform course sand
- Sabbia media ben assortita: well graded medium sand
- Sabbia media uniforme: uniform medium sand
- Sabbia fine ben assortita: well graded fine sand
- Sabbia media uniforme: uniform fine sand

Fig. 6.20: Correlation between the internal friction angle (ϕ') and the relative density (Dr) (Schmertmann, 1978; from Viggiani, 1999)

6.3.5 Stress conditions and soil densities from field data interpretation

Typical results from the interpretation of the field data reported by Hamada et al. (1994) are listed in Table 6.10 and Table 6.11, where the stress conditions and the relative density of soil of the slopes of the natural levee at Ebigase in Niigata City (1964 Niigata earthquake) and Maeyama hill in Noshiro City (1983 Nihonkai-Chubu earthquake), respectively, are estimated. In Fig. 6.21 and Fig. 6.22, the points selected for the analysis of the stress conditions and the relative density of soil on site are indicated.

As shown in Fig. 6.21:

- E1-1 and E2-1 are two points at the top of liquefied layer; it should be noted that, also the water table level is at the same location;
- E1-2 and E2-2 are two points at the bottom of liquefied layer;
- E1-3 and E1-3 are two points at the bottom of sand layer which was not interested by liquefaction during the 1964 Niigata earthquake, as reported by Hamada et al. (1994).

As shown in Fig. 6.22:

- N1-1 is a point at the top of sand dune where the water table is located;
- N1-2 is a point in-between a liquefied sandy layer;
- N1-3 and N1-4 are two points within and at the bottom of alluvial sand layer, respectively.

Table 6.10: Estimation of the stress conditions and the soil density at Ebisage area in Niigata City.

	z (m) *	z_w (m) *	a_{max} (g) **	β (%) *	*N-SPT* **	*Dr* (%) Table (6.6)	K_0 Eq. (6.36)	*CSR* Eq. (6.23)	*SSR* Eq. (6.33)	*MPSR* ***	*CSR/ MPSR*	*SSR/ MPSR*
E1-1	2.1	0.0	0.16	2	10	35	0.460	0.315	0.031	0.237	1.329	0.132
E1-2	8.2	6.1	0.16	2	10	35	0.460	0.285	0.050	0.237	1.203	0.210
E1-3	9.4	7.3	0.16	2	30	65	0.405	0.296	0.054	0.341	0.869	0.159
E2-1	2.0	0.0	0.16	1	10	35	0.460	0.315	0.016	0.236	1.336	0.066
E2-2	5.2	3.2	0.16	1	20	50	0.432	0.309	0.023	0.284	1.087	0.082
E2-3	9.1	7.1	0.16	1	35	70	0.396	0.301	0.027	0.361	0.833	0.076

* Evaluated graphically using Fig. 6.21

** From Hamada et al., (1994)

*** Evaluated using Eq. (6.10) or by referring to the Table 6.4

Table 6.11: Estimation of the stress conditions and the soil density at Noshiro City.

	z (m) *	z_w (m) *	a_{max} (g) **	β (%) *	*N-SPT* **	*Dr* (%) Table (6.6)	K_0 Eq. (6.36)	*CSR* Eq. (6.23)	*SSR* Eq. (6.33)	*MPSR* ***	*CSR/ MPSR*	*SSR/ MPSR*
N1-1	0.6	0.0	0.25	2.5	5	25	0.478	0.494	0.038	0.209	2.362	0.183
N1-2	5.2	4.6	0.25	2.5	10	35	0.460	0.468	0.070	0.238	1.968	0.294
N1-3	8.8	8.2	0.25	2.5	20	50	0.432	0.454	0.075	0.286	1.588	0.263
N1-4	11.2	10.6	0.25	2.5	20	50	0.432	0.435	0.076	0.286	1.522	0.267

* Evaluated graphically using Fig. 6.22

** From Hamada et al., (1994)

*** Evaluated using Eq. (6.10) or by referring to the Table 6.4

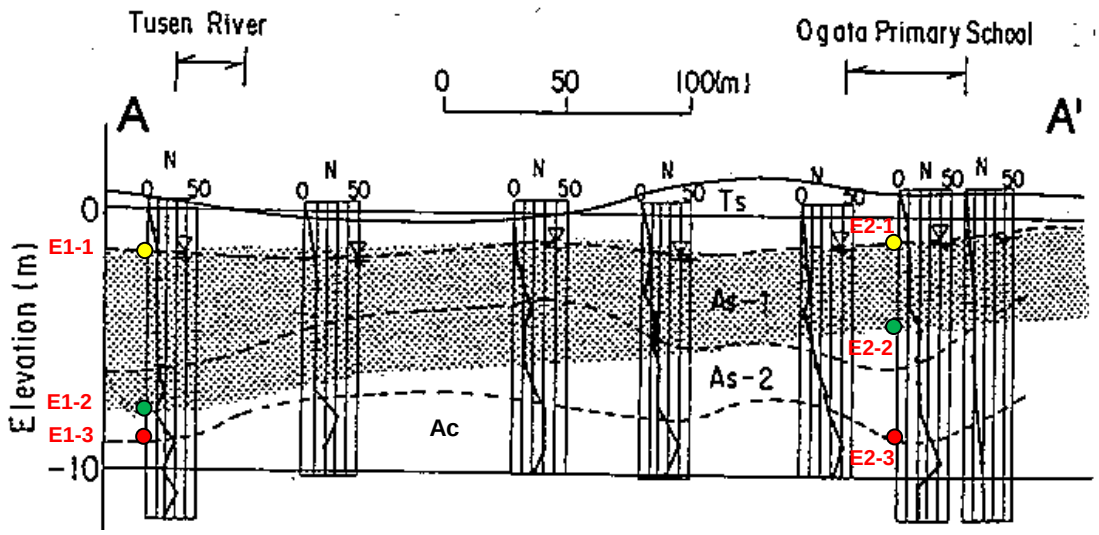

(Ts) surface dune sand; (As) alluvial sandy soil; (Ac) alluvial clayey soil

Fig. 6.21: Soil conditions and estimated liquefied layer along section A-A' at Ebigase area in Niigata City as reported by Hamada et al. (1994). In this study the stress conditions and soil density at points E1through E6 were evaluated.

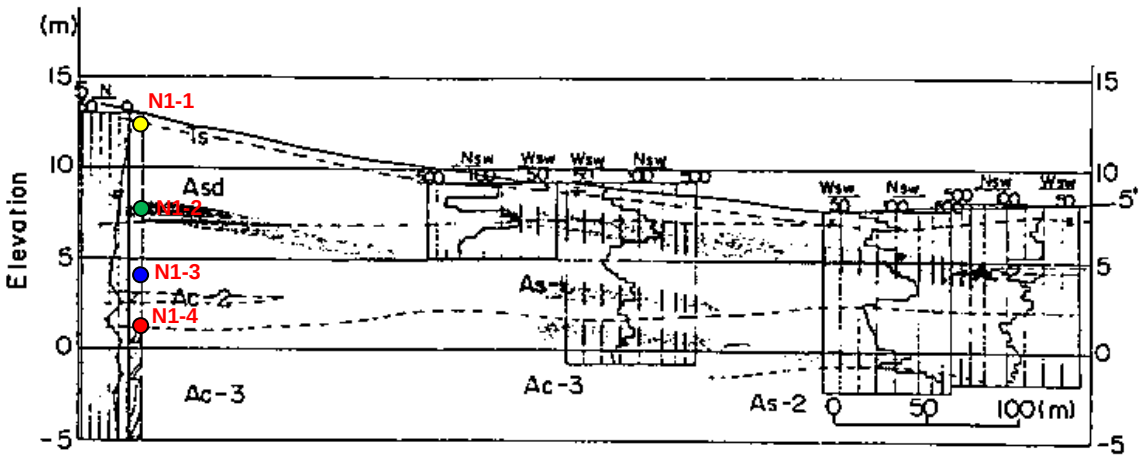

(Ts) surface soil; (Asd) dune sand; (As) alluvial sandy soil; (Ac) alluvial clayey soil

Fig. 6.22: Soil conditions and estimated liquefied layers along section B-B' in Noshiro City (Hamada et al., 1994). In this study the stress conditions and soil density at points N1through N4 were evaluated.

6.4 Evaluation of failure behavior of natural slopes using the CSR/MPSR-SSR/MPSR method

In order to directly compare the liquefaction-induced failure behavior of natural slopes of sandy deposits observed during past earthquakes with the failure behavior of saturated Toyoura sand specimens subjected to undrained cyclic torsional shear loading observed in laboratory, in the current study an attempt to analyze the field data considering the torsional shear conditions was made.

The comparison between the prediction by the CSR/MPSR-SSR/MPSR method and the failure behavior of natural slopes observed on site are presented in Fig.6.23 and Fig. 6.24.

In Fig. 6.23, the case of the slopes at Ebigase area is analyzed. It can be seen that, for the points E1-1, E1-2, E2-1 and E2-2 at the top and bottom of the liquefied layer, the method confirm that liquefaction took place due to the RF failure behavior of sand. On the contrary, for the points E1-3 and E2-3 at the bottom of sandy layer which did not experience liquefaction, as reported by Hamada et al. (1994), the method predicts LQ failure behavior for the point E1-3 and RF failure for the point E2-3. However, it should be noted that, LQ failure means that the soil experiences liquefaction only if the number of cycles of the earthquake is large enough to achieve liquefaction.

In Fig. 6.24, the case of the slopes in Noshiro City is analyzed. In this case due to the relatively large ground acceleration (i.e., a_{max} = 0.25g) for all the investigated points the method predicts RF failure behavior.

The results of this analysis show that the predictions are consistent with field observation; in addition, prediction results confirm that the greater the relative density of soil and the depth below the ground surface the higher is the liquefaction resistance of soil on site.

Therefore, the proposed CSR/MPSR – SSR/MPSR method can be used to compare the liquefaction-induced failure behavior of natural slopes of sandy deposits observed during past earthquakes with the failure behavior of saturated Toyoura sand specimens subjected to undrained cyclic torsional shear loading observed in laboratory.

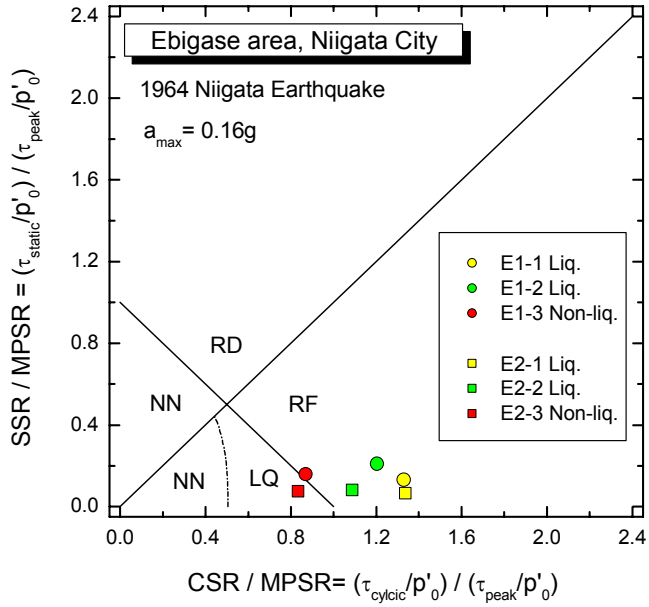

Fig. 6.23: Liquefaction characteristics of the gentle slopes of a natural levee at Ebigase area during the 1964 Niigata earthquake evaluated using the proposed CSR/MPSR vs. SSR/MPSR method

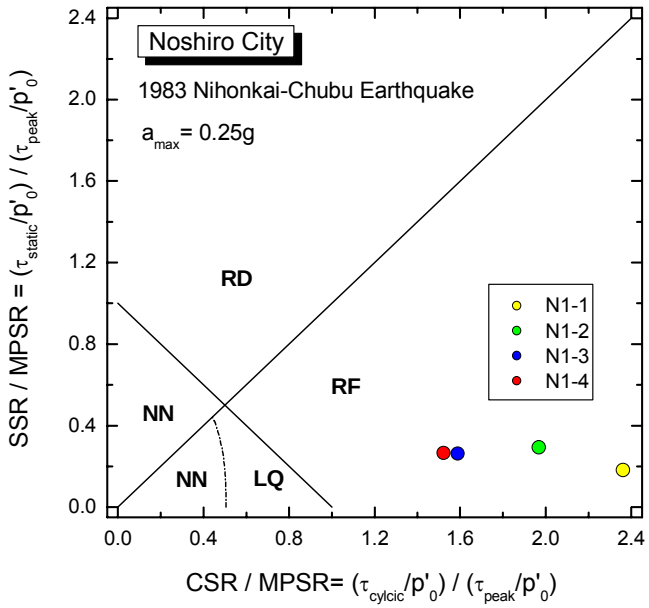

Fig. 6.24: Liquefaction behavior of the gentle slopes of Maeyama hill in Noshiro City during the 1983 Nihonkai-Chubu earthquake evaluated using the proposed CSR/MPSR vs. SSR/MPSR method

6.5 Summary

With the aim of gaining a better understanding of the failure mechanisms of saturated sand, a method to assess the failure behavior of sand specimens with initial static shear under undrained cyclic torsional shear loading is presented.

This method called the "*four-zone CSR/MPSR vs. SSR/MPSR method*" presented in this study is a unique framework in which the failure behavior of saturated sand subjected to undrained cyclic torsional loading can be assessed irrespective of the degree of relative density of the specimens.

The initial static shear stress and the cyclic shear stress, measured in terms of SSR/MPSR and CSR/MPSR, respectively, are compared with the stress reversal line and the undrained peak strength line. Therefore, in accordance with the failure zone that these stress conditions correspond, the type of failure behavior of sand can be established.

The effects of relative density and the initial static shear on the failure behavior of sand are taken into consideration by means of the parameter MPSR.

As well, the resistance against liquefaction of the investigated sand is taken into account using a boundary that establishes whether the liquefaction is achieved or not after applying 100 cycles.

Its applicability has been investigated on a wide range of combinations of static and cyclic shear stresses on very loose, loose and dense sand by referring to: (i) the results of undrained cyclic torsional shear tests; and (ii) a number of single-element numerical simulations by employing the elasto-plastic constitutive model described in chapter 5.

On the basis of field data investigations from case histories of liquefaction-induced failure of sandy slopes during past earthquakes, the proposed method was used directly to compare the sand failure characteristics observed in the laboratory with the failure of slope on site.

6.6 References

1. Bishop, A.W. (1958): "Test requirements for measuring the coefficient of earth pressure at rest", Proc. of Brussels Conference on Earth Pressure Problems, Vol. 1, 2-14
2. De Silva, L.I.N. (2008): "Deformation characteristics of sand subjected to cyclic drained and undrained torsional loadings and their modeling", Ph.D. thesis, Dep. of Civil Engineering, University of Tokyo, Japan
3. Hamada, M., O'Rourke, T. D. and Yoshida, N. (1994): "Liquefaction-induced large ground displacement", Performance of Ground Soil during Earthquake, 13th International Conference on Soil Mechanics and Foundation Engineering, 93-108
4. Hardin, B. O. and Richart Jr., F. E. (1963): "Elastic wave velocities in granular soils", Journal of Soil Mechanics and Foundation Division, ASCE, 89 (SM1), 33-65
5. Idriss, M. and Boulanger, R.W. (2003): "Estimating Ka for using in evaluating cyclic resistance of sloping ground", Proc. 8th US-Japan Workshop on Earthquake Resistant Design of Lifeline Facilities and Countermeasures for Soil Liquefaction, Hamada, O'Rourke and Bardet (Eds.), Baffalo, N.Y., 449-468
6. Iwasaki, T., Tatsuoka, F., Tokida, K. and Yasuda, S. (1978): "A practical method for assessing soil liquefaction potential based on case studies at various sites in Japan", Proc. 2nd International Conference on Microzonation for Safer Construction - Research and Application, Vol. 2, San Francisco, CA, 885-896
7. Jaky, J. (1944): "The coefficient of earth pressure at rest", Journal for Society of Hungarian Architects and Engineers, 355-358
8. Japan Road Association (2002): "Specifications for highway bridges", Part 5, Earthquake Resistant Design (in Japanese)
9. Kiyota, T. (2007): "Liquefaction strength and small strain properties of in-situ frozen and reconstituted sandy soils", Ph.D. thesis, Dep. of Civil Engineering, University of Tokyo, Japan
10. Lambe, T. W. and Whitman, R. V. (1969): "Soil mechanics", John Wiley and Sons, Inc.
11. Railway Technical Research Institute (1999): "Design standards for Railway Structures and Commentaries" (in Japanese)
12. Schmertmann, J. H. (1978): "Use the SPT to measure dynamic soil properties? - Yes, But..!", Dynamic Geotechnical Testing, STP 654, ASTM, Philadelphia, PA

13. Seed H. B., Idriss I. M., Makdisi F. and Banerjee N. (1975): "Representation of irregular stress time histories by equivalent uniform stress series in liquefaction analyses," Rpt. UCB/EERC-75-29, U.C. Berkeley

14. Seed, H. B. (1987): "Design problems in soil liquefaction", Journal of Geotechnical Engineering Division, ASCE, 113 (8), 827–845

15. Seed, H. B. and Idriss, I. M. (1971): "Simplified procedure for evaluating soil liquefaction potential", Journal of Soil Mechanics and Foundation Division, ASCE, 97 (SM9), 1249-1273

16. Seed, H. B., Tokimatsu, K., Harder, L.F., Jr. and Chung, R. (1985): "Influence of SPT procedures in soil liquefaction resistance evaluations", Journal of Geotechnical Engineering Division, ASCE, 111 (12), 1425-1445

17. Terzaghi, K. and Peck, R. B. (1967): "Soil Mechanics in Engineering Practice", John Wiley and Sons, Inc.

18. Viggiani, C. (1999): "Fondazioni", Eds. Hevelius (in Italian)

CHAPTER 7

Conclusions

and recommendations for future study

7.1 Conclusions

Experimental observations

With the intention of investigating the effects of initial shear stress on the large deformation properties of loose sand with initial static shear, a series of undrained cyclic torsional shear tests were performed on saturated loose Toyoura sand specimens up to single amplitude of shear strain of about 50 % under various combinations of static and subsequent cyclic shear stresses.

From the study of failure mechanisms, based on the difference in the effective stress path and the modes of development of shear strain during both monotonic and cyclic undrained torsional shear loading, the observed types of failure could be distinguished into three types: cyclic liquefaction (LQ), rapid flow liquefaction (RF) and residual deformation (RD) failures.

It was found that the failure behavior is a consequence of the degree of reversal loading. In fact, in case of stress reversal and intermediate loadings, failure could be associated with full liquefaction, followed by extremely large deformation in the post-liquefaction process (i.e., LQ and RF failure behaviors). On the other hand, in the case of non-reversal loading, the residual deformation brought the specimen to failure (i.e., formation of spiral shear band) although liquefaction did not occur.

The test results showed that the presence of initial static shear does not always lead to an increase in the resistance to liquefaction and strain accumulation; in fact, both can either increase or decrease by increasing the static shear depending on the extent of stress reversal and the failure behavior. However, in this study it was found that the two-phase change in liquefaction resistance (i.e., strictly speaking resistance against strain accumulation) can be associated with a two-phase change in the failure behavior from LQ to RF and from RF to RD.

The mode of development of residual deformation exceeding 50% was also investigated. It was found that large deformation could be developed in different ways according with the type of failure that sand experienced.

Numerical simulations

With the aim of simulating the behavior of saturated sand with initial static shear undergoing undrained cyclic loading which leads to liquefaction and large cyclic shear

strain development, an elasto-plastic constitutive model which can describe both monotonic and cyclic torsional shear behaviors of saturated sand with initial static shear under drained or undrained condition was presented in this study.

The proposed model could simulate the behavior of loose saturated sand subjected to undrained torsional shear loading, under general conditions of stress reversal, intermediate and non-reversal loadings by varying the initial static shear and the amplitude of the subsequent cyclic shear stresses (i.e., varying the degree of reversal stress).

The liquefaction behavior of sand, described in terms of effective stress path, could be qualitatively modeled until the specimen enters into a full liquefaction state ($p'=0$), as well as during the cyclic mobility process. The stress-strain relationship could be qualitatively simulated up to a strain level of 8% until the specimens enter into a steady state.

The simulation results of both monotonic and cyclic undrained behavior could be employed to evaluate the failure behavior of sand. Therefore, cyclic liquefaction (LQ), rapid flow liquefaction (RF) and residual deformation (RD) failures were simulated. As well, by conducting additional numerical simulations, the behavior called as no-liquefaction and no-failure (NN), in which either liquefaction or failure did not take place even after applying several tens of cycles, could be defined.

Simulation results confirmed that the resistance against strain accumulation can either increase or decrease depending on the extent of reversal stress and the type of failure; in addition, it was confirmed by numerical simulations that the mode of development of residual deformation depends on the type of failure of sand.

Method to assess the failure behavior of sand

With the scope of gaining a better understanding of the failure mechanisms of saturated sand, a method used to assess the failure behavior of sand specimens with initial static shear under undrained cyclic torsional shear loading was presented.

The proposed method is defined by means of three parameters namely: (i) static stress ratio $SSR = \tau_{static} / p_0'$, (ii) cyclic stress ratio $CSR = \tau_{cyclic} / p_0'$, and (iii) undrained monotonic peak stress ratio $MPSR = \tau_{peak} / p_0'$; where: τ_{static} = the initial static shear stress; τ_{cyclic} = the single amplitude cyclic shear stress; τ_{peak} = the shear stress at peak state during the undrained monotonic loading ; and p_0' = the initial effective confining pressure. The

SSR corresponds to the driving shear force induced by the inclination of slopes; the *CSR* represents the inertial force exerted by earthquakes; while the *MPSR* takes into account the strength of soil which depends on the soil properties (e.g., relative density, etc) and the stress conditions.

By this method, called the "*Four-zone CSR/MPSR vs. SSR/MPSR method*", the initial static shear stress and the cyclic shear stress, measured in terms of SSR/MPSR and CSR/MPSR, respectively, were compared with the stress reversal line (i.e., SSR/MPSR = CSR/MPSR) and the undrained peak strength line (i.e., SSR/MPSR + CSR/MPSR =1). In accordance with the failure zone that these stress conditions correspond, the type of failure behavior of sand (i.e., LQ, RF, RD or NN) could be established.

Its applicability was investigated on a wide range of combinations of static and cyclic shear stresses on very loose, loose and dense sand by referring to: (i) the results of undrained cyclic torsional shear tests; and (ii) a number of single-element numerical simulations by employing the elasto-plastic constitutive model presented in this study.

On the basis of field data investigations from case histories of liquefaction-induced failure of sandy slopes during past earthquakes, the proposed method was used to compare the sand failure characteristics observed in the laboratory with the failure of slopes on site.

7.2 Recommendations for future study

With the reference to the results of the present study, the following recommendations for future research can be identified.

Recommended experimental investigations related to the present study

1) In the current study, only loose Toyoura sand specimens were tested. Therefore, in order to have a comprehensive understanding of the effects of initial static shear on the undrained cyclic torsional behavior of sand, it is recommended that the behavior of very loose as well as dense specimens under the same stress conditions as that used in this study for loose sand be investigated.
2) Further investigations are required to confirm experimentally the NN behavior of sand which in this study was carried out by performing numerical simulations.
3) The effects of over-consolidations, degree of saturations and fines content on the failure behavior of sand need to be studied also.
4) The effects of the drained creep loading were not considered in this study. However, this issue needs to be addressed since it may have relevant effects on the rapid flow failure of soil.

Recommended modifications to the proposed elasto-plastic model

1) In the actual case, in-situ soils are frequently subjected to cyclic loading histories, which might include previous liquefaction as well. Therefore, further investigations on the effects of such cyclic loading histories under drained and undrained conditions on liquefaction properties of soil and apply the proposed model to simulate such cases is recommended. In order to model such a case, the proposed model only needs the stress-strain relationship of a drained monotonic torsional shear test, which was subjected to the same stress history as the one to be modeled.
2) The current model is capable of simulating the stress paths and stress-strain relationships up to the peak stress level of the material, while it was observed in this study that the soil will undergo strain softening behavior at extremely large shear strain amplitudes. Therefore, it is required to extend the proposed model to take the strain softening behavior of the material into account to model the liquefaction behavior at extremely large strain amplitudes.
3) The proposed model is developed based on the experimental evidences obtained from torsional shear tests and applied to simulate the liquefaction behavior under torsional

shear loading conditions. Therefore, it is recommended to investigate the applicability of the proposed model for general stress conditions to address the practical engineering issues.

4) Application of the proposed model to other geomaterials is also left for future investigations.
5) Time-dependent effects such as viscous effects, ageing effects and drained creep loading effects are neglected in the current study since the time taken for cyclic undrained loading is small. However, it is required to properly address the above issues in the model to simulate the cases where strain rate (or stress rate) is not a constant.

Recommendations for the validations of the propose CSR/MPSR vs. SSR/MPSR method

1) Application of the proposed method to evaluate and compare the large deformation behavior of sand observed in the laboratory with the failure of slopes on site is one of the possible extensions of this method.
2) Field data investigations from case histories of slopes that did not experience liquefaction and/or failure are necessary to validate the predictions of the NN behavior by the proposed method.
3) Triaxial apparatus is widely used in laboratory tests; in literature a wide number of tests results can be found. If the triaxial conditions are converted into torsional shear conditions, then the proposed method can be used to compare the failure behaviors of sand specimens under triaxial conditions with the one observed for specimens subjected to torsional shear loading. This attempt is left for future study.

Appendix A

Sensitivity of the correction factors $\Delta\tau$ and $\Delta p'$

A.1 Sensitivity of the correction factors Δτ and Δp'

In Fig. 4.31, it was shown that, the unstable behavior of stress ratio due to division by zero (i.e., *p'=0* at full liquefaction state) disappears after correcting for $\Delta\tau$ and $\Delta p'$. In addition, in Fig. 4.30 (a) the method employed to define both $\Delta\tau$ and $\Delta p'$ was shown.

However, the evaluation of $\Delta\tau$ and $\Delta p'$ is not easy task. In fact, by looking carefully the stress ratio after the correction, it can be seen that the unstable behavior could be still observed in the regions where the loading direction reversed, as shown in the close-up in Fig. A.1. This is a clear evidence that the parameters $\Delta\tau$ and $\Delta p'$ were not properly calibrated. In order to address the above issue and understand the meaning of both $\Delta\tau$ and $\Delta p'$ correction factors, the following parametric study was performed.

In accordance with Koseki et al. (2005), an apparent increase in effective stress state ($\Delta p'$) and the shift in shear stress ($\Delta\tau$) were introduced to correct for the effects of mobilization of shear resistance under extremely low effective stress states.

In this study, the effect of the parameter $\Delta\tau$ was evaluated by keeping $\Delta p'$ as a constant value, as shown in Fig. A.2. Therefore, $\Delta\tau$ was set at the values of 0.5 and - 0.5, which are respectively higher and lower than $\Delta\tau = 0.20$ which was determined by the method in Fig 4.30 (a).

Thus, as shown in Fig. A.2 (a), when $\Delta\tau$ was set to a value of $\Delta\tau = 0.50$, the stress ratio was well defined in the upper part, while in the lower part an unstable behavior could be observed.

On the contrary, as shown in Fig. A.2 (b), when $\Delta\tau$ was set to a value of $\Delta\tau = -0.50$, the unstable behavior appeared in the upper part, while the stress ratio was well defined in the lower part.

This suggested that, the appropriate value of $\Delta\tau$ should be set as the value necessary to obtain the symmetry of the stress ratio with respect to the vertical direction. In this study, for Test 8 subjected to fully reversal loading (*R*=1*), $\Delta\tau = 0.17$ was found suitable to obtained a good symmetry of the stress ratio, as shown Fig. A.2 (c).

As shown in Fig. A.3, the effect of the parameter $\Delta p'$ was evaluated by keeping $\Delta\tau$ as a constant value. Therefore, $\Delta p'$ was set at the values of 1.0 and 4.0, which are respectively lower and higher than $\Delta p' = 1.8$ which was determined by the method in Fig 4.30 (a).

Thus, as shown in Fig. A.3 (a), when $\Delta p'$ was set to a value of $\Delta p' = 1.0$, an unstable behavior of stress ratio and two peak stress states that were followed by strain softening were observed in both upper and lower parts.

On the contrary, as shown in Fig. A.3 (b), when $\Delta p'$ was set to a value of $\Delta p' = 4.0$, the unstable behavior disappeared; however, no clear peak(s) could be observed anymore.

This suggested that, the appropriate value of $\Delta p'$ should be set as the value necessary to reduce as much as possible the instability as observed in Fig. A.1, and to obtain a clear peak followed by strain softening. In this study, for Test 8 subjected to fully reversal loading ($R^*=1$), $\Delta p'=2.5$ was found suitable to obtained a stress ratio with such characteristics described above, as shown Fig. A.3 (c).

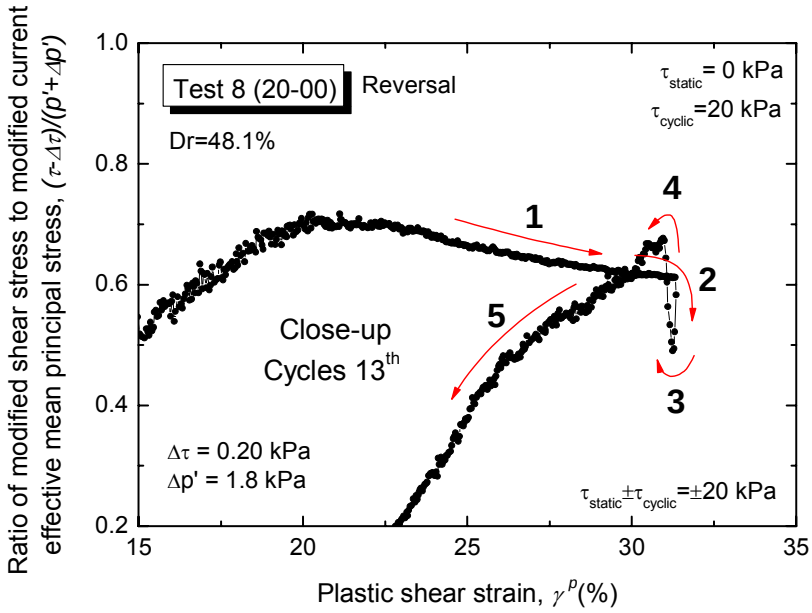

Fig. A.1: Unstable stress ratio behavior due to the not perfect evaluation of $\Delta\tau$ and $\Delta p'$

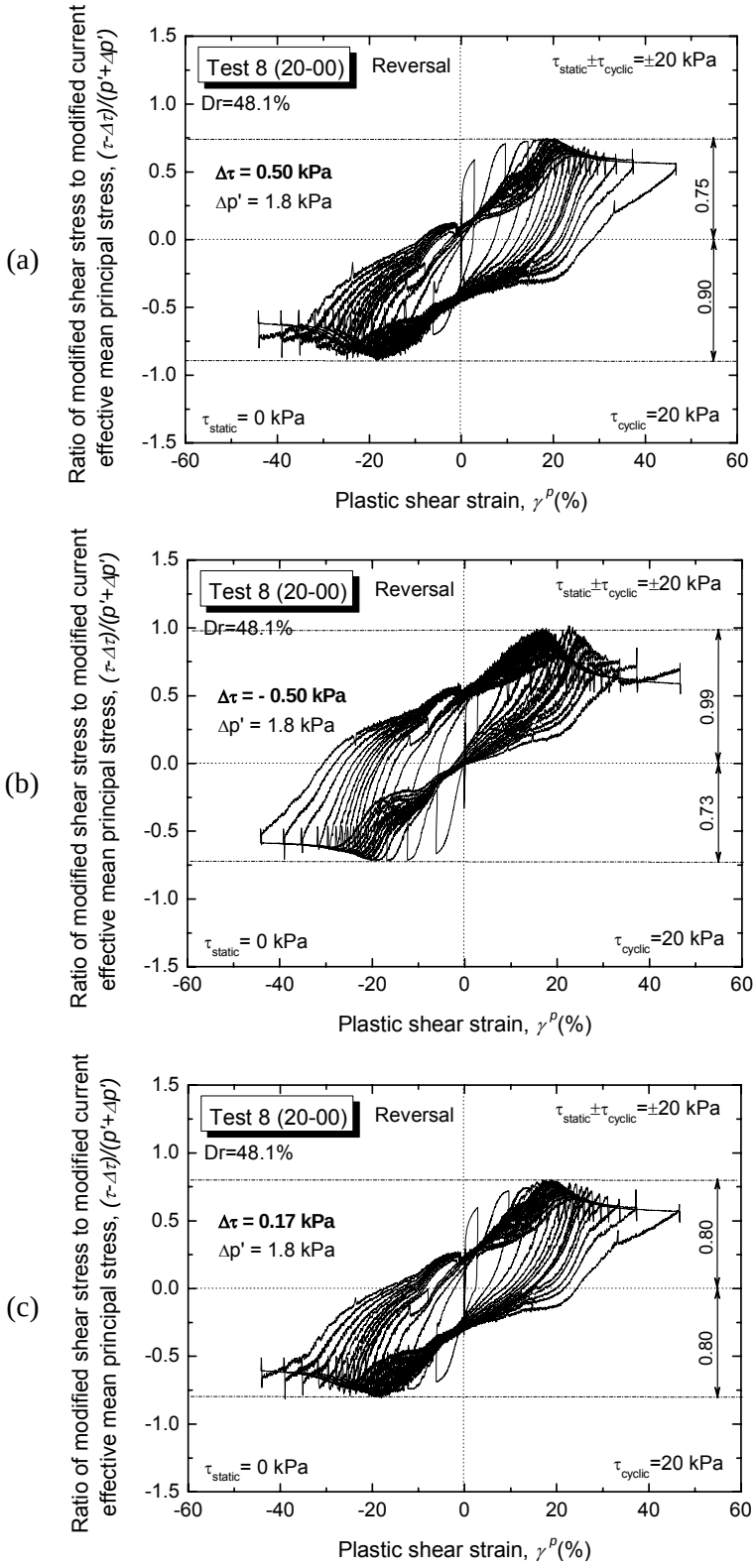

Fig. A.2: Effects of Δτ on the modified stress-strain relationship in fully reversal loading test

(a)

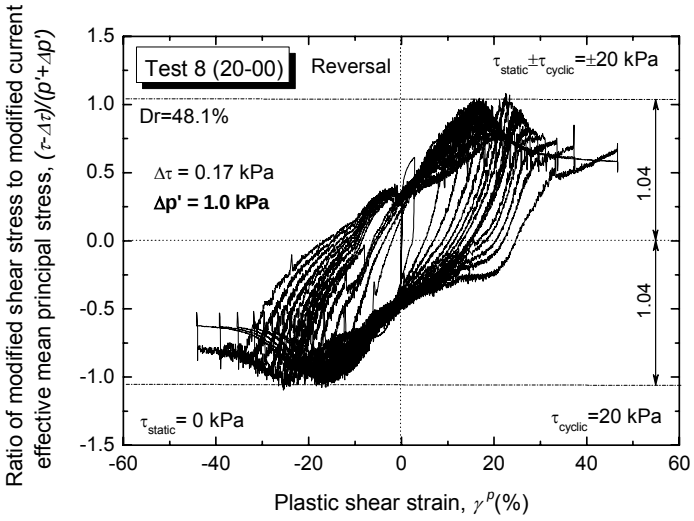

(b)

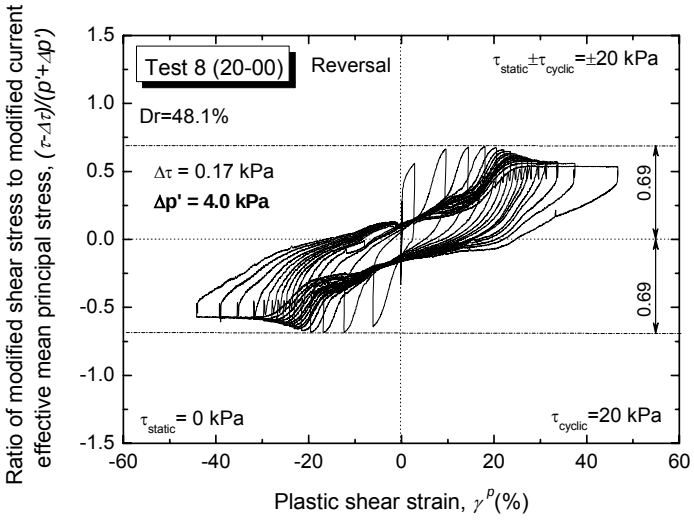

(c)

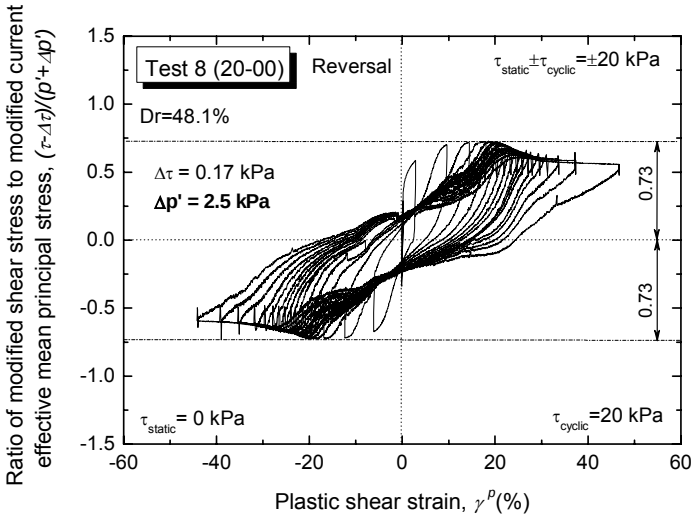

Fig. A.3: Effects of *Δp'* on the modified stress-strain relationship of fully reversal loading test

Appendix B

Rowe's stress-dilatancy equation and its applicability in torsional shear tests

B.1 Rowe's stress-dilatancy equation

Based on the assumption that the ratio of energy increment input to output of an assembly of spherical or cylindrical granular media is a constant (K), Rowe derived stress-dilatancy relationships for (a) triaxial compression, (b) triaxial extension and (c) simple shear loading conditions as shown below.

(a) Triaxial compression loading condition

Two equations were proposed according to the relative directions of σ_1' and $d\varepsilon_1^p$ (δ') as follows (refer to Fig. A.1 for the definition of δ'):

- When σ_1' direction coincides with the direction of $d\varepsilon_1^p$ (i.e., $\delta' = 0^0$)

$$\frac{\sigma_1'}{\sigma_3'} = K\left(\frac{-2d\varepsilon_3^p}{d\varepsilon_1^p}\right) \tag{B.1}$$

"p" denotes the plastic components of strain.

K is linked with the mobilized angle of friction ϕ_m at zero dilatancy ($d\varepsilon^p_{vol} = 0$) as shown below (note that *K* is different from the bulk modulus):

$$K = \frac{1+\sin\phi_m}{1-\sin\phi_m} \tag{B.2}$$

- When σ_1' direction coincides with the direction of $d\varepsilon_3^p$ (i.e., $\delta' = 90^0$)

$$\frac{\sigma_3'}{\sigma_1'} = K\left(\frac{-2d\varepsilon_3^p}{d\varepsilon_1^p}\right) \tag{B.3}$$

(b) Triaxial extension loading condition

- When σ_1' direction coincides with the direction of $d\varepsilon_1^p$ (i.e., $\delta' = 0^0$)

$$\frac{\sigma_1'}{\sigma_3'} = K\left(\frac{-d\varepsilon_1^p}{2d\varepsilon_3^p}\right) \tag{B.4}$$

- When $\sigma_1^{'}$ direction coincides with the direction of $d\varepsilon_3^p$ (i.e., $\delta' = 90^0$)

$$\frac{\sigma_3^{'}}{\sigma_1^{'}} = K\left(\frac{-d\varepsilon_1^p}{2d\varepsilon_3^p}\right) \tag{B.5}$$

(c) *Simple shear loading condition ($d\varepsilon_2 = 0$)*

$$\frac{\sigma_1^{'}}{\sigma_3^{'}} = K\left(\frac{-d\varepsilon_3^p}{d\varepsilon_1^p}\right) \tag{B.6}$$

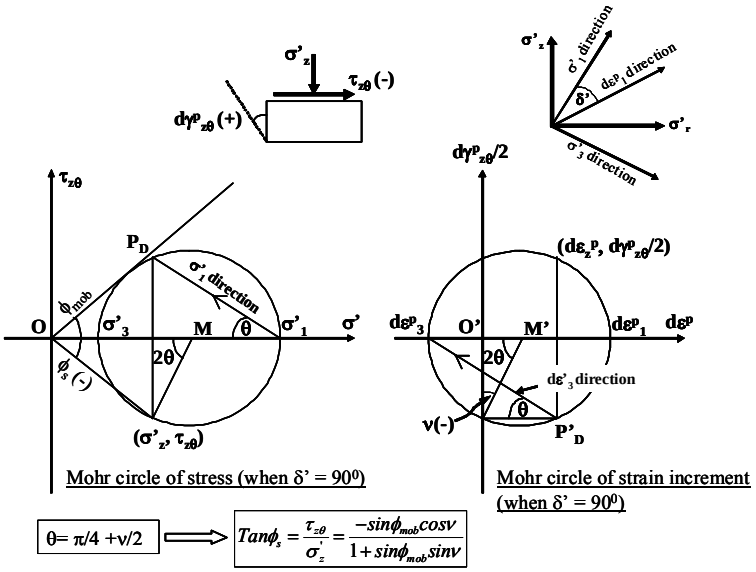

Fig. B.1: Mohr's circles of stress and strain increments
for simple shear deformation mode (after De Silva, 2008)

A.2 Applicability of Rowe's stress-dilatancy equation in torsional shear

De Silva (2008) attempted to investigate the applicability of Rowe's stress-dilatancy relationships in case of cyclic torsional shear loadings. In his study $\sigma_z'=\sigma_r'=\sigma_q'$=100 kPa and only $\tau_{z\theta}$ was varied (i.e., isotropic torsional shear, ITS), therefore

$$\sigma_1^{'} = p'+\left|\tau_{z\theta}\right| \tag{B.7}$$

$$\sigma_3^{'} = p'-\left|\tau_{z\theta}\right| \tag{B.8}$$

Note that Eq. (B.7) and Eq. (B.8) are valid only when $\sigma_z'=\sigma_r'=\sigma_q'$. Then the stress ratio can be expressed as follows

$$\frac{\sigma_1^{'}}{\sigma_3^{'}} = \frac{1+\dfrac{\left|\tau_{z\theta}\right|}{p'}}{1-\dfrac{\left|\tau_{z\theta}\right|}{p'}} \tag{B.9}$$

If it is assumed that $d\varepsilon_2^p = d\varepsilon_3^p$ during ITS loading, then $d\varepsilon_{vol}^p = (d\varepsilon_1^p + 2d\varepsilon_3^p)$. In addition, if $d\varepsilon_z^p \approx d\varepsilon_\theta^p \approx 0$ then $d\gamma_{z\theta}^p \approx (d\varepsilon_1^p - d\varepsilon_3^p)$. Therefore it can be written

$$-\frac{d\varepsilon_1^p}{d\varepsilon_3^p} = \frac{2-\left(-\dfrac{d\varepsilon_{vol}^p}{d\gamma_{z\theta}^p}\right)}{1+\left(-\dfrac{d\varepsilon_{vol}^p}{d\gamma_{z\theta}^p}\right)} \tag{B.10}$$

Subsequently the same formulation as derived for triaxial compression and extension can be used for torsional shear loadings as shown below:

- <u>When $\tau_{z\theta} > 0$ and $d\gamma_{z\theta}^p > 0$ ($\delta' = 0^0$)</u>

By substituting Eq. (B.9) and Eq. (B.10) into the Eq. (B.1) with the appropriate sign for $\tau_{z\theta}$, the following expression in terms of $\tau_{z\theta}/p'$ and $(-d\varepsilon_{vol}^p/d\gamma^p)$ can be written:

$$\frac{\tau_{z\theta}}{p'} = \frac{\left(\frac{-d\varepsilon_{vol}^{p}}{d\gamma^{p}}\right)(2K+1)+2(K-1)}{\left(\frac{-d\varepsilon_{vol}^{p}}{d\gamma^{p}}\right)(2K-1)+2(K+1)} \tag{B.11}$$

- When $\tau_{z\theta} > 0$ and $d\gamma_{z\theta}^{p} < 0$ ($\delta' = 90^{0}$),

By substituting Eq. (B.9) and Eq. (B.10) into the Eq. (B.5) with the appropriate sign for $\tau_{z\theta}$, the following expression in terms of $\tau_{z\theta} / p'$ and $(-d\varepsilon_{vol}^{p} / d\gamma^{p})$ can be derived:

$$\frac{\tau_{z\theta}}{p'} = \frac{-\left(\frac{-d\varepsilon_{vol}^{p}}{d\gamma^{p}}\right)(K+2)+2(K-1)}{\left(\frac{-d\varepsilon_{vol}^{p}}{d\gamma^{p}}\right)(K-2)-2(K+1)} \tag{B.12}$$

- When $\tau_{z\theta} < 0$ and $d\gamma_{z\theta}^{p} < 0$ ($\delta' = 0^{0}$),

By substituting Eq. (B.9) and Eq. (B.10) into the Eq. (B.4) with the appropriate sign for $\tau_{z\theta}$, the following expression in terms of $\tau_{z\theta} / p'$ and $(-d\varepsilon_{vol}^{p} / d\gamma^{p})$ can be formulated:

$$\frac{\tau_{z\theta}}{p'} = \frac{-\left(\frac{-d\varepsilon_{vol}^{p}}{d\gamma^{p}}\right)(K+2)+2(K-1)}{\left(\frac{-d\varepsilon_{vol}^{p}}{d\gamma^{p}}\right)(K-2)-2(K+1)} \tag{B.13}$$

- When $\tau_{z\theta} < 0$ and $d\gamma_{z\theta}^{p} > 0$ ($\delta' = 90^{0}$),

By substituting Eq. (B.9) and Eq. (B.10) into the Eq. (B.3) with the appropriate sign for $\tau_{z\theta}$, the following expression in terms of $\tau_{z\theta} / p'$ and $(-d\varepsilon_{vol}^{p} / d\gamma^{p})$ can be formulated:

$$\frac{\tau_{z\theta}}{p'} = \frac{\left(\frac{-d\varepsilon_{vol}^{p}}{d\gamma^{p}}\right)(2K+1)+2(K-1)}{\left(\frac{-d\varepsilon_{vol}^{p}}{d\gamma^{p}}\right)(2K-1)+2(K+1)} \tag{B.14}$$

Note that Eq. (B.11) and Eq. (B.14) are identical, and Eq. (B.12) and Eq. (B.13) are also identical. Therefore, two unique equations in terms of $\tau_{z\theta} / p'$ and $(-d\varepsilon_{vol}^{p} / d\gamma^{p})$ can be derived for $d\gamma_{z\theta}^{p} > 0$ (loading) and $d\gamma_{z\theta}^{p} < 0$ (unloading), irrespective of the sign of $\tau_{z\theta}$.

Similarly, other two unique equations in terms of $\tau_{z\theta} / p'$ and $(-d\varepsilon_{vol}^{p} / d\gamma^{p})$ for $d\gamma_{z\theta}^{p} > 0$ (loading) and $d\gamma_{z\theta}^{p} < 0$ (unloading) can be derived by assuming that the loading conditions in torsional shear are similar to those of simple shear (assuming $d\varepsilon_{2}^{p} = 0$ and $d\gamma_{z\theta}^{p} \approx (d\varepsilon_{1}^{p} - d\varepsilon_{3}^{p})$) as shown below.

- When $d\gamma_{z\theta}^{p} > 0$ (loading)

$$\frac{\tau_{z\theta}}{p'} = \frac{\left(\frac{-d\varepsilon_{vol}^{p}}{d\gamma^{p}}\right)(K+1)+(K-1)}{\left(\frac{-d\varepsilon_{vol}^{p}}{d\gamma^{p}}\right)(K-1)+(K+1)} \tag{B.15}$$

- When $d\gamma_{z\theta}^{p} < 0$ (unloading)

$$\frac{\tau_{z\theta}}{p'} = \frac{-\left(\frac{-d\varepsilon_{vol}^{p}}{d\gamma^{p}}\right)(K+1)+(K-1)}{\left(\frac{-d\varepsilon_{vol}^{p}}{d\gamma^{p}}\right)(K-1)-(K+1)} \tag{B.16}$$

The schematic illustration of stress-dilatancy relationships assuming simple shear loading conditions is shown in Fig. B.2

By referring to the Mohr's circles of stress and strain increments as shown in Fig. B.1 (for $\delta' = 90^{0}$ case), Pradhan (1990) derived more generalized stress-dilatancy relationships for cyclic simple shear loading conditions in which σ_{z}' and σ_{θ}' are not necessarily equal to each other, and $d\gamma_{z\theta}^{p}$ is not necessarily equal to $d\varepsilon_{1}^{p}$-$d\varepsilon_{3}^{p}$.

- When $\tau_{z\theta} > 0$ and $d\gamma^p_{z\theta} > 0$ ($\delta' = 0^0$)

$$\frac{\tau_{z\theta}}{\sigma'_z} = \frac{sin\phi_{mob} cos\nu}{1 - sin\phi_{mob} sin\nu} \tag{B.17}$$

where

ϕ_{mob} = mobilized angle of internal friction; and

ν = angle of dilatancy as shown in Fig. B.1.

It results that

$$\sin\nu = -\frac{\varepsilon^p_1 + \varepsilon^p_3}{\varepsilon^p_1 - \varepsilon^p_3} \tag{B.18}$$

$$\sin\nu = -\frac{\varepsilon^p_{vol}}{d\gamma^p_{z\theta}} \qquad (\text{since } d\varepsilon^p_{vol} = d\varepsilon^p_1 + d\varepsilon^p_3) \tag{B.19}$$

Furthermore,

$$sin\phi_{mob} = \frac{\sigma'_1 - \sigma'_3}{\sigma'_1 + \sigma'_3} \tag{B.20}$$

By combining Eq. (B.18) and Eq. (B.20) with Eq. (B.16) yields

$$sin\phi_{mob} = \frac{(K+1)sin\nu + K - 1}{(K-1)sin\nu + K + 1} \tag{B.21}$$

Then, by combining Eq. (B.19) and Eq. (B.21) with Eq. (B.17) yields

$$\frac{\tau_{z\theta}}{\sigma'_z} = \frac{(K+1)\left(-\frac{d\varepsilon^p_{vol}}{d\gamma^p_{z\theta}}\right) + (K-1)\left[1 + \left(-\frac{d\varepsilon^p_{vol}}{d\gamma^p_{z\theta}}\right)^2\right]^{\frac{1}{2}}}{(K+1)} \tag{B.22}$$

- When $\tau_{z\theta} > 0$ and $d\gamma^p_{z\theta} < 0$ ($\delta' = 90^0$)

$$\frac{\tau_{z\theta}}{\sigma'_z} = \frac{sin\phi_{mob} cos\nu}{1 + sin\phi_{mob} sin\nu} \tag{B.23}$$

$$\sin\nu = -\frac{\varepsilon^p_{vol}}{d\gamma^p_{z\theta}} \tag{B.24}$$

$$sin\phi_{mob} = \frac{-(K+1)sin\nu - K + 1}{(K-1)sin\nu + K + 1} \tag{B.25}$$

By combining Eq. (B.25) and Eq. (B.24) with Eq. (B.23) yields

$$\frac{\tau_{z\theta}}{\sigma_z^{'}} = \frac{(K+1)\left(-\frac{d\varepsilon_{vol}^{p}}{d\gamma_{z\theta}^{p}}\right) - (K-1)\left[1+\left(-\frac{d\varepsilon_{vol}^{p}}{d\gamma_{z\theta}^{p}}\right)^{2}\right]^{\frac{1}{2}}}{(K+1)} \qquad \text{(B.26)}$$

- When $\tau_{z\theta} < 0$ and $d\gamma_{z\theta}^{p} < 0$ ($\delta' = 0^0$)

The same equation as Eq. (B.26) can be derived.

- When $\tau_{z\theta} < 0$ and $d\gamma_{z\theta}^{p} > 0$ ($\delta' = 90^0$)

The same equation as Eq. (B.22) can be derived.

Therefore, two identical stress-dilatancy equations for $d\gamma_{z\theta}^{p} > 0$ and $d\gamma_{z\theta}^{p} < 0$, respectively can be derived in terms of $\tau_{z\theta}/\sigma_z^{'}$ and $-d\varepsilon^{p}{}_{vol}/d\gamma^{p}{}_{z\theta}$) for simple shear loading condition.

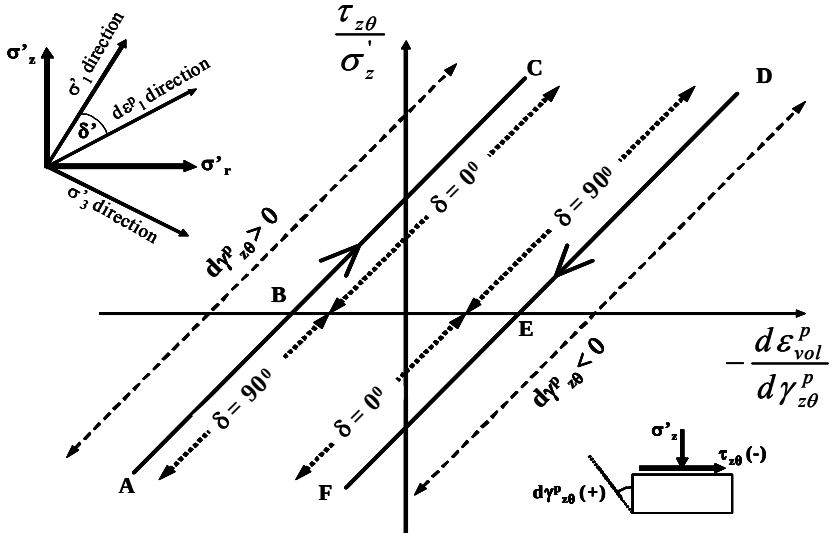

Fig. B.2: Schematic illustration of stress-dilatancy relationship for cyclic simple shear loading (after De Silva, 2008)